FATIGUE DAMAGE ACCUMULATION IN NICKEL BASE SUPERALLOYS

David Lambert

August 1994

Thesis submitted for the degree of Doctor of Philosophy

Department of Engineering Materials

University of Sheffield

FATIGUE DAMAGE ACCUMULATION IN NICKEL BASE SUPERALLOYS

David Lambert

Summary

Tangentially oriented Waspaloy specimens taken from the bore section of a turbine disc were subjected to low cycle fatigue in the form of cyclic four point bend tests. Substantial differences in grain size and structure occurred across the section of the disc. Fatigue damage occurred primarily as a result of persistent slip band formation, cell formation, Orowan looping and precipitate shearing. A small number of grains exhibited dislocation cells, normally associated with higher stacking fault energy materials. The number and width of persistent slip bands increased with the number of cycles, but varied both between grains and stress levels. It is proposed that initially looped precipitates were subsequently sheared. Crack initiation was observed as early as 1/12 of fatigue lifetime, predominantly from inclusions. A stage-I/stage-II crack propagation transition occurred at approximate ΔK_1 values of $30 MPa.m^{1/2}$, when the plastic zone size was comparable to the material grain size. Results imply that short crack growth requires prior slip band formation.

Acknowledgements

Contents

1 Introduction

1.1 The Gas Turbine

An aero engine provides thrust by the expansion of hot combustion gases through its turbine section. Air enters the engine and is compressed, fuel is then injected and the mixture is burned; this hot oxygen-rich exhaust gas then enters the turbine [1]. As with all heat engines, the efficiency is related to the maximum and minimum temperatures in the thermodynamic cycle; throughout the history of gas turbine development there has been a continuous rise in turbine entry temperature (TET) from 700°C for the Whittle engine in the 1940s, to the order of 1400°C in todays engines [1].

The hot gases expanding through the turbine stages rotate the turbine discs, which in turn rotate the compressor discs, hence generating thrust. Turbine discs are critical components which were originally designed for burst resistance, should overspeed occur, in the event of a shaft break [2]. The highest stresses were found at the bore of the disc where temperatures were lowest; at the rim, the temperatures were highest but stresses were relatively low [3]. Hence, the discs were initially specified for high creep and tensile strength.

However, in the late 1960s it was realised that the life limiting factor of turbine discs was low cycle fatigue (LCF), associated with temperature changes during the start-up and shut-down of the engine and with load changes during operation [4]. The LCF approach to this problem

involved retiring a component from service after its design life (based on LCF data) had been reached. However, this was very conservative and hence extremely expensive when compared to the "retirement for cause" approach. The latter approach allowed a component to be kept in service until a fatigue crack had been detected, relying on good non-destructive testing and the accurate prediction of fatigue crack propagation (FCP) behaviour. The economic benefits of the above approach encouraged the generation of many of the FCP and threshold data in existence for nickel base superalloys [5].

In recent years it has been shown that small fatigue cracks, the size of the order of a microstructural feature, propagate at higher rates than those of longer cracks [6]. If this was not accounted for by the "retirement for cause" method, then non-conservative life predictions could result in human and financial loss [7]. A significant amount of research into short fatigue crack behaviour has been undertaken in recent years, but there is scope for a better understanding. It was considered that an in-depth investigation of material damage accumulation leading to crack initiation, ought to allow more accurate fatigue lifetime prediction.

1.2 Turbine Disc Alloy Development

In the 1950s turbine discs were made from alloys of the G18B type, simple extensions of the austenitic steels available at that time [8]. Following the G18B alloys, were

Fe-Ni-Cr alloys such as Discaloy, V57 and A286, all hardened by additions of Al and Ti; also, using air cooling to reduce disc rim temperatures, facilitated the use of the modified 12%Cr steels such as FV448 and FV555 [8]. The specialist techniques of Electroslag Remelting (ESR) and Vacuum Arc-Remelting (VAR) allowed the development and service of these 12%Cr steels, which gave the necessary increase in creep and tensile strength until service temperatures rose to a point where nickel base superalloys had to be introduced. Waspaloy, Inconel 718 and Inconel 901 were introduced in the 1950s and became the major alloys for high pressure turbine discs [9].

The alloy development following the early nickel base superalloys slowed somewhat from the mid 1960s. Ever increasing TET requirements meant that alloys had to have higher strengths and therefore higher hardening contents, which consequently imposed forging difficulties [2].

This led to the more recent powder metallurgy superalloys such as hot-isostatically pressed (HIP) Astroloy, hot-isostatically pressed and forged (H+F) Astroloy, H+F Rene' 95, Merl 76 and NASA IIB-7 [10]. However, a major problem with these alloys was the presence of small scale inclusions, limiting their burst resistance and therefore the maximum stresses at which they could operate [2]. The conventional forged, wrought nickel base superalloy, Waspaloy, is therefore still used in civil engines such as the Rolls Royce RB211, where a disc burst would be catastrophic in terms of human and financial loss.

1.3 Project Aims

The aims of this investigation were:

* To investigate the grain size and mechanical properties of the tangentially oriented material in the bore section of a turbine disc.

* To investigate the fatigue endurance characteristics of tangentially oriented specimens from the bore section of a turbine disc, when subjected to different stress levels. In-service stresses are greatest in this region of a disc, especially the tangential or hoop stress.

* To establish the number of cycles to fatigue crack initiation and the prominent sites from which cracks initiate.

* To obtain back-thinned and cross-sectional thin foils from specimens cycled to various fractions of lifetime, to facilitate a three dimensional investigation of dislocation behaviour and study deformation with depth. In addition, to study fatigue damage accumulation in terms of dislocation behaviour and its interaction with crack initiation.

* To investigate differences in fatigue damage mechanisms or characteristics in terms of dislocation activity and slip band behaviour between different applied stress levels.

2 Literature Survey

Nickel base superalloys play an important role in the successful operation of aero engines; they are considered to possess the most complex microstructures of all superalloys, but are perhaps the best understood. The fatigue life of a component has two distinct aspects: the initiation of a crack, and the subsequent propagation of that crack, which results in failure. Fatigue crack initiation is strongly believed to be microstructure sensitive and dependent on temperature; in contrast, fatigue crack propagation (FCP) is normally treated as a linear elastic fracture mechanics problem, and hence microstructure does not play such an important role in its behaviour. A considerable amount of research has concentrated on crack propagation, and a great many design results obtained, however, substantially less attention has been directed towards crack initiation and the dislocation behaviour associated with it.

For the above reasons this literature survey will discuss nickel base superalloys in terms of the following:

Microstructure

Fatigue testing methods

Wrought superalloy low cycle fatigue

Cast, single crystal and columnar grained superalloys

Modelling of fatigue damage accumulation.

There will also be a short discussion concerning the fatigue of pure and lightly alloyed copper.

2.1 Microstructure

The microstructures of nickel base superalloys have received considerable attention, as reviewed extensively by Sabol and Stickler [11], Jena and Chaturvedi [12] and Ross and Sims [13]. Microstructures generally consist of an austenitic fcc matrix commonly called gamma (γ); this matrix contains a number of solid solution strengthening elements such as Co, Cr, Mo and W [13]. Cr and Al give the alloys oxidation resistance, and the high melting points of Ni and Co provide a basis for good mechanical properties at elevated temperatures [14].

The majority of nickel base superalloys are strengthened by the precipitation of gamma-prime (γ'), which provides antiphase boundary (APB) strengthening and precipitate/matrix mismatch strengthening. γ' consists of $Ni_3(Al, Ti)$ with an ordered fcc structure; Al and Ti are taken into solution during solution treatment and after quenching, a supersaturated solid solution is formed. During ageing treatments the γ' precipitates coherently with the matrix; examples of heat treatments and corresponding precipitate type, size and shape are given in Table 2.1. The particles are of $L1_2$ type structure, and may be spherical as in the alloys Inconel 700 [11], Waspaloy [15-18], Inconel 901 [15], Nimonic 80 [19-21] and Nimonic PE16 [22-24], or cuboidal like those contained in Mar-M200 and Udimet 700 [11]. Rene' 77 [25], Rene' 80 [26], Udimet 500 [27] and IN-738LC [28] are examples of cast superalloys which contain coarse cubic γ', surrounded by fine spherical γ'.

Alloy	Particle Type and Size (nm)	Heat Treatment
Inconel 901 [15]	γ' 25-30	A: 2h/1093/WQ + 2h/788/AC + 24h/718/AC.
Inconel 718 [29]	γ'' discs 30x5 thick γ' 20	B: 1h/955/AC + 8h/720, FC to 620 + 8h/620/AC.
Inconel 718 [15]	γ'' discs 20-30 x 5-9 thick	C: 1h/1066/AC + 8h/718, FC to 621 + 10h/621/AC.
IN-738LC [28, 30]	γ' 150 cube & 60	D: 2h/1120/? + 24h/845/?
Nimonic PE16 [22-24]	γ' 12.5	E: 0.5h/1040/OQ + 8h/750/?
Nimonic PE16 [22-24]	γ' 21	F: 0.5h/1040/OQ + 20h/750/?
Nimonic PE16 [22-24]	γ' 30	G: 0.5h/1040/OQ + 100h/750/?
Nimonic 80 [20, 21]	γ' 13	H: 2h/1050/AC + 16h/700/WQ.
Nimonic 80 [21]	γ' 5	I: 2h/1050/AC.
Nimonic 80 [21]	γ' 20	J: 2h/1050/AC + 40h/700/WQ.
Nimonic 80 [21]	γ' 13 & 100	K: 2h/1050/AC + 16h/700/WQ + 3h/950/WQ + 16h/700/WQ.
Rene' 77 [25]	γ' 250 cube & 50	L: 4h/1168/AC + 4h/1080 + 24h/843/AC + 16h/760/AC.
Rene' 80 [26, 31]	γ' cubes & small	M: 2h/1205/HeQ (to RT) + 4h/1093/HeQ (to RT) + 4h/1052/FC to 649 + 1/3h/649/AC + 16h/843/AC.
Udimet 500 [32]	γ' coarse & fine	N: 4h/1168/AC + 4h/1080/AC + 16h/760/AC.

<u>continued</u>

Alloy	Particle Type and Size (nm)		Heat Treatment
Udimet 700 [33]	γ'	blocky	O: 4h/1163/AC + 4h/1080/AC + 4h/843/AC + 16h/760/AC.
Waspaloy [15]	γ'	30-40 & 200-250	P: 4h/1010/OQ + 4h/843/AC + 16h/760/AC.
Waspaloy [15]	γ'	40-50	Q: 4h/1038/? + 16h/760/AC.
Waspaloy [16]	γ'	8	R: 2h/1040/OQ + 6h/730/?
Waspaloy [16]	γ'	25	S: 4h/1010/OQ + 4h/850/AC + 15h/760/?
Waspaloy [16]	γ'	50	T: 2h/1040/OQ + 24h/825/?
Waspaloy [16]	γ'	90	U: 2h/1040/OQ + 24h/875/?
Waspaloy [17, 34]	γ'	5-8	V: 2h/1010/OQ + 24h/875/OQ.
Waspaloy [17, 34]	γ'	90 & 300	W: 2h/1100/OQ + 6h/730/OQ.
Waspaloy [35]	γ'	30 & 150	X: 4h/1010/OQ + 4h/850/AC + 16h/720/AC.
Waspaloy [18]	γ'	?	Y: 4h/1020/OQ + 4h/850/AC + 16h/760/AC.
Waspaloy [36]	γ'	30 & 160	Z: 4h/1010/OQ + 4h/850/AC + 16h/760/AC.

AC: air cool, FC: furnace cool, WQ: water quench, OQ: oil quench, HeQ: helium quench. (All temperatures in °C).

Table 2.1: Superalloy Heat Treatments.

The addition of carbon combines with reactive and refractory elements to form MC type carbides. During heat treatment and service these decompose and may generate lower carbides, for example $M_{23}C_6$ [13]. The MC usually has a

blocky morphology and is found throughout the matrix [14];
the "M" typically represents Ti, but may be substituted for
by Nb, Ta, W, Mo or Cr [11]. The $M_{23}C_6$ is generally situated
on grain boundaries, where "M" is usually Cr, but may be
replaced by Mo, Ni, Co, Ti, W or Nb [11].

Under certain conditions, topologically close packed
(TCP) type phases such as sigma, mu and Laves may form,
which are detrimental to the rupture strength and ductility
of superalloys [13]. Waspaloy is not, in general,
susceptible to TCP phase formation but it is conceivable
that in extreme cases some may form [14].

Heat treatment determines the microstructural features
present in superalloys; Waspaloy can be conditioned for
small, large and bimodally distributed precipitate sizes. In
fatigue studies Stoltz and Pineau [16], Lerch et al. [17]
and Jayaraman and Ditmars [34], all employed Waspaloy
specimens containing either small, or large γ'. With such
materials, the differences in deformation behaviour could be
correlated with the different particle sizes. Alternatively,
Merrick [15] and Clavel et al. [35], have tested Waspaloy
having bimodal distributions, the results of which are
probably more representative of real life turbine disc
alloys, which also have bimodal distributions, but are
perhaps more difficult to interpret.

2.2 Fatigue Testing Methods

Low cycle fatigue tests in general were carried out on
servohydraulic machines, with dog bone, button head or hour

glass types of specimen [15-18, 20-23, 25, 29, 33, 35-39] using fully reversed (R = -1) push pull cycling [10, 15, 17, 18, 21-23, 33, 35-38, 40] under either total or plastic strain control [10, 15, 16, 20-25, 29, 33-39, 40].

Triangular waveforms were utilised by a number of workers [18, 21, 41] and frequencies in the range 0.03-0.33Hz were typical [10, 19, 21, 25, 35, 41], allowing plotters adequate time to record hysterisis loop data [33, 42]. Frequencies were often varied between elevated temperature tests, or in some cases, periods of dwell were introduced in order to study the effects of creep and oxidation at low frequencies [10, 39].

Specimens were either manufactured from billet or bar stock and conditioned accordingly [16, 17, 25, 35], or were machined from actual turbine discs [18, 43, 44]. Those from the former group gave the advantage of allowing fatigue to be studied, for example, as a function of precipitate size [16, 17, 22-24] whereas the latter specimens would obviously exhibit behaviour more representative of real life applications.

Fatigue work was carried out with configurations different to the tension tests previously noted, i.e. torsion [34, 44, 45], bending [44-48] and combinations [34], since it was reported that real life fatigue was not as straightforward as simple tension [34]. Yates [45] and Grabowski and Yates [44] undertook a significant amount of research into what effects the different geometries had on fatigue behaviour. The findings indicated that torsion

10

testing gave an equivalent lifetime to tension, four point
bending gave a slightly longer life, whereas three point
bending gave a much greater life [45]. Grabowski and Yates
[44] noted that the torsion geometry exhibited a large
degree of scatter, whereas the three point bend
configuration had the least [44]. Yates [45] did, however,
report that three point bending was considered unsuitable
due to its rapidly changing stress field on the surface at
the centre of the specimen.

2.3 Wrought Superalloys

2.3.1 Room Temperature Low Cycle Fatigue

2.3.1.1 Cyclic Response

During a fatigue test under strain control, the
response stress will fluctuate according to the strain
applied and the influence of the microstructure (see Table
2.2).

In general, superalloys containing small precipitates
exhibit hardening to a peak stress followed by softening,
e.g. Nimonic PE16 [22, 23, 49], Nimonic 80 [19-21], Udimet
700 [33, 49] and Waspaloy [16, 17, 50]. In the case of
Inconel 718, the precipitates involved were extremely small
and the alloy essentially softened, if there was a hardening
component it was very small [15, 36].

For alloys having large precipitates, the response
stress increased to such a level where saturation occurred,
followed by fracture without any softening, eg. Waspaloy
[16, 17]. For alloys containing bimodal distributions of

Alloy	Particle Type and Size (nm)		HT*	Behaviour
Inconel 901 [15]	γ'	25-30	A	RT & 538°C: hardening then softening/looping then shearing.
Inconel 718 [29]	γ'' discs γ'	30x5 thick 20	B	RT: slight hardening then softening. 550°C: softening.
Inconel 718 [36]	γ'' discs	30x5 thick	B	RT & 650°C: essentially softening.
Inconel 718 [35]	γ'' discs γ'	30x5 thick 20	B	RT & 650°C: softening/ shearing.
Inconel 718 [15]	γ'' discs	20-30 x 5-9 thick	C	RT: slight hardening then softening/shearing. 538°C: softening/shearing.
Nimonic PE16 [22-24]	γ'	12.5	E	RT: hardening then softening /shearing and dissolution.
Nimonic PE16 [22-24]	γ'	21	F	hardening then softening /shearing and fragmentation.
Nimonic PE16 [22-24]	γ'	30	G	hardening then softening /shearing and fragmentation.
Nimonic 80 [20, 21]	γ'	13	H	RT: hardening then softening/cells.
Nimonic 80 [19]	γ'	13	H	RT: hardening then softening. 300 & 500°C: hardening. 700 & 800°C: softening.
Nimonic 80 [21]	γ'	5	I	RT: hardening then softening.
Nimonic 80 [21]	γ'	20	J	RT: hardening then softening.
Nimonic 80 [21]	γ'	13 & 100	K	RT: hardening then softening.

<u>continued</u>

Alloy	Particle Type and Size (nm)		HT*	Behaviour
Udimet 700 [33]	γ' blocky		O	RT: hardening then softening.
Udimet 700 [37]	γ' blocky		O	760°C: less hardening/ more softening.
Udimet 700 [38]	γ' blocky		O	205°C: hardening to saturation. 327 & 427°C: hardening.
Waspaloy [15]	γ' 30-40 &	200-250	P	RT: hardening then softening /looping then shearing. 538°C: more hardening some softening/more looping.
Waspaloy [15]	γ' 40-50		Q	RT: less hardening more rapid softening/looping then shearing.
Waspaloy [16]	γ' 8		R	RT: hardening then rapid softening/shearing.
Waspaloy [16]	γ' 25		S	RT: hardening some softening /looping and shearing
Waspaloy [16]	γ' 50		T	RT: hardening to saturation/ looping.
Waspaloy [16]	γ' 90		U	RT: greater hardening to saturation/looping.
Waspaloy [17, 34]	γ' 5-8		V	RT & ET: dislocation pairing /planar deformation.
Waspaloy [17, 34]	γ' 90 &	300	W	RT & ET: looping.
Waspaloy [35]	γ' 30 &	150	X	RT: hardening then softening /looping then shearing. 650°C: more hardening.
Waspaloy [18]	γ' ?		Y	500 & 650°C: planar slip/ shearing.
Waspaloy [36]	γ' 30 &	160	Z	RT & 650°C: hardening then slight softening.

* HT: heat treatment, from Table 2.1.
RT: room temperature, ET: elevated temperatures.

Table 2.2: Wrought Superalloy Deformation Behaviour.

precipitates, the cyclic response behaviour was similar to that of the small precipitate alloys, i.e. hardening to a maximum then softening [15, 35].

2.3.1.2 Cyclic Hardening

In nickel base superalloys, cyclic hardening was associated with increases in dislocation densities [17, 51], and the restriction of mobile dislocations by the dislocation tangles at slip band intersections [21, 51]. It was reported that during cyclic hardening, localised areas of increasing strain necessitated the formation of slip bands, the number of bands being dependent on the strains involved [16, 20, 23, 51]. Numerous observations were made of slip bands forming from the onset of cycling [16, 20, 21, 33, 49], and although Fournier and Pineau [29] reported slip bands developing gradually during cyclic softening, their Inconel 718 alloy contained very small precipitates and hardened for only a very small proportion of lifetime.

Miner et al. [10] noted that response stress increased with increasing volume fraction of γ' for numerous alloys which were tested under identical conditions; in addition, the degree of hardening increased with increasing precipitate size [15, 16, 23]. Dislocations bowed between the larger precipitates, which resulted in Orowan loops in the slip plane [15-17]. Merrick [15] explained that this would give local hardening in the slip plane and hence the resultant hardening in fatigue would be greater.

Both the degree of hardening [10, 17, 23] and the

14

response stress [19-21] also increased with increasing strain amplitude. Antolovich and Lerch [51] proposed that the reason for less work hardening at lower strain ranges (see Fig. 2.1) was that deformation occurred on only one slip plane. Numerous workers observed only single slip after testing at low strain ranges [10, 21-24] and in certain cases maintaining low strains during testing was actually specified [10, 22]. Miner et al. [10] stated that inelastic strains were kept low in gas turbine discs because of the long lives required; it was perhaps for this reason that such test conditions were specified. At higher strains, as multiple slip occurred [20, 21, 23], and the deformation substructure restricted the dislocation motion to a greater extent, then work hardening increased [51]. Lerch and Gerold [21] proposed that at low strain ranges ($\Delta\varepsilon < 0.42\%$), dislocations moved back and forth from one side of a grain to the other, on one slip system only, therefore experiencing long range stresses only from grain boundary pile-ups. At higher strain ranges, where more than one slip system was operative, the dislocations could only move from one intersection to the next and pile-up; dislocation movement was therefore more restricted and gave rise to greater hardening [21]. Lerch and Gerold [21] formed a relationship between the cyclic hardening component and the slip band spacing which is detailed in section 2.7.2.

At low plastic strain ranges ($\Delta\varepsilon_p < 2\%$ [20, 21]) the number of cycles at which the response stress peaked was fairly constant, irrespective of strain amplitude [16, 19,
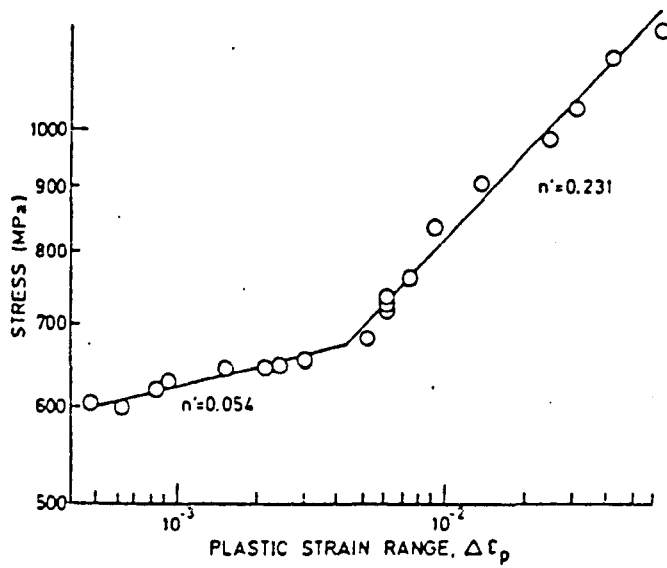
Fig. 2.1. Cyclic stress-strain curve for Nimonic 80 tested at room temperature. Specimens work hardened less when tested at low plastic strain ranges [51].

20, 23], whereas at higher strain levels the number of cycles to attain peak stress was observed to reduce with increasing strain amplitude [20, 23, 29]. At the low strain amplitudes where only a single slip system was operative [21, 23, 51] if, as Stoltz and Pineau [16] assumed, the kinetics of hardening and softening within each slip band were independent of strain amplitude, then the maximum response stress should be achieved within a constant number of cycles. At the higher strain amplitudes, Lerch and Gerold [20] proposed that the full slip band density was quickly reached and since no new bands could be added, the amount of shear in each band must have increased which led to the movement of the peak stress to lower cycle numbers. The authors explained that this shift could have been accomplished by other mechanisms such as grain rotation or twinning [20].

The above descriptions were based on observations of slip band formation at the onset of cycling [16, 20, 21, 33, 49]. However, for alloys which hardened to a saturation stress, the dislocation behaviour was not localised within slip bands and therefore Stoltz and Pineau [16] proposed the following mechanism. Dislocation interactions that occur around the precipitates force dislocations out of their primary slip plane, creating a plastic zone around each particle. The link up of these zones, it was suggested, results in a three dimensional homogeneous substructure, with a dislocation network filling the grain volumes, and the eventual cyclic stability of the material [16].

2.3.1.3 Cyclic Softening

Fatigue softening was associated with the shearing of
small precipitates [15, 16, 33], by the paired glide motion
of a/2<011> dislocations [10, 49, 52-56], in slip bands
aligned in {111} orientations [19-21, 55], right from the
onset of cyclic deformation [20].

It appears that the mechanism proceeds in the following
manner: once the dislocation density within a material has
built up sufficiently (during hardening), the effective
stress is high enough for a dislocation to penetrate a
particle [17]. The cutting of an ordered precipitate creates
an antiphase boundary (APB) within the γ', which has a
positive energy associated with it, and this energy is
minimised by the pairing of dislocations [5, 19, 55]. The
first dislocation introduces the APB, the next one removes
it [5, 19]. The passage of dislocation pairs reduces the
effective precipitate diameter within the slip plane, by a
distance of two Burgers vectors [5, 19]; since cross-slip is
unlikely at low temperatures, the next pair of dislocations
will continue to shear the precipitate along the same plane
as the first pair [51]. The reduced cross-section in the
slip plane makes it easier for the next dislocation pair to
shear the precipitate at a lower stress level, and the
result is softening [17].

Antolovich and Lerch [51] suggested that it was
possible for particle shearing mechanisms to be in operation
early in the fatigue process. They proposed that the
softening was masked by the rapid hardening previously

17

discussed, and the fact that both hardening and softening mechanisms were in operation simultaneously would explain why alloys containing small precipitates hardened to a lesser extent than those with large particles. Merrick [15] supported this comment by demonstrating that if precipitates were sheared at the beginning of deformation in the first cycle, then softening should have occurred earliest in Inconel 718, compared to Waspaloy and Inconel 901, since 718 contained the finest dispersed precipitates. Lerch and Gerold [21] agreed that softening occurred from the onset of cycling, but was masked by the hardening component which ceased when an equilibrium number of slip bands were present to accommodate the plastic strain.

Merrick [15] proposed that the larger the precipitate, the lesser was the softening rate. This is consistent with the studies of Stoltz and Pineau [16] for their Waspaloy alloys, who proposed that in order for softening to be complete, shearing must have occurred on each slip plane that intercepted the particle. The occasional Orowan loop remaining around a large precipitate in the slip band, would interact with dislocations on other slip planes. This would spread out the shearing action over a wider distance, and instead of being sheared on each slip plane, the precipitates would be fragmented. Some softening would occur, but not to the extent of an alloy which contained small precipitates [16].

Antolovich and Lerch [51] proposed that as cycling proceeded, and an increasing number of dislocations sheared

the precipitates, particles could become completely sheared and offer no further resistance to dislocation motion in that particular slip plane.

Uncertainty exists concerning the mechanism ultimately responsible for fatigue softening. Numerous workers have reported particle shearing by dislocations [15-17, 20-24]; Merrick [15], King [5] and Decker [57], suggested that in addition to particles being cut by dislocations, they were eventually dissolved in the slip bands. One reason Merrick [15] offered for this, was his inability to image any precipitate fragments within the slip bands of his fatigued alloys.

Stoltz and Pineau [16] applied the work on an Al-4%Cu alloy of Calabrese and Laird [58] to their small γ′ Waspaloy alloy. Calabrese and Laird [58] proposed that during cyclic hardening, dislocations continually sheared particles and formed APBs; since the dislocations were highly jogged and ragged and continually reacted, their to and fro motion took irreproduceable paths. This to and fro motion of dislocations through different paths caused a mechanical scrambling of the atoms in the precipitates i.e., they became disordered [58]. Stoltz and Pineau [16] adopted the above explanation for softening since they found it impossible to image γ′ within deformation bands from superlattice reflections. They reported that within slip bands, particles were sufficiently randomly sheared so as not to produce any superlattice intensity [16]. Stoltz and Pineau [16] reinforced the above hypothesis by explaining

19

that if precipitates had been disordered, then intermediate short time annealing treatments ought to have re-established the local order and recovered the softening component, which was what they observed.

Lerch and Gerold [20] claimed that softening in their Nimonic 80 specimens occurred through continual reduction in size of the γ' strengthening phase within the slip plane, which led to an increasing ease of dislocation movement. In this case the γ' free slip bands were attributed to i) the extremely high dislocation density within a band whose strain contrast obscured the image of the precipitates and/or ii) local tilting of the matrix region between two slip planes sheared in opposite directions [20]. Lerch and Gerold [20] demonstrated that tilting of this matrix region to the Bragg condition revealed the γ' and it had therefore not been dissolved. In addition, Lerch [14] agreed that γ' was stable up to very high temperatures, hence dissolution was extremely unlikely.

Sundararaman et al. [22] however, disagreed with the tilted local matrix proposition of Lerch and Gerold [20], since tilting experiments performed on their Nimonic PE16 alloys did not reveal any γ' particles within deformation bands. The authors agreed somewhat with Stoltz and Pineau [16], in so far as that if precipitates were disordered during cycling, then short time annealing ought to have restored their order, leading to the observed strengthening. Indeed, similar experiments performed on Nimonic PE16 [23] showed an increase in response stress after intermediate

annealing, test conditions being similar to that of Stoltz and Pineau [16]. However, Sundararaman et al. [23] argued that if mechanical shearing had resulted in atomic rearrangements over small distances of the order of a few atom spacings leading to disordering of precipitates, then intermediate annealing experiments should have given rise to γ' particles of initial size within deformation bands. The results of Sundararaman et al. [22, 23] were contrary to this; microstructural investigations after annealing but before re-deforming revealed very fine precipitates, much smaller than the initial γ' size. Consequently they proposed the mechanism of particle dissolution which was dependant on fatigue life for their alloy containing 12.5nm γ' and particle fragmentation for their alloys with 21 and 30nm γ' [22]. Should a specimen have failed prematurely, then fragmented particles would remain in such a condition; if a specimen had a long life, then fragmented particles would continue to be further fragmented until they were dissolved within slip bands [22]. A qualitative model describing the softening process was offered [22], which is detailed in section 2.7.3.

2.3.1.4 Deformation Homogeneity

Inhomogeneous planar slip, where deformation is confined to slip bands was associated with the shearing of small particles [5, 10, 15, 17, 34, 35, 41, 51, 59-61]. King [5] explained that the low stacking fault energy (SFE), inherent in many superalloys, made cross-slip difficult,

resulting in strongly planar deformation. She noted that in addition to the low SFE of the matrix, dislocation pairing also encouraged planar deformation by making cross-slip difficult. Antolovich and Lerch [51] agreed with the dislocation pairing, adding that the coherency of the precipitates with the matrix also discouraged cross-slip. Lerch and Gerold [19] further agreed that for γ' strengthened alloys, the shearing of γ' in a single glide plane reduced the resistance against further shearing for following dislocations but only in that particular glide plane, hence making cross-slip extremely difficult.

Homogeneous slip, that is, a dislocation substructure which completely fills the grains, interband volume in addition to slip band volume, was associated with the dislocation looping of large particles [15-17, 34, 51, 61]. Alloys containing bimodal distributions of precipitates deformed in a planar manner, similar to those alloys containing only small particles [15, 35].

Numerous attempts were made to study the tendency of an alloy to deform inhomogeneously [15-17, 35, 52, 54, 62, 63]. Decker [52] reported that beyond a certain γ' size, dislocation by-passing would occur by either looping or climb; Hornbogen and Verpoort [62] constructed the graph shown in Fig. 2.2 describing the transition from shearing to looping in terms of shear stress. Graf and Hornbogen [63] indicated that the tendency for homogeneity was also dependent on particle volume fraction, APB energy and the distribution of the precipitates. Stoltz and Pineau [16]

22
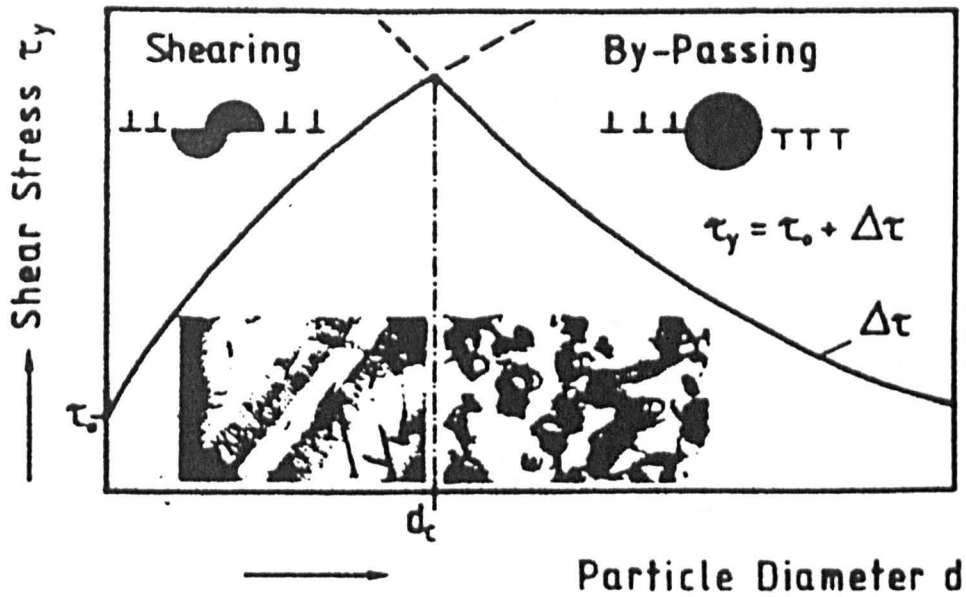
Fig. 2.2. Transition from shearing to by-passing as a function of particle diameter [62].

investigated the inhomogeneity of deformation in Waspaloy specimens conditioned in numerous ways to contain various sizes of γ′. They reported that the critical particle size for the shearing/looping transition was 25nm [16]. Lerch et al. [17] supported this statement, noting that their 8nm γ′ Waspaloy alloys failed due to precipitate shearing, whereas Orowan looping was responsible for failure of their 100nm γ′ alloy. Behaviour contrary to the above was reported by Merrick [15] and Clavel et al. [35], for their bimodally distributed γ′ Waspaloy alloys. Shearing had occurred in both 200-250nm γ′ [15] and 150nm γ′ [35], i.e. shearing in γ′ larger than the critical size reported by Stoltz and Pineau [16].

Merrick [15] proposed that initially, dislocations bowed between the large particles generating dislocation loops, but eventually shearing of the γ′ resulted. In direct agreement, Brechet and Louchet [64] demonstrated that Orowan loops around spherical coherent ordered precipitates by-passed by dislocations may become unstable when the stress was greater than a critical value. This method of "delayed shearing" was demonstrated in an overaged Al-Li alloy and Brechet and Louchet [64] proposed that it ought to be observed in superalloys. In addition, Nembach et al. [65] observed the immediate shearing of small γ′, the cutting of the larger γ′ in Nimonic 105 occurred later; this in-situ work was however, carried out during tensile testing as opposed to fatigue.

As discussed in section 2.2, most of the fatigue work

23

reported was undertaken with low cycle fatigue type specimens in push pull mode. In general, discs for thin foil manufacture were cut adjacent to the fracture surface, i.e. normal to the tensile axis [10, 16, 22-24, 29, 41]. The distance from the thin foil useable area to the fracture surface was not usually stated, however, Diederich et al. [41] estimated this as 0.2μm in their analysis of Waspaloy. The inhomogeneous deformation extensively reported in the literature was observed from this type of foil, i.e. workers were reporting fatigue behaviour in the interior of specimens [10, 22, 23, 29, 33]. Lerch and Gerold [19, 20] reported similar observations in their foils taken perpendicular to the stress axis, but by back-thinning surface foils taken parallel to the stress axis, they observed more homogeneously distributed dislocation structures. Dislocation cells and hexagonal networks of dislocations along with slip bands running parallel to {111} planes were present. Lerch and Gerold [19, 20] reported that the cellular structures were related to the bands, and that this surface deformation was not observed in the interior grains of their specimens. A homogeneous cellular dislocation structure was observed in Astroloy [10] which contained 44% volume fraction γ' in the form of large cuboids. Miner et al. [10] noted that the dislocations had difficulty cutting the large particles and were consequently jammed in between them, so generating the cells.

2.3.1.5 Crack Initiation

At room temperature, crack initiation in wrought superalloys generally occurs transgranularly [29, 33, 36] in regions of localised plastic strain [66].

Slip band cracking was observed by numerous workers [20, 29, 43, 45, 49, 62, 67] where it was reported that cracking occurred along slip bands inclined at between 30° and 60° to the stress axis [43], along side of the band [45], on intrusions at the edges of slip steps [62] and at the interface between slip band extrusions and the matrix [29]. Slip band cracking was in fact reported to be the dominant deformation mechanism of fatigue crack formation [43], and has been associated with the slip planarity noted in superalloys [51]. Antolovich and Lerch [51] explained that planar deformation caused slip steps at the surface of the material, which acted as stress raisers, and initiated cracks.

Both Lerch et al. [17] and Merrick et al. [60], suggested that inhomogeneous planar slip was the possible reason for early crack initiation. The former blamed the high concentration of dislocation activity contained within the slip bands, while the latter related the problem to the large slip offsets present. Feltner and Beardmore [66] added that where γ' had been sheared by dislocations, precipitate free regions would be present and strain concentrations could occur at these soft spots hence promoting crack initiation.

Lerch and Gerold [19] noted that the slip band

extrusions observed on their Nimonic 80 specimens were formed just after the response stress peak, i.e. during the initial stages of softening. Antolovich and Lerch [51] proposed that for alloys containing large precipitates, because the slip bands were less well defined and were less frequent on the surface, crack initiation was more difficult as compared to a small γ' material. They suggested that microcracks did form and were responsible for the stress drop after the saturation value [51]. Wells and Sullivan [33] explained that the final drop off in response stress was due to the propagation of a large microcrack to a critical area for brittle fracture.

Suresh and Ritchie [68] reported that cracks in pure metals and alloys tended to initiate from slip bands whereas in commercial materials, inclusions and intermetallics were the responsible sites. MC and titanium carbides were commonly observed as crack iniators in wrought alloys by Gell et al. [49], who explained that MC carbides may contain cracks from processing, may become fractured from machining, or, initially sound carbides could become fractured by the impingement of slip bands on the high tensile strain matrix. It was mentioned that although the residual compressive stress on the carbide from processing may have prevented particle fractures from opening up under tension, it far from eliminated the problem [49].

Coherent twin boundaries were reported as the most prominent sites for crack initiation in Udimet 700 [33] and as significant for cracking in wrought superalloys in

general [49]. Gell et al. [49] suggested that the absence of γ' precipitation across twin boundaries would account for the low resistance to crack initiation.

Other observed room temperature crack initiation sites were grains containing slip bands where the crack was not aligned parallel to the bands, grains with no apparent slip bands and grain boundaries [45]. In addition, inclusions were noted as strain concentrators and just how detrimental to the fatigue resistance of the alloy they were, depended on size and shape, location relative to the fatigue surface and orientation to the tensile stress axis [66]. Furthermore, Wells and Sullivan [33] stated that it was possible for a crack to cause enough increased activity on a slip system ahead of itself, to promote further cracking there.

It is apparent that fatigue crack initiation is not independent of strain. At low strains, fracture usually occurred from a single surface source, whereas the link up of numerous cracks was responsible for fatigue failure when high strains were involved [37, 49].

A considerable amount of work was carried out on small fatigue cracks [6, 46, 67-69, 70-74] because it became apparent that linear elastic fracture mechanics (LEFM) could not accurately describe the behaviour of such small cracks [6, 46, 70]. Miller [6, 69] proposed that crack initiation occurred immediately in metal fatigue, the initial crack size being 2-3μm corresponding to the roughness of the best engineered surface [69], or zero since the growth of a crack

from 0 to 3μm made minimal difference to lifetime [6].
Miller [69] explained that the reason no cracks were
observed in the first few cycles of a fatigue test was
because they were extremely difficult to locate. Anton and
Fine [75] supported Miller's views, reporting cracks as
small as 45nm observed almost immediately upon the cycling
of their Ni-Al alloy.

Miller [73] argued with reports which related the
fatigue limit to the inability of a material to initiate a
crack, alternatively, he proposed that the fatigue limit was
a limit on the ability of a crack, whatever its length, to
propagate to failure. Supporting the above, Yamada et al.
[72] and Lukas et al. [71] reported the existence of
non-damaging notches and tolerant microflaw sizes,
rationalised as cracks which could nucleate but not
propagate below the fatigue limit.

2.3.1.6 Crack Propagation

Fatigue crack propagation at room temperature generally
occurs in a transgranular mode [17, 33, 49], or in a mixture
of trans- and intergranular modes [15]; cracks of a size
comparable to the scale of the grain size in a material,
were shown [76] to propagate at several times the speed of
long cracks at nominally identical stress intensity factors.
In addition, microstructural barriers, e.g. grain boundaries
and the different orientations of slip from grain to grain,
were effective in retarding or even arresting the
propagation rate of these small cracks [6, 77, 78]. Hence it

was considered that the growth of cracks whose lengths were less than two or three grain diameters, was strongly associated with material anisotropy and textures [6].

Initial (Stage-I) crack propagation was reported to occur along {111} slip bands, i.e. crystallographic slip planes experiencing the maximum resolved shear stress [79] within the crack tip plastic zone [80], leaving a highly crystallographic and faceted fracture surface [80-83]. King [5] reported that faceted growth generally occurred in superalloys when the plastic zone was confined to individual grains at the crack tip, i.e. low values of stress intensity factor (non-continuum mechanics), so that the centre of each grain deformed primarily as a single crystal and only a single slip system was active. The regularly observed {111} oriented facets formed on fracture surfaces during stage-I propagation were reported to be due to the highly localised slip on {111} planes, i.e. due to the low SFE inherent within superalloys and APB formation and anihilation [55].

After a specific crack length, propagation was reported to undergo a transition from a stage-I mode to a stage-II mode occurring in a direction perpendicular to the maximum opening stress [79]. In this regime flatter, often striated fracture surfaces were observed when the crack tip plastic zone had extended across numerous grains and had activated several slip systems; this was necessary for compatible deformation and led to the development of more homogeneous deformation structures [81-83]. It is within this stage-II or "Paris" regime that the LEFM techniques apply and are

discussed in section 2.7.7.

2.3.2 Elevated Temperature Low Cycle Fatigue

As temperature is increased, deformation becomes more complex, since creep and the effects of the environment become more significant [5, 51, 84], as discussed below.

2.3.2.1 Cyclic Response

Confusion exists concerning the elevated temperature cyclic response of superalloys. Reports of alloys exhibiting a lesser hardening or greater softening effect were made for Waspaloy [17], Udimet 700 [37], Nimonic 80 [19] and Inconel 718 [29]. Fournier and Pineau [29] stated that the inhomogeneity of plastic deformation was more pronounced at elevated temperatures, from their observations of more intense slip bands and more pronounced twinning. The authors proposed that greater twinning at higher temperatures would have a significant effect on the cyclic response curves, but did admit that further work and a clearer understanding were required [29].

In direct contrast, a greater hardening or lesser softening effect was exhibited by Waspaloy [35] and Inconel 718 [15, 35]. Clavel et al. [35] explained that the greater homogeneity of deformation at elevated temperatures i.e., the somewhat reluctant occurrence of precipitate shearing and the much more evenly dispersed deformation, led to a greater hardening in their Waspaloy specimens.

In addition, some superalloys which had exhibited

hardening to a peak stress followed by softening at room temperature, were reported to harden to a saturation stress at certain elevated temperatures. Waspaloy at 500°C [17], Udimet 700 at 205°C [38] and Nimonic 80 at both 300 and 500°C [19] all exhibited this continual hardening to saturation characteristic. Strain ageing was the mechanism suggested as responsible [17, 19, 38, 85] and is discussed in section 2.3.2.3.

2.3.2.2 Deformation Homogeneity

Confusion also exists concerning the changes in fatigue deformation mechanisms at elevated temperatures. As temperature was increased, deformation became more homogeneous [19, 42, 5, 17, 35], since thermally activated cross-slip [5, 38, 51] and climb processes [5] became more involved. Lerch et al. [17] noticed a difference in deformation in their large γ' Waspaloy between room temperature and 800°C; at room temperature, although dislocation looping was reported as dominant, precipitate shearing in slip bands was evident whereas at 800°C no bands were reported. Also, Clavel et al. [35] reported their Waspaloy specimens to go through a transition from precipitate shearing at room temperature, to dislocation looping at 650°C; the authors proposed that the greater homogeneity of deformation at 650°C resulted in more dislocation looping with precipitate shearing not occurring so readily [35].

However, a number of workers have reported behaviour

inconsistent with that above. King [5] noted that up to 600°C slip was still primarily planar and Bressers and Verhegghe [18] observed precipitate shearing in Waspaloy tested at both 500 and 650°C. Inconel 901 and Inconel 718 exhibited no difference in behaviour between room temperature and 538°C [15] and Waspaloy, employed in various heat treated conditions had the same deformation behaviour when cycled at both room temperature and 538°C [15], room temperature and 800°C [17], and between 500°C and 650°C [18]. Similarly, as King [5] reported, the strength of several turbine disc alloys was relatively independent of temperature over the range of disc operation, from 25 to 600°C.

2.3.2.3 Strain Ageing

Lerch et al. [17], attempted to explain the continual hardening and extremely high dislocation density observed in both of their Waspaloy alloys at 500°C as strain ageing, i.e. the locking of dislocations by solutes, or precipitation of carbides on dislocation lines. The main difference between the two Waspaloy alloys was the way in which the slip bands were more homogeneously distributed for the large γ' alloy, than the small precipitate material [17]. The softening mechanism was found to be in operation in the small γ' alloy, from the observations of numerous paired dislocations within the slip bands, but the extremely high dislocation density contributed a significant hardening effect, which more than offset the softening characteristic

[17].

Such continual hardening behaviour is not unique to Waspaloy [51]; other materials have exhibited similar effects at corresponding temperatures, Astroloy at 400°C [86], Nimonic 80 at 300 and 500°C [19], Nimonic 901 between 230 and 420°C [87] and Udimet 700 at 210°C [38].

Wells and Sullivan [38] noted an increase of life together with the observation of strain ageing in Udimet 700 at 210°C and therefore indicated that the extra hardening had a beneficial effect.

The exact cause of strain ageing is not known [51]. Hayes and Hayes [88], suggested that γ' acted as a sink for carbon, which diffused down the dislocation line to the particles, while the line was arrested by the precipitates. Alternatively, Mulford and Kocks [89] proposed that the mobile dislocations drained the solutes from forest dislocations as they were waiting for thermal activation. Bloom et al. [90] agreed that at the temperatures involved, there was irrefutable evidence of solute mobility. However, Koul and Pickering [91] claimed that in these temperature ranges, carbon was too mobile to exert a drag force on dislocations. Antolovich and Lerch [51] responded by explaining that at such temperatures, γ' would definitely precipitate and coarsen, and both of these effects would restrict dislocation movement.

Strain ageing effects were also observed in stainless steel alloy 800H [92], which has no γ' precipitates. This suggests that the mechanism may be a matrix effect.

2.3.2.4 Precipitation and Coarsening

In the range 700-800°C, carbides were found to precipitate on grain boundaries and slip bands in Waspaloy [17, 51], Nimonic 80 [19] and Udimet 700 [49]. Antolovich and Lerch [51] explained that slip bands were preferential sites for carbide precipitation since they were locations of high defect concentration. Lerch and Gerold [19] added that slip band intersections were locations of low nucleation energy, hence promoting precipitation at these sites. Antolovich and Lerch [51] proposed that this effect was an advanced stage of the dynamic strain ageing mechanism, as discussed in section 2.3.2.3; furthermore, Gell et al. [49] reported carbide precipitation on active slip bands as responsible for the strain ageing hardening in their Udimet 700, stating that whereas a little was beneficial for fatigue resistance, too much was detrimental.

2.3.3 Fatigue Life

At both high and low temperatures, superalloys conditioned to deform by planar slip do not offer as high a resistance to crack initiation as those heat treated for wavy slip [17, 23, 34, 49, 62]. However, planar slip superalloys have a greater resistance to crack propagation than wavy slip alloys [17, 34, 49, 61, 62, 93, 94], the net result being that the fatigue lives are essentially equivalent.

Singh et al. [23] explained that crack initiation occurred only after a particular glide step height had been

reached in the slip plane. Since the number of cycles to achieve this particular step height decreased with decreasing homogeneity of deformation, crack initiation therefore occurred sooner with a planar slip alloy than a wavy slip material [23].

Landgraff [94] suggested that the ideal material for optimum fatigue resistance should be conditioned for planar slip and reversible strain hardening, should contain small grains and a stable precipitate structure/dislocation substructure and be free of metallurgical defects, stress concentrators or dislocation pinning elements. Somewhat more practically, Lerch et al. [17] proposed that a duplex structure of fine grains and large γ' at the surface, with coarse grains and small γ' in the interior, ought to give the maximum total fatigue life. The surface structure would retard crack initiation; once formed the crack would propagate with less speed through the interior structure of the superalloy.

Hornbogen and Verpoort [62] argued that optimum fatigue resistance could be gained by conditioning for easy crack initiation and slow propagation, i.e. inhomogeneous slip, adding a shot peening operation to deform the surface. Wells and Sullivan [42] claimed that surface coating techniques appreciably improved resistance to crack initiation in their Udimet 700 at 927°C, but Hornbogen and Verpoort [62] argued that hard surface layers were less effective at retarding crack initiation than surface deformation. Landgraff [94] explained that surface hardening techniques increased

surface strength and lowered ductility which was
detrimental; Hornbogen and Verpoort [62] added that although
surface treatments had been utilised and successfully
reduced initiation at the surface, additional initiation
subsurface often resulted in deterioration of fatigue
properties. These authors did however, admit that the shot
peening option would be beneficial at high temperatures,
only if there was no recrystallisation on the surface [62].

Numerous workers reported a reduction in fatigue life
with an increase in test temperature [15, 17, 19, 29, 36,
37, 42]; for Udimet 700 cycled at 760°C, the life was
reduced by 80% of that at room temperature [42]. Consistent
with this, Clavel and Pineau [36] reported that when
Waspaloy and Inconel 718 were cycled at 650°C, their lives
were reduced by a factor of between 5 and 10 when compared
to their respective room temperature lives.

Wells and Sullivan [42] explained that the reduction in
life at 760°C in Udimet 700 was due to the relative ease of
intergranular surface crack propagation, by the link up of
individual microcracks. In contrast, when Lerch and Gerold
[19] cycled their Nimonic 80 specimens at 700°C, they
observed an increase in fatigue life of 2 or 3 times that at
room temperature. They did not propose any explanation for
this somewhat strange behaviour, but reported observations
of a more homogeneous dislocation structure at this
temperature as compared to others [19].

When fatigued at room temperature, the cyclic behaviour
of superalloys was not sensitive to different test

36

frequencies however, at elevated temperatures, as the frequency was lowered, the fatigue lives of various alloys were significantly reduced [29, 39, 49]. Organ and Gell [39] stated that at low frequencies and elevated temperatures, intergranular notches produced by oxidation and creep deformation were more significant and therefore reduced the fatigue life.

2.4 Cast Superalloys

Turbine blades are manufactured from casting superalloys due to the complexities of the profiles required; blades are subjected to higher temperatures than discs, typically a temperature profile of 660°C at the base to 1090°C at the tip [61]. Cast superalloys contain higher

Alloy	Particle Type and Size (nm)	HT*	Behaviour
IN-738LC [28]	γ' 150 cube & 60	D	RT: hardening.
IN-738LC [95, 96]	γ' 150 cube & 60	D	900°C: softening/ coarsening.
Rene' 77 [25]	γ' 250 cube & 50	L	927°C: softening/ coarsening.
Rene' 80 [26]	γ' cubes & small	M	871 and 982°C: softening/ coarsening.
Udimet 500 [32]	γ' coarse & fine	N	730°C: hardening 815°C: slight hardening/ softening 900°C: softening.

* HT: heat treatment, from Table 2.1.
RT: room temperature.

Table 2.3: Cast Superalloy Deformation Behaviour.

volume fractions of γ' than wrought alloys (48% in IN-738LC [95] compared to 7% in Nimonic PE16 [23]) which precipitates to form large cuboids (for added creep resistance) surrounded by small spherical γ' (for tensile strength) [61].

In general, softening was reported at elevated temperatures [25, 26, 32, 95, 97] (see Table 2.3), although Udimet 500 essentially hardened to failure at 730°C [32]; IN-738LC hardened to failure when tested at room temperature [28].

The deformation structures of fatigued specimens differed significantly between wrought and cast superalloys. Surface slip bands were observed in optical microscopy [25], but in TEM studies the dislocation substructure was very homogeneous and cellular. Jianting and Ranucci [28] reported dislocations bowing around the particles and eventually filling the grain volumes in their IN-738LC, while Antolovich et al. [25, 26, 98] reported networks of edge or near edge dislocations forming on the γ' in Rene' 80 and Rene' 77. Antolovich et al. [26, 98] added that in Rene' 80 there was a relative absence of dislocations in the matrix, the networks of near edge dislocations were very much confined to the γ'.

At elevated temperatures, the γ' was reported as quite unstable, with coarsening [25, 26, 95, 96] and the formation of γ' plates [98] observed. Antolovich and Jayaraman [99] explained that the instabilities were due to the high γ/γ' mismatch of cast superalloys compared to wrought alloys.

38

These workers also suggested that the networks of edge dislocations stored at the large γ'/γ interface [25, 26, 98] would provide rapid diffusion paths for the observed coarsening.

2.5 Single Crystal and Columnar Grained Superalloys

One successful method of reducing the intergranular failure at high temperatures was to use directionally solidified alloys where grains were columnar, or single crystals. In the former case, if crack initiation occurred in a grain boundary, propagation was severely restricted if the grain boundaries were aligned parallel to the stress axis [49, 100], in the case of the single crystal alloy, the problem was eliminated completely [49, 100]. Under equivalent conditions, fatigue lives of polycrystalline alloys were 1-2 orders of magnitude less than both columnar grained and single crystal materials [100].

Observations were made of γ' shearing by parallel arrays of {111}<101> aligned bands in single crystals of Mar-M200 [101], also, the pairwise motion of dislocations, near screw in character, was noted in PWA 1480 [102]. Cyclic response was orientation dependent; when Mar-M200 was cycled at 760 and 870°C response curves were stable, i.e. hardening and softening were absent, unless the crystals were oriented for single slip in which case softening occurred [100, 101]. Milligan et al. [101] explained that the short fatigue lives associated with the stable response curves were due to the resolved shear stresses being equal on more than one slip

plane, whereas crystal orientations exhibiting softening deformed on one octahedral plane only, hence fatigue lives were greater.

Crack initiation occurred primarily from MC carbides [49, 100, 103, 104] where occasionally the carbides were pre-cracked from casting [100, 103]. Such pre-cracks always ran parallel to the long dimension of the carbide [100, 103]. Micropores were also reported as initiating sites [49, 100, 101, 103, 104], but not as frequently as carbides since they were less of a stress concentrator [103]. Gell and Leverant [103] reported that during fatigue of Mar-M200, the pre-cracks in MC carbides opened up and eventually propagated into the alloy matrix. In addition, uncracked particles often became cracked by the impingement of slip bands; in such cases, the carbides were always cracked across the short dimension [103].

2.6 Dislocation Types in Fatigue

Very few reports of dislocation type are available in the literature concerning fatigue deformation of superalloys. Except for occasional reports of edge or near edge dislocations stored at the γ/γ' interface in cast superalloys [25, 26, 98], and near screw dislocation pairs gliding on octahedral planes in superalloy PWA 1480 [102], the dislocation type responsible for damage in superalloys was not found. Perhaps the reason for this was the extremely high dislocation density contained within the slip bands [20] rendered it impossible to analyse individual

dislocations. Attention has therefore been directed towards the studies of dislocation theory and the more fundamental work on fatigue in order to gain insight into dislocation type and slip band structure.

During the fatigue of annealed copper single crystals, as soon as the first plastic strain cycle was experienced, primary dislocation motion began [105]. Dislocation bundles in dipole and multipole configurations contributed to rapid hardening by providing effective barriers to continued dislocation motion [106]. The initial rapid hardening occurred by the mutual trapping of edge dislocations and their formation into cellular bundles of dense loop patches, between which screw dislocations found it relatively easy to glide [105]. These loop patches, as Kuhlmann-Wilsdorf [107, 108] suggested, would behave like Taylor lattices provided that frictional stresses were small. Mughrabi [109] observed that at low stresses, the cellular loop patch structure remained, i.e. persistent slip bands (PSBs) did not form and indicated that this threshold implied a fatigue limit in copper.

With increasing shear stress the dislocation cells which were homogeneously distributed throughout the crystals, gradually increased in number until an equilibrium was reached between the edge loop patches and the matrix channels transversed by screw dislocations. The equilibrium state was represented by saturation [105] and the onset of this state was associated with the formation of PSBs. According to Ramaswami [110], the defect microstructure

41

consisted of a three dimensional network of interconnected
loop patches containing mainly primary positive and negative
edge dislocations with resulting little misorientation
across the veining. Primary screw dislocations were present,
straddling the regions between the veins; the vein structure
gradually gave way to the PSBs which lay parallel to the
slip plane [110] as shown in Fig. 2.3.

Kuhlmann-Wilsdorf and Laird [111] suggested that due to
the critical stresses and temperatures involved, the
mechanisms of cross-slip, defect dragging and/or forest
cutting were operative in the formation of these matrix
channels or PSBs. Provan and Zhai [106] reported that the
screw dislocation density between the walls of PSBs was an
order of magnitude greater than that between the veins in
the matrix, therefore the volume fraction of hard walls in
PSBs was significantly less than the volume fraction of hard
veins in the bulk, hence PSBs were much softer than the bulk
material and the strain was therefore localised in the
bands.

Kuhlmann-Wilsdorf and Laird [112] proposed that when a
stress was imposed on a classical PSB, the edge dislocations
on one dipolar wall were transferred to the other across the
channel by similarly signed screw dislocations (see Figs.
2.4 and 2.5). It was in this way that the PSB was able to
accommodate the high magnitudes of fatigue strain [112].
Kuhlmann-Wilsdorf and Laird [113] continued their work on
copper single crystals and formulated relationships between
yield stress, maximum stress, frictional stress and back
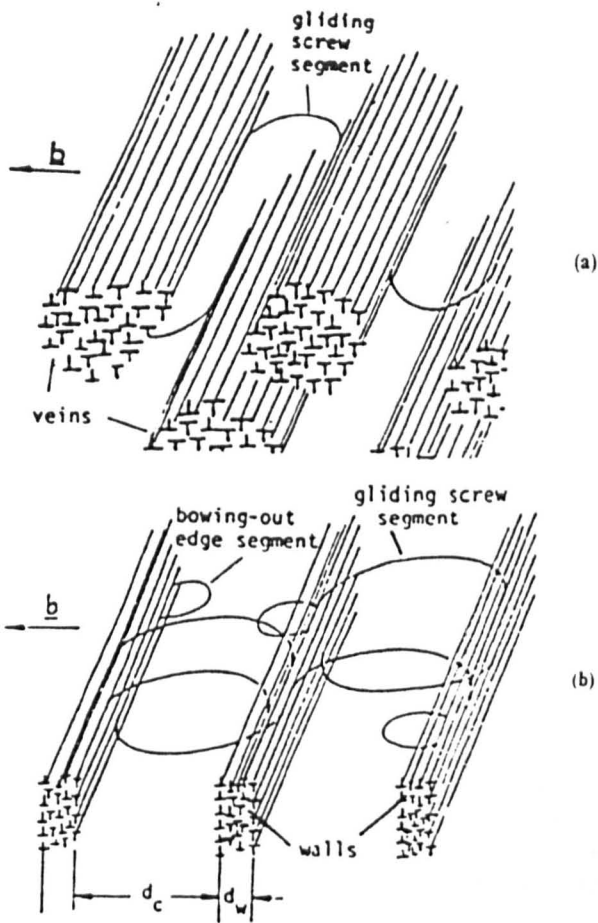
Fig. 2.3. Schematic arrangement of dislocations (a) matrix and (b) persistent slip band [110].
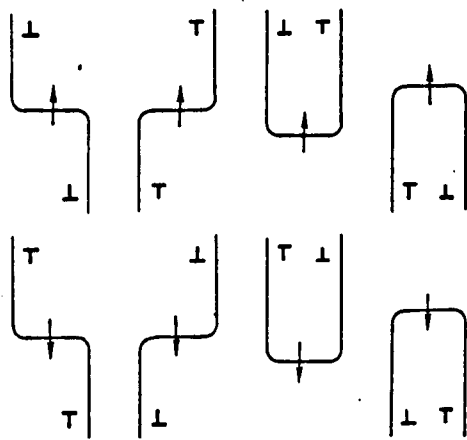
Fig. 2.4. Basic dislocation configurations by which edge
dislocations could be transferred from one dipolar wall to
the other across the channel, and thus accomplish the the
fatigue strain. The plane of the drawing is assumed to lie
parallel with the active slip plane, with positive and
negative edge dislocations having their extra half plane
above and below the plane of the drawing, respectively. If
the shear stress is applied so as to move the material above
the slip plane to the right relative to the material below
it, then the arrows indicating right-handed (up) and
left-handed (down) screw dislocations, respectively, at the
same time indicate their direction of motion [112].
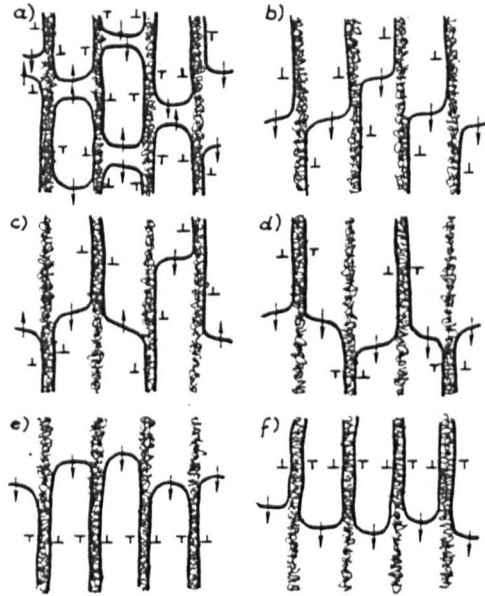
Fig. 2.5. Possible combinations of the dislocation
configurations in Fig. 2.5 that could accommodate the
straining in fatigue. Among these, (a) is unstable as the
opposite screw dislocations in any one channel would
annihilate. The arrangements in (b) and (c) are
energetically unfavourable, and correspondingly would
require for their motion a rather high stress, because they
do not permit maintenance of the essentially dipolar
arrangement of the glide dislocation tilt walls which,
together with the entrapped debris, constitute the dipolar
walls [112].

stress to further describe the motion of dislocations within slip bands. The authors determined the above stresses from hysterisis loops and reported that the frictional stress was due to jog dragging on the screw dislocations in the matrix channels, and dispersed point defects [113], whereas the back stress was related to the glide dislocations being spun out and taken up again at the channel/loop patch interfaces [113]. The models formulated are discussed and applied in section 2.7.1.

Extrusions and Intrusions were found to occur at the boundaries of PSBs in monocrystalline copper [106]. Kuhlmann-Wilsdorf and Laird [112] proposed that edge dislocations, aided by the motion of screw dislocations, glided either out of, or into the PSB boundary to form extrusions or intrusions respectively (see Fig. 2.6). The authors reported that the warping of the dipolar walls within a PSB was responsible for the height limit of the extrusions [112]. Alternatively, Essmann et al. [114] suggested that extrusions/intrusions were generated due to a combination of glide and annihilation of dislocations within slip bands. In the case of polycrystalline material, Provan [105] explained that due to the rigidity of the surrounding material, grain boundaries only allowed so much displacement, either as localised shearing of PSB walls (Fig. 2.7(a)), or in the pile up of the PSB/matrix interface dislocations at the grain boundaries, as shown in Fig. 2.7(b). Extrusions/intrusions were reported as initiators of microcracks since they acted as stress raisers [106, 112].
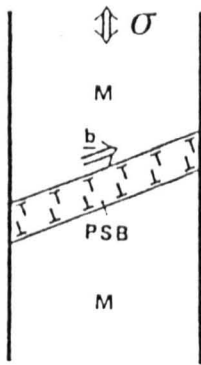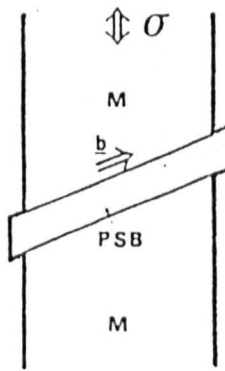
Fig. 2.6. PSB formation of extrusions [105].
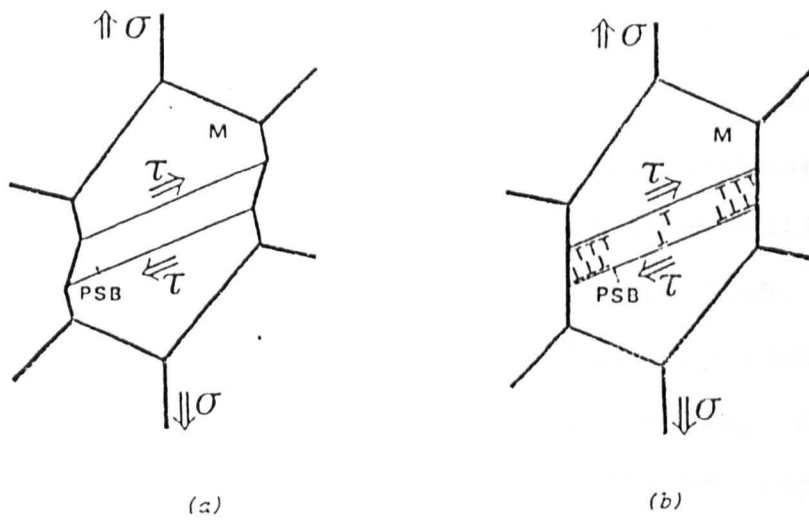
Fig. 2.7. Interaction of a PSB with grain boundaries [105].

At higher shear stresses, mono and polycrystalline copper specimens tended not to exhibit the PSB structure detailed above; homogeneous deformation structures of dislocation cells were observed [105, 106, 112, 115]. Ramaswami [110] reported a three dimensional network of loop patches and cell walls in single crystal copper containing alumina particles. Extrusions were observed with such cellular structures but Provan and Zhai [106] reported that they were not severe enough to cause transgranular cracking. Alternatively, microcracks tended to form intergranularly at high angle grain boundaries, resulting from small slip steps or notches generated by slip reversibility [105, 106]. Provan [105] stated that the steps gradually increased into sufficient stress raisers to initiate cracking. Consistent with the above, Kim and Laird [116] observed crack initiation from small steps which increased in size with increasing number of cycles until microcracks developed. The most favourable initiation sites in the high strain fatigue of their polycrystalline copper were intersections between grain boundaries and the surface; the authors indicated that crack initiation could be defined as a grain boundary step with a height of 1-2μm [117].

Feltner and Laird [118, 119] undertook research into polycrystalline pure copper and Cu-7.5%Al and found that at low strains their specimens' hardening rates increased with increasing temperature; the dislocation structure was comprised almost entirely of prismatic dislocation loops or dipoles. At higher strains, hardening was attributed to

44

dislocation tangles; in wavy slip specimens the tangles formed cell walls, whereas in the planar slip conditioned materials, tangling occurred within the dense bands of dislocations [119].

Abel et al. [120] noted that hardening rates decreased and saturation stresses increased with decreasing stacking fault energy (SFE) from work on single crystal copper containing small additions of aluminium. In the low SFE alloys, initial cyclic deformation occurred inhomogeneously, however the appearance of random slip lines on the surfaces of specimens resulted in a more homogeneous slip distribution [120]. Additionally, Karjalainen [121] observed that materials with high SFE exhibited a well developed cell structure after high strain cycling, whereas the Cu-Zn alloy displayed planar arrays, evidently owing to the difficulty of cross-slip of dissociated dislocations.

Feltner and Laird [119] suggested that since plastic strain was a prerequisite for fatigue, then reversed plastic strain was a must for softening; they proposed that only slight changes in dislocation density and re-arrangement were necessary for dislocations to find annihilation or low energy sites [119]. They suggested that jog dragging and forest cutting processes were operative, from their TEM observations of heavily jogged and tangled dislocations [119].

Wells [122] stated that the tendency for an fcc material to exhibit planar or wavy slip depended on the degree to which dislocations were confined to their slip

planes. Wells [122] assumed that the waviness of slip was governed by the ease by which screw dislocations could cross-slip; the idea being that all materials would exhibit planar slip at sufficiently small strains, and homogeneous deformation at sufficiently large strains.

From their high strain fatigue of polycrystalline copper, Kim and Laird [117] explained that crack propagation was slower in a planar slip material due to the fact that slip was more reversible, as compared to that in a wavy slip material.

2.7 The Modelling of Fatigue Damage Accumulation
2.7.1 Cyclic Response

Models have been developed which predict the cyclic response behaviour of metals and alloys. The following expressions were derived by Kuhlmann-Wilsdorf and Laird [112, 113], from their investigations into the fatigue behaviour of pure monocrystalline copper:

$$\tau_F = (\tau_E + \tau_S)/2 \qquad\qquad (2.1)$$
$$\tau_B = (\tau_E - \tau_S)/2 \qquad\qquad (2.2)$$

where τ_F = friction stress

τ_B = back stress

τ_E = peak stress

τ_S = yield stress.

The friction stress was due to Peierls forces, jog

dragging and the presence of precipitates or similar obstacles, whereas the back stress depended on the long range dislocation interactions. τ_E and τ_S were obtained from hysteresis loops where τ_E was the maximum stress within a loop and τ_S was the stress at which reverse plastic deformation began [113].

Although the models were initially advanced from work on copper single crystals [113], they were applied to an Al-4%Cu alloy containing θ'' precipitates. The alloy was analysed in monocrystalline form by Lee and Laird [123] and polycrystalline form by Bhat and Laird [124]. Fig. 2.8 shows the cyclic response predicted for the two forms of this alloy. In both cases the back stress built up gradually, saturated and remained virtually unchanged for the remainder of the life. The friction stress reached a maximum then continuously decreased at a similar rate to the observed softening of the actual alloys tested [123, 124].

However, the models were not without problems or limitations; Lee and Laird [123] experienced difficulty measuring τ_E and τ_S from the hysteresis loops of their single crystal alloy, especially at low strains. Bhat and Laird [124] stated that the application of equations (2.1) and (2.2) to two-phase alloys was not straightforward, since the dislocation structures would be different from those in the copper single crystal work of Kuhlmann-Wilsdorf and Laird [113]. However, they did consider that the basic principles of the method should apply, and achieved good agreement between predicted and observed behaviour for a

47
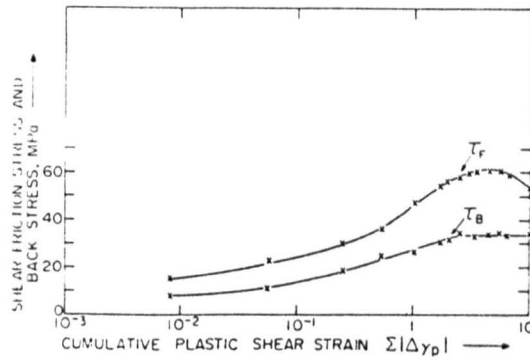
(a)
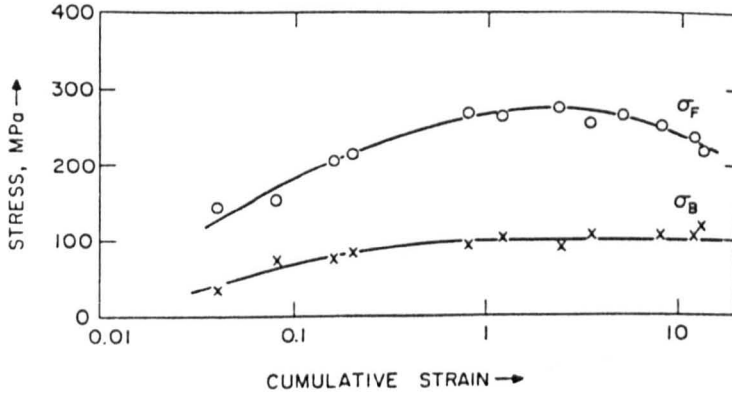
(b)

Fig. 2.8. Cyclic response curves for the Al-4%Cu alloy from hysteresis loops, (a) shear friction stress (τ_F) and back stress (τ_B) for the single crystal alloy cycled at γ_p = 1.8×10^{-3} [123], (b) friction stress (σ_F) and back stress (σ_B) for the polycrystalline alloy cycled at a plastic strain amplitude of 1% [124].

plastic strain amplitude of 1% [124].

2.7.2 Cyclic Hardening

Attempts to model the fatigue hardening of two phase alloys have tended to be based on modifications of unidirectional concepts and Hall-Petch type relationships. For those alloys which hardened to a saturation stress, the unidirectional concepts of Russel and Ashby [125] and Feltner and Laird [119], were applied by Calabrese and Laird [126] to their Al-4%Cu alloy containing non-shearable θ' plates.

Russel and Ashby [125] developed the following expression from their work on single crystals containing θ' plates oriented for single slip:

$$\tau_S = \tau_o + 0.35G(b\gamma/\lambda_g)^{1/2} \qquad (2.3)$$

where τ_S = saturation stress

τ_o = initial flow stress

G = shear modulus

b = burgers vector

γ = shear strain = $3.06(\epsilon_p)^5$

λ_g = inter-particle spacing

ϵ_p = plastic strain.

The model was based on the assumption that when an alloy containing non-deformable plates was plastically deformed, the plates would rotate at an angle equal to the

48

shear strain (γ).

Alternatively, assuming that the interaction between stored and mobile dislocations was responsible for saturation, it was proposed [119] that the saturation stress was that necessary to force dislocation cells to move freely within the material. This led to the "bowing link" model of Feltner and Laird [119] where the shear stress at saturation is given by:

$$\tau = Gb/\beta l \qquad (2.4)$$

where G = shear modulus

     b = burgers vector

     β = 3 (for dislocations of various lengths)

     l = inter-particle spacing.

Calabrese and Laird [126] substituted known or estimated values for the Al-4%Cu alloy with the non-shearable θ' plates, into the variables of the above equations in an attempt to verify the models. Equations (2.3) and (2.4) yielded values of 170 and 200MPa respectively, compared to the actual specimen saturation value of 208MPa.

These saturation stresses appear to be comparable to the experimental results, but equation (2.3) was only applicable for describing the unidirectional flow stress in the case of simple single slip [125]. Applying the equation to fatigue would cause complications due to the formation of

point defect concentrations and dislocation debris. Calabrese and Laird [126] concluded therefore, that calculated and experimentally measured values were in reasonable agreement.

The "bowing link" model (equation (2.4)) is not without its limitations; it was found to be inapplicable at low strains for both coarse and fine θ' Al-4%Cu alloys and at high strains in the fine θ' alloy [126]. Hence, this model was only useful for predictions of the coarse θ' alloy's behaviour when subjected to high strains.

The work carried out by Hall and Petch [127] has also been applied to describe the cyclic hardening of alloys. Both Lerch et al. [17] and Lerch and Gerold [21] proposed that if a grain could be considered as being divided into smaller grains, i.e., by slip band intersections, then a relationship may exist between applied stress and slip band spacing for the case of fatigue. Whereas the Hall-Petch expression was concerned with a correlation between yield stress and the inverse square root of the grain diameter, attempts were made to correlate applied stress and the inverse square root of the slip band spacing [17, 21]. Fig. 2.9(a) shows an example of the results of the work carried out on Nimonic 80 by Lerch and Gerold [21]. At high strains a good correlation was obtained, however at lower strains this was not the case.

From a similar investigation on Waspaloy by Lerch et al. [17], the Hall-Petch expression was determined as

STRESS (MPa)

γ' diameter (nm)

○ ●   13
△ ▲   20
□   < 5
◇   100 + 13

1200

1000

800

600

400

0.1 0.2 0.3 0.4 0.5 0.6 0.7

$i^{-1/2}$ ($\mu m^{-1/2}$)

(a)

STRESS RANGE (MPa)

1900
1800
1700
1600
1500
1400
1300
1200
1100
1000
900

0.4 0.5 0.6 0.7 0.8 0.9 1.0 1.1 1.2 1.3 1.4

(SLIP BAND SPACING)$^{\frac{1}{2}}$ ($\mu m^{-\frac{1}{2}}$)
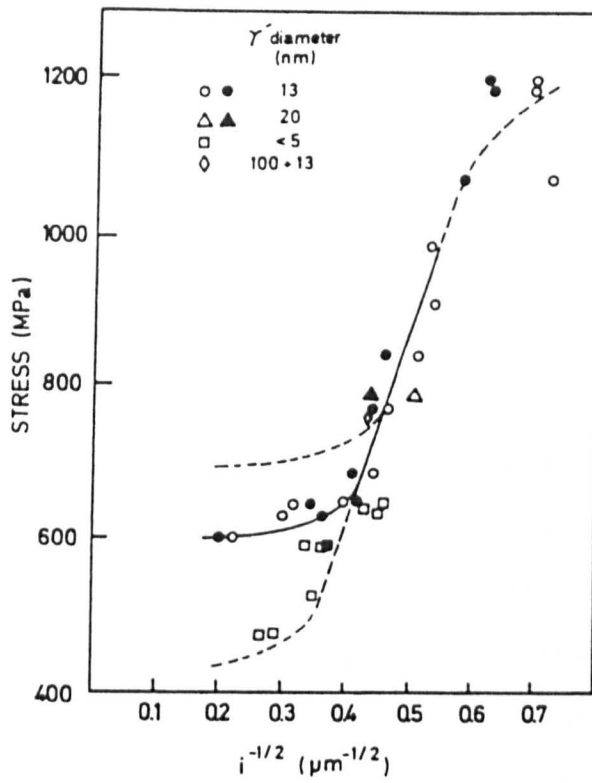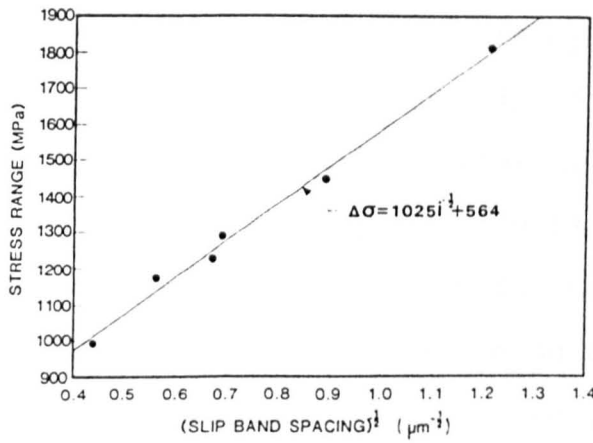
$\Delta\sigma = 1025 i^{\frac{1}{2}} + 564$

(b)

Fig. 2.9. Hall-Petch representations for the hardening behaviour of (a) Nimonic 80 [21] and (b) Waspaloy [17].

$$\Delta\sigma = 1025(i)^{-1/2} + 564 \qquad\qquad (2.5)$$

where $\Delta\sigma$ = applied stress range

i = slip band spacing = $1.212(\Delta\varepsilon_p)^{-0.518}$

$\Delta\varepsilon_p$ = plastic strain range.

Fig. 2.9(b) shows the straight line fit of the results obtained and whereas the authors claimed an excellent correlation between $(i)^{-1/2}$ and the mid life stress range, they did not comment on higher and lower stress levels.

It is clear that severe limitations are associated with the above hardening models. When alloys contain shearable precipitates, i.e., the mechanism of softening is in competition with that of hardening, the quantitative modelling of such behaviour was considered somewhat more difficult [58].

The unidirectional hardening of two-phase alloys has a contribution from many sources including interface dislocations, coherency strains, differences in elastic constants and APB creation. Expressions have been derived which account for some of these factors but are only valid for simple cases [58]. In order to use such expressions, interface energy, line tension, APB energy, dislocation flexibility and precipitate volume fractions are but a few of the parameters which need to be established.

Calabrese and Laird [58] reported that it was difficult, if not impossible, to determine the above quantities and therefore proposed a qualitative model of the

cyclic hardening process:

Precipitates imposed a friction stress on dislocations by interaction with their coherency stress fields, and by the creation of APBs within the precipitates through cutting. The close spacing of particles ensured that they sheared since the bowing stress was high. Additional hardening was gained from the accumulation of dislocations generally through grains, but especially within deformation bands [58].

2.7.3 Cyclic Softening

The mechanisms responsible for cyclic softening of precipitation strengthened alloys at room temperature have been identified as precipitate disorder, fragmentation or dissolution.

The disorder model was put forward by Calabrese and Laird [58] to explain fatigue softening in their Al-4%Cu alloy containing θ'' plates. The model was based on experimental evidence that within a few cycles the dislocation density within deformation bands increased considerably leading to tangle formation. In such a network, dislocations moved in all possible slip systems within the slip band in a random to and fro motion and destroyed order in the precipitates. Stoltz and Pineau [16] reported that this model successfully described the observed softening behaviour in Waspaloy containing very fine (8nm) γ' particles.

The disorder model consisted of expressions advanced by

Gleiter and Hornbogen [128] and Guyot [129] concerning dislocation/ precipitate interactions. Gleiter and Hornbogen [128] proposed the following expression to determine the additional stress over that of the matrix ($\Delta\tau$), needed to force the first dislocation through a particle:

$$\Delta\tau = \frac{0.28(\gamma)^{3/2}(f)^{1/3}(R)^{1/2}}{(G)^{1/2}(b)^2} \qquad (2.6)$$

where γ = APB energy

   f = precipitate volume fraction

   R = precipitate diameter.

   G = shear modulus

   b = burgers vector.

A similar relationship obtained by Guyot [129] which described the motion of a single dislocation through a random array of obstacles in its slip plane, is shown below:

$$\Delta\tau = \frac{K(\gamma)^{3/2}(Rf)^{1/2}}{b(\Gamma)^{1/2}} \qquad (2.7)$$

where K = constant

   γ = APB energy

   R = precipitate diameter.

   f = precipitate volume fraction

   b = burgers vector

   Γ = dislocation line tension.

Calabrese and Laird [58] substituted known or estimated values for the Al-4%Cu alloy into the variables of the above equations to compare predictions with actual observations. Equations (2.6) and (2.7) gave shear stress increments of 12,000 and 22,000 psi respectively whereas the specimen under test softened by 3,000-10,000 psi, depending on the level of applied plastic strain. The authors claimed that, due to uncertainties in the hardening parameters, this could be considered as a good comparison. It does appear strange, however, that predictions of an individual dislocation's behaviour have been compared to the behaviour of what must be thousands in an actual specimen. Equations (2.6) and (2.7) are satisfactory for alloys having simple precipitate geometries, such as the spherical γ' contained by Waspaloy, although determining the APB energy of such an alloy may present a problem.

An alternative model to explain fatigue softening was proposed which is concerned with particle fragmentation in Nimonic PE16. Sundararaman et al. [22] disagreed with the disorder hypothesis [16, 58] since it was found that intermediate annealing treatments had re-nucleated extremely fine γ' in deformation bands in Nimonic PE16 [22-24]; the precipitates had therefore not been disordered, but dissolved [22].

As a result of the above, Sundararaman et al. [22] proposed the following fragmentation model based on experimental observations:

Initially, the paired motion of dislocations sheared γ'

particles resulting in various configurations (Fig. 2.10(a-g)). Continued deformation resulted in high dislocation densities and dislocation tangles; the tangles would act as barriers to dislocation motion therefore the resistance to motion was increased. If a sheared particle was in the path of a cross-slipping dislocation, it would be fragmented as shown in Fig. 2.10(h, i). On a given slip plane shear could take place in more than one slip direction, therefore an initially sheared slice of γ' may be fragmented into tiny pieces and distributed within the bands (Fig. 2.10(j, k)).

It was suggested [22] that the distribution of precipitate fragments was dependant on the amount of deformation the band had undergone. If the specimen failed early, the distribution would resemble Fig. 2.10(l), but for a specimen with a long life, fragments would be so small that they would almost be in solution (Fig. 2.10(m)).

2.7.4 Deformation Homogeneity

The tendency for an alloy containing ordered coherent particles to deform inhomogeneously when subjected to cyclic strain, was predicted by Graf and Hornbogen [63] and Hornbogen and Verpoort [62]. In terms of the decrease in critically resolved shear stress, the tendency is determined by the following expression:

$$\frac{d}{dn} \Delta \tau_{(n)} = \frac{-C\gamma(f)^{1/3}}{d} \qquad (2.8)$$
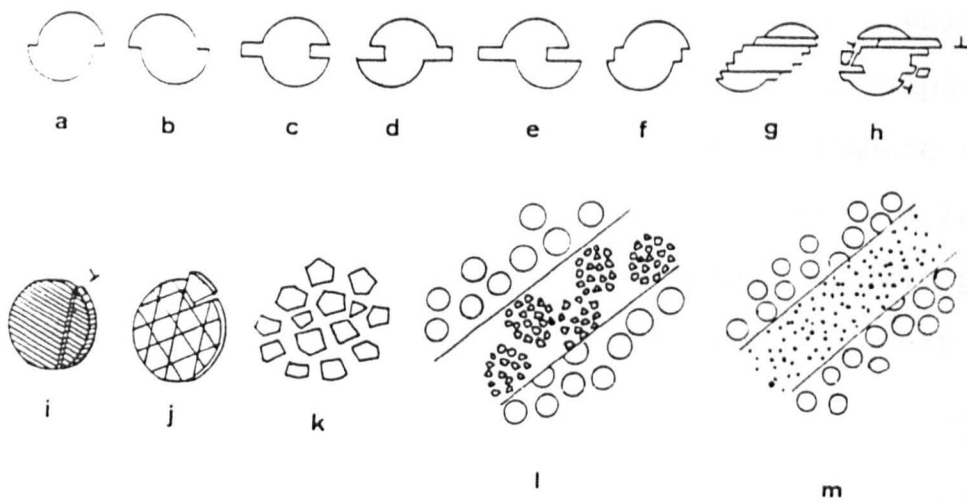
Fig. 2.10. Schematic model for fragmentation of γ′ particles within deformation bands for Nimonic PE16, see text for details [22].

where $\Delta\tau_{(n)}$ = the decrease of critically resolved shear

stress per dislocation passing through a

particular slip plane.

C = dimensionless factor considering shape

and distribution of precipitates

γ = APB energy

f = precipitate volume fraction

d = precipitate size.

Therefore, the tendency for inhomogeneous deformation would increase with an increase in precipitate volume fraction and APB energy, and a decrease in precipitate size. The expression was developed from work on Nimonic 80 [62, 63] and is not without its limitations. The calculation of APB energy may prove difficult, as Ardell and Huang [130] experienced when estimating APB energies for their Al-Li and Ni-Al alloys.

2.7.5 Slip Band Extension

During Photoemission Electron Microscopy studies concerning the fatigue of 6061-T6 aluminium, Baxter [131] observed the joining of surface extrusions related to persistent slip band (PSB) growth. Based on evidence [131] that the interior of a PSB was softer than the matrix of a grain and that the strain within a PSB was much greater than that within a grain, a model was advanced relating the length of a slip band to the number of cycles [131].

Baxter assumed that the rate of extension was

proportional to the cyclic strain within the band, assuming the strain was uniform [131]. The expression takes the form:

$$l^2 = \frac{2B(D)^2}{t}(\varepsilon_t - \varepsilon_g)(N - N_o) \qquad (2.9)$$

where l = slip band length

B = constant

D = grain diameter

t = PSB thickness

ε_t = total surface cyclic strain

ε_g = cyclic strain in matrix of grain

N = number of cycles

N_o = number of cycles to produce first extrusion.

The model was considered somewhat oversimplified, since the slip band and matrix are assumed to deform independently of each other, also interfacial stresses and strains are ignored [132].

2.7.6 Crack Initiation

Radhakrishnan and Mutoh [133] proposed the following dislocation based model for the initiation of cracks on a smooth surface. For a deforming material, when the maximum applied shear stress was greater than or equal to the yield stress in shear, then PSBs would form in any grain orientated for easy slip. The PSBs would be transformed into a small crack which, as it approached a grain boundary, would unlock a dislocation source in the next grain

providing the stress concentration was sufficient. The model
is shown below:

$$(\tau_{max} - \tau_i)(2a)^{1/2} = (\tau_{ys} - \tau_i)(d)^{1/2} \qquad (2.10)$$

where τ_{max} = maximum applied stress

τ_i = internal stress

a = crack length

τ_{ys} = yield stress in shear

d = grain diameter.

Equation (2.10) illustrates that if the bulk yield
stress of the material increases, the endurance limit (τ_{max})
also increases [133].

Polak [134] also proposed a dislocation based model for
the initiation of cracks along slip bands involving point
defects, produced from the non-conservative motion of the
jogs on screw dislocations in the early stages of cyclic
hardening. The model was based on the fact that since edge
dislocation densities in the PSB channels and the walls
differed by a factor of 20, then there was a resultant mass
transfer. Polak [134] claimed that since an alternating
stress field existed, material was extruded along the
channels and intruded into the walls, hence generating
extrusions and intrusions; surface cracks formed by the
mutual interconnection of deep intrusions along the PSB
line. The predictions of the model were reported to be in
agreement with surface relief formation and shallow surface
crack initiation observed for single and polycrystals [134].

Lin et al. [135] applied continuous dislocation theory to describe crack initiation along slip bands; assuming that the accumulation of dislocations within slip bands could be represented by elliptical domains, a crack would initiate when the accumulated dislocation dipoles reached the number required to give the critical displacement to cause fracture in a perfect metal. The number of cycles leading to initiation, N_i, was given by:

$$N_i = \frac{0.2}{\pi} \frac{b (a_1 + a_2)}{a_1 a_2} \frac{\mu \sigma_f}{(\sigma_{max})^2} \frac{v_f}{f} \frac{1}{\Delta \varepsilon_{p}/2} \qquad (2.11)$$

where b = burgers vector

a_1, a_2 = principal elliptical axes

μ = shear modulus

σ_f = friction stress

σ_{max} = applied tensile stress

v_f = PSB volume fraction

f = damage accumulation efficiency factor

$\Delta \varepsilon_p$ = applied tensile plastic strain

Lin et al. [135] stated that all quantities in equation (2.11) except for f could be determined by experiment; f was estimated by two methods, one based on stored energy, the other on the back stress from hysterisis loop data. The authors reported rather good agreement between the model and experimental data for crack initiation in iron [136] and copper [135].

2.7.7 Crack Propagation

Linear elastic fracture mechanics (LEFM) techniques have been shown to be inadequate for the description of short fatigue crack behaviour in several materials [137]. One such equation, the "Paris" law:

$$da/dN = C(\Delta K)^m \qquad\qquad (2.12)$$

where da/dN = crack growth rate

C, m = material constants

ΔK = stress intensity factor

describes crack growth in terms of parameters including crack length (a) and stress range (via ΔK), but is somewhat insensitive to microstructural features.

From plastic replica studies it was noted that short cracks had higher growth rates than long cracks [137], and that the microstructure of a material had a significant influence on the growth behaviour of a crack within the first grain [138]. To account for these factors, Hobson et al. [137] derived the following expression for crack growth up to the first grain boundary:

$$da/dN = C(d - a)^{1-n}(a)^n \qquad\qquad (2.13)$$

where d = distance to an obstacle to crack growth

a = crack length

C, n = material constants.

The model was applied to describe short crack behaviour within the first grain in a 7075-T6 aluminium alloy by Hobson [138], and a medium carbon steel by Brown [139]. The obstacle to crack growth in the aluminium alloy was considered to be the first grain boundary [138], whereas in the steel the dominant barrier was pearlite, being of high strength compared to the ferrite in which cracks initiated [139].

For a crack spanning a number of grains the effect of microstructural barriers on growth was small [140] and for propagation in this regime, both Hobson [138] and Brown [139] applied "Paris" type equations to their materials. Fig. 2.11 shows the growth loci for the aluminium alloy.

Yates and Grabowski [141], Yates et al. [47] and Wang et al. [74] noted that it was not just the first microstructural barrier which significantly affected short crack growth, and modified the model of Hobson et al. [137] to account for this in Waspaloy. Assuming that short crack growth occurred by a Stage-I Mode-II process in which growth rate was proportional to slip band length, and that slip bands extended right across the grains, the proposed model took the form:

$$da/dN = C(\Delta\varepsilon)^n(d_i - a)$$ (2.14)

where $\Delta\varepsilon$ = applied strain range

d_i = distance from initiation site to next
        barrier

61
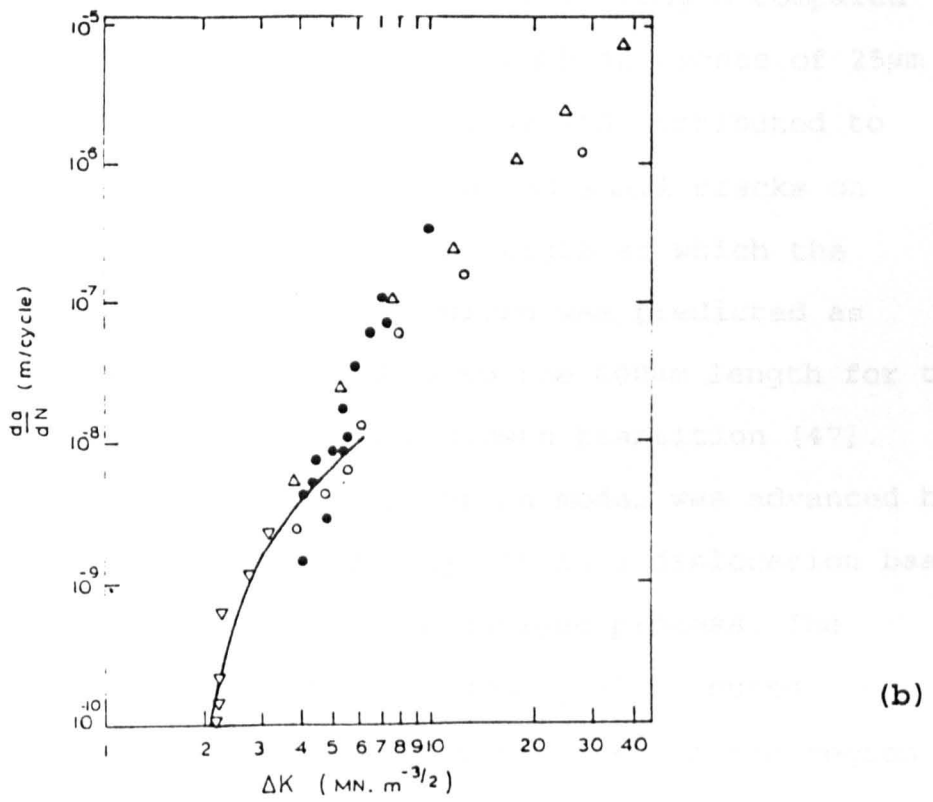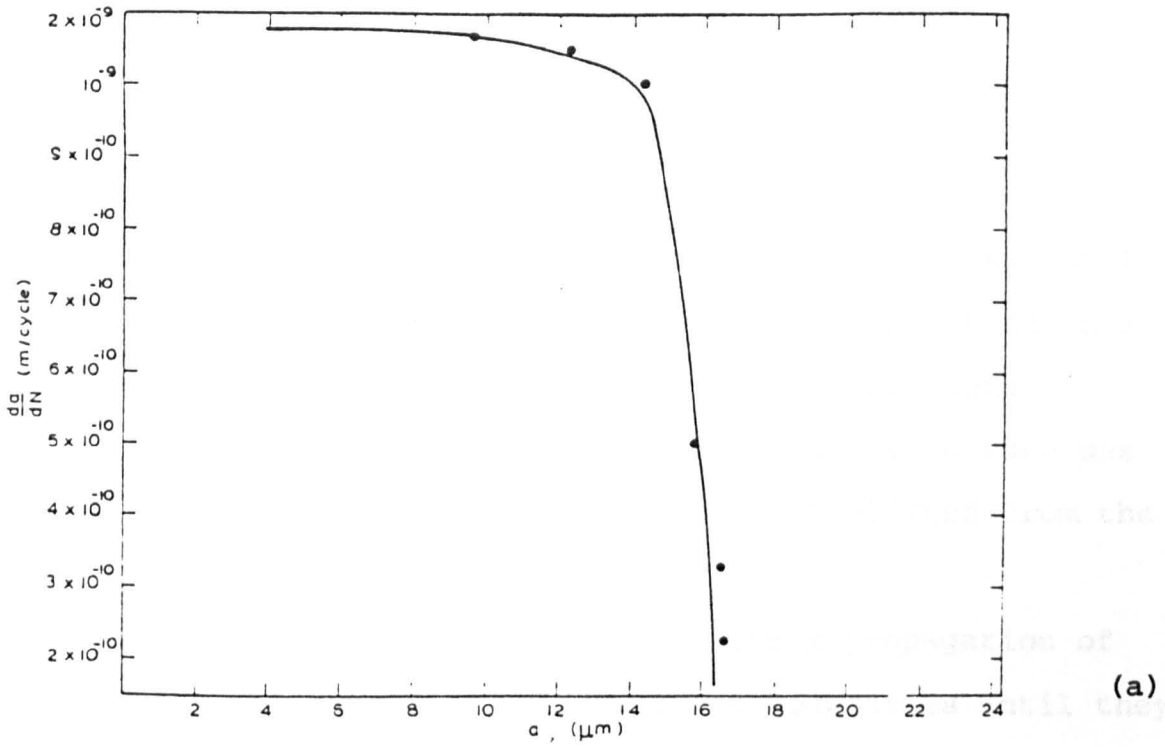
Fig. 2.11. Short crack growth behaviour in 7075-T6 aluminium
alloy [138], (a) up to first grain boundary from equation
(2.13), (b) after first grain boundary.

a = crack length

C, n = material constants.

Yates and Grabowski [141] reported that equation (2.14) was adequate to predict the propagation of cracks, until more favourable growth kinetics led to a transition to a Stage-II Mode-I mechanism. They proposed that this transition occurred when the short crack growth rate was overtaken by that of the long crack, established from the "Paris" law (equation (2.12)).

Fig. 2.12 shows the predicted crack propagation of Waspaloy, illustrating the arrest at boundaries until they no longer affect the growth rate. Predictions of the number of cycles for a crack to reach a certain length compared well with observed results for a length in excess of 25μm [141]. The poor estimation below 15μm was attributed to difficulties in locating and measuring small cracks on acetate replicas [141]. The crack length at which the short/long growth transition occurred was predicted as 518μm, which compared favourably to the 600μm length for the observed faceted/striated crack growth transition [47].

An alternative crack propagation model was advanced by Navarro and de los Rios [142-144]; it is a dislocation based model which describes the entire fatigue process. The authors used the theory of continuously distributed dislocations to represent the slip produced in the region ahead of the crack. It was assumed that slip bands extended right across the grain, or more precisely, when slip was
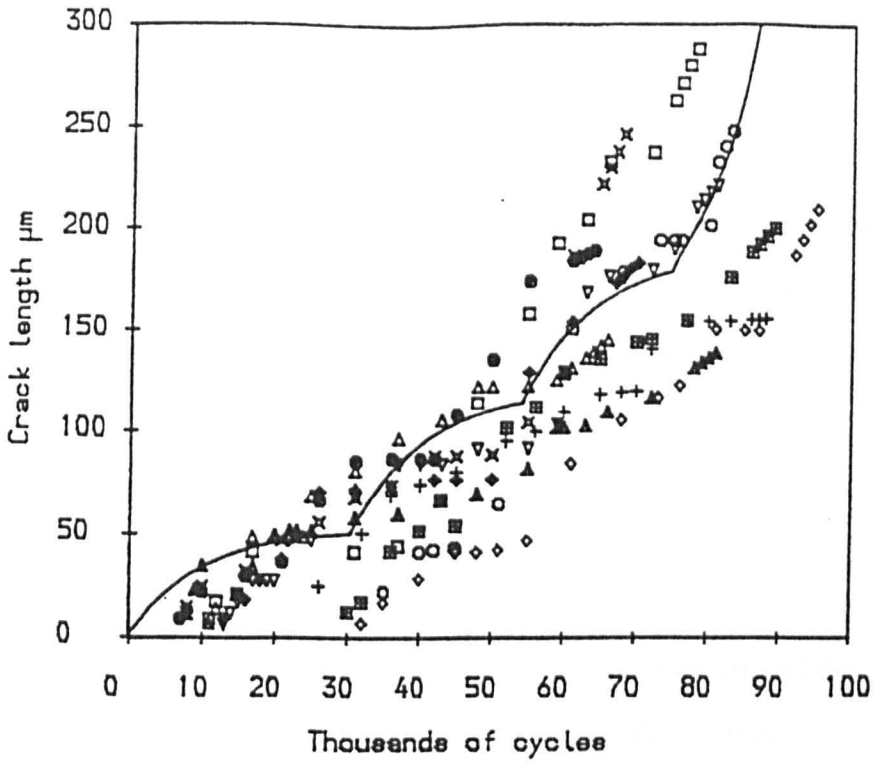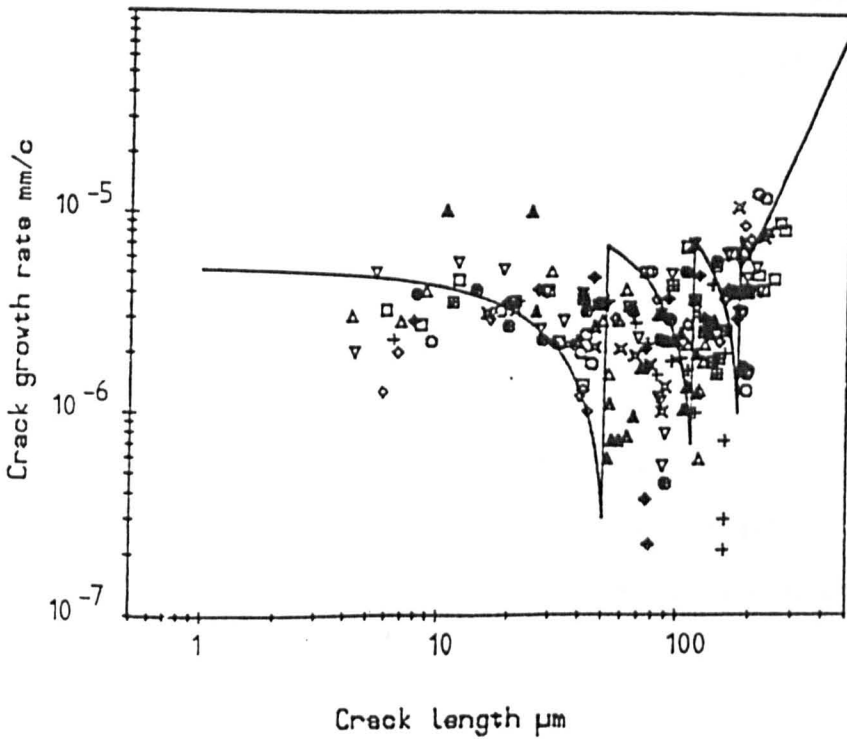
Fig. 2.12. Predicted crack growth behaviour of Waspaloy
[141].

initiated in a grain the whole grain was deforming. Navarro and de los Rios [142-144] applied the criterion that a crack would propagate past each successive grain boundary, if the stress concentration was sufficient to unlock a dislocation source in the next grain. If this was not the case then propagation was arrested. Assuming that crack extension was proportional to the plastic displacement along the slip band (ϕ) then:

$$da/dN = f\phi \qquad (2.15)$$

where f = fraction of dislocations on slip band which participate in the extension

then the growth rate was estimated using an expression for plastic displacement at the root of a crack:

$$\phi = \frac{b\tau}{\pi A} \frac{cn}{cos^{-1}(n)} \ln(1/n) \qquad (2.16)$$

where b = Burgers vector

τ = shear stress

n, c = dimensionless coordinates

A = $Gb/2\pi$ for screw dislocations

A = $Gb/2\pi(1 - v)$ for edge dislocations

G = shear modulus

v = Poissons ratio

The result is illustrated in Fig. 2.13.
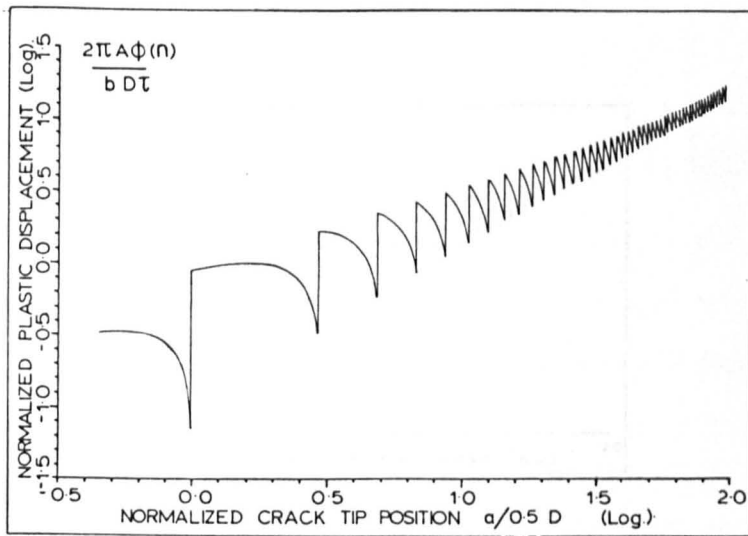
Fig. 2.13. Modelled crack propagation characteristic showing barriers having less effect as crack grows [142].

The propagation process is described as a number of slip jumps, i.e. growth rate decelerates to a minimum as a grain boundary is met, then accelerates to the next. The location of each minima on the growth rate locus depends on grain size distribution and particular conditions, eg. orientation, required to initiate slip in successive grains [144]. The transition between short and long crack propagation was determined as the point at which the influence of slip jumps on the overall description of crack growth became negligible. After this point LEFM was used [144].

The authors admitted that a number of inter-related factors including dislocation locking, generation of unlocked sources during deformation, increase in dislocation density and strain hardening would affect certain parameters within the model which were not accounted for [144].

An attempt was made to introduce some microstructural effects to the Navarro and de los Rios model [142-144] by Zuyu Sun et al [145]. It was proposed that in single phase polycrystals, the strength of a grain boundary was dependent on the differences in orientation between the two grains, consequently a probabilistic distribution of grain orientation factors was incorporated [145]. The authors assumed that i) the crack was associated with one slip band which was simulated by a linear distribution of long straight dislocations blocked by a microstructural barrier, and ii) when a slip band was nucleated in the next grain, the linear distribution was assumed to lie in the same slip

plane extending to the next microstructural barrier.

When applied to the Al-Li system shown in Fig. 2.14, most of the experimental points were found to lie within the prediction envelopes, those outside reflected the microstructural variability of a real as opposed to ideal equiaxed grain structure [145].
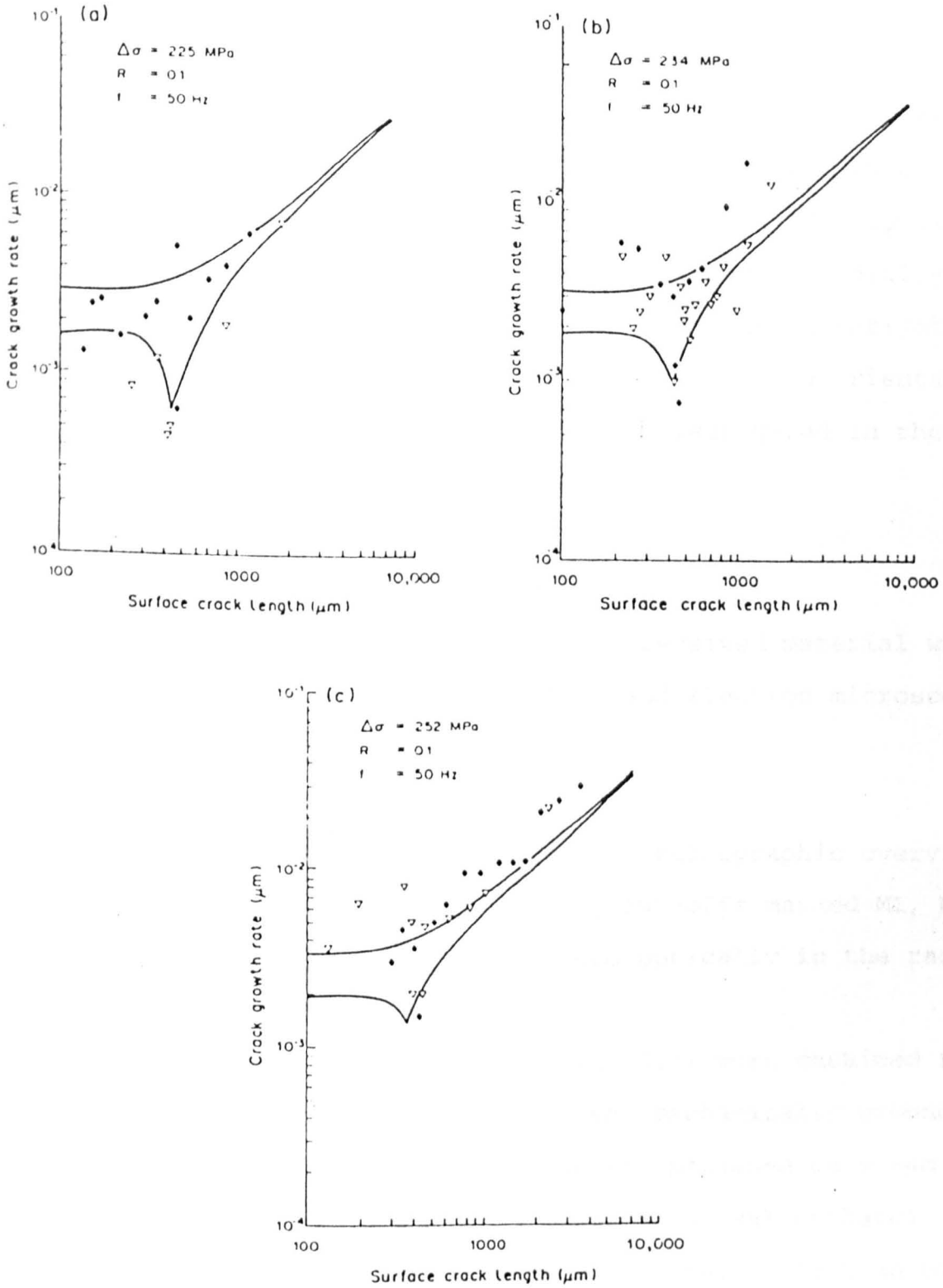
Fig. 2.14. A comparison between theoretical short crack
growth rate curves and experimental results from the Al-Li
alloy [145].

3 Experimental Procedure

3.1 Material

The composition of the turbine disc alloy Waspaloy, as supplied by Rolls Royce, Derby, was nominally: (wt %) 19.5 Cr, 13.5 Co, 4.2 Mo, 1.4 Al, 3.0 Ti, 1.0 Fe, 0.06 C, balance Ni. A disc forging was machined into 80x10x10mm specimens as shown in Fig. 3.1; specimens were orientated radially, axially and tangentially to facilitate the investigation of differences in behaviour associated with such orientations. However, only one orientation was investigated in the current work.

3.2 Material Characterisation

The microstructure of the as-received material was characterised using both optical and electron microscopy.

3.2.1 Optical Microscopy

To gain a three dimensional metallographic overview of the starting material, the scrap cut-offs marked M1, M3, M5 and M6 in Fig. 3.1 were inspected optically in the radial, axial and tangential directions.

Specimens OP1-OP12 (see Fig. 3.2) were machined from the cut-offs, mounted in Bakelite, mechanically ground on successively finer grinding papers, polished on a 6μm diamond pad and etched in a 4% bromine, 96% methanol solution. Optical micrographs were obtained from an Olympus Vanox microscope using conventional reflected light.

66
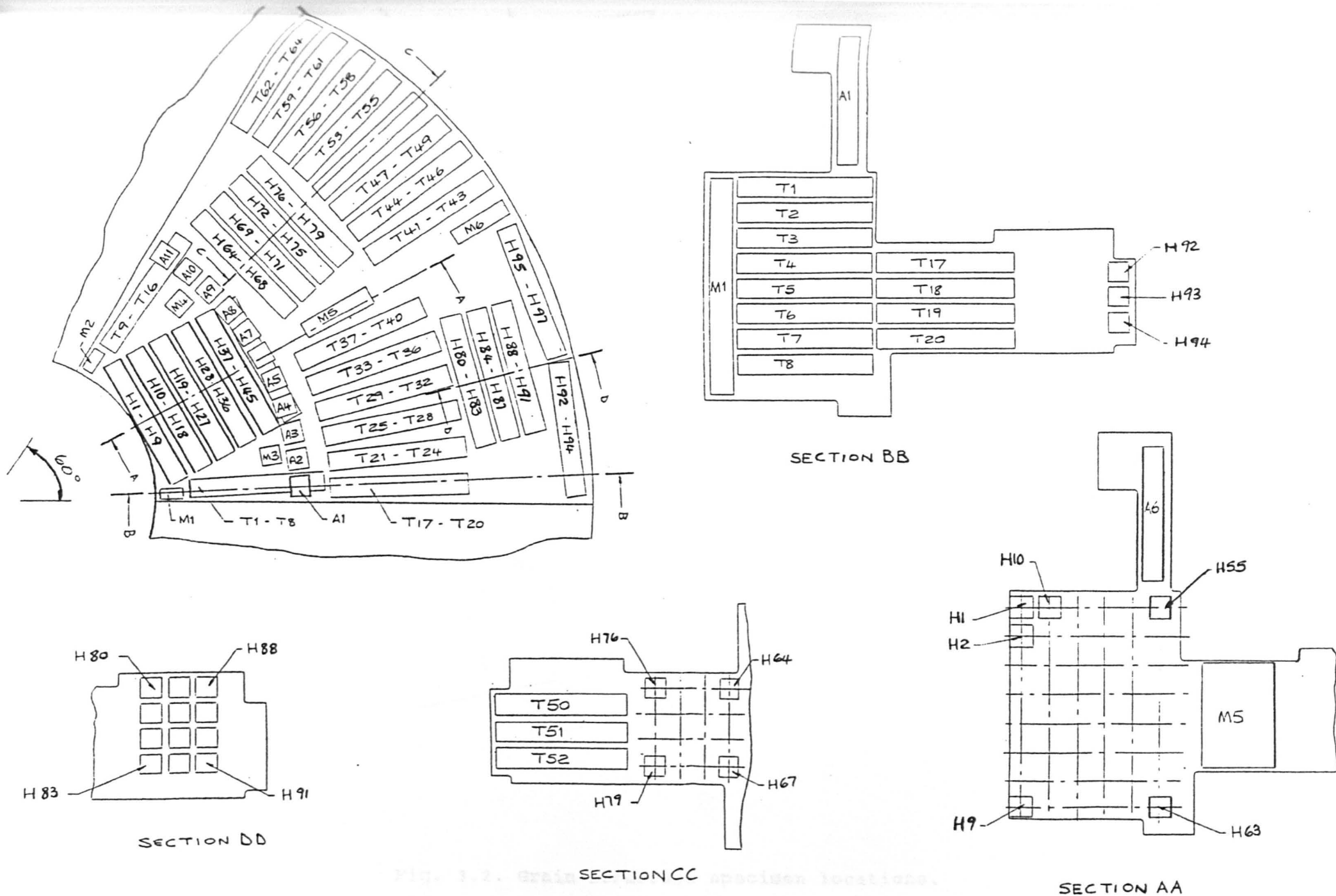
Fig. 3.1. Turbine disc cut up drawing.

SECTION BB

SECTION DD

SECTION CC

SECTION AA
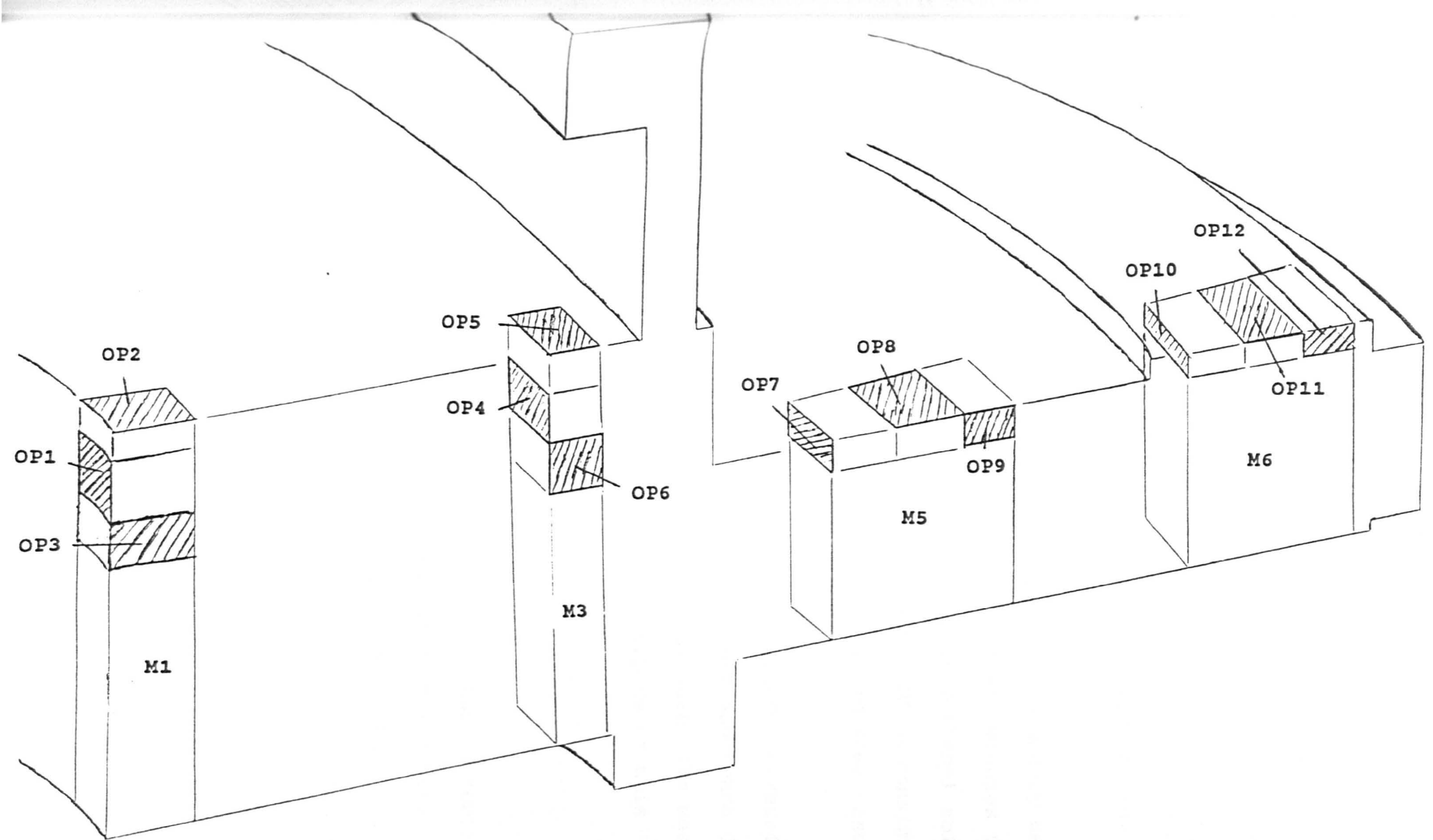
Fig. 3.2. Grain structure specimen locations.

3.2.2 Transmission Electron Microscopy (TEM)

Thin foils taken from a spare piece of material were examined in a Jeol 200 CX microscope. Slivers of the material (0.7-0.8mm thick) were obtained by a Struers Accutom unit fitted with silicon carbide slitting wheels. The sections were wet ground on P800 and P1200 paper to a thickness of 200μm, from which 3mm diameter discs were mechanically punched. Further grinding reduced the thickness of the discs to 120μm.

Discs were thinned to electron transparency using a Struers Tenupol jet thinning unit for six minutes in a 10% perchloric acid, 35% butoxyethanol, in methanol solution, at a temperature of -50°C and voltage of 40V. A consistently small perforation was achieved even if in some cases this occurred off centre.

Numerous micrographs taken from these as-received material foils were used to point count and hence determine the sizes of the second phase precipitates. The mean linear intercept method was used for the purpose of this measurement.

3.3 Mechanical Properties

The work presented in this thesis has concentrated on the tangentially orientated specimens in the bore region of the turbine disc, since the tangential or hoop stress in this region is considered to be the most damaging to a disc in service. Also, the bore facing side of each specimen was made its gauge surface, since fatigue cracks in turbine

discs tended to initiate at the bore and propagate towards the rim. For these reasons, grain size measurements and tensile tests were restricted to the bore facing sides of specimens in the bore region.

3.3.1 Grain Size

An Olympus BHM microscope equipped with an AH-MPS micro projection screen was utilised to point count and hence establish the grain size of the material. The mean linear intercept method was applied and specimens H4 and H60 were observed for this purpose.

3.3.2 Tensile Testing

Although a 0.2% Proof Stress (PS) value for Waspaloy of 860MPa was supplied by Rolls Royce, Derby and used by Zhang [46] and Brown et al. [59], this value was regarded as an overall approximation for the turbine disc, hence not strictly accurate for the bore section material. Tensile tests were carried out on bore section specimens H10 and H54 in order to gain a more accurate PS value.

The tests were undertaken with a Mayes ESM 100 machine; tensile specimens were machined from bend specimens H1 and H40 by Ashmark Engineering, Sheffield, each having a gauge length and diameter of 25mm and 3.99 ± 0.01mm respectively. Tests were in accordance with BS EN 10 002-1: 1990.

From a single tensile test a change in plotter range allowed both Proof Stress and Tensile Strength curves to be obtained; the strain rate of 0.06mm/min allowed adequate

time for the plotter to record information. Percentage reduction in area was ascertained directly from broken specimens by measuring the necked diameter at fracture.

3.4 Fatigue

Four point bend fatigue testing was selected, as opposed to the more common tensile push pull type of cycling for the reasons given below below.

A flat faced bend specimen is far simpler to machine from disc than the hour glass type of push pull specimen shown in Fig. 3.3. Prior to fatigue testing, a flat face can be mechanically ground and polished with greater ease and consistency than the necked section of an hour glass specimen. Acetate replicas can be obtained with greater ease from an upward facing flat surface than one which is curved and vertical; after cycling, TEM foils may be conveniently removed from a flat specimen, but with greater difficulty from a curved profile.

The two types of bend testing considered were three point and four point. Fig. 3.4 shows that the maximum bending moment and hence maximum stress, for the three point configuration occurs at mid-span of the "beam", as compared to over a length of the "beam" for the four point alternative. Four point bending was chosen because of the greater proportion of the surface subjected to the maximum stress, from which TEM foils could be taken and because of the inconsistent data reported from the three point bending geometry [44]. In addition, a four point bend specimen can

69
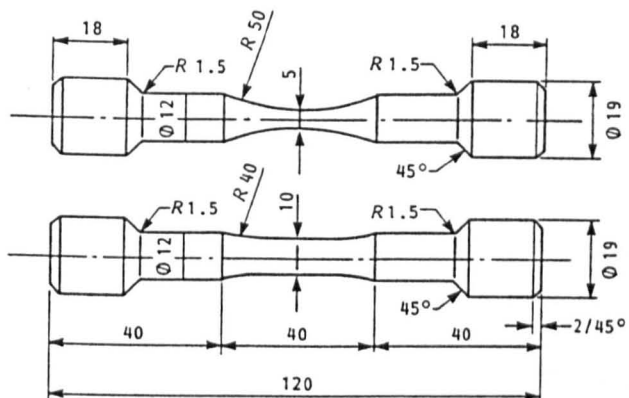
Fig. 3.3. Typical LCF hour glass specimen [44].
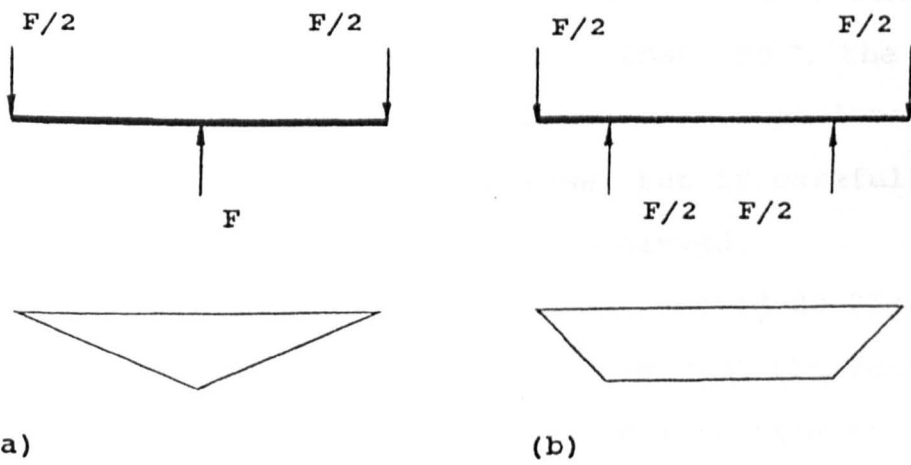
Fig. 3.4. Bending configurations (top) and respective bending moment diagrams (bottom), for (a) three point and (b) four point bending.

provide a much larger surface area for examination than a similar size hour glass specimen.

3.4.1 Fatigue Specimen Preparation

The bore facing sides of the as-supplied 80x10x10mm bend specimens were lightly ground on P1200 paper to remove machining marks, followed by polishing on a 6μm diamond pad. The P1200 paper left only fine scratches on the fatigue surface which were easily removed by the 6μm pad.

Electropolishing was undertaken on the gauge surface only; Fig. 3.5 illustrates the remainder of the specimen coated with lacomit insulating paint. Electropolishing was undertaken on a small part of the specimen sides as shown in Fig. 3.5 in order to radius the edges of the gauge surface which could otherwise provide sites for preferential cracking [45]. Specimens were electropolished in a 5% perchloric acid, 35% butoxyethanol in methanol solution for 10 minutes. For a gauge surface area of 448mm^2, conditions were 50V with the temperature lower than -50°C, the solution being stirred continuously. Problems were experienced if the temperature was allowed to increase, but if carefully monitored a consistent polish was achieved.

Electropolishing for 10 minutes removed 20-25μm of material from the fatigue surface, removing the residual stress from the residual mechanical damage from the grinding and polishing operations. The electropolish was good enough that grain boundary carbides could clearly be seen which subsequently made it possible to observe
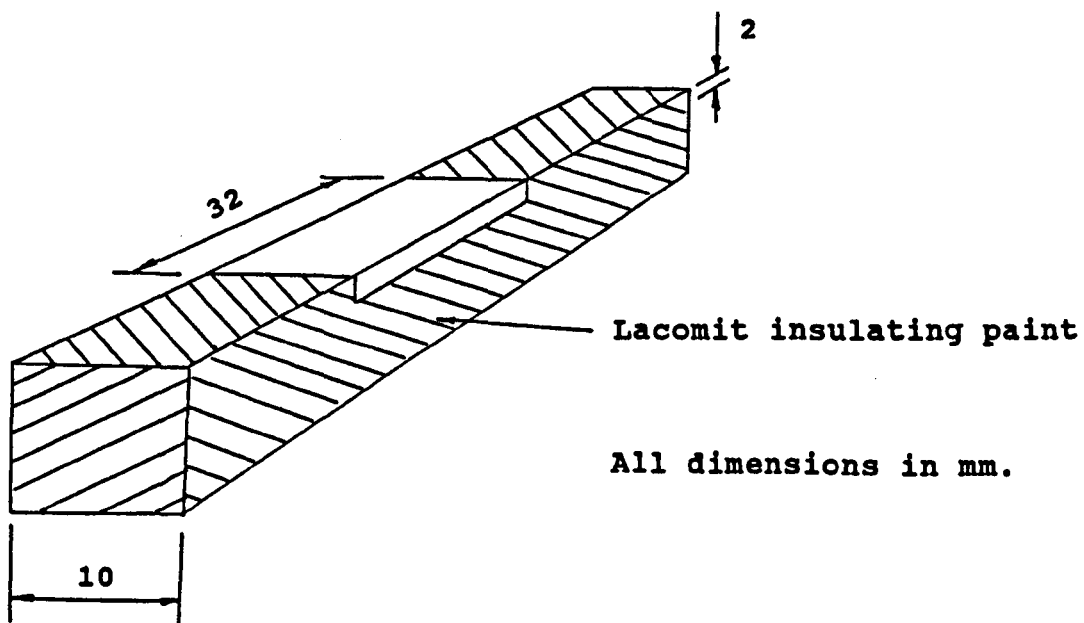
Electropolish area = 2(32 x 2) + (32 x 10) = 448mm^2

Fig. 3.5. Bend specimen coated with lacomit insulating paint to ensure electropolish of gauge surface only.

deformation/microstructure interactions.

3.4.2 Fatigue Testing

Low cycle fatigue in the form of cyclic four point bending, was undertaken on the electropolished specimens. A Mand servohydraulic testing machine in load control mode, together with a specially designed and made four point bend rig supplied by Mayes, were used for this purpose.

Using the bending configuration shown in Fig. 3.6 i.e., a span/width ratio of 2.5, and simple bending theory [146], the maximum load (F_{max}) in Newtons, applied to the fatigue specimens was calculated from:

$$F_{max} = xPSbd^2/60 \qquad\qquad (3.1)$$

where x = fraction of 0.2% Proof Stress

PS = 0.2% Proof Stress (MPa)

b = specimen breadth (mm)

d = specimen depth (mm)

Dimensions b and d were measured accurately with a micrometer in order that machining tolerances were accounted for.

3.4.2.1 SN Testing

In order to achieve a general overview of the fatigue process, thirteen specimens (H1, H3, H6, H9, H11, H14, H17, H20, H24, H27, H30, H33, H36) were cycled to failure and an
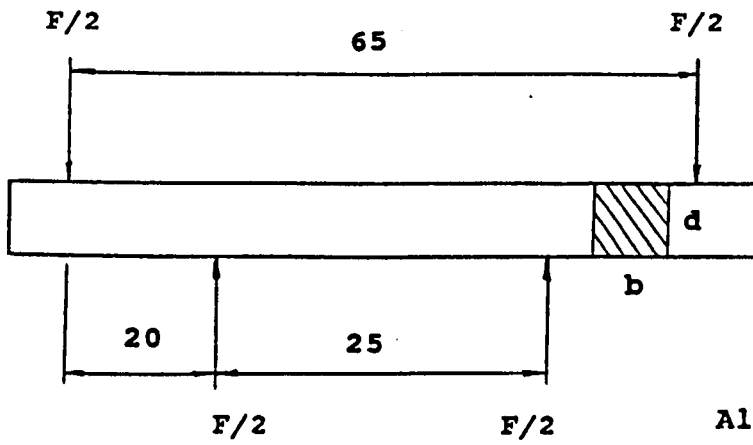
Fig. 3.6. Four point bending configuration.

SN curve was constructed. All tests were carried out in laboratory air at a frequency of 25Hz and a positive load ratio of R = 0.1. Fatigue life was determined when the primary crack had grown to approximately 2/3 thickness of the specimen; under such conditions the stress had reduced drastically and hence the load had reduced sufficiently for the machine to trip.

3.4.2.2 Fatigue Life Scatter

From the SN data two stress levels were chosen, 100%PS because of the extent of deformation observed, and 80%PS to investigate the possibility of a change in damage accumulation mechanism at a lower load.

Four more specimens (H2, H12, H8, H19) were cycled to failure under the same conditions as the SN tests at the two chosen stress levels. The extra results were used to estimate the 100% and 80% lifetimes more accurately for use in subsequent fatigue tests.

3.4.2.3 Interrupted Fatigue Tests

The aim of this part of the test programme was to determine fatigue crack initiation sites, using plastic replication techniques. Two specimens (H25 and H29) were tested to failure but stopped during the test at predetermined intervals by the function generator counter (every 25,000 cycles at 100%PS, and every 250,000 cycles at 80%PS). The fatigue surface was dowsed in acetone, the acetate positioned without force and allowed to drop off

when dry. A 10 minute hold time on mean load was adequate
for the manufacture of an acetate replica, and ensured no
relative movement between the specimen and test rig.

3.4.2.4 Fatigue Damage Accumulation Tests

The final phase of testing involved cycling specimens
to different fractions of fatigue lifetimes, to facilitate
investigations into deformation as a function of fraction of
life. Test conditions were identical to those described in
section 3.4.2.1 and the function generator counter tripped
the tests at 5,000, 10,000, 20,000, 50,000, 100,000, and
200,000 cycles at 100%PS (H5, H13, H16, H22, H28 and H34
respectively) and 75,000, 150,000, 300,000, 600,000,
1,200,000 and 2,400,000 cycles at 80%PS (H7, H15, H18, H21,
H26 and H31 respectively).

3.4.3 Optical Microscopy

Optical micrographs of the gauge surfaces of fatigued
specimens and replicas were examined using an Olympus Vanox
microscope in conjunction with Nomarski prisms and polarised
light. Nomarski interference contrast allowed the extent of
surface uplift from deformation to be assessed.

3.4.4 Scanning Electron Microscopy (SEM)

Selected fatigue surfaces and fracture surfaces were
examined in a Camscan Series 2 SEM. The back-scattered
electron mode allowed detection of secondary cracks in the
fatigue surfaces of the specimens, hence permitting

verification of optical observations. Fracture surface examination allowed short and long crack data to be gained and the associated faceted and striated regions were observed.

Acetate replicas made during interrupted fatigue testing were given a 12 minute gold sputter coating and were viewed using a Jeol JSM 6400 SEM. The combination of the thick gold coating on the replica and the 5kV accelerating voltage of the microscope minimised, but did not eliminate, electron beam damage to the replicas.

The electropolished gauge surfaces of fatigued specimens were viewed in the JSM 6400 in back-scattered electron mode to assess the extent of particle cracking. Electropolished surfaces of unfatigued specimens were also inspected, enabling comparisons to be made.

3.4.5 Transmission Electron Microscopy (TEM)

All TEM foils were examined in a Jeol 200 CX TEM fitted with a double tilt stage. Back-thinned foils were obtained from specimens cycled to various fractions of fatigue lifetimes, in order to build up a picture of damage accumulation versus cycles elapsed. Cross-sectional foils were made from failed specimens, to compare deformation at the fatigue surface with that at sub-surface depths.

3.4.5.1 Back-thinned Foils

Slivers of the gauge surfaces (0.7-0.8mm thick) were removed by a Struers Accutom unit fitted with a silicon

carbide slitting wheel, using a very slow feed rate to minimise machining damage.

The sections were back-thinned on P1200 paper to a thickness of 200µm, from which 3mm diameter discs were mechanically punched. Further mechanical back-thinning reduced the thickness of the discs to 120µm. To ensure protection of the gauge surface during back-thinning, the discs were adhered, gauge surface down, to glass slides to eliminate the possibility of mechanical damage.

Discs were thinned to electron transparency by electropolishing for 12 minutes in a 10% perchloric acid, 35% butoxyethanol, in methanol solution, at a temperature of -50°C and voltage of 40V. Initially the gauge surface of each foil was coated with lacomit insulating paint, to ensure electropolishing occurred from the back-thinned side only. This lacomit paint was removed just before perforation; electropolishing then continued from both sides until perforation. Thinning from both sides for the final 20-30 seconds gave the foils a better polish and reduced wedge angle, as opposed to back-thinning throughout, and hence provided more usable foils. However, information was only obtained from an estimated 2.5µm below the original fatigue surface.

3.4.5.2 Cross-sectional Foils

10x3x0.5mm slivers of Waspaloy were removed from gauge surfaces of failed specimens by machining with the same Struers equipment as detailed in section 3.4.5.1.

Manufacture began with the joining together of two slivers, gauge surfaces innermost, with epoxy resin. Using the same slitting equipment as above, a slot was machined in a 2mm diameter brass rod, as shown in Fig. 3.7(b). The slot was filled with epoxy resin, the sliver pair inserted and the assembly left to adhere. After encasing this assembly in 3mm outside diameter brass tube (see Fig. 3.7(c, d)), also with epoxy resin, 1mm slices were removed by a Polaron slitting lathe. The slices were glued to glass slides and wet ground to 200μm on P800 and P1200 grinding paper; the ground surface was subsequently polished on 1μm and 0.25μm pads. To reinforce the now somewhat delicate specimen, a mounting grid as shown in Fig. 3.8 was glued to the polished surface.

The central thickness of the specimen (see Fig. 3.9) was reduced to 50-60μm by dimpling with 6μm diamond paste; and further reduced to 40μm with 1μm paste. The dimpled surface was polished using 40x2mm strips of polishing pad adhered to the dimpling discs. A load of 20g was applied for all dimpling operations.

Electron transparency was achieved using Gatan Duomill ion beam milling equipment. Specimens were initially thinned at 6kV and 16° from both sides. Once a hole could be seen in the specimen it was viewed in the TEM; subsequently, 20 minute periods of thinning at 12° were carried out, in between each examination in the TEM. This allowed the thin area to be maximised and the microstructure to be evaluated as a function of depth.
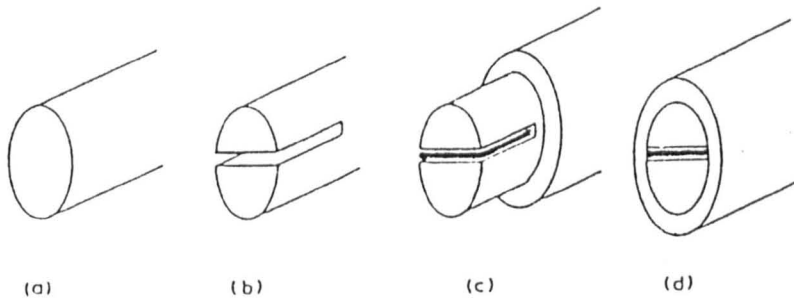
Fig. 3.7. Embedding a sliver pair for cross-sectional
thinning. A rod (a) has a slit cut in it (b), into which the
sliver pair is inserted (c). The rod is then pushed into an
epoxy-filled tube (d).

Fig. 3.8. Mounting grid for reinforcement of cross-sectional
specimen during dimpling and ion beam milling.
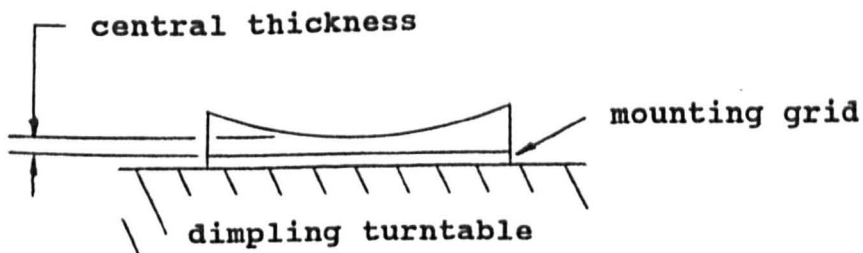
Fig. 3.9. Central thickness of dimpled specimen.

4 Results

4.1 Material Characterisation

4.1.1 Optical Microscopy

Figs. 4.1-4.3 demonstrate the significant differences in microstructure observed at various locations of the disc and for a given location, the differences in grain structure between particular orientations.

The microstructure of the turbine disc used in the investigation was generally a mixture of large and small equiaxed grains with annealing twins clearly visible. The distribution of carbides could be seen from polished sections and clearly decorated all grain boundaries. The grain size was fairly large in the bore region, but largest in the thickest section of the forging. Fig. 4.1 shows the microstructure of the orientation used in fatigue testing (OP1) which was the same as that observed at OP2. Fig. 4.2(a) shows the largest grains, observed at positions OP4, OP5 and OP6. The finest microstructure was observed in the thinnest section of the disc as shown by Fig. 4.2(b) (OP7 and OP8) while the grains were slightly larger than this at the rim as illustrated by Fig. 4.2(c) (OP10, OP11 and OP12).

When certain sections were viewed tangentially, a definite grain directionality was observed; Fig. 4.3(a) shows the coarse elongated necklace microstructure observed at OP3, and the finer structure observed at OP9 is shown by Fig. 4.3(b). Additionally, a somewhat unusual feature of the microstructure was the way in which a massive isolated grain was found to be completely surrounded by smaller grains, as

(a)

(b)

250µm
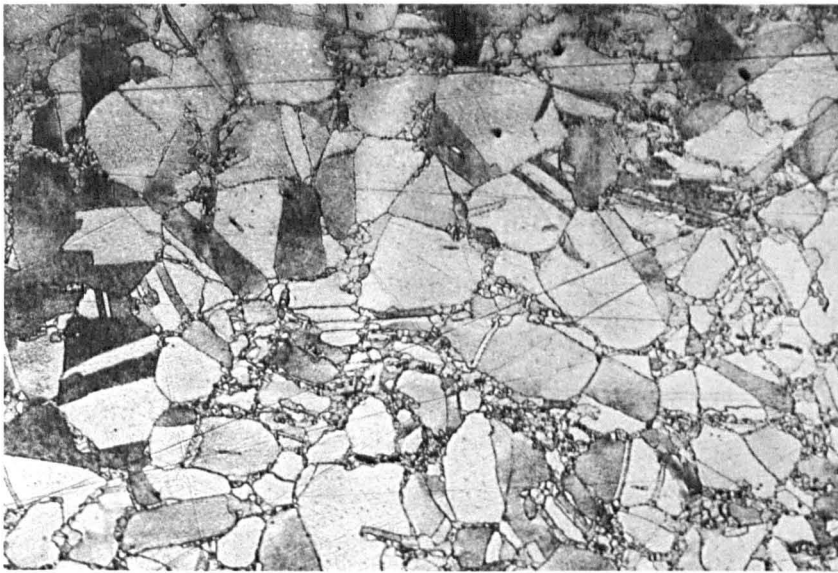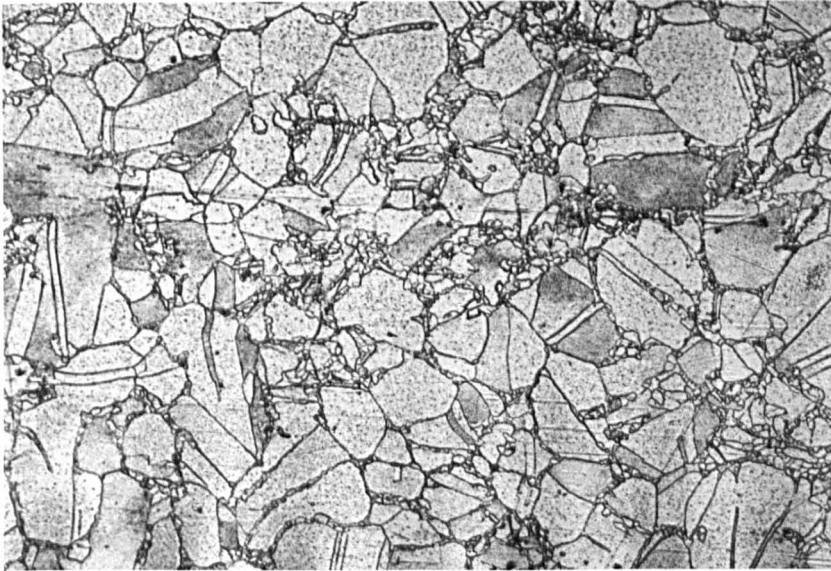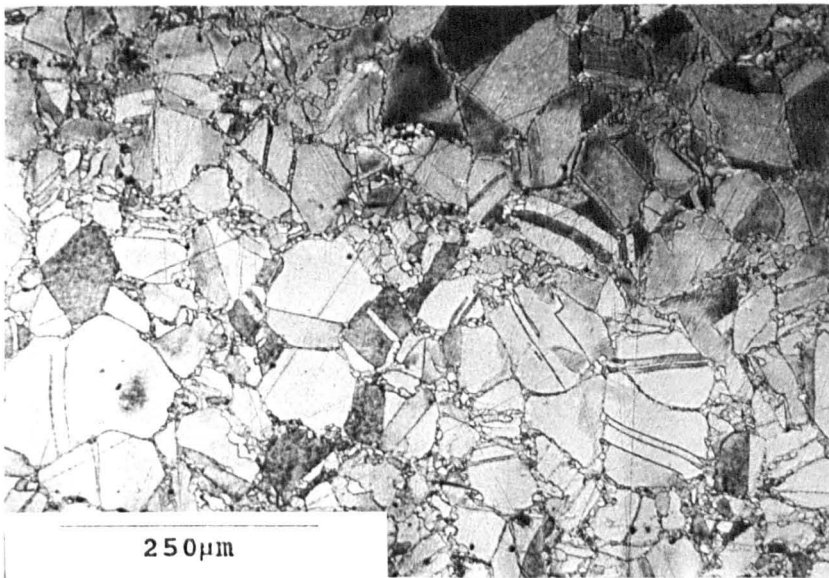
(c)

Fig. 4.1. Optical micrographs showing fairly large grains of as-received material from bore section specimens OP1 (the fatigue gauge surface orientation) and OP2 (see Fig. 3.2).

(a)

(b)

250μm
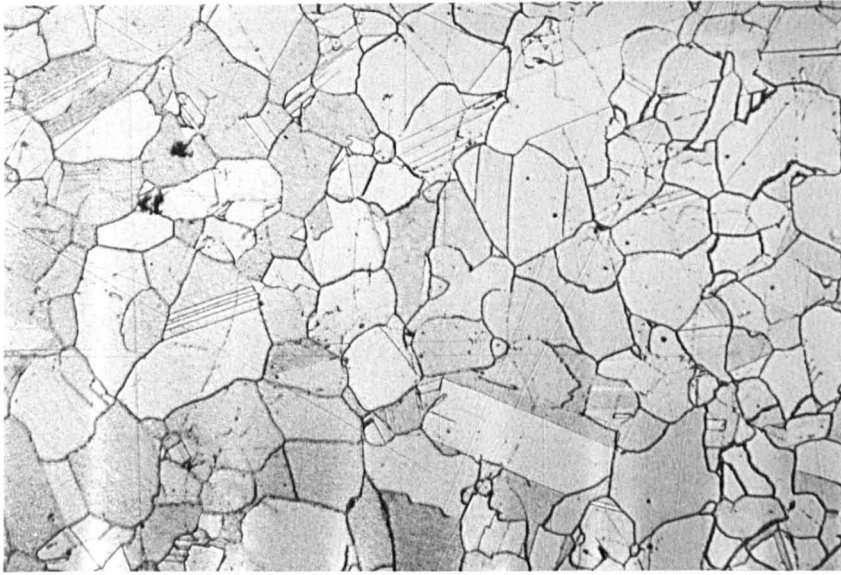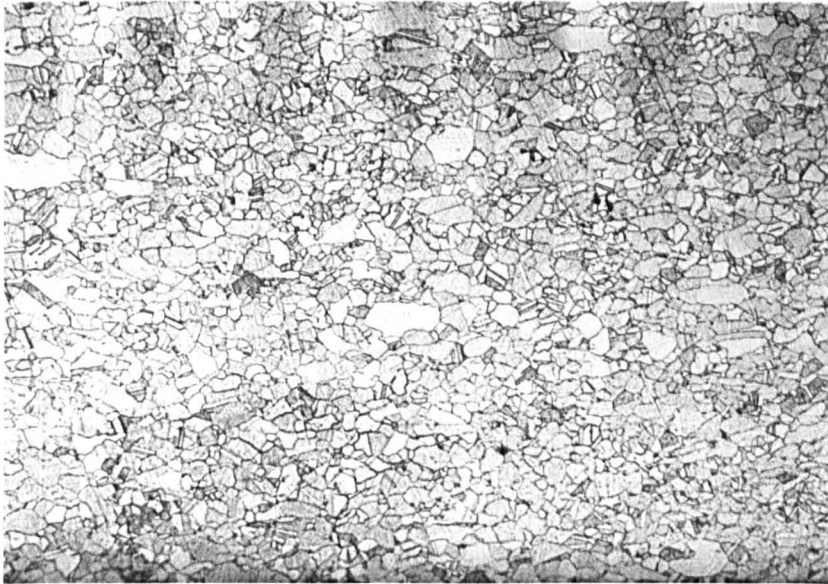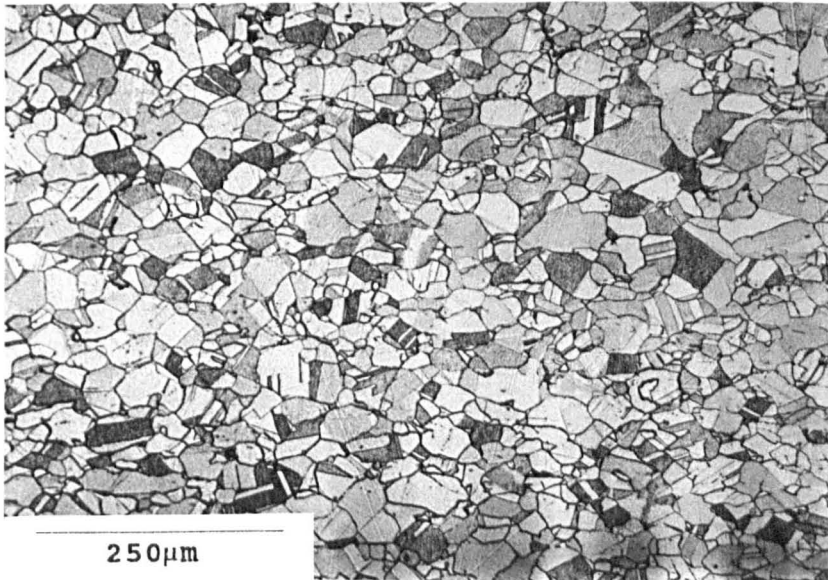
(c)

Fig. 4.2. Optical micrographs showing (a) largest grains from specimens OP4, OP5 and OP6, (b) finest grains from specimens OP7 and OP8 and (c) grain structure at the rim of the disc (specimens OP10, OP11 and OP12) (see Fig. 3.2).

(a)

(b)

(c)

250μm
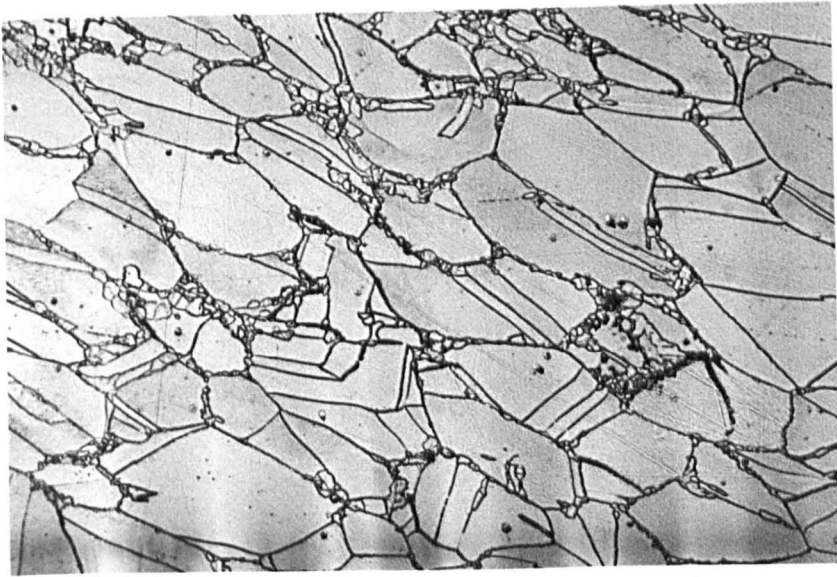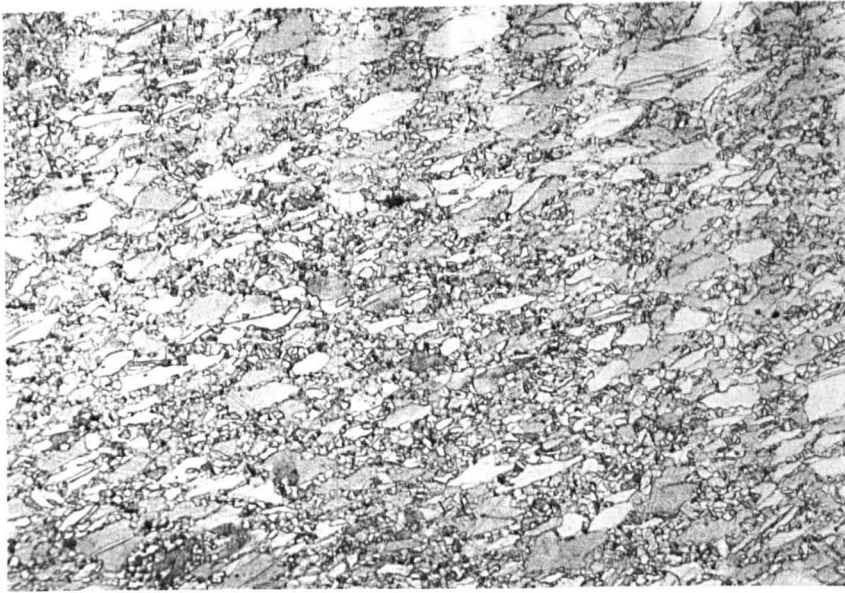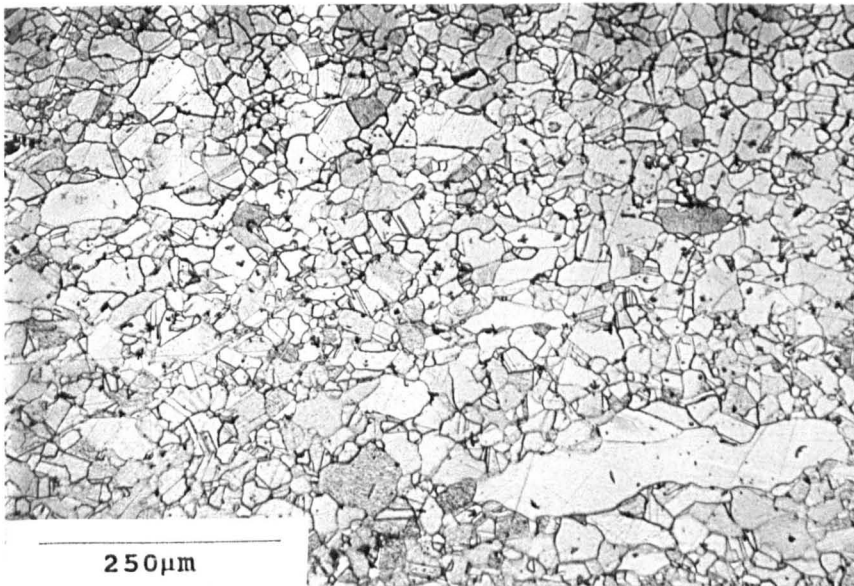
Fig. 4.3. Optical micrographs showing (a) coarse elongated grains from specimen OP3, (b) fine elongated grains from specimen OP9 and (c) a large isolated grain surrounded by smaller grains as observed from specimens OP7, OP11 and OP12 (see Fig. 3.2).

shown by Fig. 4.3(c) (OP7, OP11 and OP12).

4.1.2 Transmission Electron Microscopy (TEM)

The microstructure of the as-received material is illustrated at high magnification by Figs. 4.4-4.7. Fig. 4.4(a) shows a high angle grain boundary between two adjoining grains. The upper grain was imaged under strong 2-beam conditions and therefore microstructural features are easily observed, while negligible diffraction was occurring in the bottom grain where features are only weakly visible. Fig. 4.4(b) shows the same area as that of Fig. 4.4(a) under dark field conditions from a carbide reflection. The image illustrates the discrete carbides which pin the grain boundary; these carbides were identified as most probably of type $M_{23}C_6$ by electron diffraction [11]. Also, the boundary is wavy, indicating that the carbides had retarded grain growth during heat treatment.

The primary strengthening phase, γ', was found to be spherical in shape with a bimodal size distribution, as demonstrated by Fig. 4.5. Average sizes of the precipitates were measured as 47 and 231nm, and Fig. 4.5 displays the region immediately surrounding the large γ' to be depleted of small γ'.

Although no fatigue work was carried out on these specimens, residual dislocation structures were observed in the foils. Fig. 4.6(a) demonstrates the way in which dislocations are present in the microstructure and tend to curve around the large γ', clearly pinned by the large γ'/γ

(a)

900nm

(b)

900nm
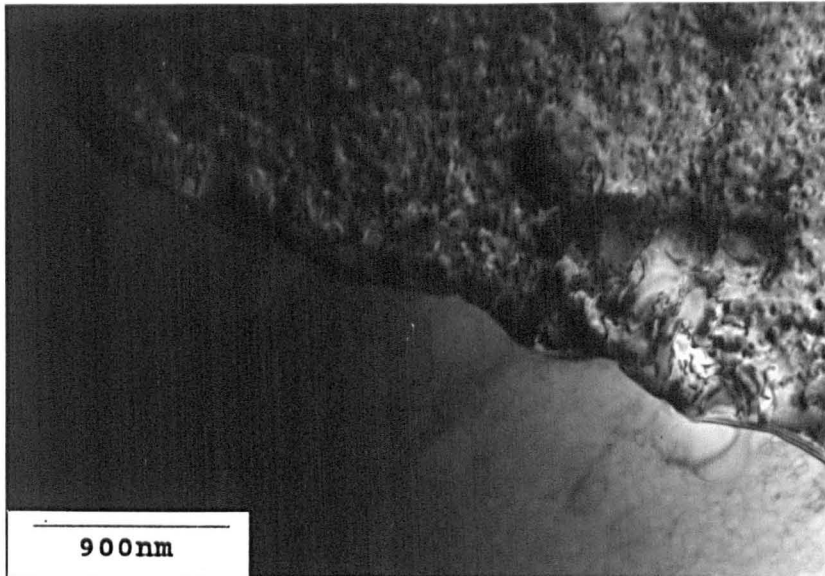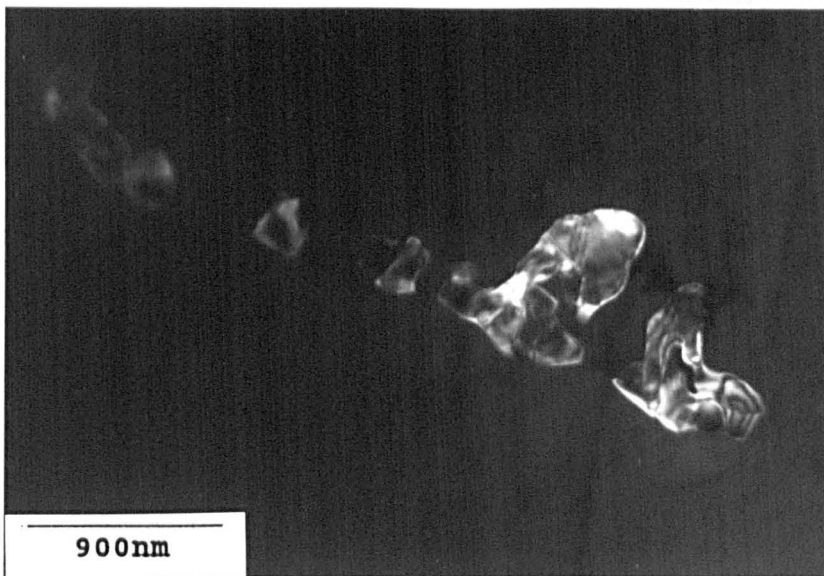
Fig. 4.4. Transmission electron micrographs of as-received material, (a) bright field image showing two grains intersected by a high angle grain boundary and (b) dark field image of (a) taken from a carbide reflection showing discrete carbides pinning the boundary.
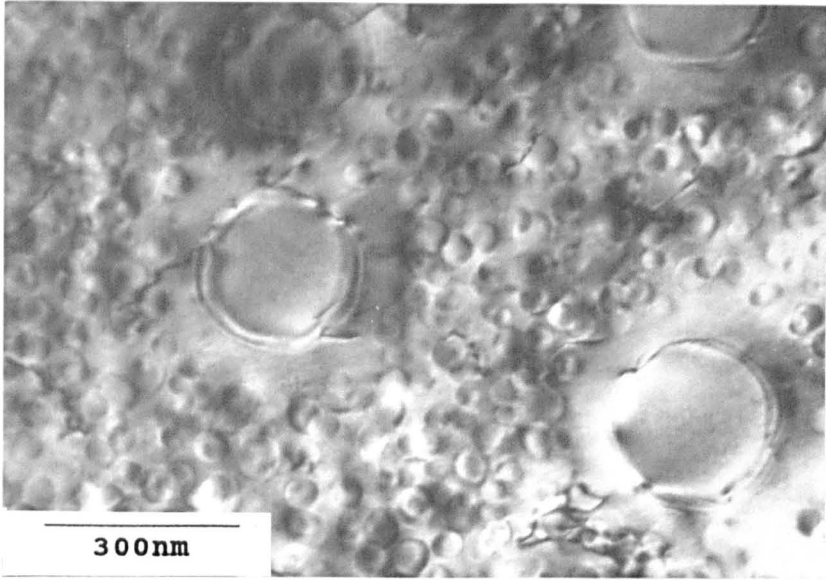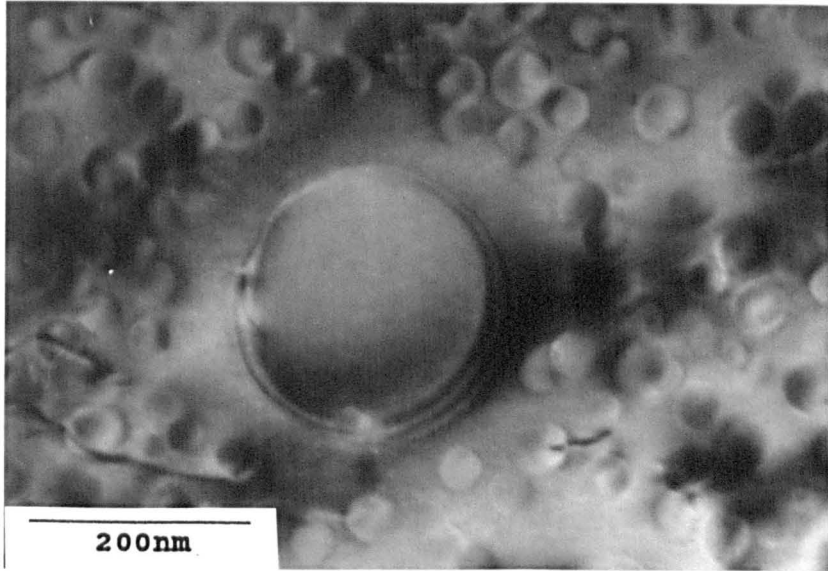
Fig. 4.5. Bright field transmission electron micrographs of as-received material showing the bimodal distribution of γ', and the depleted regions surrounding the large γ' (a) low magnification and (b) high magnification; <011> orientations.

400nm

(a)

140nm
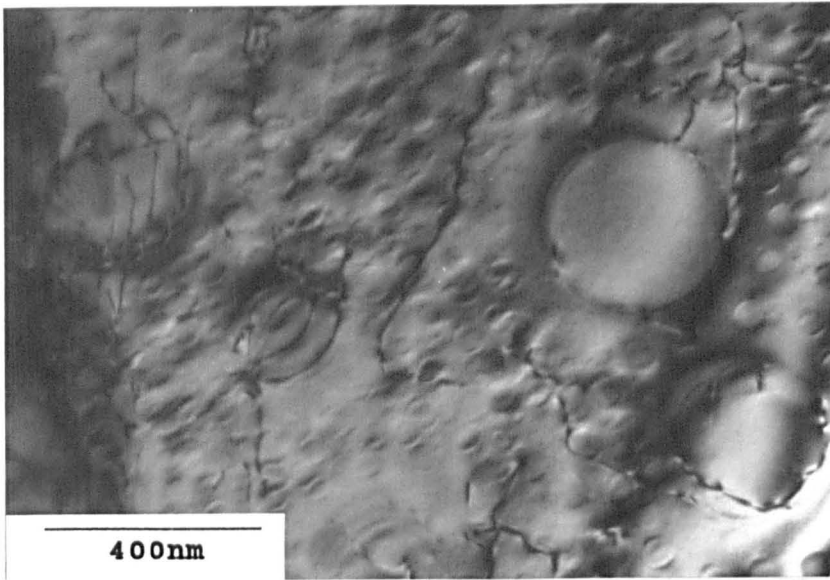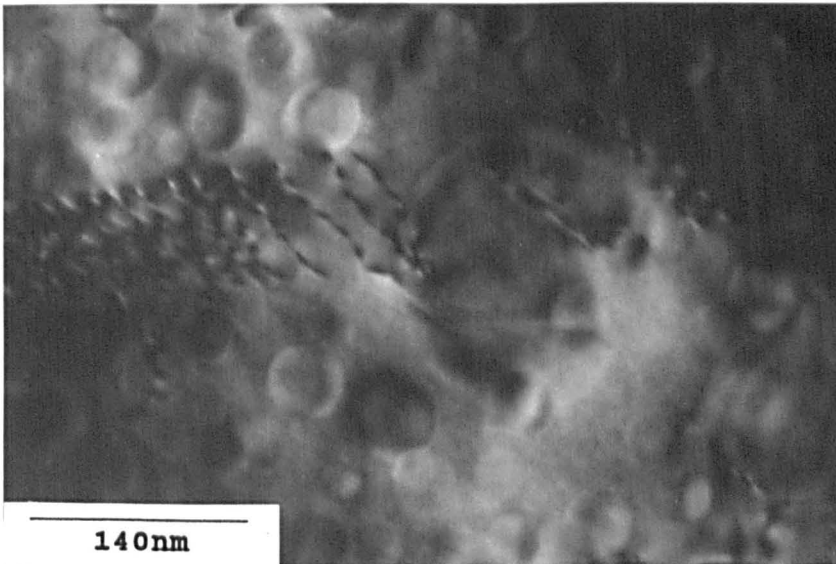
(b)

Fig. 4.6. Bright field transmission electron micrographs
showing examples of the residual dislocation structures
present in the as-received material, (a) dislocations pinned
by the large γ′ and (b) a dislocation pile up in the
material, the dislocations being pinned by the large γ′.
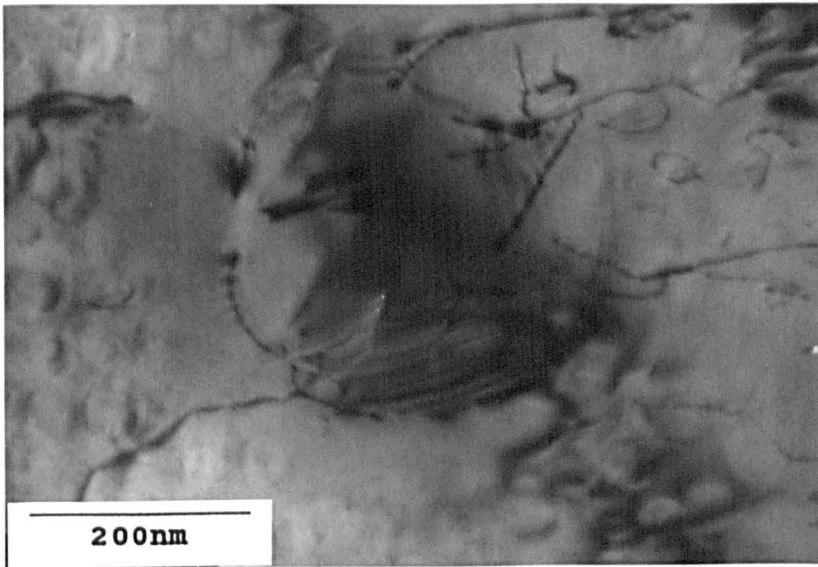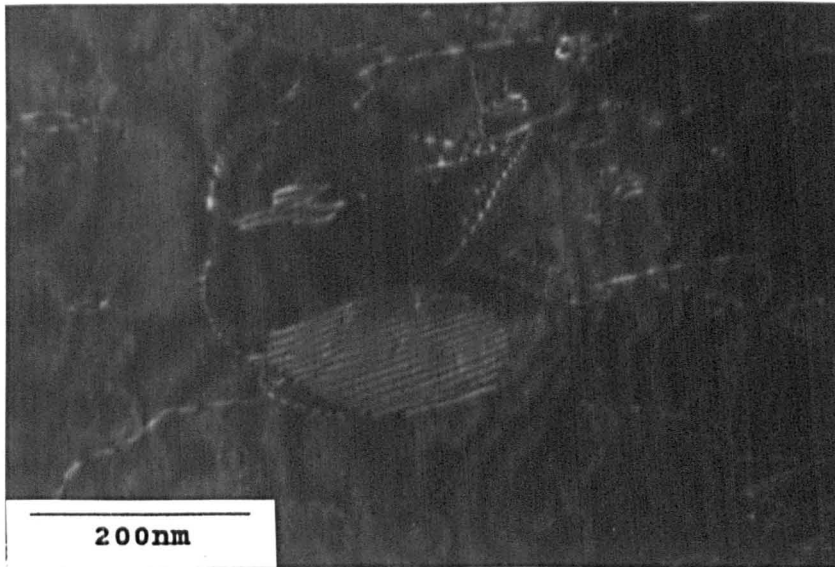
Fig. 4.7. Transmission electron micrographs of as-received material showing stacking fault contrast in some of the γ′; (a) bright field and (b) weak beam dark field image; <011> orientations.

interface. Fig. 4.6(b) displays a dislocation pile-up within the material and also shows pinning of the dislocations by the large γ'. Fig. 4.7 shows stacking fault contrast in one of the large γ' particles and in several of the smaller; it is obvious from this pair of micrographs, that the features are seen much more clearly in the weak beam image of Fig. 4.7(b). The damage was most probably a result of residual stresses from forging or heat treatment; the dislocation densities observed from Figs. 4.6 and 4.7 are notably lower than those seen in early fatigue specimens (see section 4.3.5.3.1).

4.2 Mechanical Properties

4.2.1 Grain Size

Grain sizes for specimens H4 and H60 are given below in Table 4.1.

Specimen No.	Grain Size (μm)	Standard Deviation (μm)
H4	166.4	21.7
H60	159.6	26.8

Table 4.1: Grain Size Measurements

4.2.2 Tensile Properties

Tensile test results can be seen in Table 4.2. The 0.2% proof stress (PS) values of 907 and 953MPa for specimens H10 and H54 respectively suggest that the value of 860MPa used by Zhang [46] and Brown et al. [59], can only be taken as an overall approximate figure for the turbine disc.

Specimen No.	0.2% Proof Stress (MPa)	Tensile Strength (MPa)	% Reduction in Area (%)
H10	907	1300	32
H54	953	1308	24

Table 4.2: Tensile Test Results

4.3 Fatigue Behaviour

4.3.1 SN Results

Thirteen bend specimens were tested to failure, the results are presented in Table 4.3 and the SN curve is plotted in Fig. 4.8.

Stress Range (MPa)	Max. Surface Stress Actual (MPa)	%PS (%)	Specimen No.	Cycles to failure (x10^6)
612	680	75	H1	4.43
653	726	80	H3	4.24
694	771	85	H6	1.46
694	771	85	H9	0.77
734	816	90	H11	2.40
734	816	90	H14	0.60
776	862	95	H17	0.52
776	862	95	H20	0.48
816	907	100	H24	0.32
857	952	105	H27	0.22
898	998	110	H30	0.34
898	998	110	H33	0.33
980	1088	120	H36	0.32

Table 4.3: SN Results

Prior to failure, the fatal cracks were seen on some of the specimens by the naked eye from the uplift of the gauge surface. In some cases this was observed only a fraction of lifetime before failure, for example, on specimen H24 (100%PS) an estimated 2mm crack was noticed after 279,600
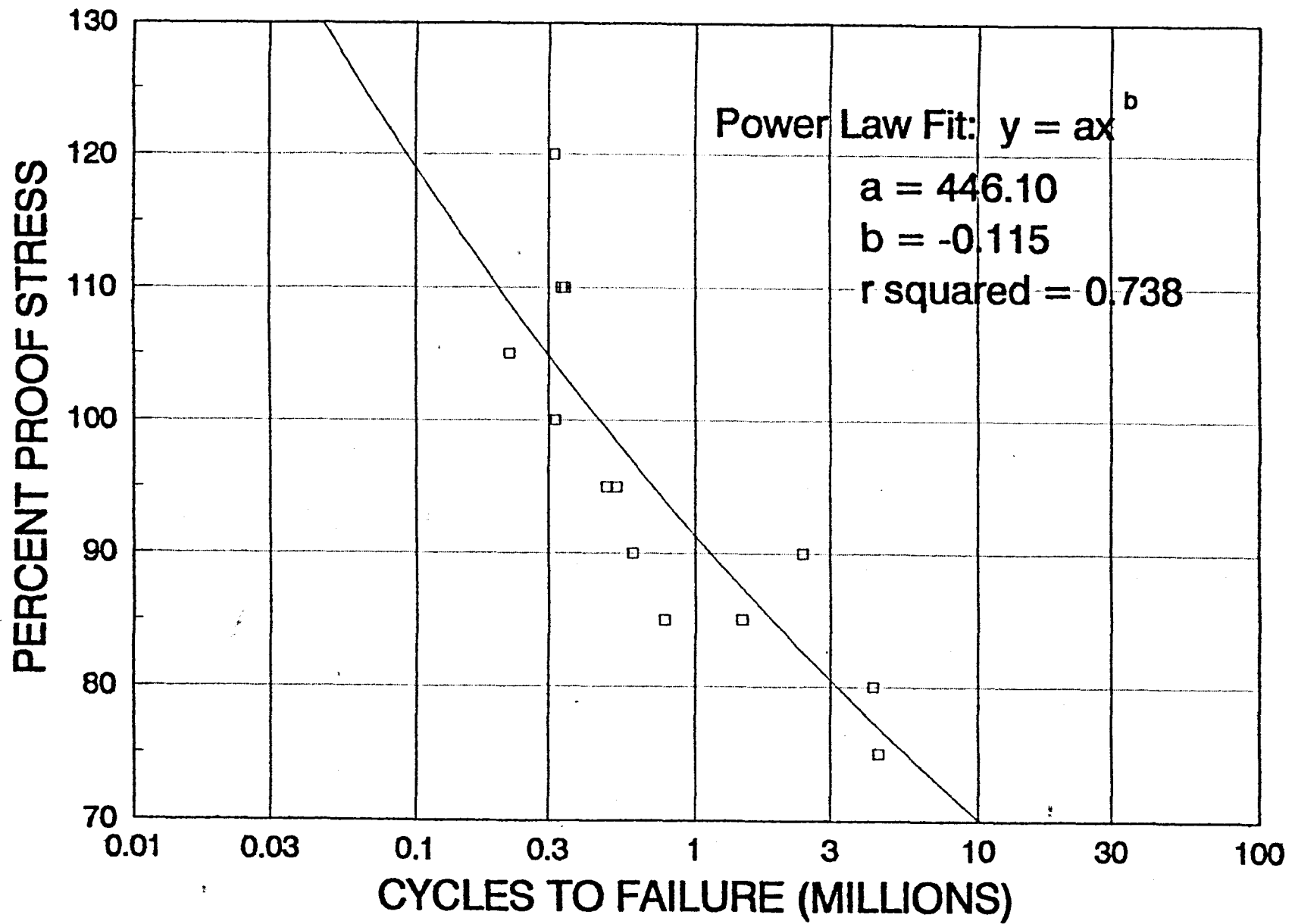
Fig. 4.8. SN Curve.

cycles, yet it failed after only 316,700 cycles; in contrast, an estimated 1mm crack was visible on specimen H11 (90%PS) after only 746,600 cycles, but failure of this specimen did not occur until 2,403,400 cycles. However, certain specimens appeared crack free throughout the tests; this was the situation for specimen H6 (85%PS) which was visibly crack free after 1,400,000 cycles, but snapped after just 60,000 more (1,460,000 cycles in total).

Virtually all of the SN specimens tested were cracked close to one of the load points of the 25mm span, perhaps suggesting uneven roller contact. Exceptions to this were specimens H11 (90%PS) and H24 (100%PS) which were cracked near to the centre of the span, also H36 (120%PS) which had fractured right in the centre of the gauge surface. Five SN test specimens failed as a result of cracks propagating from edge initiation sites on the gauge surfaces; four had cracks initiate from within the interior of the gauge surface. In the remainder of the tests, the initiation sites were not seen. In almost every SN specimen, fracture occurred by the propagation of a single crack as observed from the gauge surface; the only exception was specimen H30 (110%PS) whose crack had two visible forks in it, probably as a result of crack coalescence from two initiation sites.

All of the SN specimens tested to failure exhibited slip bands adjacent to the primary crack, either along the entire length, or a part of the length of the crack. The density of slip bands in some areas adjacent to the primary crack was extremely high, with multiple slip a common

81

observation. The propagation of slip bands in adjoining grains was frequently observed in the areas of high slip band density, along with surface uplift often making focussing difficult in high magnification optical microscopy. Fig. 4.9 illustrates the way in which the primary crack path followed slip band traces, this was an observation common to all of the SN specimens and is associated with a strong crack closure effect [40].

It was noted that the extent of deformation as indicated by surface slip bands was greater at higher stress levels. For specimens tested at 95%PS or greater, densely distributed slip bands were observed along the entire lengths of the primary cracks, an example of such deformation is illustrated in Fig. 4.10(a). Well defined slip bands extending across most of the grains were observed over the majority of the gauge surface, as shown in Fig. 4.11(a).

In contrast to the above, specimens tested at lower stress levels, for example 80%PS, exhibited significant deformation over only a fraction of the length of their primary cracks (as shown by Fig. 4.10(b)), the remaining length having zero or negligible slip as demonstrated by Fig 4.10(c). For such specimens, slip was obviously very localised on the gauge surface since only very slight deformation was observed at locations a small distance from the primary crack, (see Fig. 4.11(b, c)).

Numerous secondary cracks were observed on specimens' gauge surfaces, an example is shown by Fig. 4.12. It is not

100µm
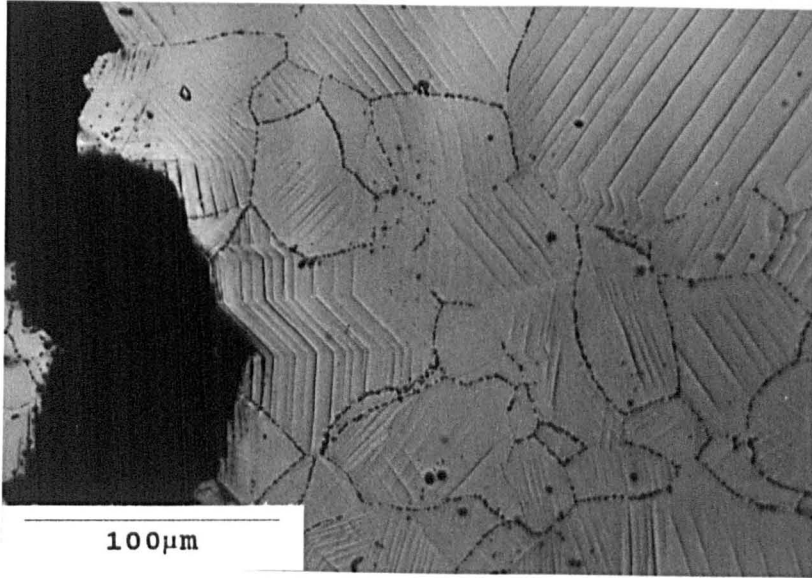
Fig. 4.9. Optical micrograph from failed SN specimen H3 (80%PS) showing slip bands adjacent to the primary crack, (stress axis horizontal).

(a)

(b)

100μm
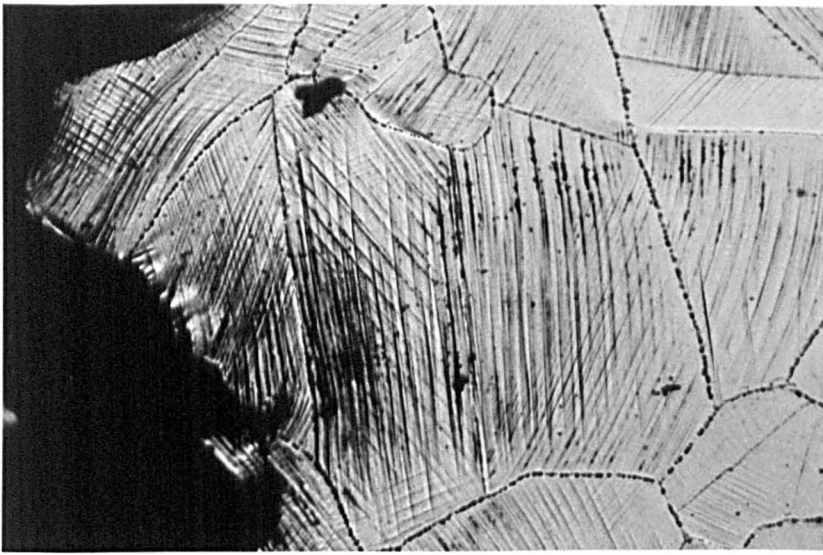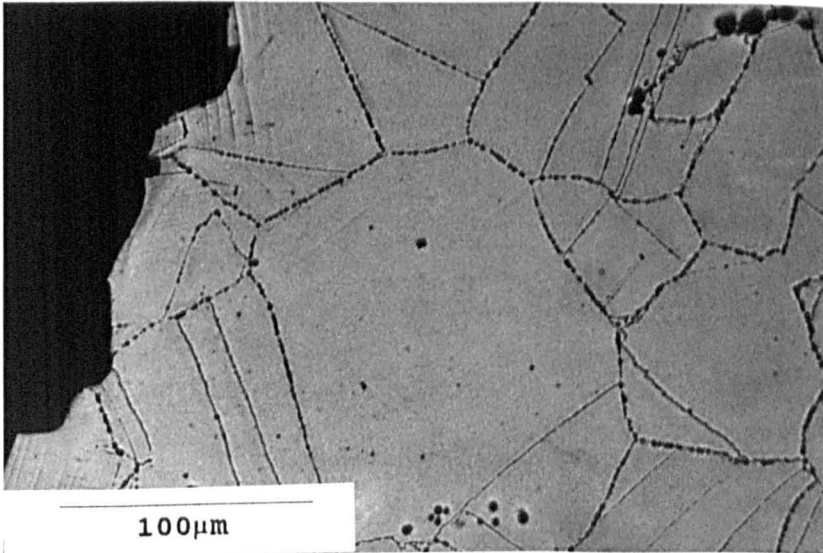
(c)

Fig. 4.10. Optical micrographs from failed SN specimens showing slip bands adjacent to primary cracks, stress axis horizontal, (a) slip bands representative of those over the entire primary crack length of specimen H24 (100%PS), (b) slip bands seen only in the region of initiation of the primary crack of specimen H3 (80%PS), and (c) lack of deformation along most of the primary crack of H3.

(a)

(b)

100μm
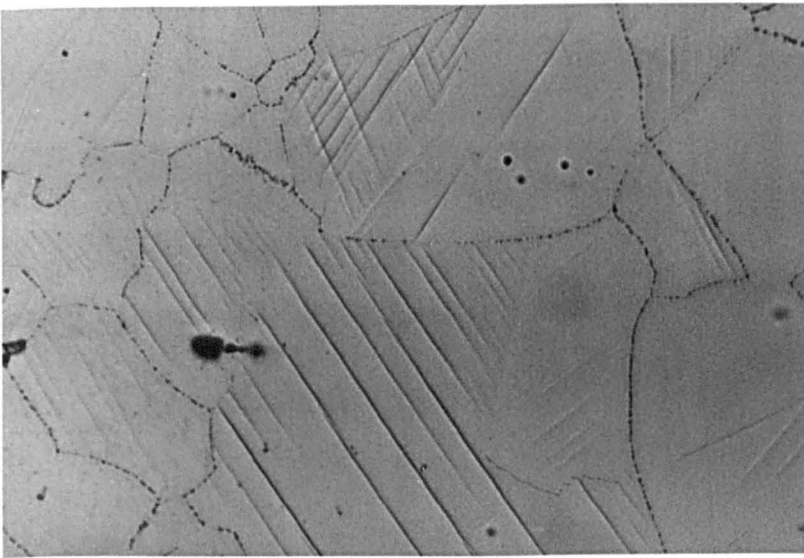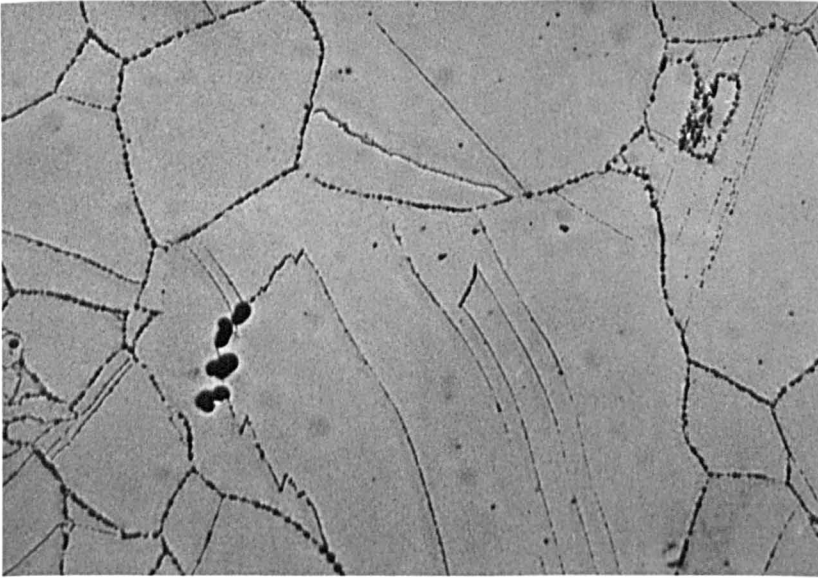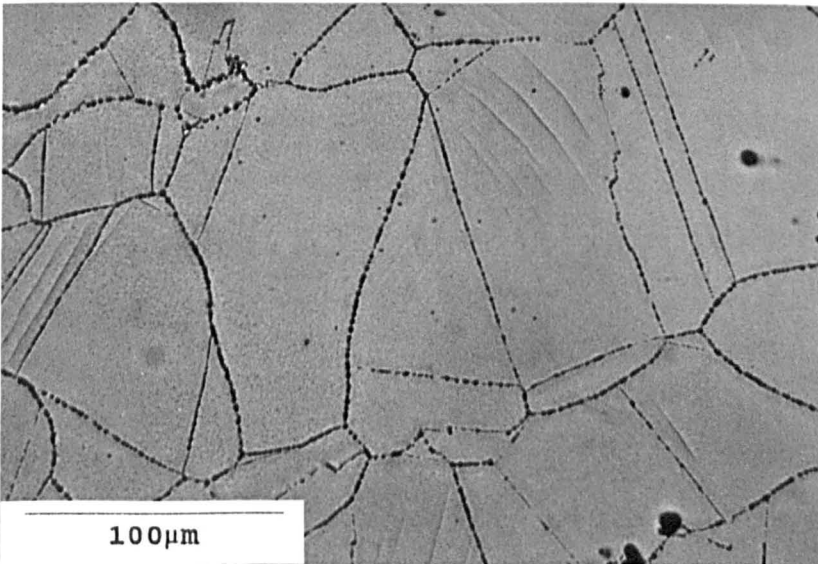
(c)

Fig. 4.11. Optical micrographs from failed SN specimens showing (a) significant deformation 10mm from the primary crack of specimen H24 (100%PS), (b) and (c) negligible deformation 1mm and 5mm respectively from the primary crack of specimen H3 (80%PS). Stress axis horizontal.
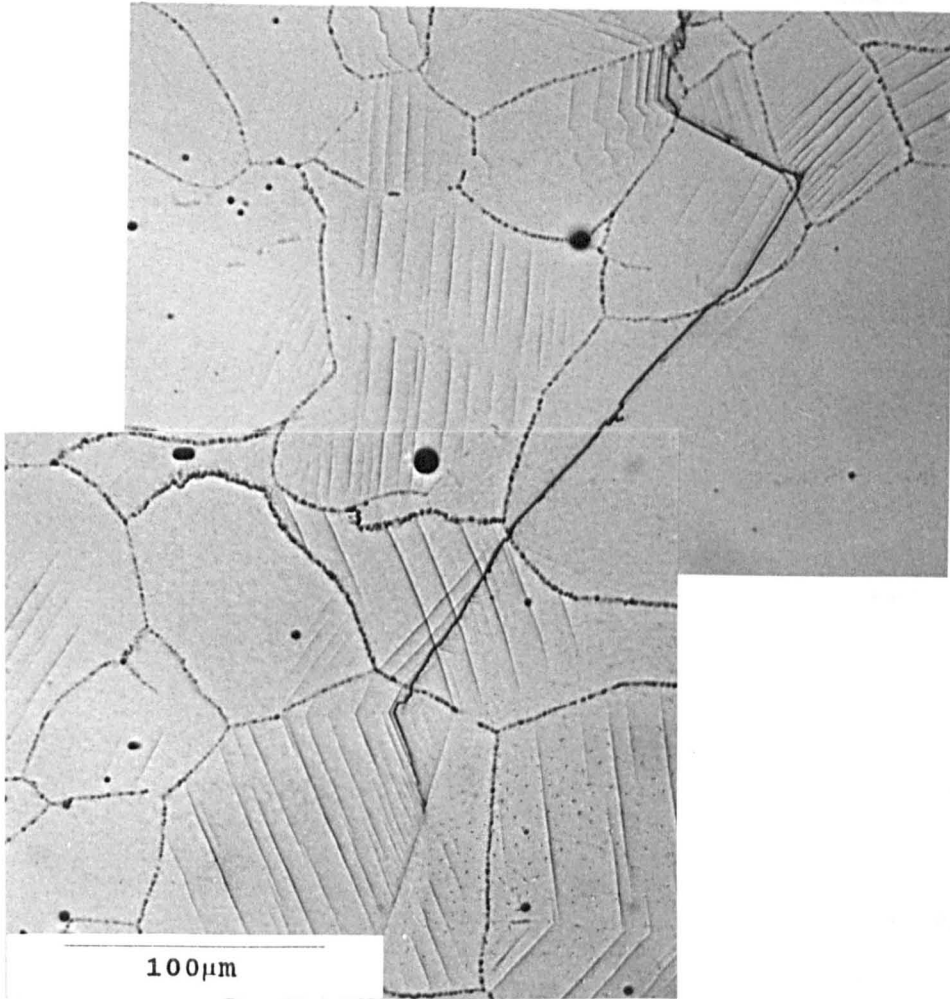
Fig. 4.12. Optical micrograph of a secondary crack 9mm from the primary crack on failed SN specimen H27 (105%PS). Stress axis horizontal.

clear from this type of micrograph as to how the crack initiated but, since the crack followed slip bands along its length, it is considered to be a slip band crack.

The number of secondary cracks counted over each specimen's gauge surface are shown in Table 4.4.

Stress Range (MPa)	Max. Surface Actual (MPa)	Stress %PS (%)	Specimen No.	Number secondary cracks
612	680	75	H1	0
653	726	80	H3	2
694	771	85	H6	3
694	771	85	H9	5
734	816	90	H11	1
734	816	90	H14	14
776	862	95	H17	17
776	862	95	H20	8
816	907	100	H24	49
857	952	105	H27	163
898	998	110	H30	29
898	998	110	H33	33
980	1088	120	H36	36

Table 4.4: Number of Secondary Cracks Counted

Although the relationship, if any, between the number of secondary cracks and stress level is not known, it was noted that as the stress was increased, more cracks were observed. An anomalously high number was observed on specimen H27 (105%PS), but the reason for this was not clear.

4.3.2 Fatigue Life Scatter

For the chosen stress levels fatigue life scatter results are presented under the original SN results, in Table 4.5. It can be seen that a scatter range in life of 200,000 cycles has been established from the three 100%PS

Stress Range (MPa)	Max. Surface Actual (MPa)	Stress %PS (%)	Specimen No.	Cycles to failure (x10^6)
816	907	100	H24	0.32
816	907	100	H2	0.26
816	907	100	H12	0.46
653	726	80	H3	4.24
653	726	80	H8	3.49
653	726	80	H19	2.97

Table 4.5: Fatigue Life Scatter Results

specimens tested, and a range of 1,270,000 cycles for the three 80% specimens.

Specimens H2 and H8 fractured very close to one of the load points, H12 snapped in the centre of the span and the primary crack of H19 was located approximately midway between the centre of the span and a load point. All of the cracks were initiated from an edge on the gauge surface except that of specimen H19.

4.3.3 Interrupted Fatigue Tests

Interrupted test lifetimes are presented in Table 4.6, and have demonstrated that regularly interrupting the tests

Stress Range (MPa)	Max. Surface Actual (MPa)	Stress %PS (%)	Specimen No.	Cycles to failure (x10^6)
816	907	100	H25	0.31
653	726	80	H29	3.71

Table 4.6: Interrupted Test Results

apparently had no effect on fatigue lives.

In general, crack initiation was found to occur between 25,000 and 50,000 cycles at 100%PS and around 500,000 cycles at 80%PS. The primary crack of specimen H25 was traced back every 25,000 cycles to its initiation; the primary crack had formed from the link up of two smaller cracks, which had initiated from inclusions after 25,000 cycles. Fig 4.13(a) shows the fatal crack after 75,000 cycles, the tips of the two cracks can be seen extending into the matrix of the alloy surrounding the inclusions (as shown by arrows). After 125,000 cycles (Fig. 4.13(b)) the cracks were more developed, had each extended across 5-6 grains and at 150,000 cycles were just about to link up to form the fatal crack (Fig. 4.13(c)).

A similar observation was made on a secondary crack on specimen H25 shown in Fig. 4.14, located by replicas. The crack can be seen at 50,000 cycles propagating away from a line of inclusions (see arrow on Fig. 4.15(a)). After 300,000 cycles the crack is virtually in its final condition, and is shown by Fig. 4.15(b). Other examples of cracks initiating from inclusions are shown by Figs. 4.16 and 4.17; these examples are from the 80%PS replicas taken from specimen H29 and show initiation taking place at 500,000 cycles. Inclusions have been reported as one of the most common fatigue crack initiation sites for nickel base superalloys [49]. The above cracks from the 80%PS replicas are shown by Figs. 4.16(b) and 4.17(b) as spanning 5 grains and 4 grains respectively, i.e. they are still considered to be short cracks.

85
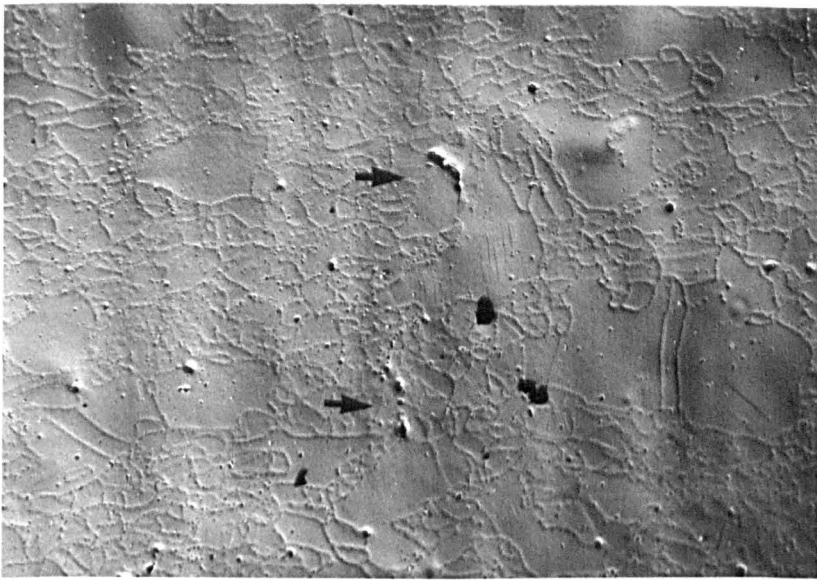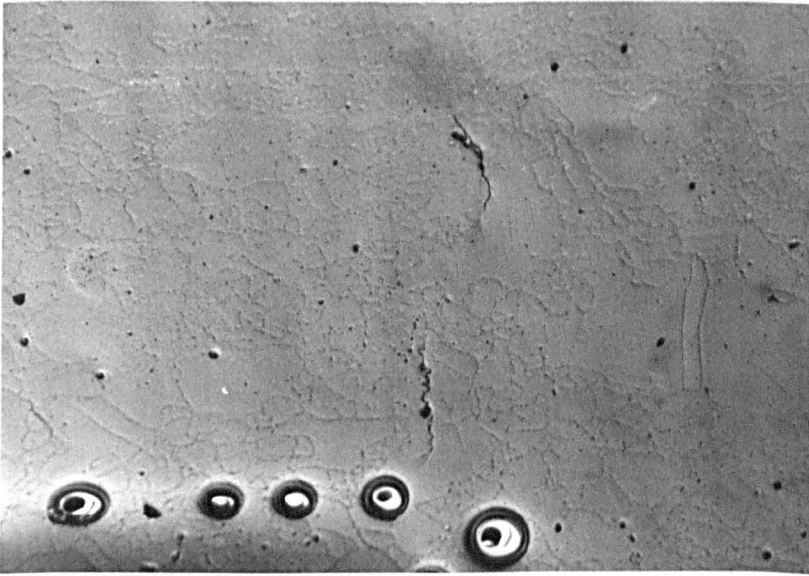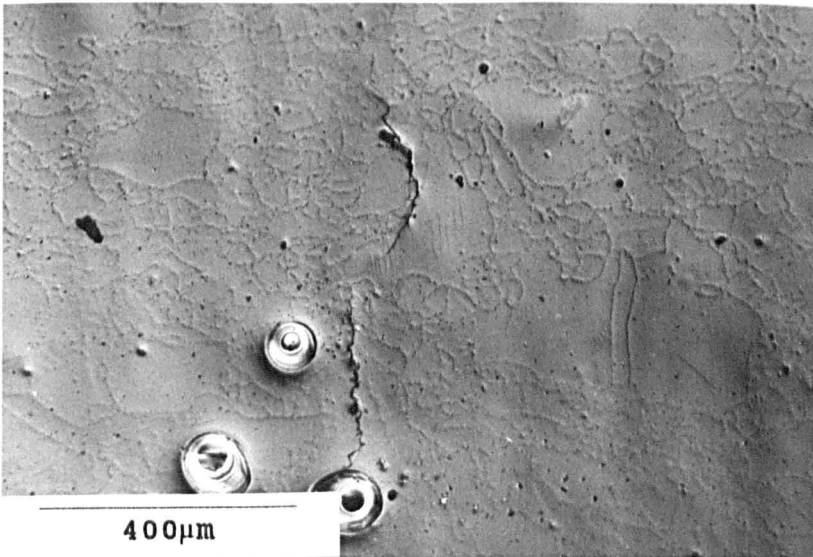
Fig. 4.13. Optical micrographs from 1-stage replicas taken from specimen H25 (100%PS), showing propagation of the primary crack after (a) 75,000, (b) 125,000 and (c) 150,000 cycles. Arrows on (a) show initiation sites after 75,000 cycles. Stress axis horizontal.

100μm
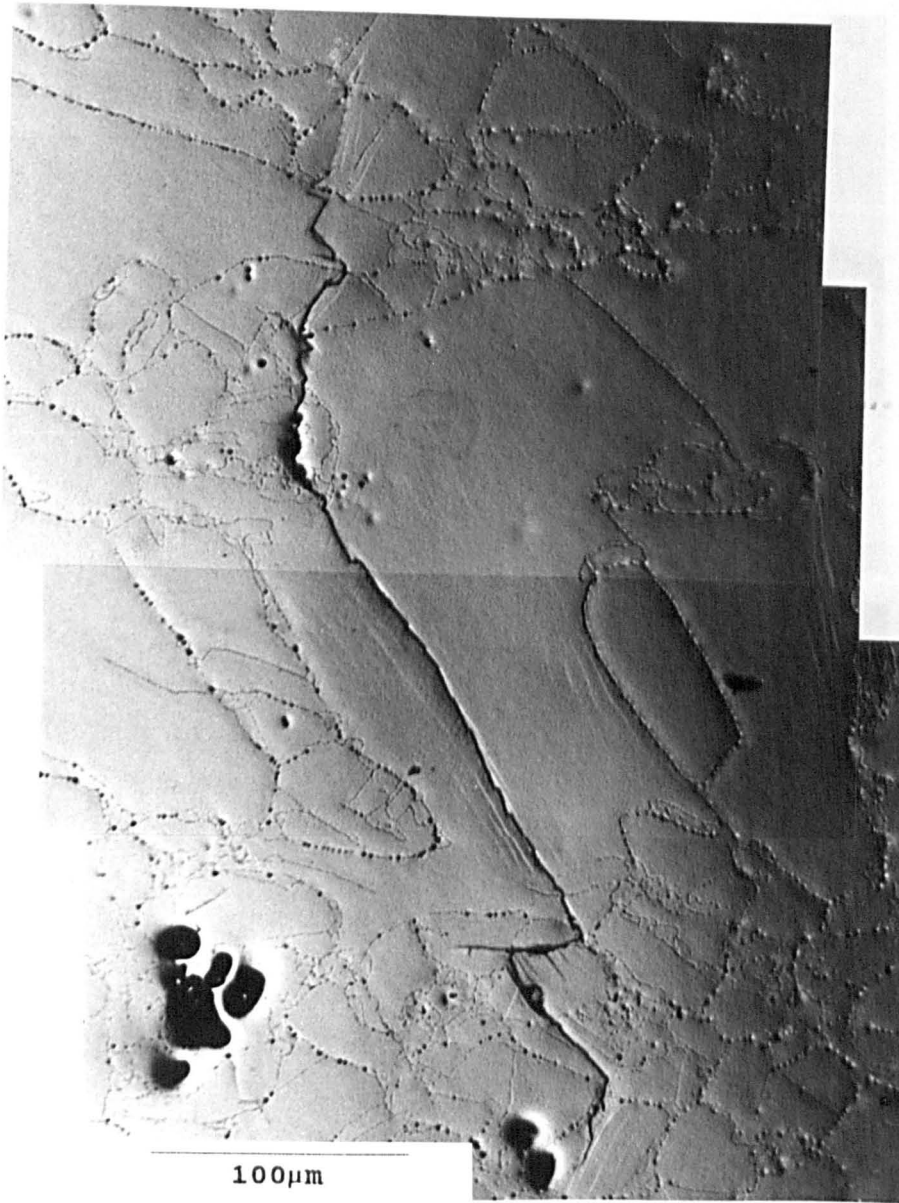
Fig. 4.14. Optical micrograph of a secondary crack 5mm from the primary crack on fatigued specimen H25 (100%PS). Stress axis horizontal.
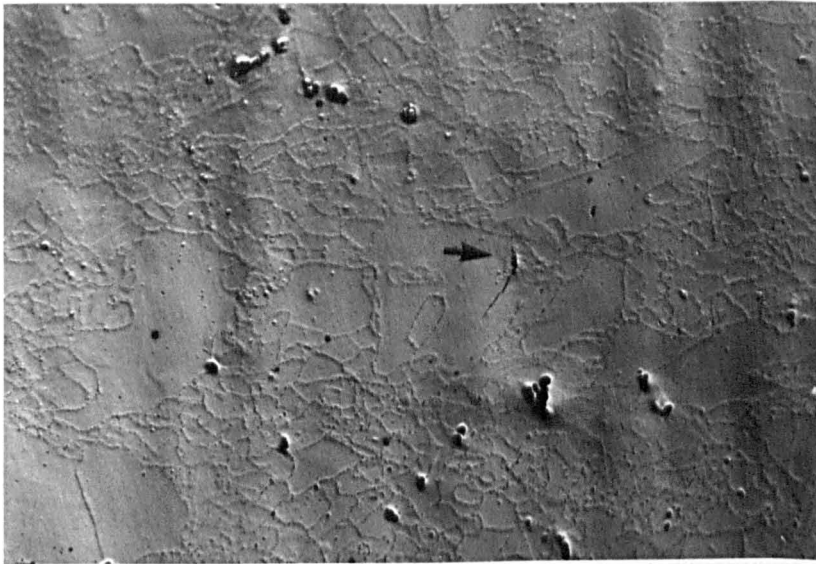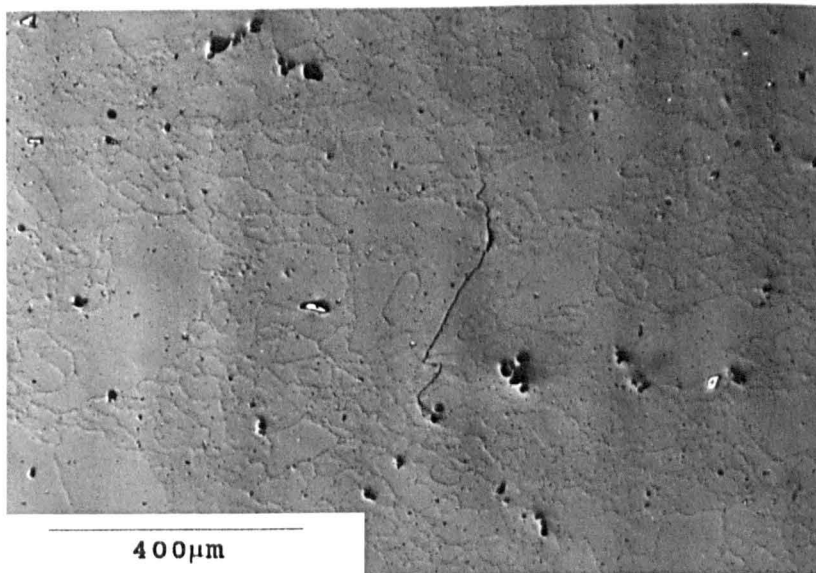
Fig. 4.15. Optical micrographs from 1-stage replicas taken from specimen H25 (100%PS) showing the secondary crack of Fig. 4.14, after (a) 50,000 and (b) 300,000 cycles. Arrow on (a) shows initiation site. Stress axis horizontal.
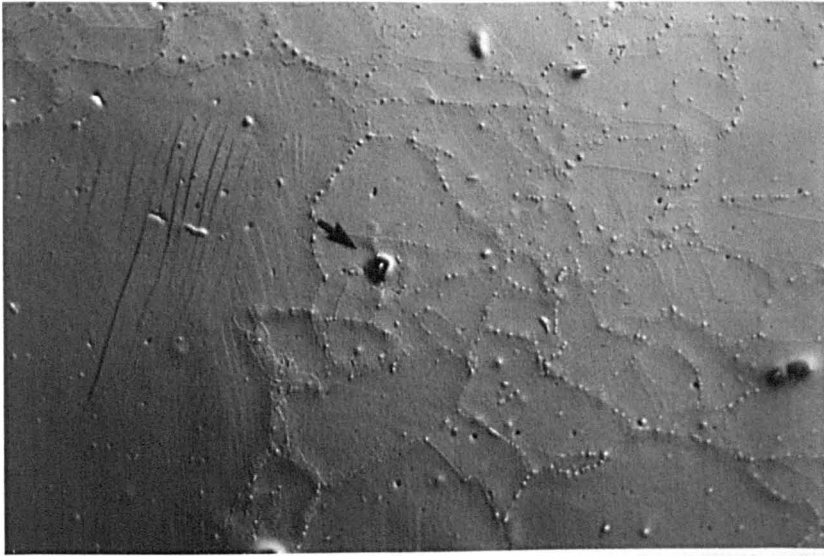
(a)
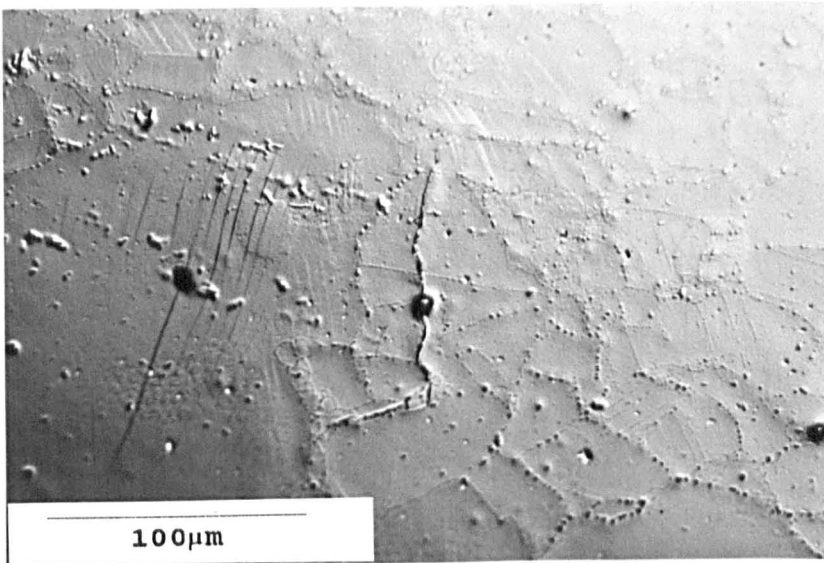
(b)

Fig. 4.16. Optical micrographs from 1-stage replicas taken
from specimen H29 (80%PS) showing a secondary crack after
(a) 500,000 and (b) 1,750,000 cycles. Arrow on (a) shows
initiating inclusion. Stress axis horizontal.

(a)

(b)

100μm
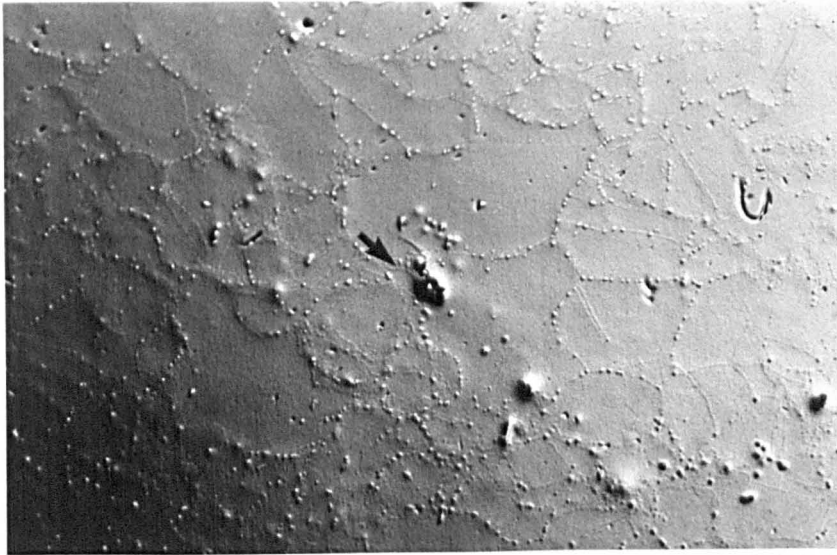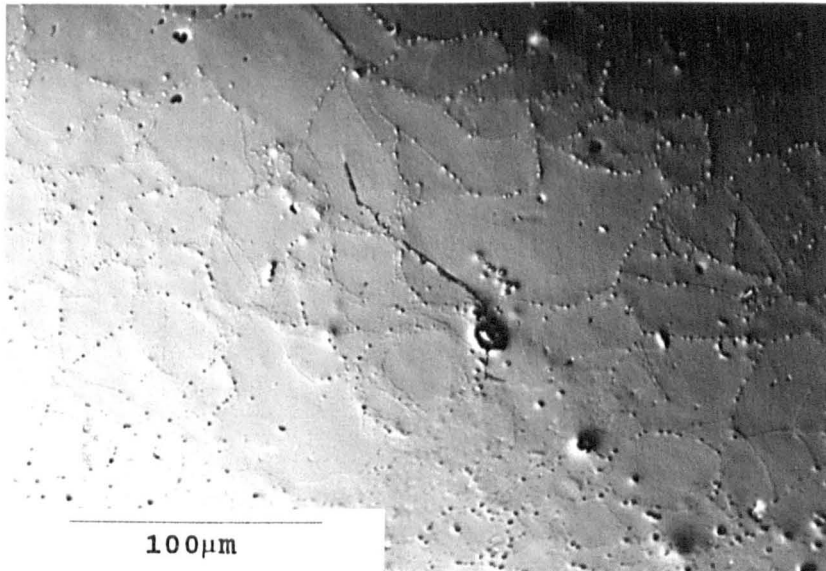
Fig. 4.17. Optical micrographs from 1-stage replicas taken
from specimen H29 (80%PS) showing a secondary crack after
(a) 500,000 and (b) 1,250,000 cycles. Arrow on (a) shows
initiating inclusion. Stress axis horizontal.

Two secondary cracks which did not appear to initiate from inclusions at 100%PS are shown by Figs. 4.18 and 4.20. The two cracks were located on the replicas and were traced back through the cycles as far as was possible. Fig. 4.19 shows optical micrographs from three replicas and it can be seen that initiation of the crack in Fig. 4.18 appears to have occurred close to or on a grain boundary (arrow on Fig. 4.19(a)); slip band/crack tip interactions around the time of initiation (25,000-50,000 cycles) were not observed either optically or in SEM, however, the crack does appear to propagate along slip bands in the first 4-5 grains (shown by Fig. 4.19(c)).

A similar situation exists for the crack shown in Fig. 4.20; the replica micrographs (Fig. 4.21) allowed this crack to be traced back to the initiating twin boundary arrowed in Fig. 4.21(a). Both SEM and optical microscopy again failed to show any substantial slip band activity at the crack tips but the crack does appear to follow some slip bands in the first 3-4 grains (shown by Fig. 4.21(c)).

4.3.4 Inclusion Cracking

Cracked inclusions were present in the Waspaloy prior to fatigue testing. The electropolished surface of an unfatigued specimen is shown in Fig. 4.22(a) where it is obvious that a number of cracks are present within a cluster of inclusions.

One particular inclusion was imaged from specimen H22 fatigued to 50,000 cycles at 100%PS. Fig. 4.22(b) shows the
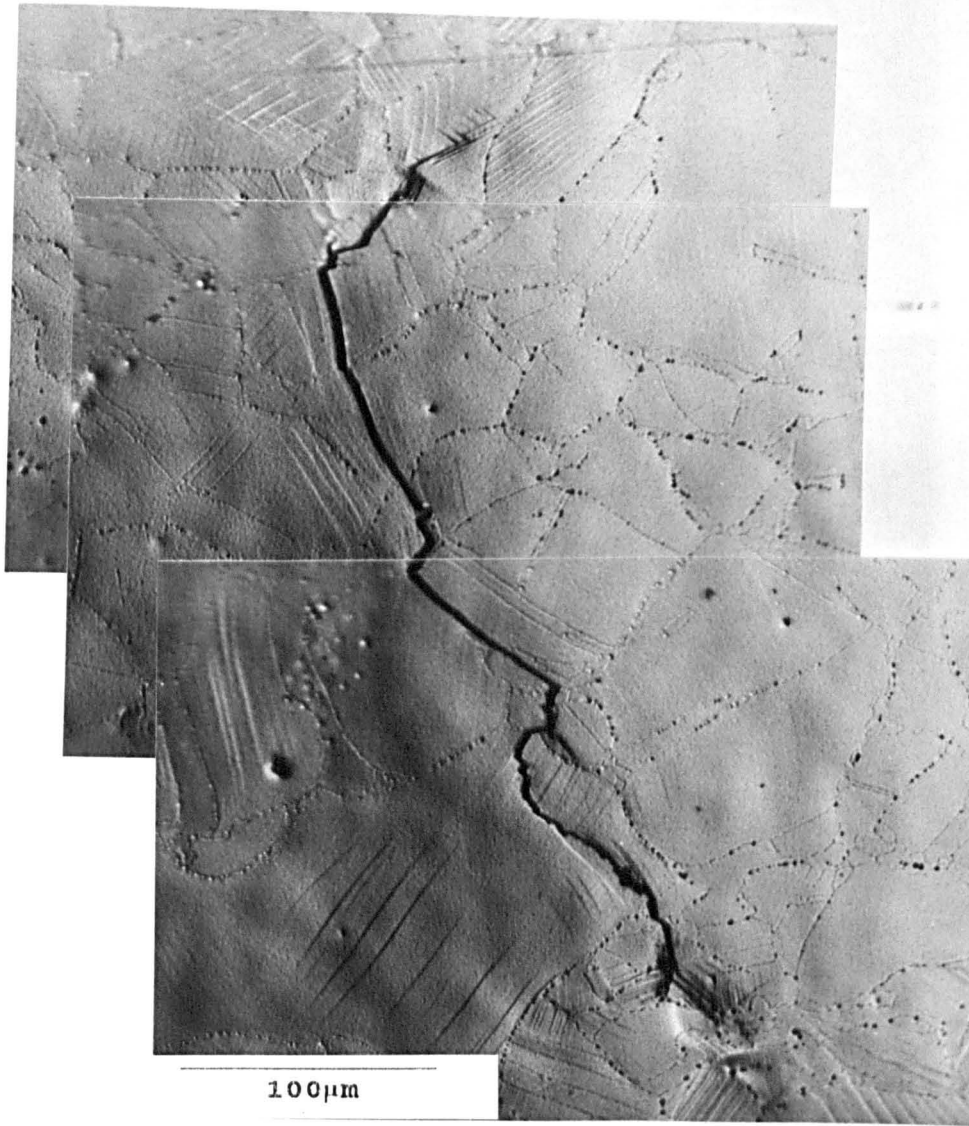
Fig. 4.18. Optical micrograph of a secondary crack 2mm from the primary crack on fatigued specimen H25 (100%PS). Stress axis horizontal.
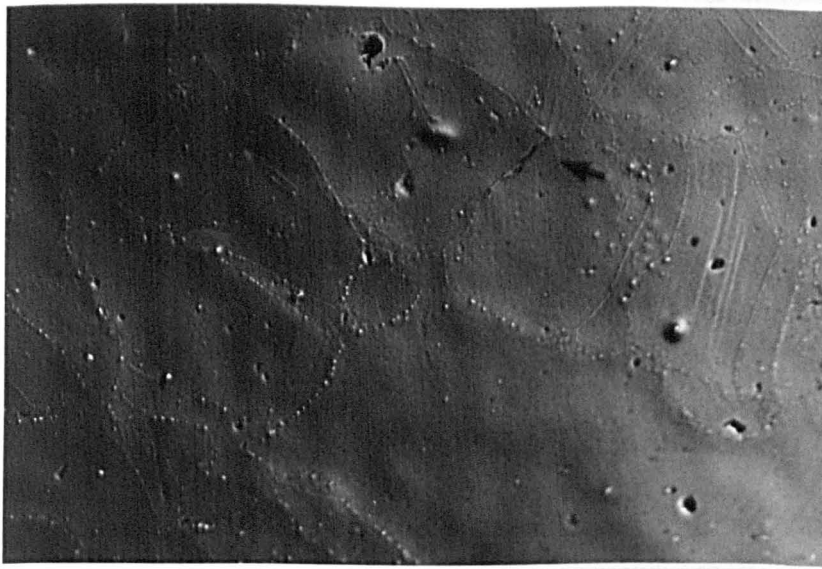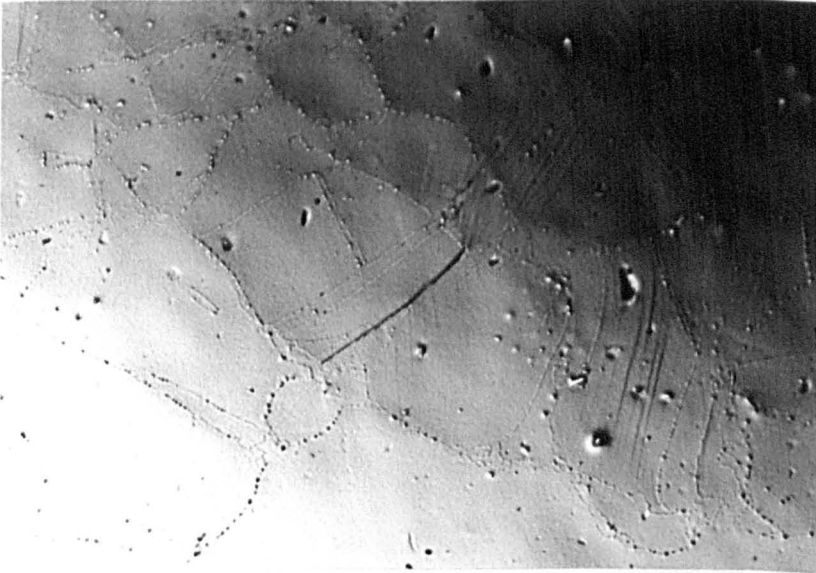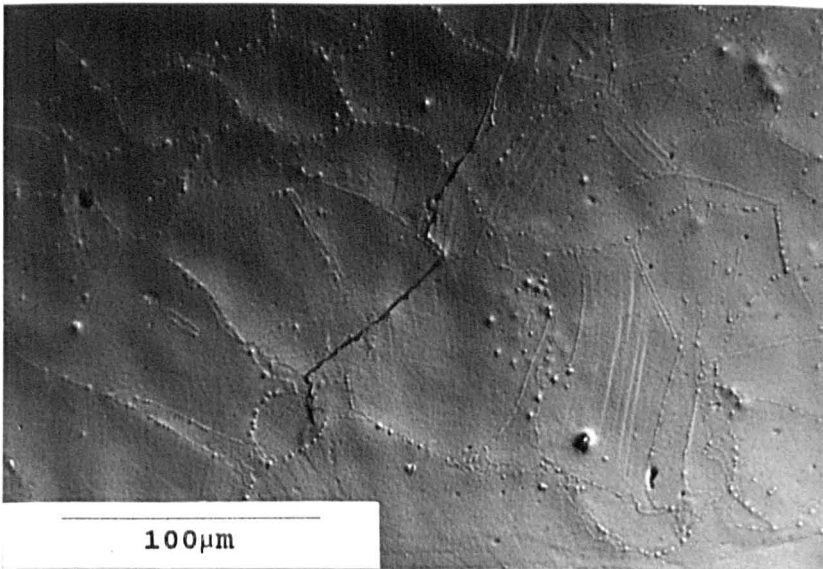
Fig. 4.19. Optical micrographs from 1-stage replicas taken from specimen H25 (100%PS) showing the secondary crack of Fig. 4.18 after (a) 50,000, (b) 175,000 and (c) 225,000 cycles. Arrow on (a) shows initiation site. Stress axis horizontal.

100μm
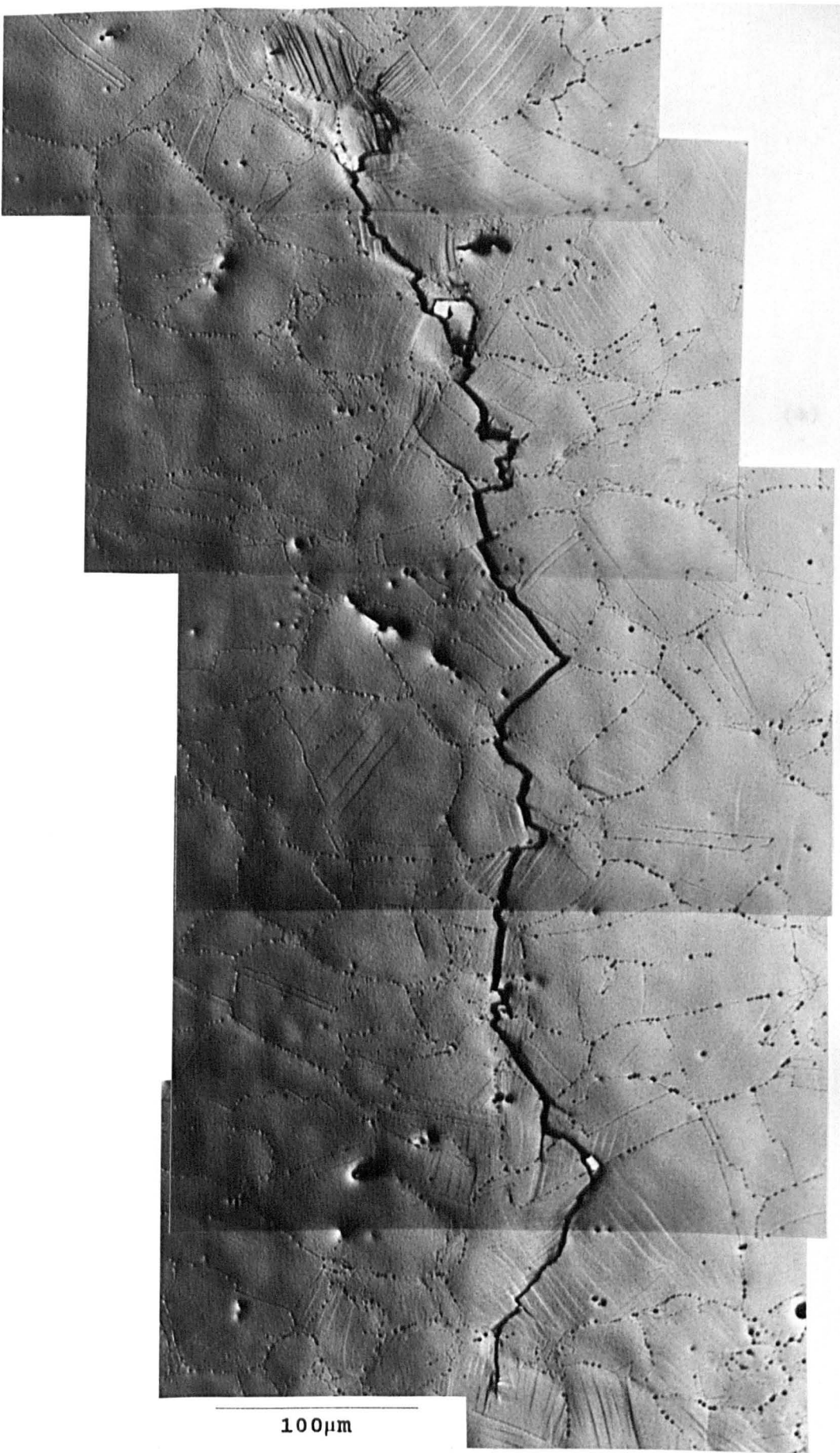
Fig. 4.20. Optical micrograph of a secondary crack 2mm from
the primary crack on fatigued specimen H25 (100%PS). Stress
axis horizontal.
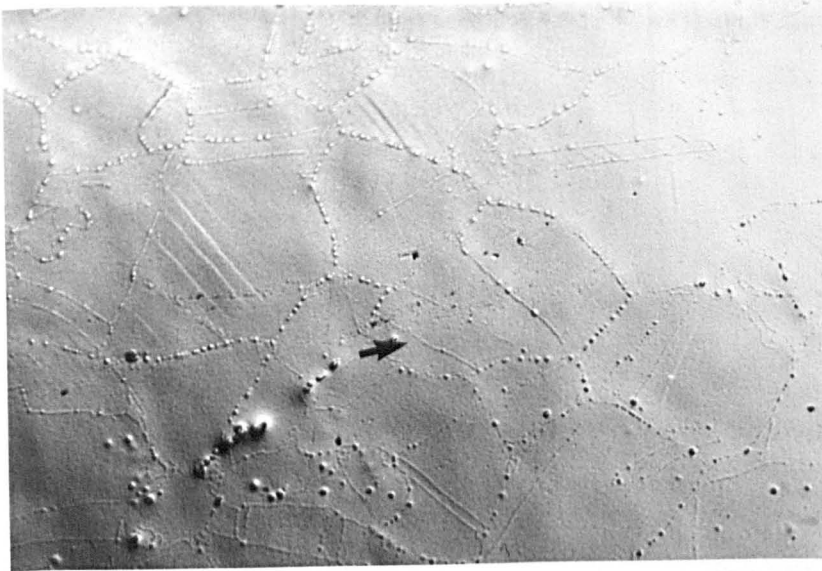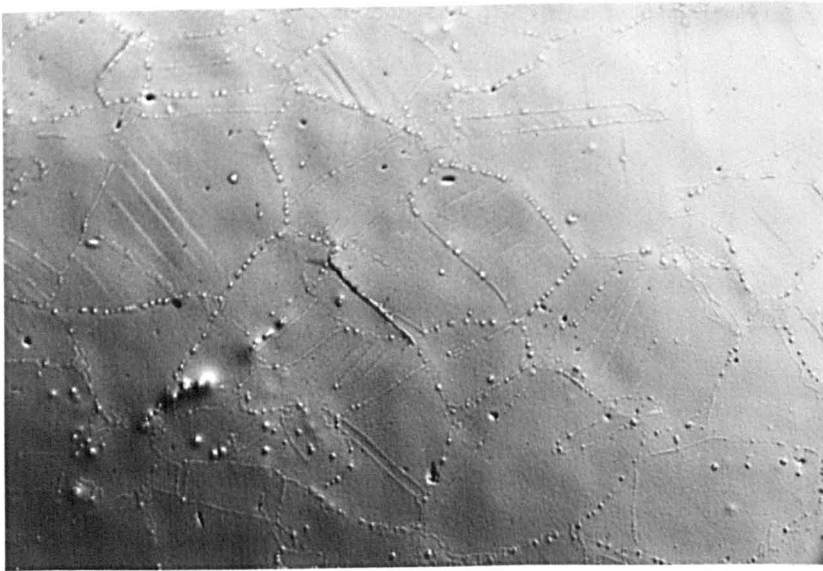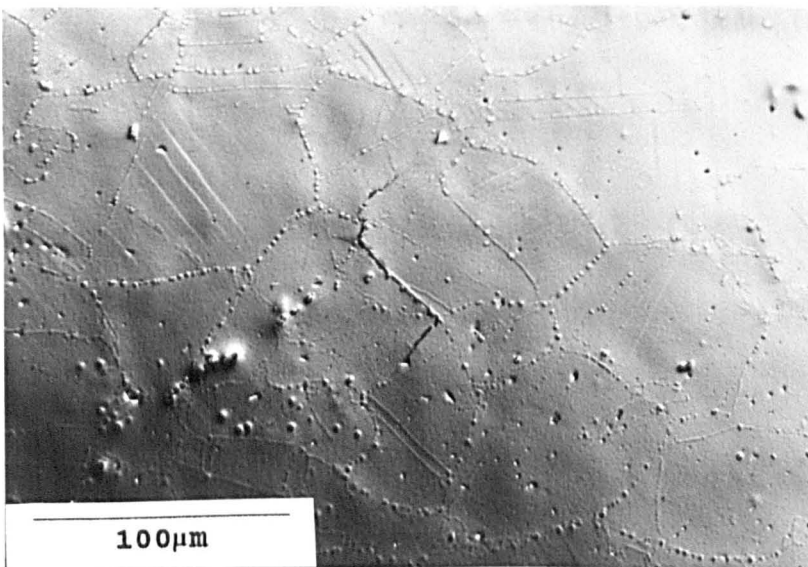
Fig. 4.21. Optical micrographs from 1-stage replicas taken from specimen H25 (100%PS) showing the secondary crack of Fig. 4.20 after (a) 25,000, (b) 100,000 and (c) 125,000 cycles. Arrow on (a) shows initiation site. Stress axis horizontal.
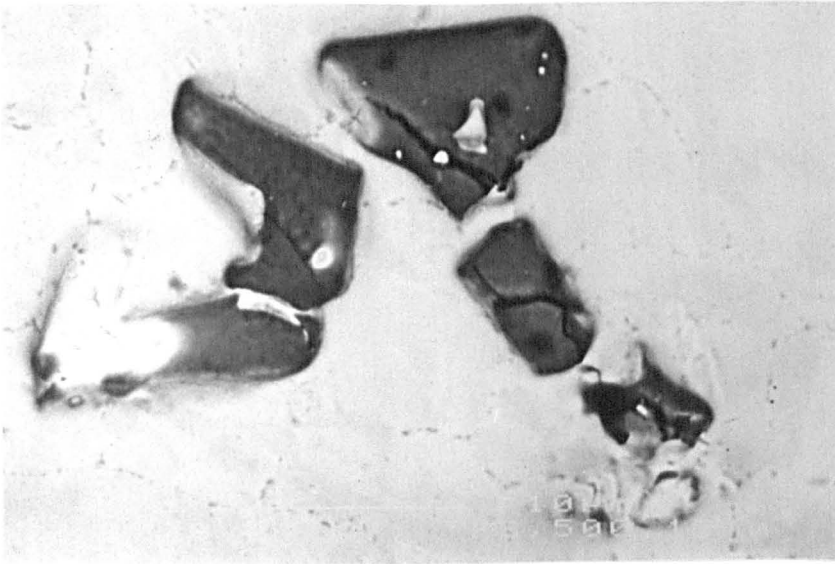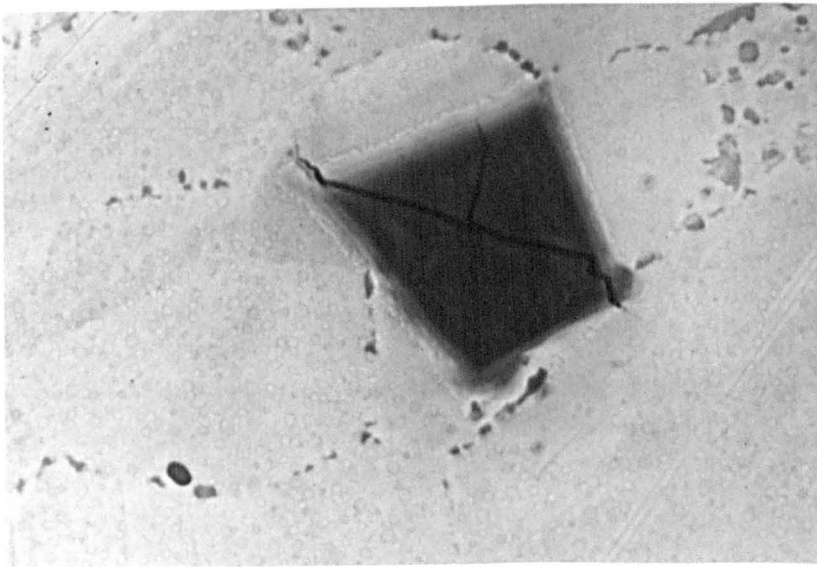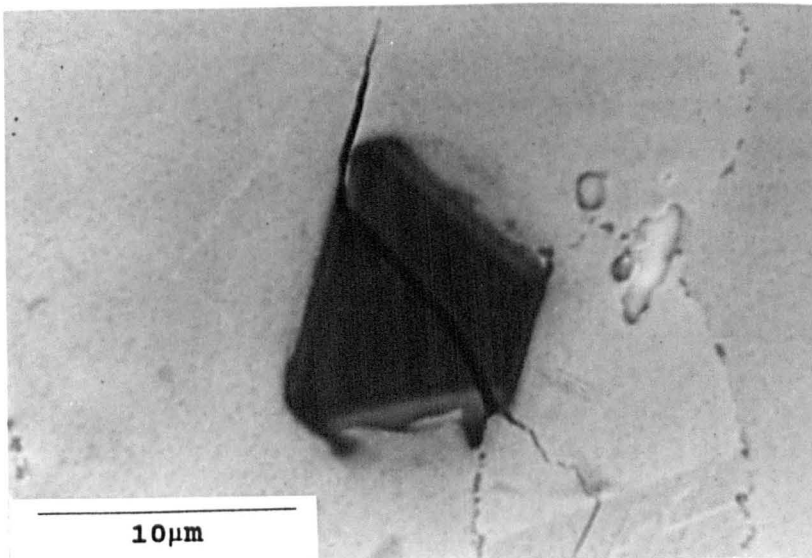
Fig. 4.22. Scanning electron micrographs showing cracked inclusions on the gauge surfaces of 100%PS specimens, (a) unfatigued specimen, (b) specimen H22 after 50,000 cycles and (c) specimen H12 at failure. Stress axis horizontal.

way that the cracks have just began to propagate into the matrix.

Fig. 4.22(c) illustrates an inclusion contained in a specimen cycled to failure; the crack has propagated well into the alloy matrix but it is not clear whether a slip band was its path or if another mechanism was responsible.

4.3.5 Fatigue Damage Accumulation.

4.3.5.1 Optical Microscopy

Fig. 4.23 shows a number of micrographs taken from 100%PS specimens and the results indicate that during fatigue, as the number of cycles increased, the slip band density and the number of grains containing slip bands increased. Similar results were obtained from 80%PS specimens but the area of observed deformation was much smaller in size than for the 100%PS specimens, hence the following sub-sections are concerned with observations from 100%PS specimens.

4.3.5.1.1 Early Fatigue Life

Fig. 4.23(a) shows that after 5,000 cycles an occasional grain contained a few weakly defined slip bands; generally there was very little deformation observed.

4.3.5.1.2 Mid Fatigue Life

After 20,000 cycles (Fig. 4.23(b)) the appearance of the slip bands was more pronounced as they had extended across the grains in which deformation had occurred. After

(a)

(b)
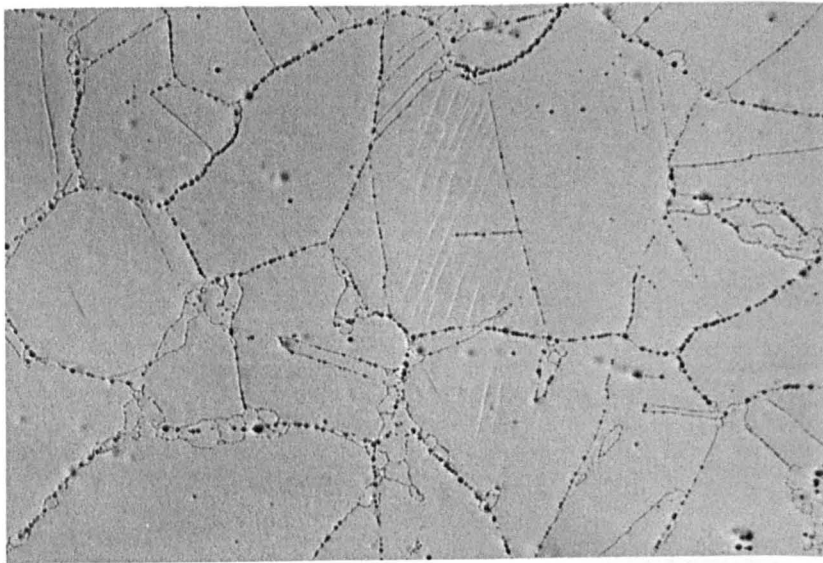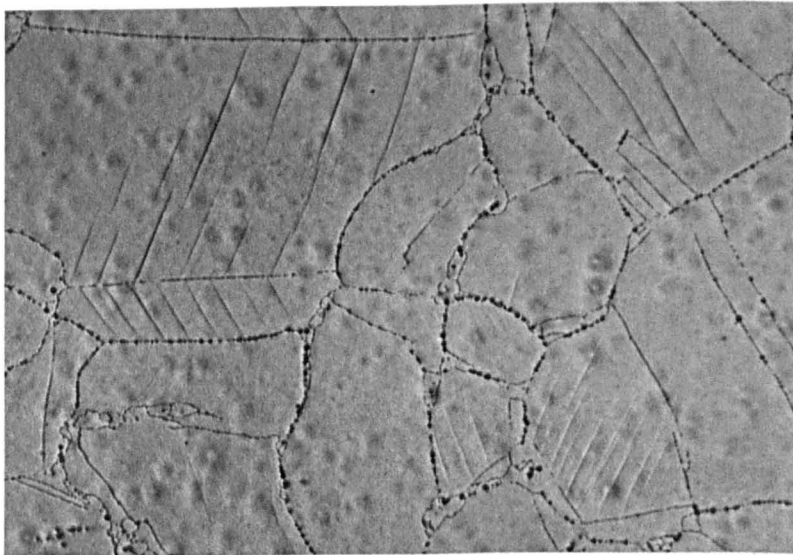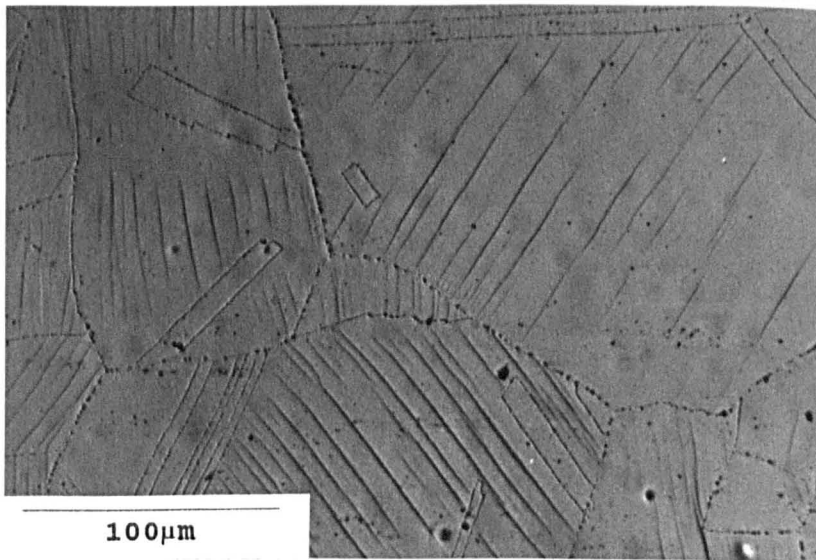
100μm

(c)

Fig. 4.23. Optical micrographs from 100%PS specimens cycled to various fractions of fatigue lifetime, stress axis horizontal; typical gauge surface slip band formation shown after (a) 5,000, (b) 20,000, (c) 50,000, (d) 100,000 and (e) 200,000 cycles.

(d)

100μm

(e)
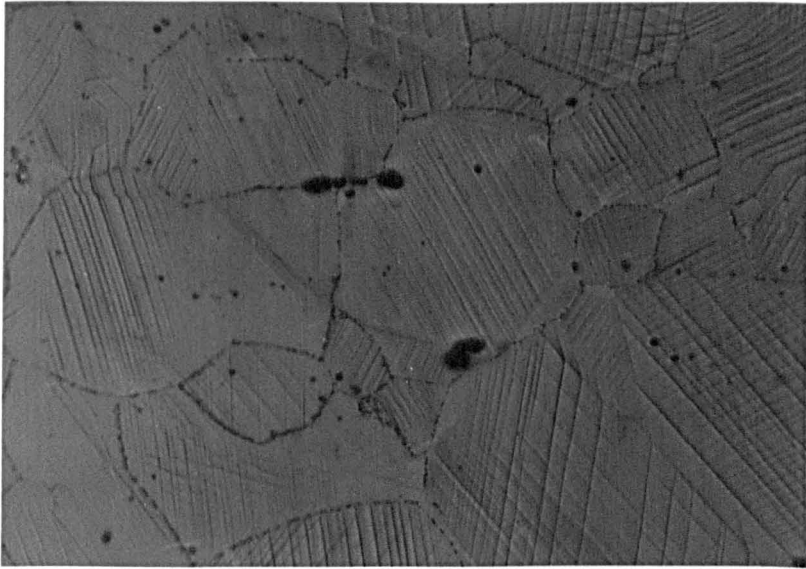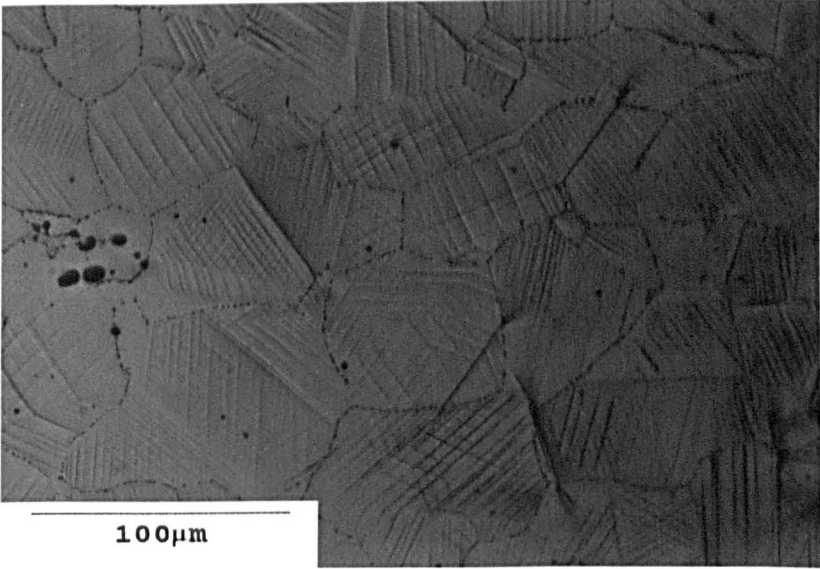
50,000 cycles some grains did in fact have slip bands
extended right across them, occasionally propagating across
grain boundaries and some of the bands had taken on a rather
intense appearance as demonstrated by Fig. 4.23(c).

4.3.5.1.3 Late Fatigue Life

Fig. 4.23(d) shows that after 100,000 cycles there was
only the occasional grain which did not exhibit any
observable deformation. Numerous grains had deformed by two
or more active slip systems and examples of slip
continuation in adjoining grains were numerous.

After 200,000 cycles the slip bands were extremely
close together, a great many had an intense appearance and
in a number of cases slip band cracking may have occurred.
Some grains exhibited deformation on three active slip
systems and the propagation of slip bands from one grain to
another was very common as shown by Fig. 4.23(e).

4.3.5.1.4. Fracture

As fatigue fracture became imminent the appearance of
the gauge surface in general, remained similar to that
illustrated by Fig. 4.23(e) however, the area immediately
surrounding the primary crack became very densely populated
with slip bands and surface uplift was evident, as discussed
in section 4.3.1 and examples are shown by Fig. 4.10.

4.3.5.2 Fracture Surfaces

Examination of fracture surfaces in SEM revealed the

initiation sites for both 100% and 80% specimens, as shown
by Figs. 4.24(a) and 4.25(a) respectively. Early crack
propagation occurred by a stage-I crystallographic mode,
leaving a faceted appearance on the surfaces as shown in
Figs. 4.24(b) and 4.25(b). As the crack lengths increased
propagation gradually underwent a transition to a stage-II
mode, characterised by fatigue striations as shown in Figs.
4.24(c) and 4.25(c). The transitional crack depths were
measured as 1.0mm at 100%PS and 2.1mm at 80%PS,
corresponding to 6 and 12 grain diameters respectively.

4.3.5.3 Transmission Electron Microscopy (TEM)
4.3.5.3.1 Early Fatigue Life

In general, early fatigue life back-thinned foils
exhibited grains containing little or no observable
deformation, showing low dislocation densities and only the
initial stages of slip band and cell formation. After 5,000
cycles at 100%PS and 75,000 cycles at 80%PS, the very early
stages of slip band formation are demonstrated by Figs.
4.26-4.28. Planar slip activity had occurred on up to 8
closely spaced slip planes as shown by Fig. 4.26 when
viewing the slip band edge-on; Fig. 4.27 illustrates a
similar situation in an 80%PS foil under similar conditions,
i.e. viewing the bands edge-on, however this image has poor
contrast due to a large foil thickness. The shorter
appearance of dislocations in the somewhat ill-defined slip
band shown in Fig. 4.28, is due to the high angle which the
dislocation line has made with the foil plane; the

(a)

(b)

(c)

20μm
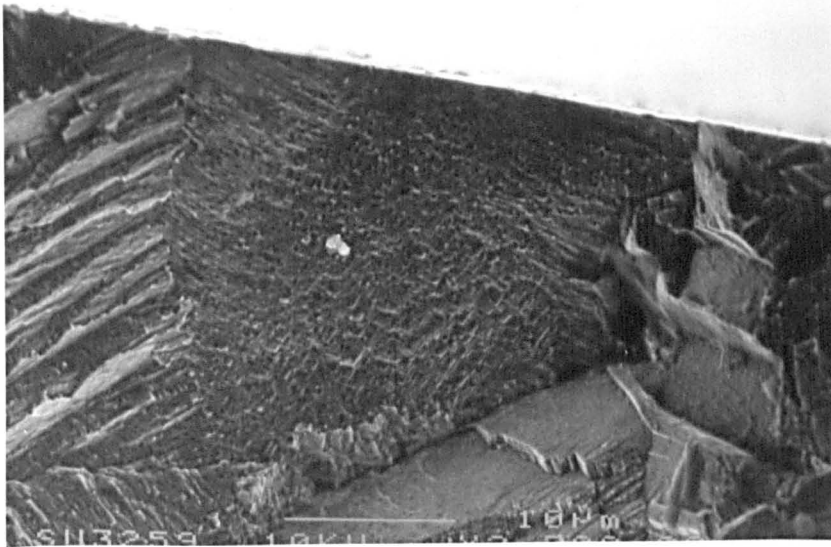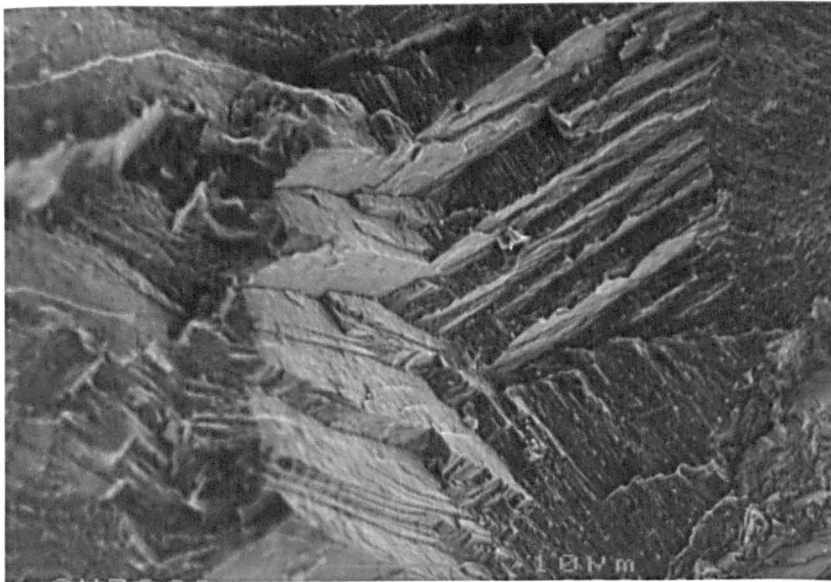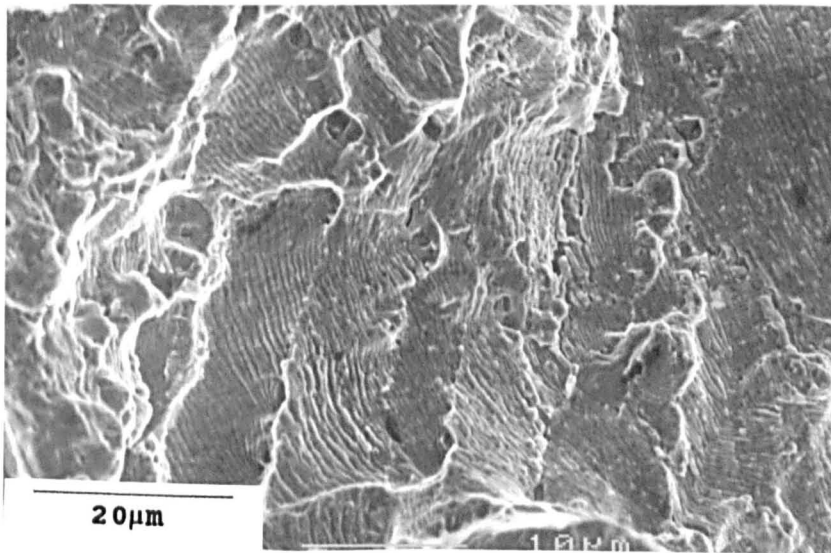
Fig. 4.24. Scanning electron micrographs from the fracture surface of specimen H24 (100%PS); (a) initiation site, (b) stage-I growth faceted appearance and (c) stage-II growth striated appearance. Propagation occurred in a near vertical direction from top to bottom.
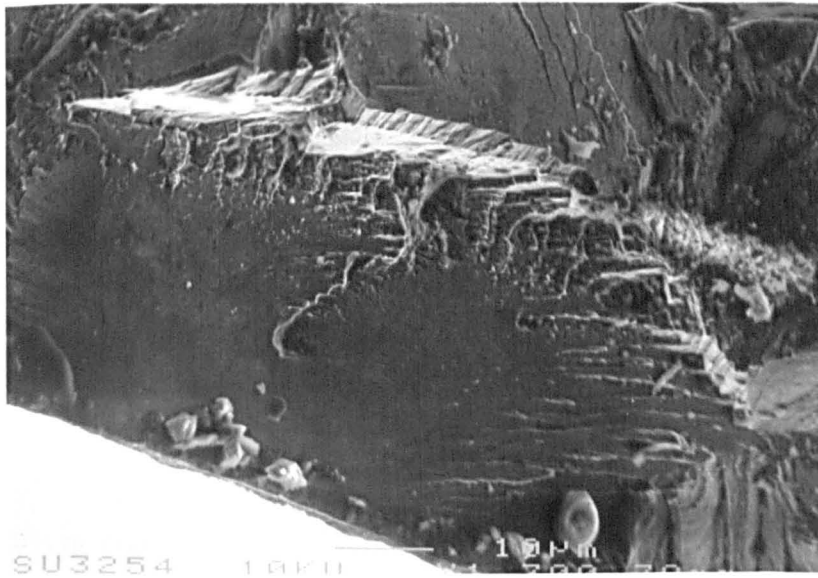
(a)
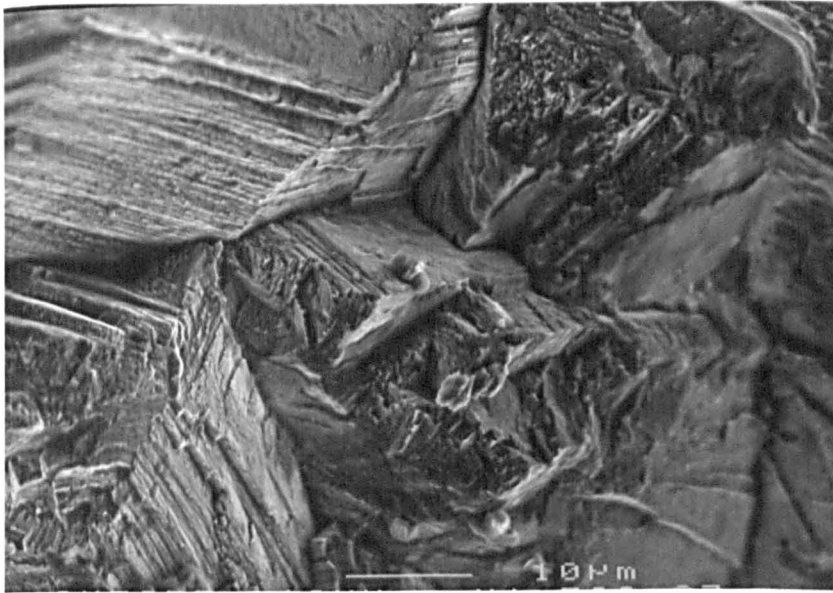
(b)
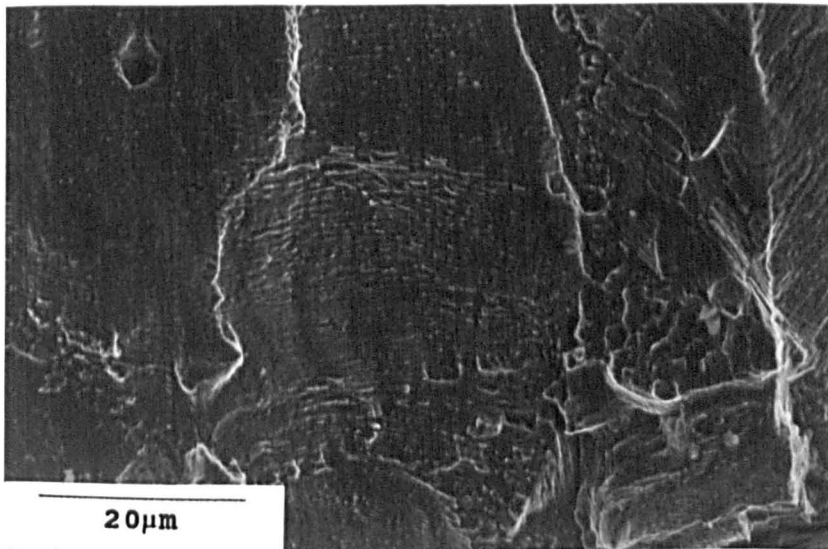
(c)

Fig. 4.25. Scanning electron micrographs from the fracture surface of specimen H3 (80%PS); (a) initiation site, (b) stage-I growth faceted appearance and (c) stage-II growth striated appearance. Propagation occurred in a near vertical direction from bottom to top.

<131>

250nm
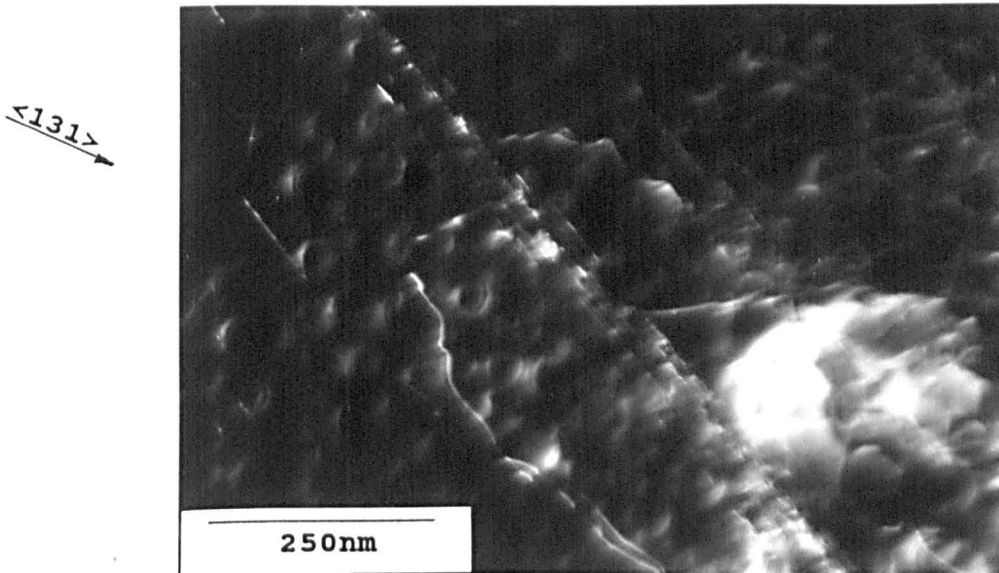
Fig. 4.26. Dark field transmission electron micrograph of a
back-thinned foil from specimen H5 (5,000 cycles at 100%PS)
illustrating slip activity on up to 8 closely spaced planes
when viewed edge on; <112> orientation.

<220>

300nm
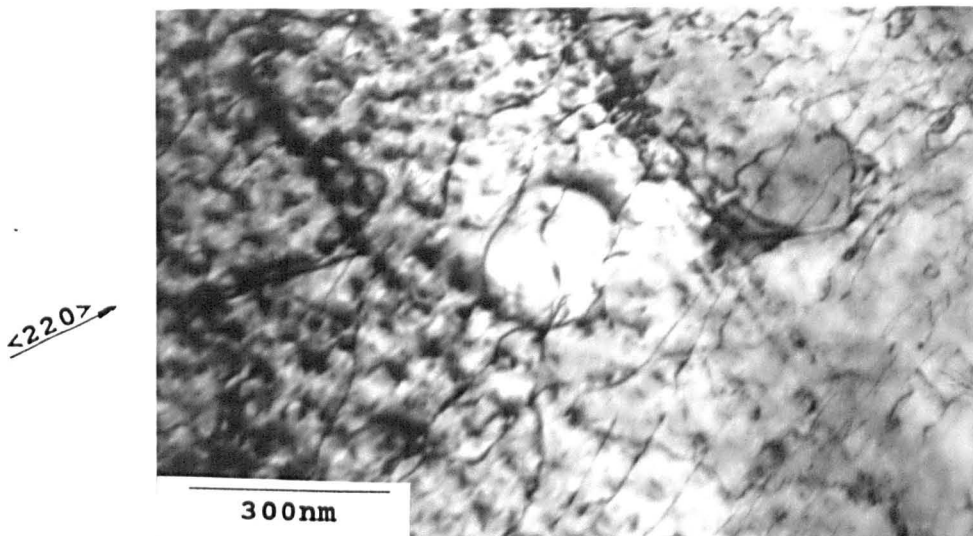
Fig. 4.27. Bright field transmission electron micrograph of
a back-thinned foil from specimen H7 (75,000 cycles at
80%PS) showing early slip band formation when viewed edge
on; <113> orientation.
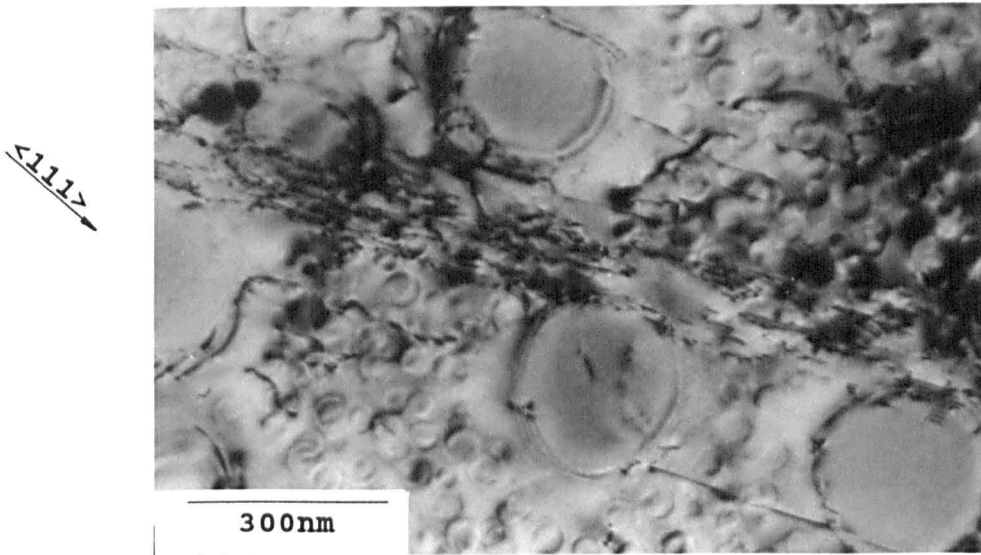
Fig. 4.28. Bright field transmission electron micrograph of
a back-thinned foil from specimen H5 (5,000 cycles at
100%PS) illustrating the development of a slip band early in
fatigue life; <112> orientation.
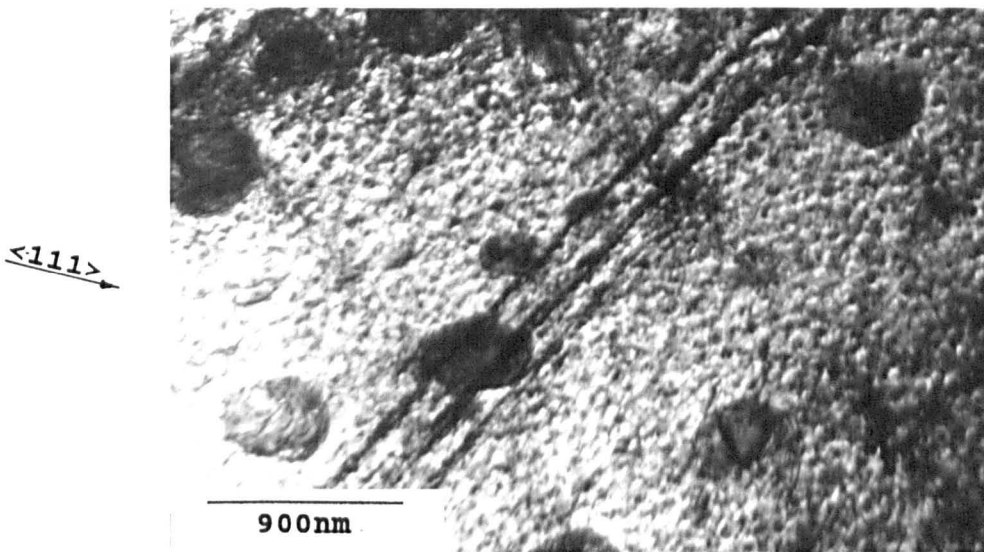
Fig. 4.29. Bright field transmission electron micrograph of
a back-thinned foil from specimen H5 (5,000 cycles at
100%PS) showing a sheared precipitate and slip on two active
planes; <112> orientation.

micrograph also shows a number of finely spaced dislocations and the presence of what may be dislocation dipoles or superdislocation pairs. In addition, Fig. 4.28 illustrates large γ' precipitates which appear to have been distorted by dislocations located at the γ/γ' interface. Shearing of large precipitates had occurred by 5,000 cycles as illustrated by Fig. 4.29; in this case, the precipitate parts were displaced from one another by a distance of approximately 60nm.

Certain grains exhibited slip on more than one active {111} type slip plane; Fig. 4.30 shows two such bands. The condition is also in evidence in Fig. 4.29, but one slip band set are imaged under weak contrast and are therefore difficult to see. Three parallel loosely defined slip bands are shown in Fig. 4.31 and wavy dislocations can be seen looping the large γ' precipitates between the bands; although these dislocations have looped several large particles, the particles have not been obscured from view since the dislocation density was still relatively low. The low dislocation density between the bands seen in Fig. 4.31 was typical of that observed during the early stages of fatigue. The middle slip band in Fig. 4.31 appears to have interacted with a large particle, but if shearing has taken place, it is not as obvious as that demonstrated by Fig. 4.29.

After 10,000 cycles at 100%PS, dislocation loops were observed around some of the small precipitates as shown clearly by Fig. 4.32; the same micrograph however, displays

$\langle 111 \rangle$
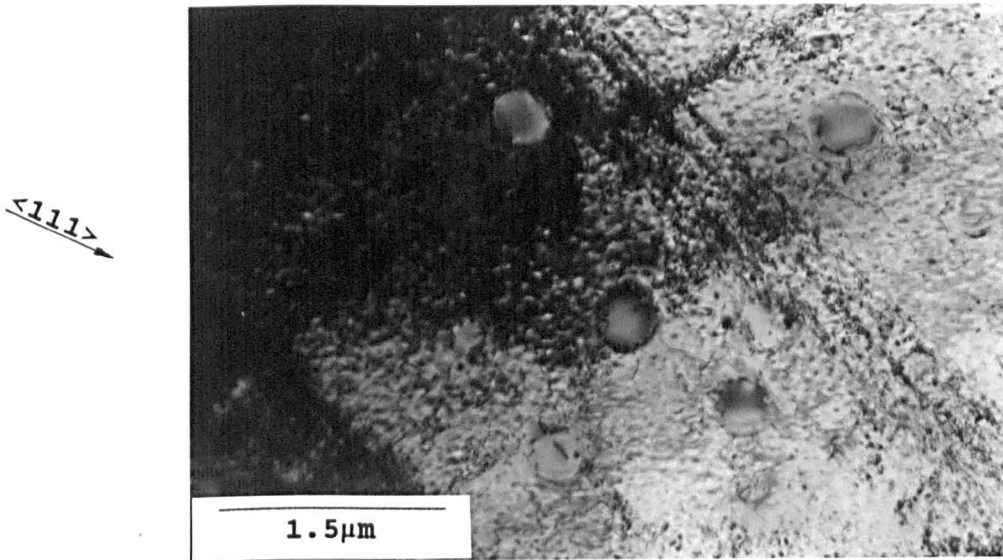
Fig. 4.30. Bright field transmission electron micrograph of
a back-thinned foil from specimen H5 (5,000 cycles at
100%PS) illustrating the evidence of two active slip planes
at low magnification; <112> orientation.

$\langle 111 \rangle$
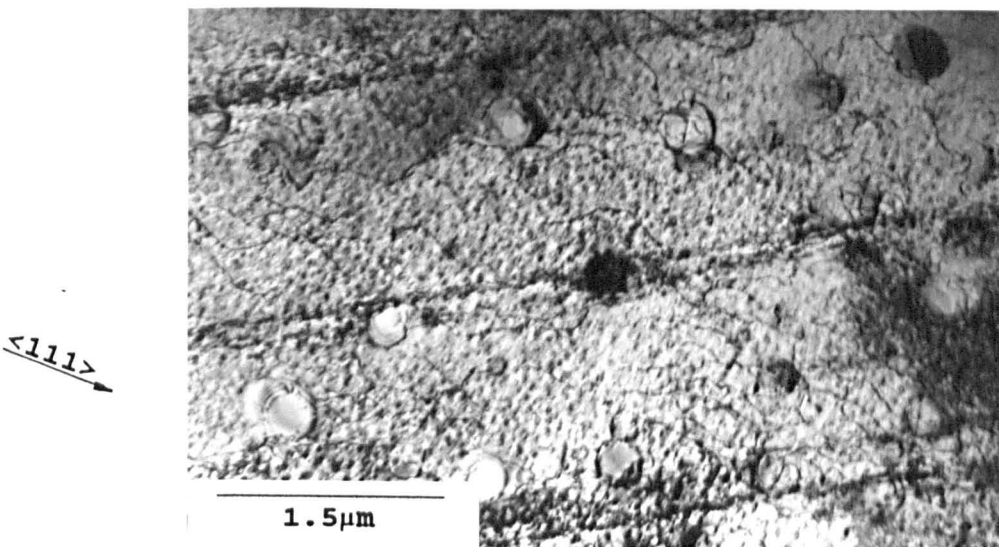
Fig. 4.31. Bright field transmission electron micrograph of
a back-thinned foil from specimen H7 (75,000 cycles at
80%PS) showing three planar slip bands in the same locality
as wavy dislocations looping the precipitates, possible
precipitate/slip band interaction in the centre of the
micrograph; <112> orientation.

<111>

300nm
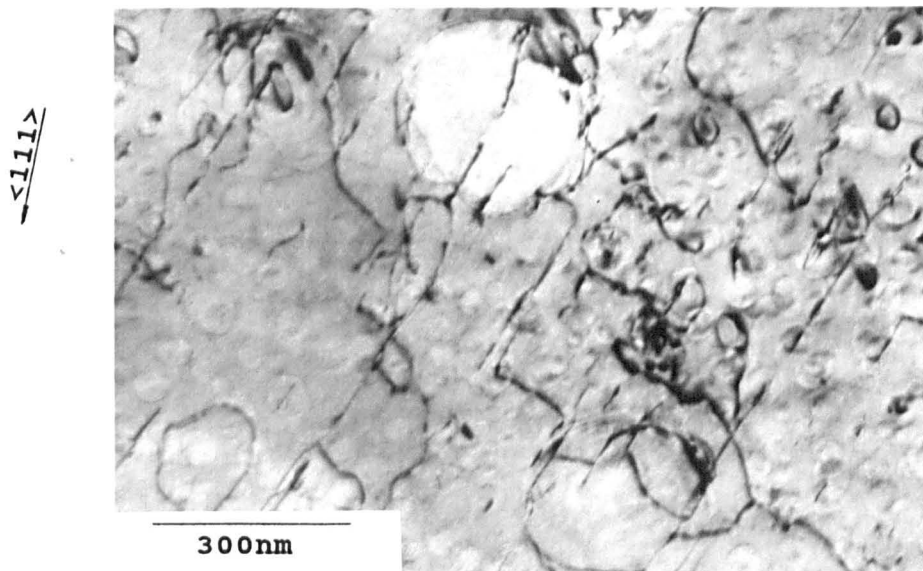
Fig. 4.32. Bright field transmission electron micrograph of
a back-thinned foil from specimen H13 (10,000 cycles at
100%PS) illustrating the looping of small precipitates in an
area exhibiting the initial stages of slip band formation;
<011> orientation.

a number of long, straight, parallel dislocations, suggesting that slip band formation has just begun in this area.

After 5,000 cycles at 100%PS and 75,000 cycles at 80%PS, certain grains in back-thinned foils exhibited the beginnings of a cellular type of dislocation structure indicating a more homogeneous deformation mode. Fig. 4.33 illustrates the way in which wavy dislocations have moved together to form the beginnings of cell walls; the low dislocation density allows easy imaging of individual dislocations, particularly under weak beam conditions (Fig. 4.33(a)). Fig. 4.34 demonstrates that in some areas, dislocations have already tangled together to form rather ill-defined cell walls. In the micrograph shown by Fig. 4.35 (10,000 cycles at 100%PS) although the majority of the dislocations appear to be the remnants of planar deformation e.g. dislocation loops, there are a number of wavy dislocations which appear to lie between both coarse and fine γ', which are believed to be the beginnings of cell wall formation.

4.3.5.3.2 Mid Fatigue Life

During mid fatigue life greater levels of deformation were observed with the appearance of slip bands and cells now more obvious. Dislocation densities were generally higher than in early life, but foils still contained grains exhibiting very little observable deformation. The increase in dislocation density had occurred in four principal areas.

<330>   250nm   (a)
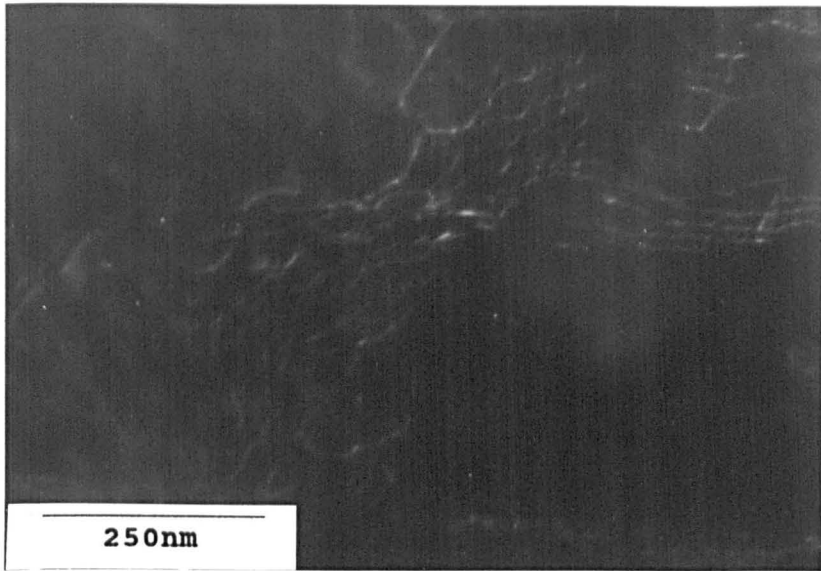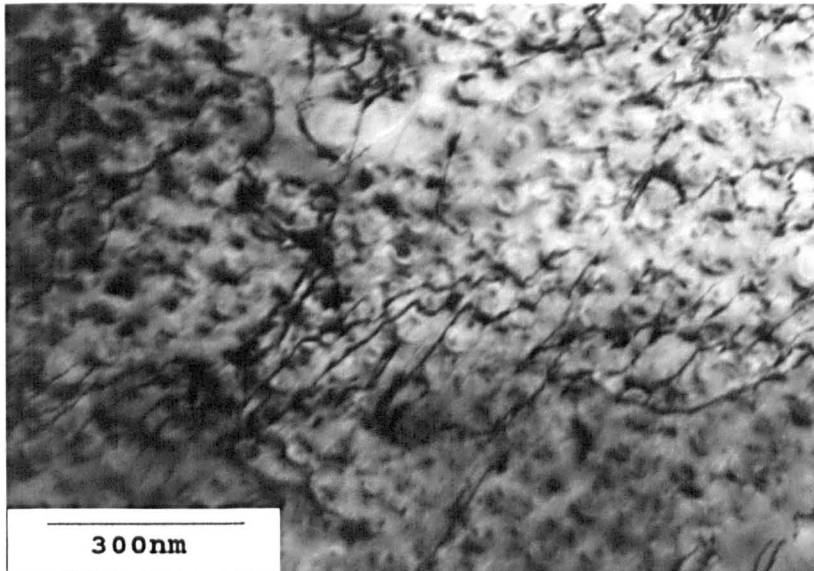
<220>   300nm   (b)

Fig. 4.33. Transmission electron micrographs of back-thinned foils showing dislocation substructures in the initial stages of cell wall formation, (a) weak beam dark field image from specimen H5 (5,000 cycles at 100%PS), <233> orientation and (b) bright field image from specimen H7 (75,000 cycles at 80%PS), <113> orientation.

‹202›

400nm

(a)

‹202›

300nm
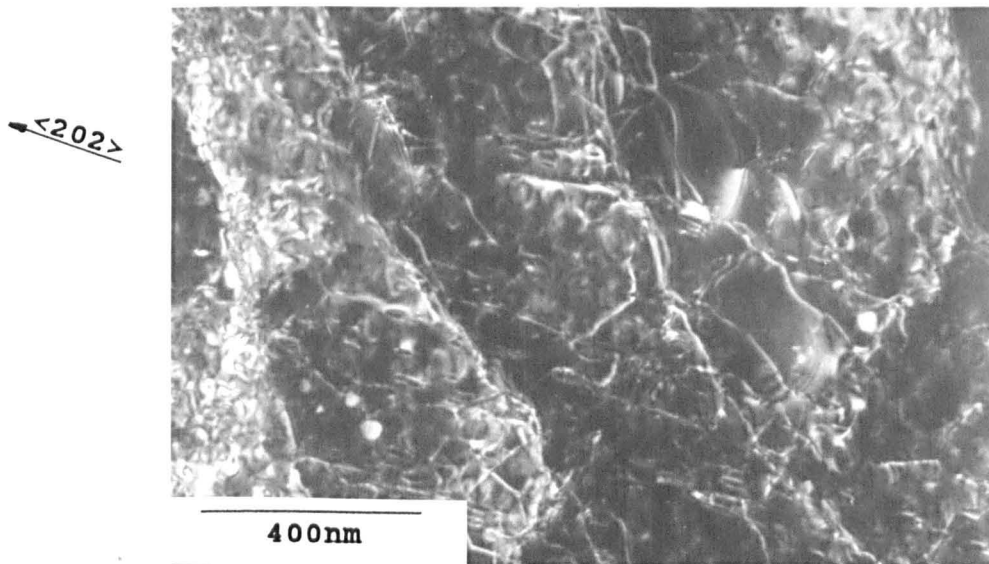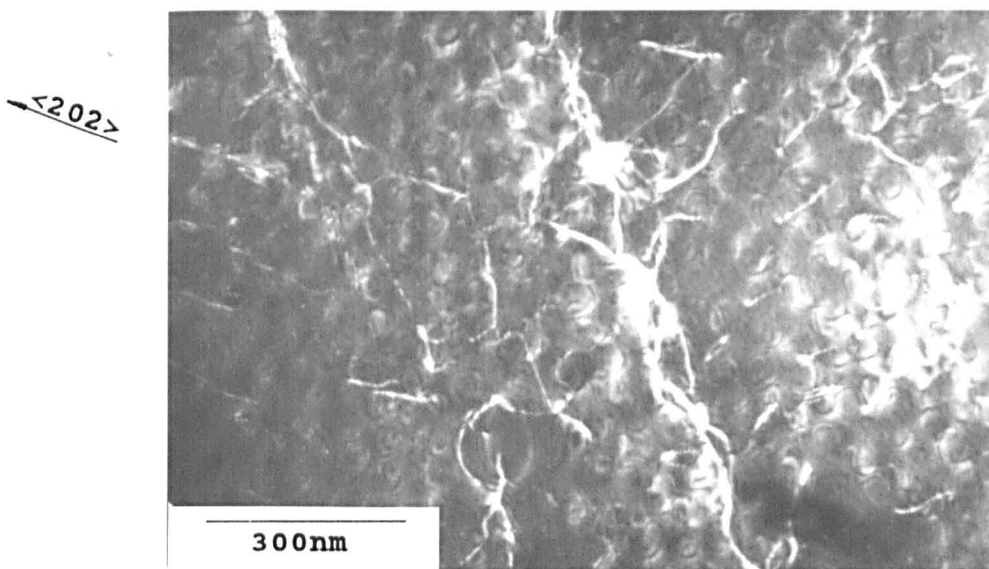
(b)

Fig. 4.34. Dark field transmission electron micrographs of back-thinned foils from specimen H5 (5,000 cycles at 100%PS) showing dislocation tangling in the initial stages of cell wall formation, (a) low magnification and (b) high magnification, <111> orientation.

〈111〉

300nm
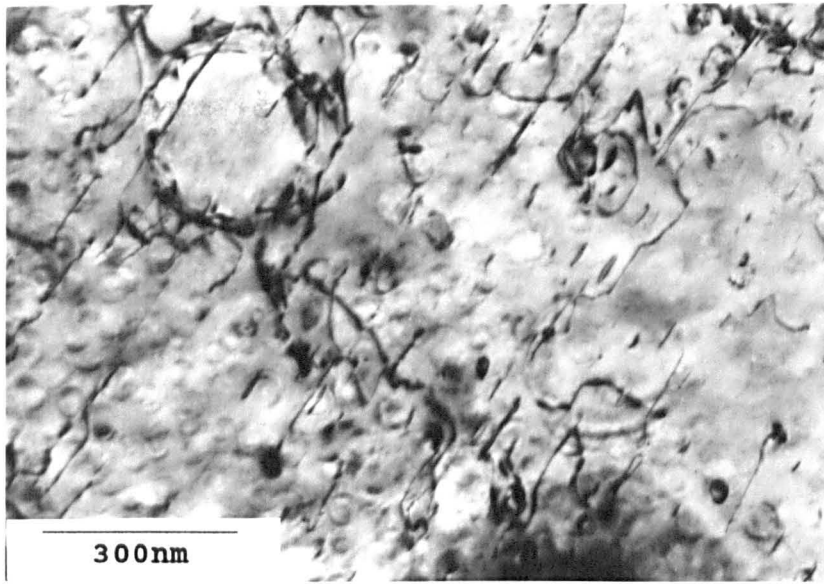
Fig. 4.35. Bright field transmission electron micrograph of
a back-thinned foil from specimen H13 (10,000 cycles at
100%PS) illustrating the beginning of slip band formation
(dislocations running from top right to lower left) in the
same region as initial cell wall formation (wavy
dislocations looping the large precipitate in upper left);
<011> orientation.

Firstly, the planar slip bands were wider and the dislocation densities within them were substantially greater. Many of these could now be clearly described as persistent slip bands. Secondly, the cell boundaries, described earlier, contained a higher dislocation density. Thirdly, an increase in dislocation density was found at the large γ'/γ interfaces. Finally, the dislocation density between the PSBs had increased, both in terms of residual dislocation loops around the fine γ' and irregular shaped dislocations that lay between the fine γ'.

After 20,000 cycles at 100%PS planar slip was widespread, shown by Fig. 4.36; this was much more commonly observed than in early life and the dislocations illustrated were irresolvable. After 50,000 cycles at 100%PS in some areas slip bands were more sharply defined, Fig. 4.37(a) shows a good example of this, thus a gradual transition from finely spaced planar slip bands to clear PSBs was observed. Fig. 4.37(b) illustrates precipitate shearing resulting in significant γ' distortion; a displacement of 34nm was measured in this case. Not only were the large γ' sheared, but also virtually all contained dislocation networks at the γ/γ' interface. For example, a dislocation array is present in the upper γ' particle illustrated by Fig. 4.37(b); in addition, the dislocation networks extended some way into the matrix as shown by the lower γ' particle of Fig. 4.37(a, b).

Fig. 4.37(c) shows the general increase in dislocation density observed between the planar slip bands. Dislocation

<111>

300nm

(a)

<200>

600nm
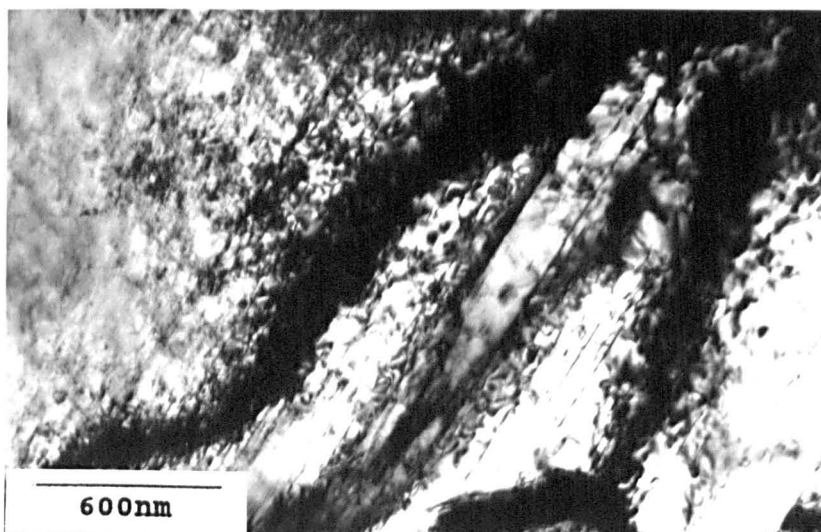
(b)

Fig. 4.36. Bright field transmission electron micrographs of back-thinned foils from specimen H16 (20,000 cycles at 100%PS) showing widespread planar slip; <011> orientations.
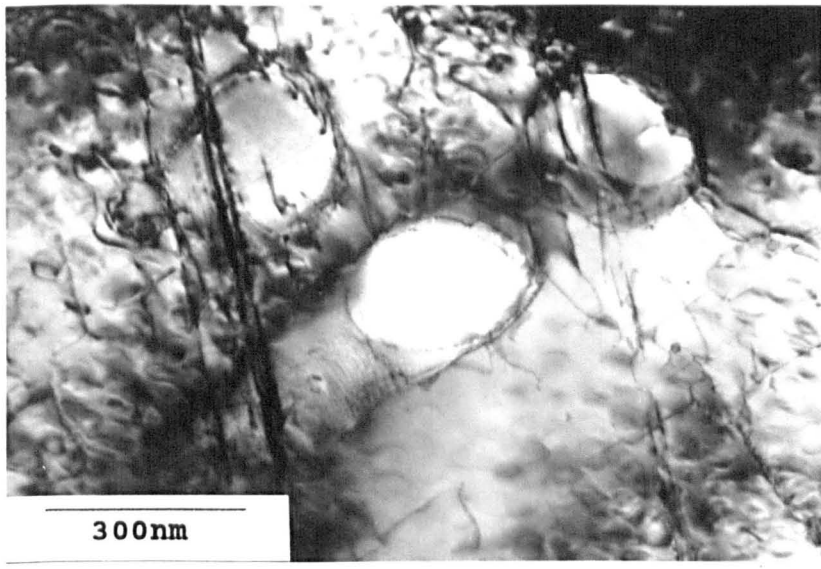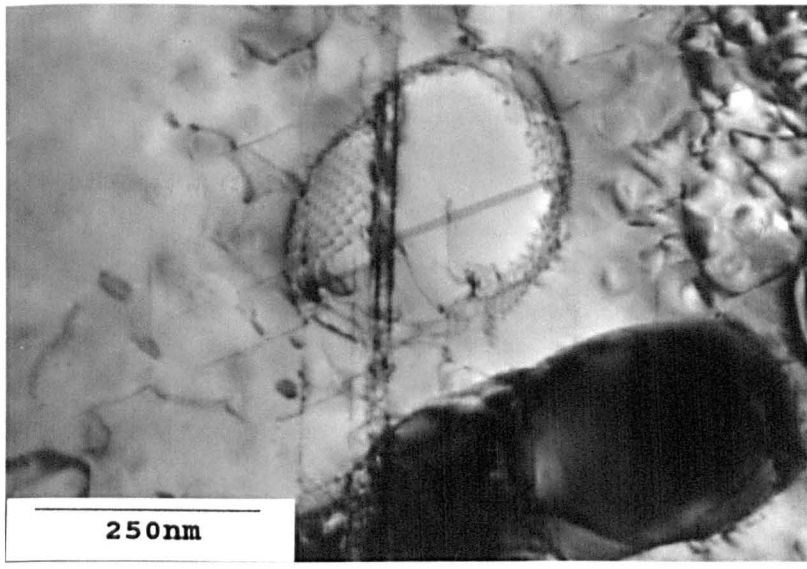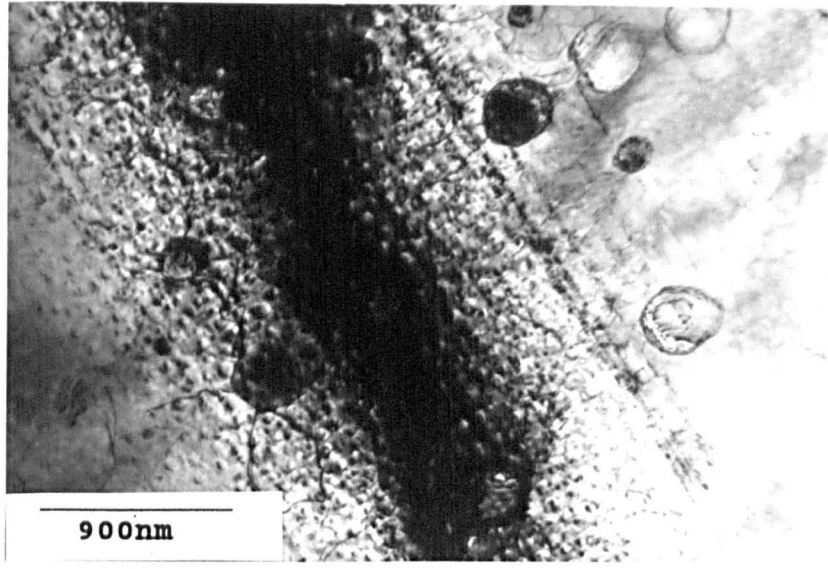
Fig. 4.37. Bright field transmission electron micrographs of back-thinned foils from specimen H22 (50,000 cycles at 100%PS) showing (a) more sharply defined slip bands, (b) precipitate distortion and (c) precipitates surrounded by dislocation networks. Orientations: (a): <113>, (b) and (c): <011>.

direction appeared to be random, but they were frequently bounded by large γ' particles. In addition, numerous evidence of dislocation loops around the fine γ' were found, e.g. Figs. 4.37(b) and 4.38(a).

Although mid life dislocation densities were generally greater than those in early life, there was still a large difference in slip activity between grains. After 600,000 cycles at 80%PS Fig. 4.38(a) illustrates a rather low overall dislocation density in addition to evidence of Orowan loops and the beginnings of slip band formation. Fig. 4.38(b) shows a grain containing planar deformation in the same area as wavy dislocations, suggesting that the material had deformed in both planar and homogeneous modes in this area. It was difficult to ascertain whether the local density of wavy dislocations between the planar slip planes had increased with number of cycles, since the distribution was rather inhomogeneous.

After 20,000 cycles at 100%PS and 300,000 cycles at 80%PS, cells observed in back-thinned samples had become more pronounced (Figs. 4.39 and 4.40), but were only seen in a small fraction of the grains. Cell wall dislocation density was sufficiently high to give appreciable misorientation across sub-boundaries, as shown by the displacement of bend contours across the boundaries in Fig. 4.39. Fig. 4.41 shows a diffraction pattern taken from a number of cells. The peripheral spot-splitting shown is due to a small angular displacement (approximately 1.5°) in orientation between neighbouring cells and therefore
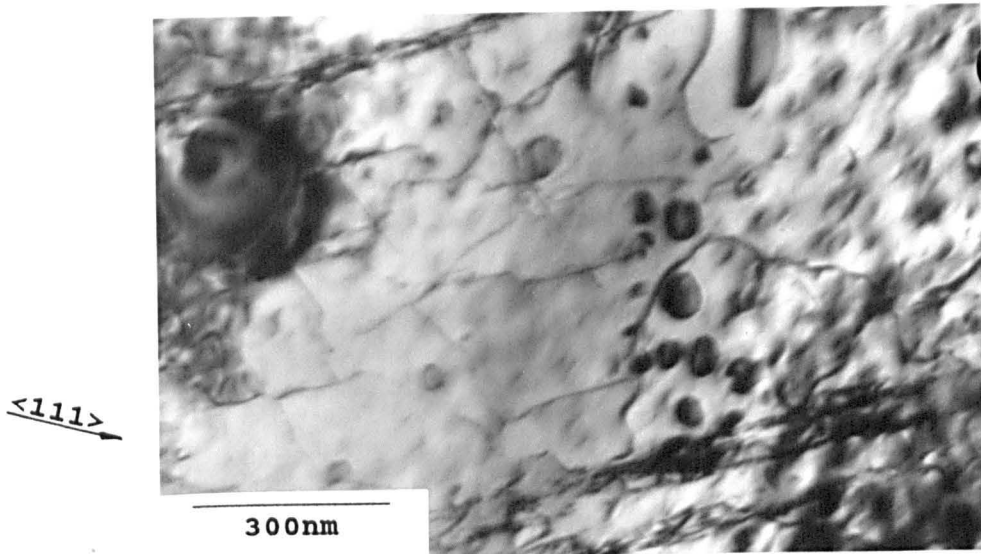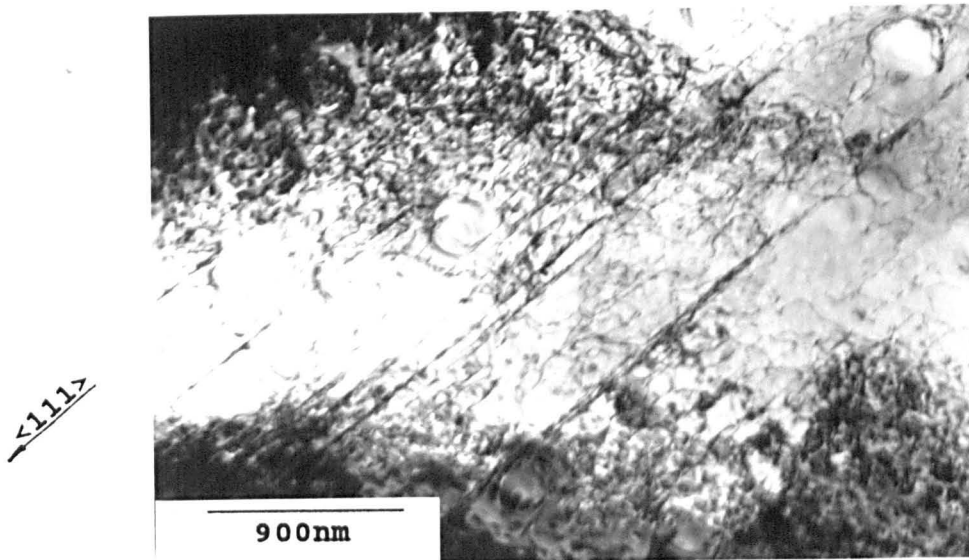
Fig. 4.38. Bright field transmission electron micrographs of back-thinned foils from specimen H21 (600,000 cycles at 80%PS) showing (a) Orowan looping of small precipitates in an area of low overall dislocation density and (b) a region containing both planar and wavy dislocations; <011> orientations.
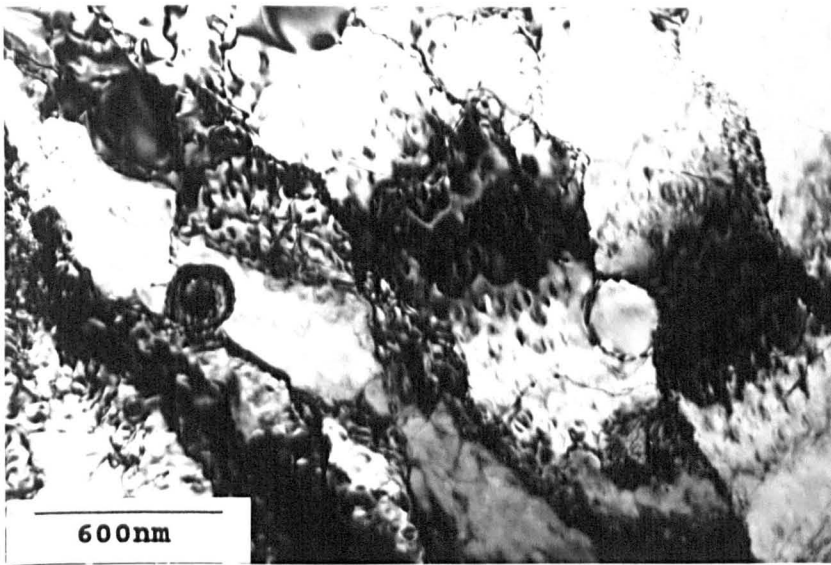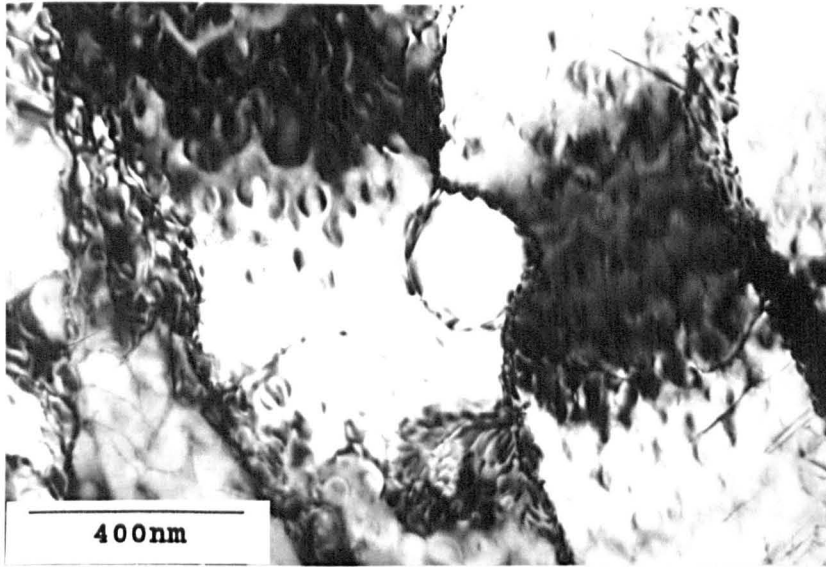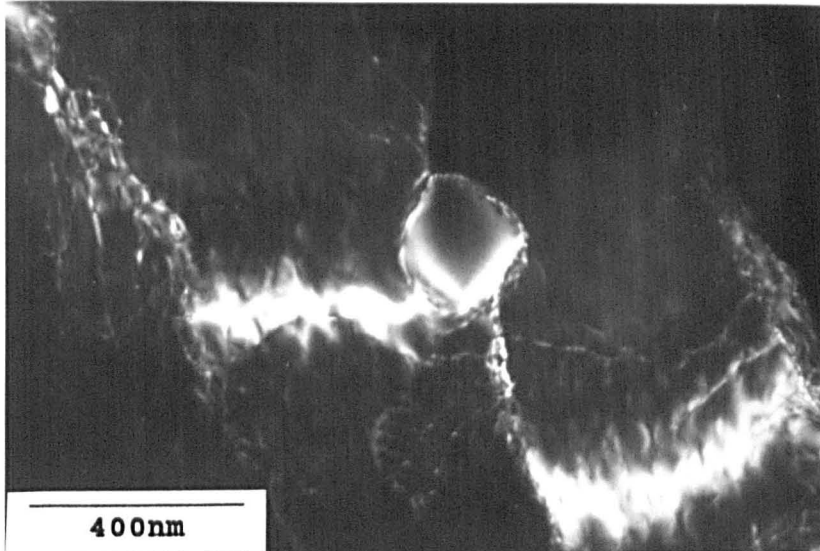
Fig. 4.39. Transmission electron micrographs of back-thinned foils from specimen H16 (20,000 cycles at 100%PS) showing the more pronounced appearance of the walls of the cellular dislocation substructures and the way the dislocations appear to go around the precipitates, (a) bright field low magnification, (b) bright field high magnification and (c) weak beam dark field of (b); <011> orientations.
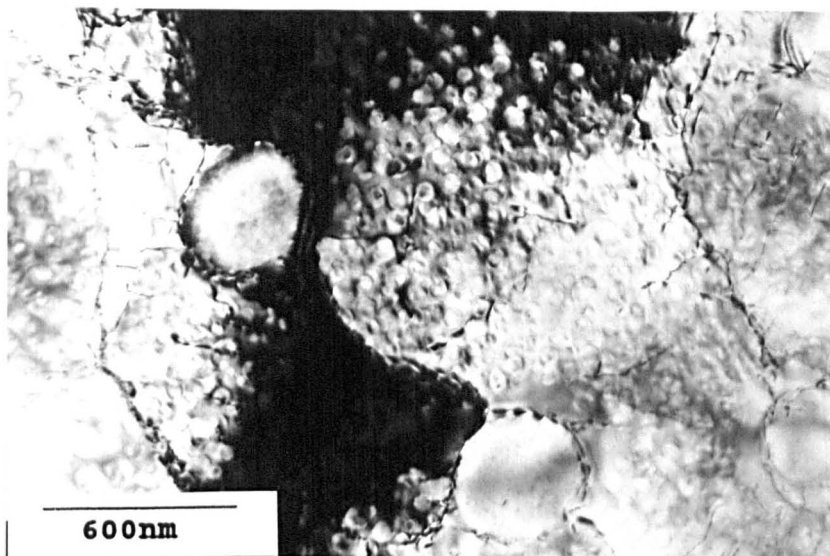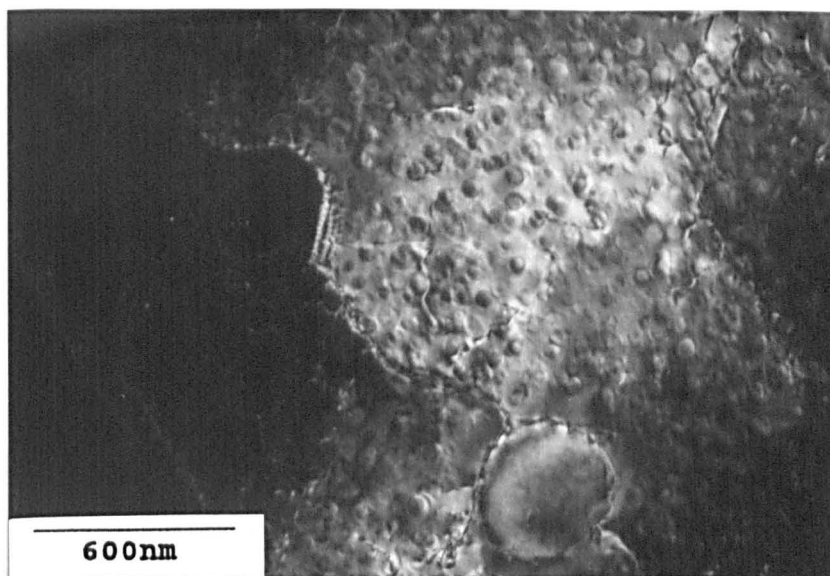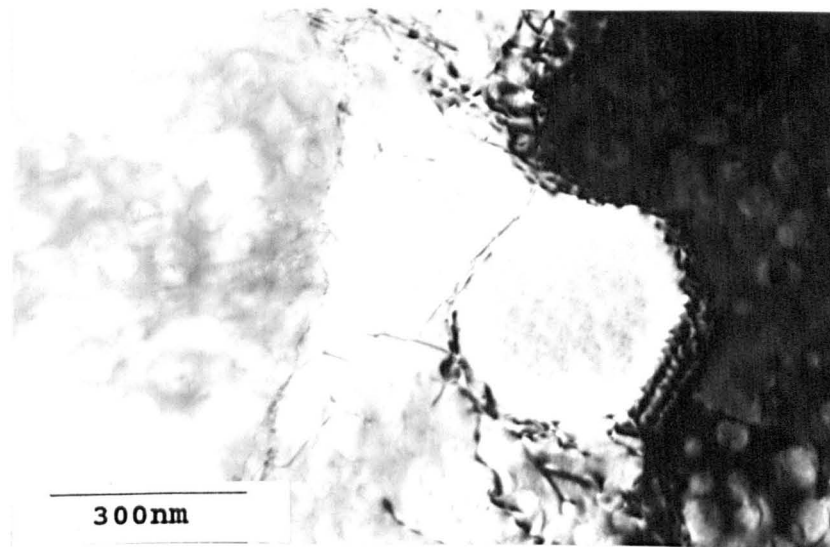
Fig. 4.40. Transmission electron micrographs of back-thinned foils from specimen H18 (300,000 cycles at 80%PS) showing the formation of low angle grain boundaries from the fringing around the large precipitates, also the low dislocation densities within the cells, (a) bright field low magnification, (b) weak beam dark field of (a) and (c) bright field high magnification; <011> orientations.

Fig. 4.41. Transmission electron micrograph of a diffraction pattern taken over a number of cells in a back thinned foil from specimen H16 (20,000 cycles at 100%PS). The orientation is almost straight down a <001> zone and the peripheral spot splitting or asterism is due to the different orientations of neighbouring cells.

supports the observations that low angle dislocation boundaries have been formed. Indeed, image fringing around large precipitates as shown in Fig. 4.40(b, c) also indicates a true low angle grain boundary has been formed.

Unlike the dislocations within a planar slip band which sheared the γ', these wavy dislocations did not penetrate the large γ' precipitates, but appeared to lie in the matrix around them. The relatively low dislocation densities within the cells and the increased densities of dislocations in the walls, is shown by the weak beam images of Figs. 4.39(c) and 4.40(b).

After 50,000 cycles at 100%PS and 600,000 cycles at 80%PS, the cell structures became more difficult to image in back-thinned foils; dislocation density was greater in between cell walls making the walls themselves appear less clearly defined (Fig. 4.42(a, b)). In addition, grains which had presumably initially deformed by homogeneous type modes, which had led to cell formation, had subsequently deformed by planar slip which tended to obscure the cell structure (Fig. 4.42(c)).

4.3.5.3.3 Late Fatigue Life

In the later stages of fatigue life a much greater density of planar slip bands was observed and deformation on two active slip systems within a single grain was commonly observed. No new features were seen, however, there was a general increase in dislocation density for all of slip bands, interfacial dislocations and interband dislocations.

(a)

<022>

(b)

<111>
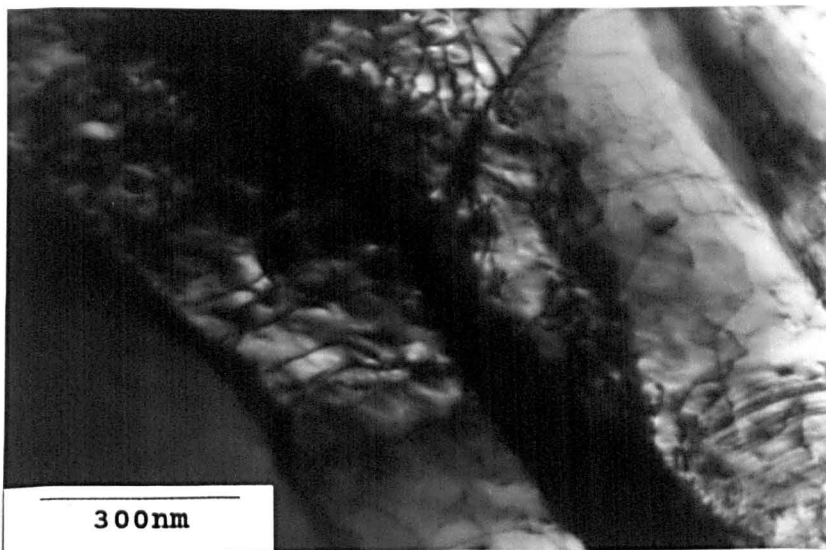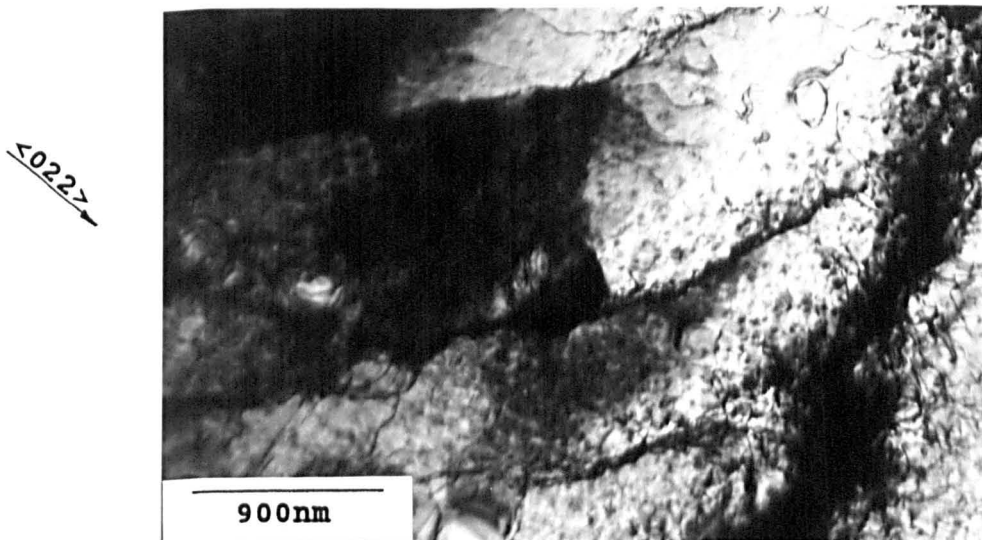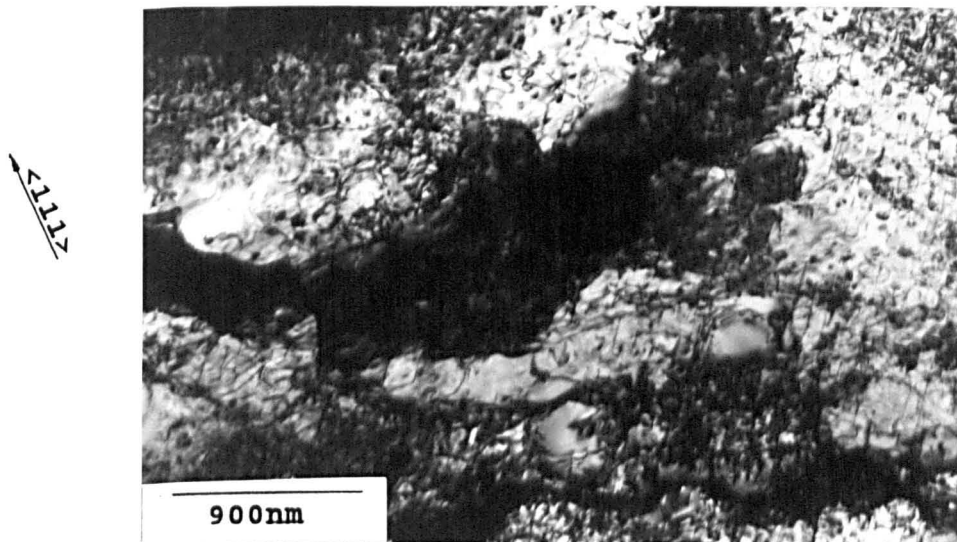
(c)

Fig. 4.42. Transmission electron micrographs of back-thinned
foils illustrating, (a) and (b) the greater dislocation
densities between cell walls, reducing the contrast of the
walls themselves and (c) grains initially exhibiting
cellular structures subsequently deforming in a planar
manner. (a): H22 (50,000 cycles at 100%PS), (b): H21
(600,000 cycles at 80%PS) <133> orientation and (c): H22,
<011> orientation.

Many slip bands could clearly be defined as PSBs, but at the same time individual slip bands were also still forming. No evidence of slip continuation in adjoining grains was found, which may have been expected, since the optical micrographs shown in Fig. 4.23 illustrate occasional examples after 50,000 cycles and numerous after 100,000 cycles at 100%PS.

After 100,000 cycles at 100%PS slip bands were broader and closer together with a much greater density of wavy dislocations present between them as illustrated by Fig. 4.43(a, b). Fig. 4.43(c) shows the extremely high dislocation density within a band, making it virtually impossible to image individual dislocations or any precipitate fragments. Fig. 4.44 shows the extremely high dislocation density typically observed after 200,000 cycles at 100%PS and 2,400,000 cycles at 80%PS, making imaging difficult and both micrographs of Fig. 4.44 clearly illustrate that deformation has taken place on two active slip systems. Fig. 4.45(a) shows a fairly well developed slip band running parallel to a series of individual dislocation lines, suggesting that slip band formation was still being initiated even in this late stage of fatigue life. Fig. 4.45(b) shows planar deformation on two active slip systems, but once again in the same area a number of wavy dislocations were observed, apparently pinned by the fine γ'. Apparently the resolved shear stress on these dislocations was too low to cause looping.

In contrast, it was possible to locate occasional areas of low dislocation density, as shown by Fig. 4.46, where it
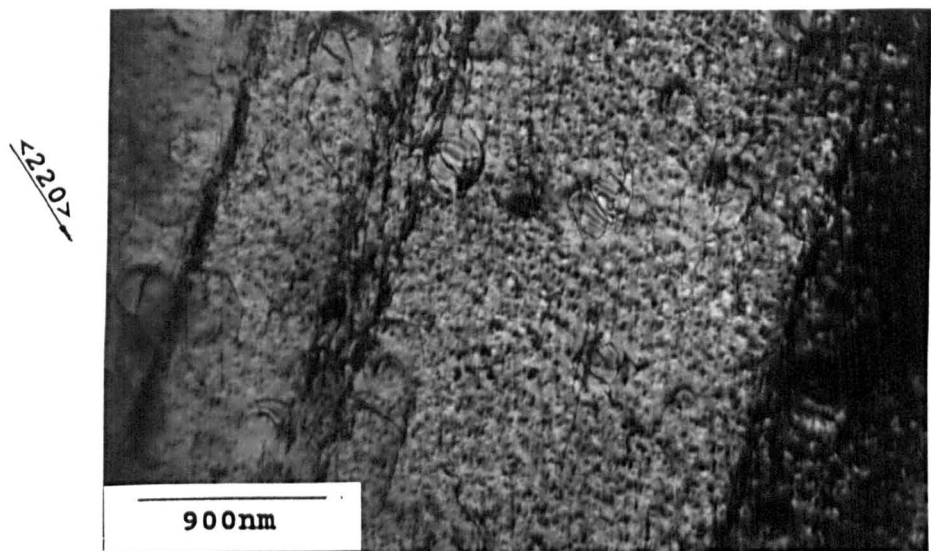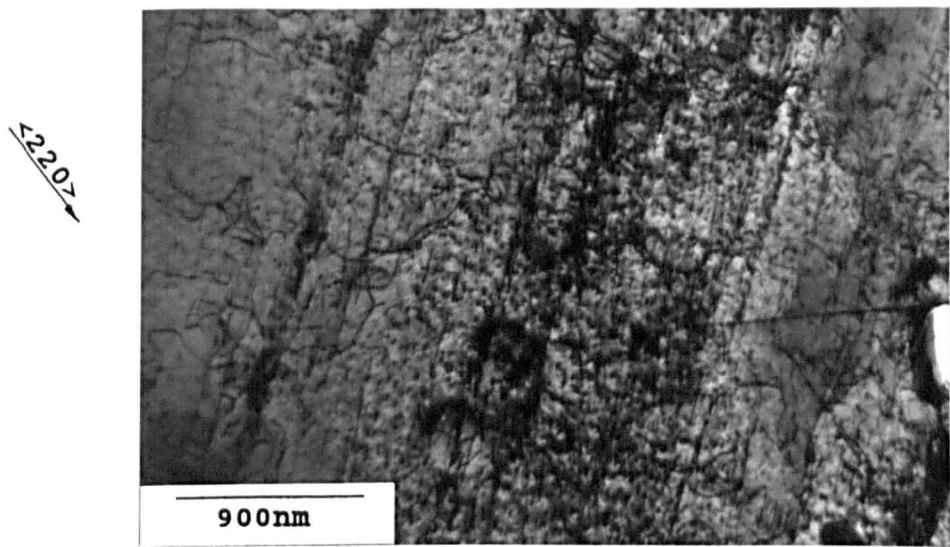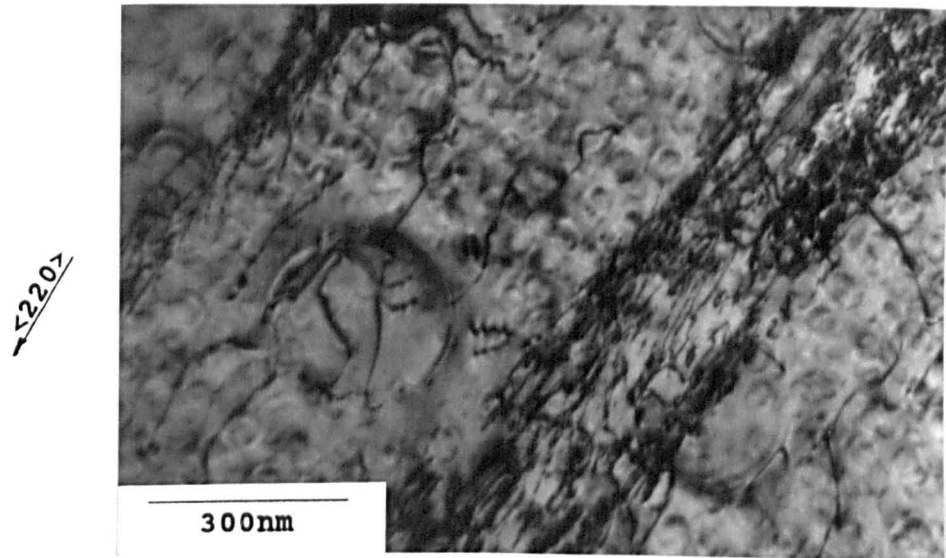
Fig. 4.43. Bright field transmission electron micrographs of back-thinned foils from specimen H28 (100,000 cycles at 100%PS) showing broader slip bands, closer together with greater dislocation densities between the bands and within the bands themselves; <113> orientations.

900nm

(a)

900nm
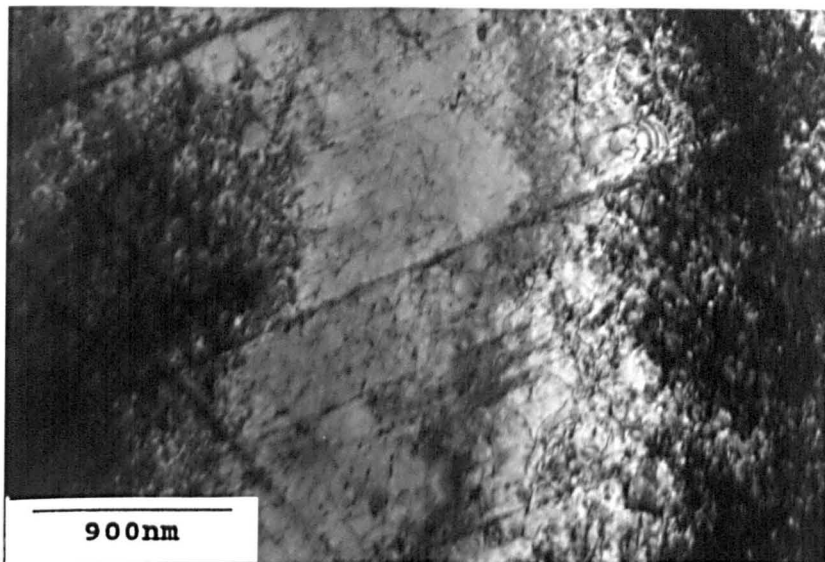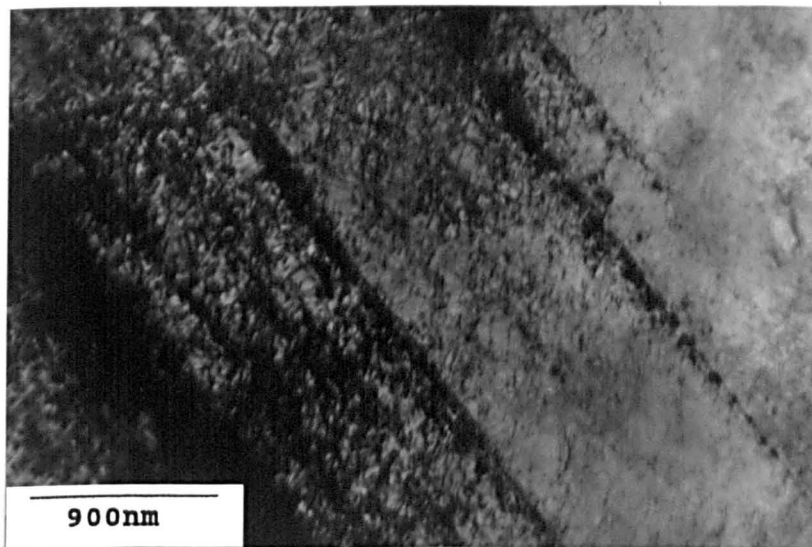
(b)

Fig. 4.44. Bright field transmission electron micrographs of back-thinned foils showing the extremely high dislocation densities typically observed after (a) 200,000 cycles at 100%PS (specimen H34) and (b) 2,400,000 cycles at 80%PS (specimen H31).

(a)

(b)
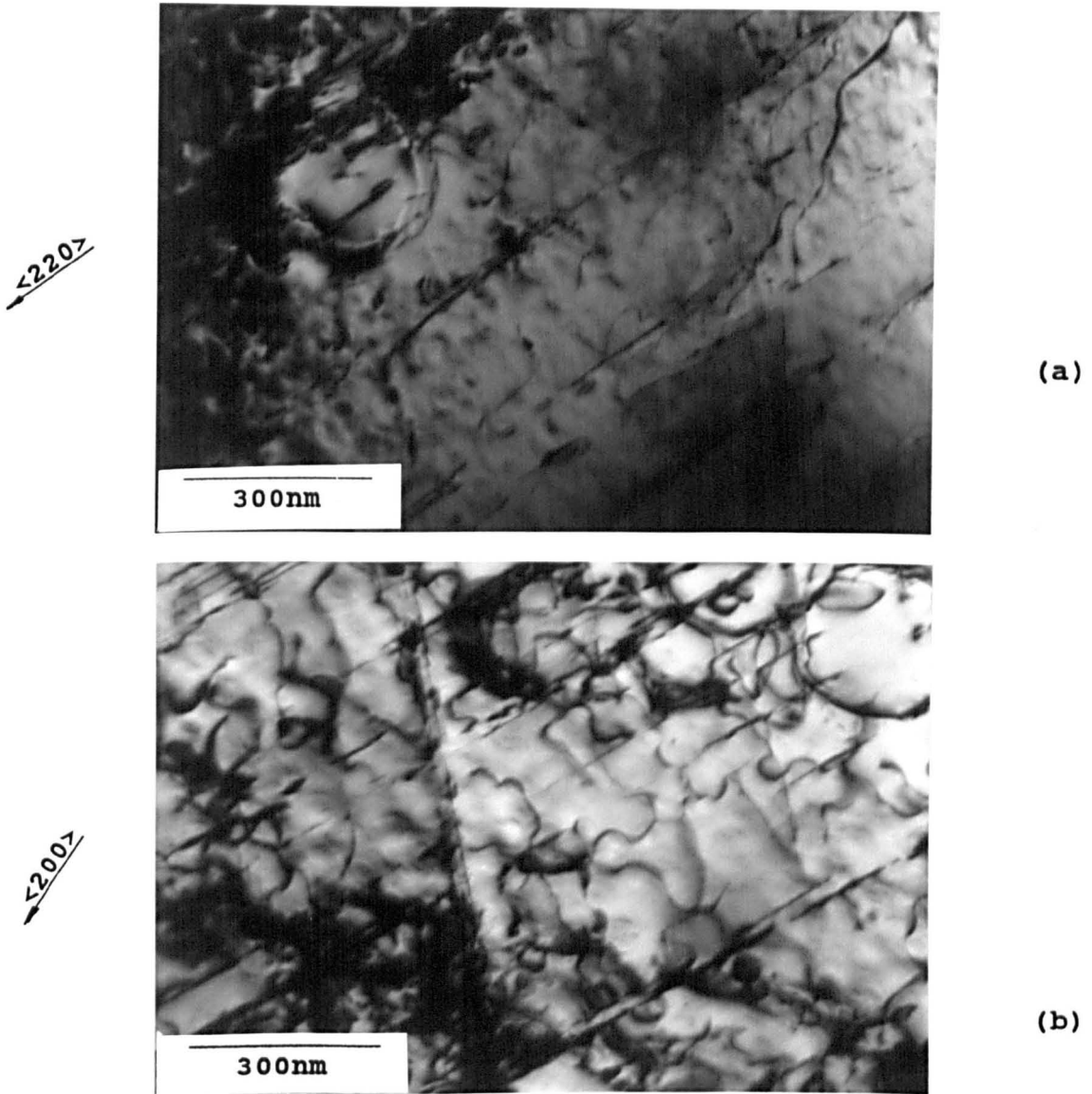
Fig. 4.45. Bright field transmission electron micrographs of back-thinned foils, (a) from specimen H34 (200,000 cycles at 100%PS) showing a fairly well developed slip band (upper left) running parallel to a series of individual dislocation lines, <112> orientation and (b) from specimen H31 (2,400,000 cycles at 80%PS) showing planar slip on two active systems in the same area as wavy dislocations, apparently pinned by the small precipitates, <011> orientation.
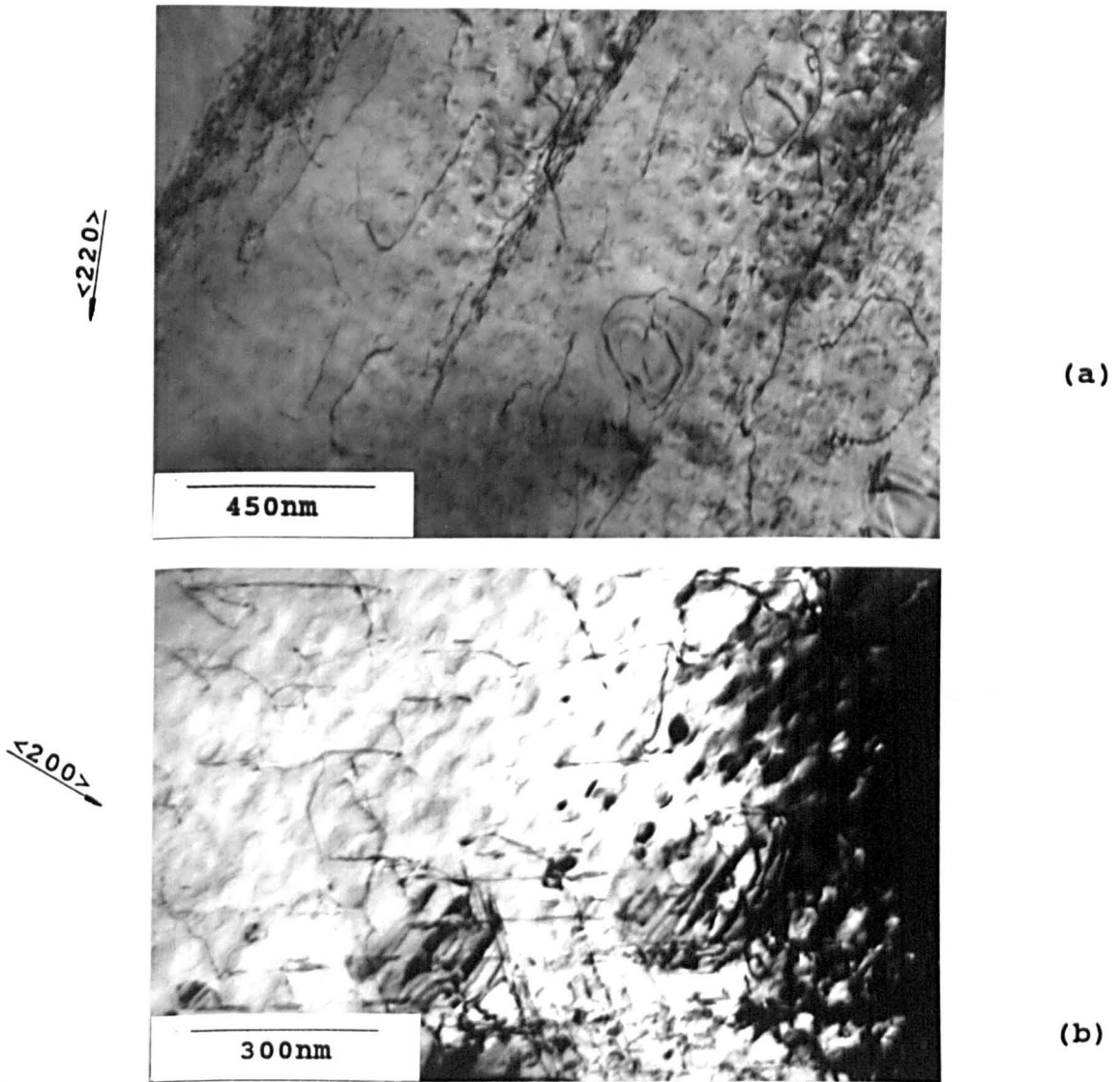
Fig. 4.46. Bright field transmission electron micrographs of
back-thinned foils from specimen H28 (100,000 cycles at
100%PS) showing some areas of lower dislocation density
observed and slip occurring on two active systems;
orientations: (a): <113> and (b): <011>.

is evident from Fig. 4.46(b) that deformation had occurred on two active slip systems even though slip bands had not yet developed.

In these late stages of fatigue, images of cell structures were almost impossible to obtain. There was an extremely high dislocation density present and planar deformation in the form of slip bands was well established. Fig. 4.47 shows that after 200,000 cycles at 100%PS the many long, straight, planar style dislocations had much stronger contrast and only a faint indication of background cell structures could be seen. In contrast, it may be seen from Fig. 4.48 that areas of low dislocation density did exist and that long wavy dislocations may have just started to tangle up to form new cell boundaries.

Dislocation density around the large γ′ was still variable at this stage of fatigue life. However, a number of large γ′ contained stacking faults, examples of which are shown by Fig. 4.48.

4.3.5.3.4 Fracture

At fracture the number of slip bands observed was extremely high; within a grain slip band appearance ranged from being broad to very fine in width as illustrated by Figs. 4.49 and 4.50. Depending on diffraction conditions, large γ′ precipitates often appeared dark, due to their encasement by dislocation substructures; this is very obvious in Fig. 4.49(b). Deformation taking place on three active slip planes was a common observation and is clearly

(a)

900nm

(b)

900nm
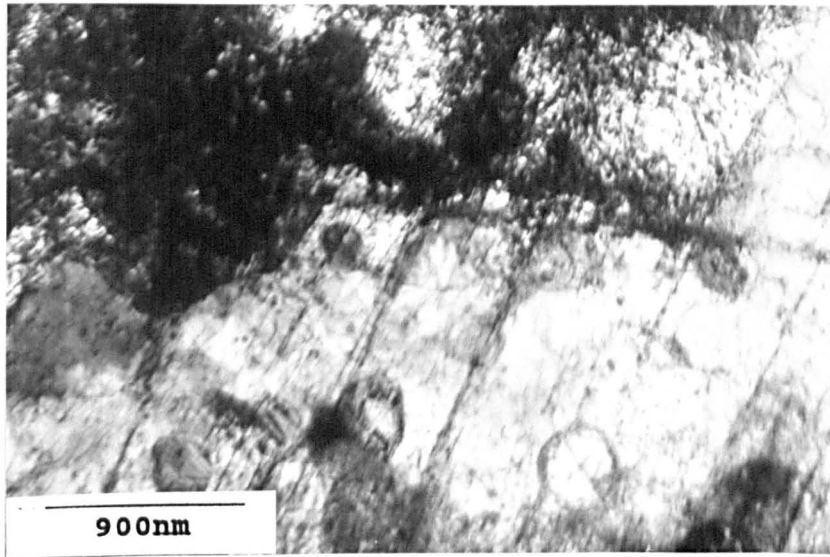
Fig. 4.47. Bright field transmission electron micrographs of back-thinned foils from specimen H34 (200,000 cycles at 100%PS) illustrating the much stronger contrast from planar dislocations, making images of cell structures very difficult to obtain; also, the extremely high overall dislocation densities typically observed.

300nm

(a)

300nm
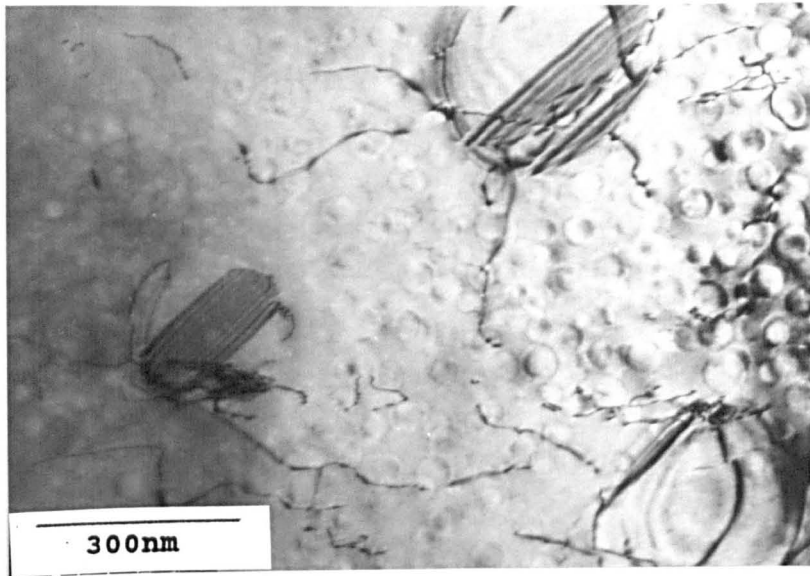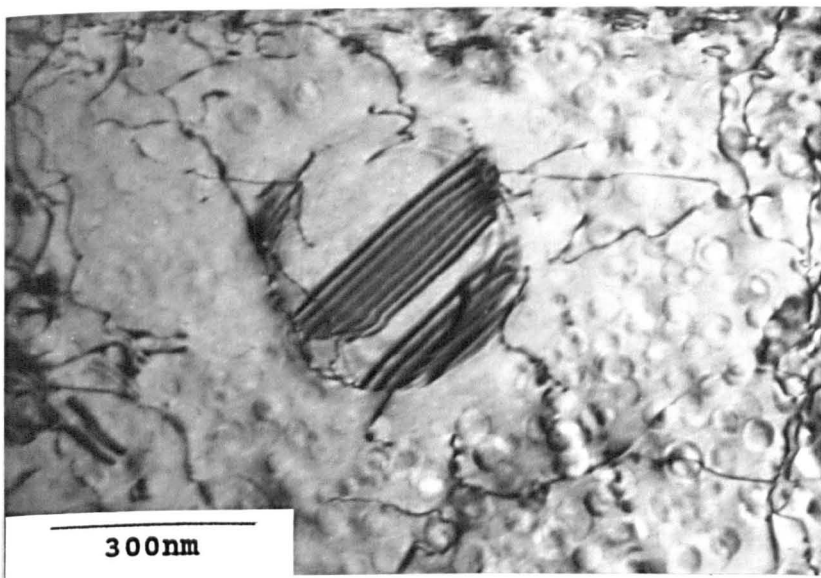
(b)

Fig. 4.48. Bright field transmission electron micrographs of back-thinned foils from specimen H34 (200,000 cycles at 100%PS) showing areas of low overall dislocation density in the late stages of fatigue lifetime and stacking fault contrast within large precipitates.

<111>

2.5µm

(a)

<111>

2.5µm
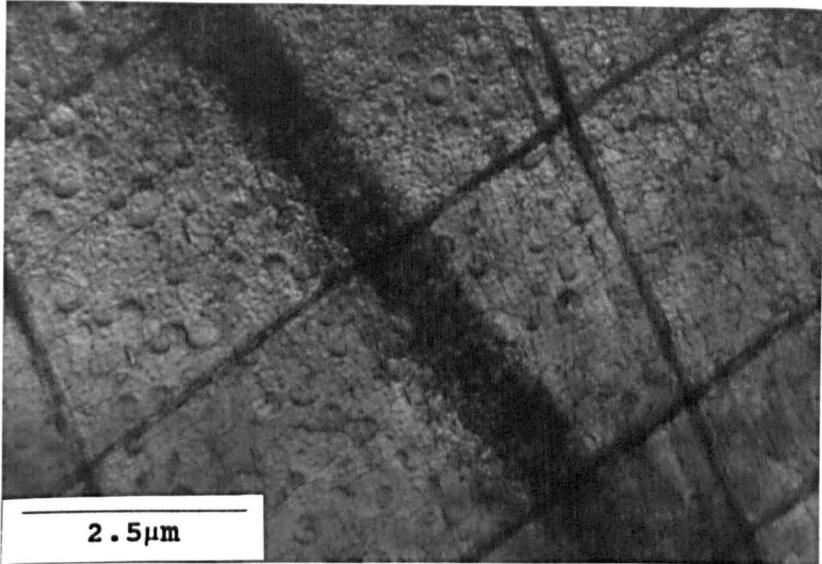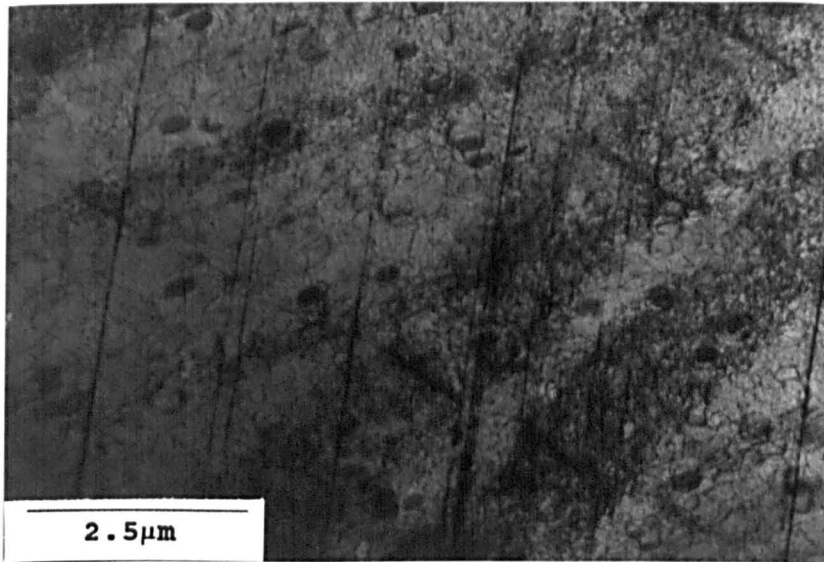
(b)

Fig. 4.49. Bright field transmission electron micrographs of
back-thinned foils from specimen H2 (fracture at 100%PS)
showing slip occurring on three active systems and bands of
various thickness; in addition, (b) illustrates precipitates
encased by dislocations giving them a dark appearance and
the planes running in an almost vertical direction are being
viewed edge on; <011> orientations.

<011> orientations labeled to the left of each micrograph; scale bars read 2.5μm.
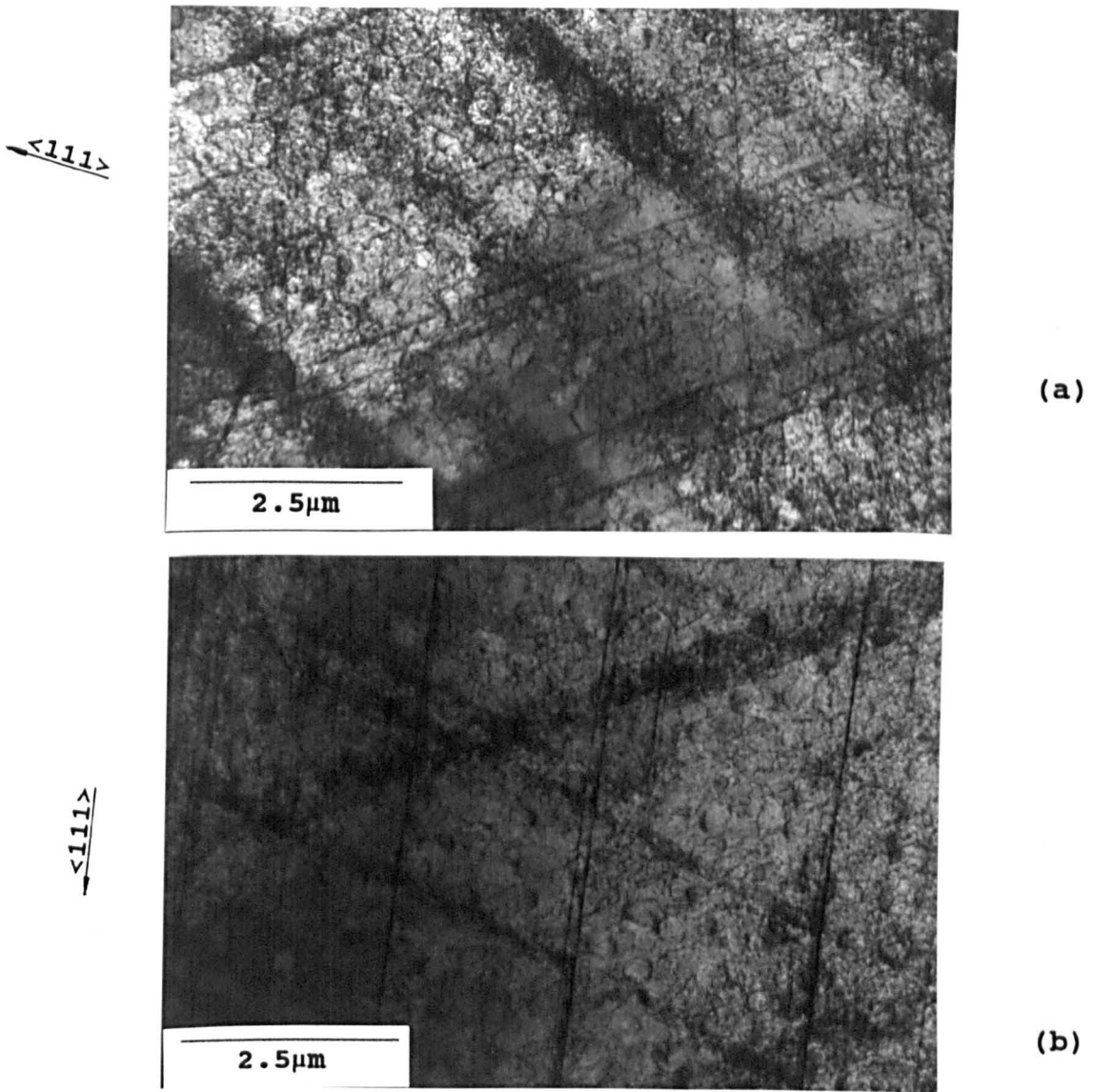
Fig. 4.50. Bright field transmission electron micrographs of back-thinned foils from failed specimens showing slip occurring on three active systems and bands of various thickness; (a) illustrates the high dislocation density typically observed at fracture from specimen H19 (fracture at 80%PS) and (b) shows the planes running in an almost vertical direction viewed edge on from specimen H2 (fracture at 100%PS); <011> orientations.

shown in Figs. 4.49 and 4.50; grains contained a very dense dislocation substructure in between bands making high magnification TEM imaging very difficult (see Figs. 4.51 and 4.52).

Slip continuation in adjoining grains and twins was also commonly observed at fracture and examples are given in Fig. 4.53; this was not seen in back-thinned foils other than those taken from fractured specimens, in contrast to the optical results (section 4.3.5.1), which illustrated occasional examples of slip continuation by 50,000 cycles at 100%PS (Fig. 4.23(c)). No evidence of cell structures were found, implying that cell formation was superceded by other deformation mechanisms later in life, rather than a transition from cell to sub-grain formation.

4.3.6 Surface and Sub-surface Deformation Results

All surface grains examined in cross-sectional foils exhibited slip bands; some were very heavily deformed while other neighbouring grains contained only two or three bands. There did not appear to be any correlation between density of slip bands seen in surface grains and the grain's orientation. Neither was there any apparent correlation between slip band thickness or spacing and grain orientation. Quantitative details of slip bands in the surface grains examined are presented in Table 4.7. Most of the surface grains observed were aligned in the <011> type orientation, other examples noted were two at <112> and one at <001>. The above orientations were obtained by tilting

<111>   (a)

900nm

<111>

                                                                         (b)

300nm
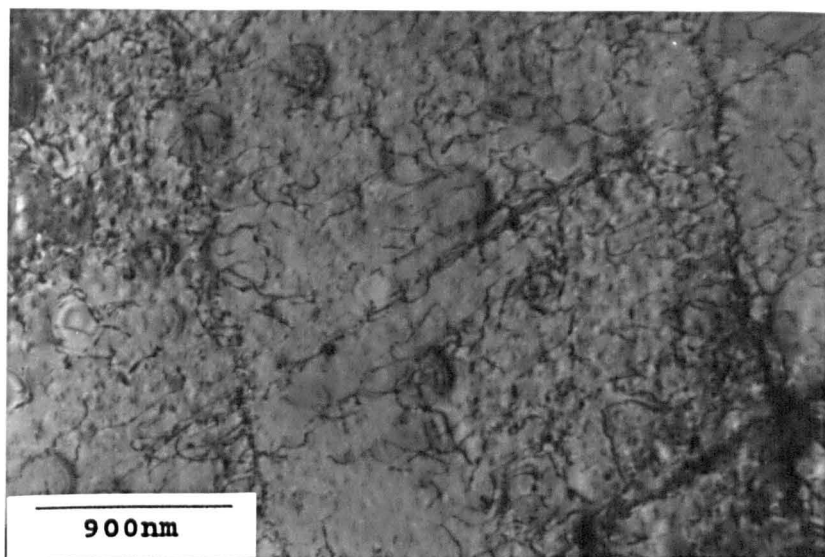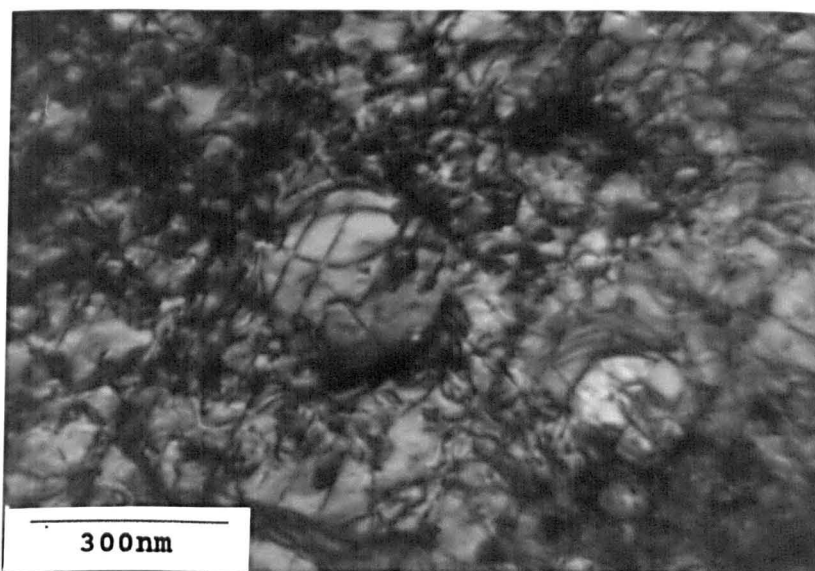
Fig. 4.51. Bright field transmission electron micrographs of
back-thinned foils from failed specimens showing (a) slip
occurring on two active systems and wavy dislocations
interacting with precipitates, (b) the high dislocation
density typically observed at fracture making the clear
imaging of individual features very difficult at high
magnification. (a): from specimen H2 (fracture at 100%PS),
(b): from specimen H19 (fracture at 80%PS); <011>
orientations.
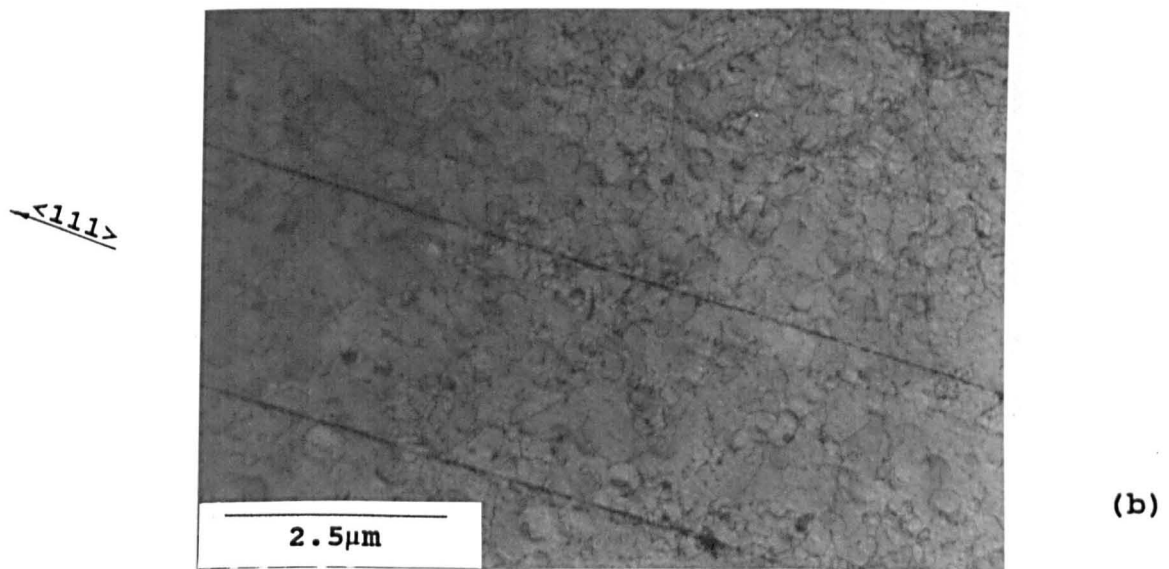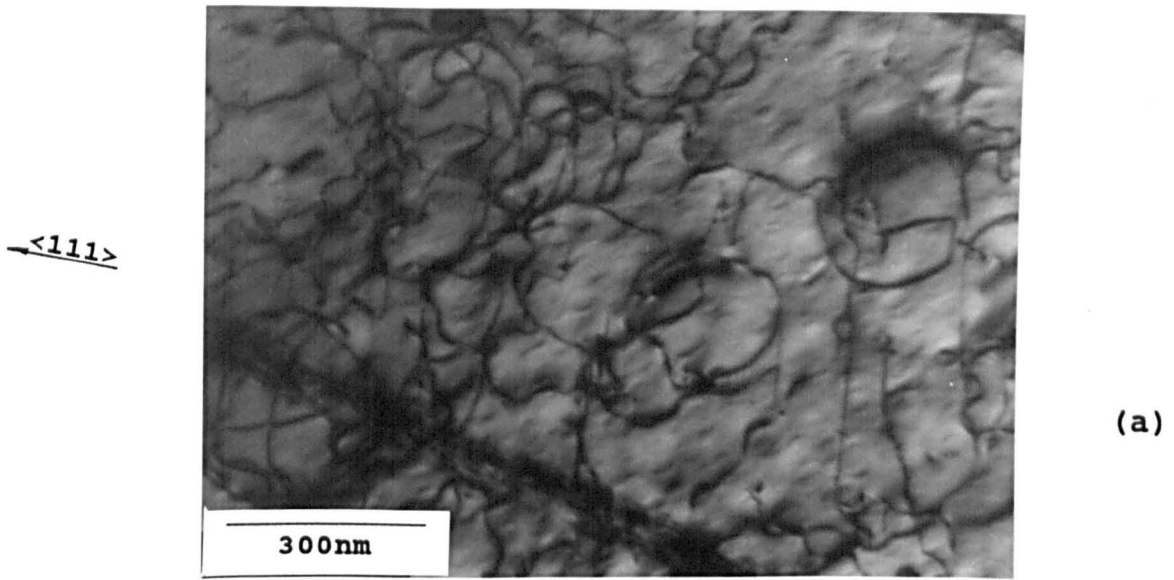
Fig. 4.52. Bright field transmission electron micrographs of back-thinned foils from specimen H3 (fracture at 80%PS) showing (a) wavy dislocations pinned by both large and small precipitates and a slip band in the bottom left and (b), the high density of wavy dislocations in existence between slip bands when viewed edge on; <011> orientations.

(a)

2.5μm

(b)

2.5μm
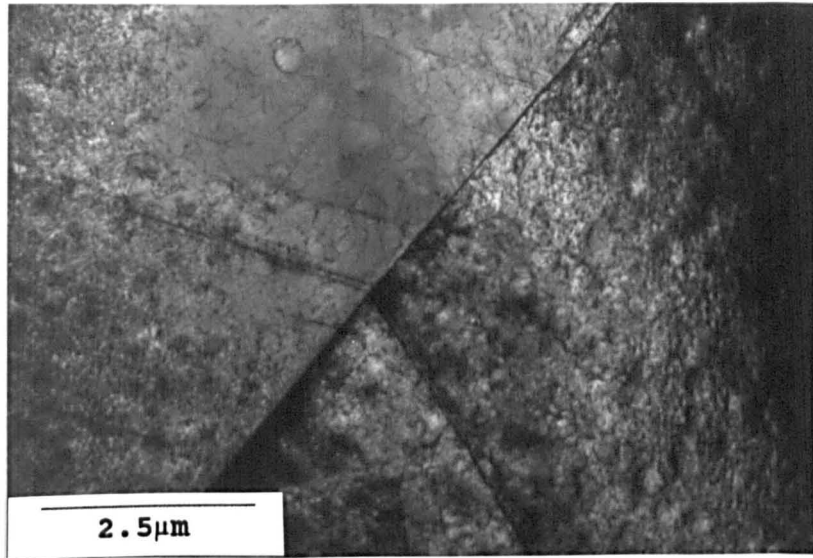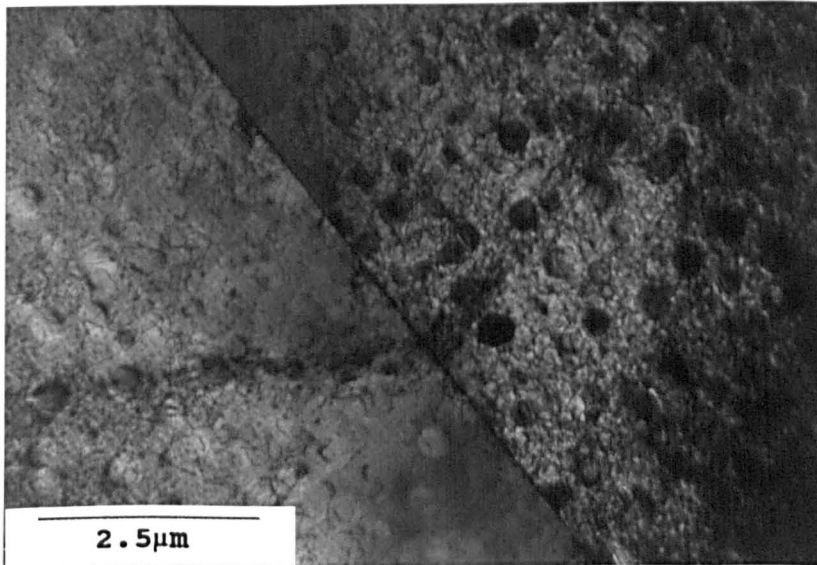
Fig. 4.53. Bright field transmission electron micrographs of back-thinned foils from specimen H12 (fracture at 100%PS) showing typical examples of slip continuation across twin boundaries; the high dislocation densities were typical, as were the numbers of precipitates surrounded by dislocations, or showing stacking fault contrast.

Grain orientation	Slip band/ surface angle (°)	Slip band width	Slip band spacing
<011>	2 68	590nm 3-4 planes	1.5µm too few
<112>	27 72	150-300nm 200nm	820nm only one
<011>	24 40	150nm 150nm	650nm too few
<011>	42 65	250-550nm 50-75nm	2.25µm only one
<001>	61	3-4 planes	1.25µm
<011>	30 35	100nm 100-175nm	only one 550nm
<011>	62 67	3-4 planes 4-5 planes	500nm 740nm
<011>	60 67	225nm 2-3 planes	5.06µm 833nm
<112>	25	2-3 planes	4.2µm
<011>	33 35	2-3 planes 180-440nm	2.5µm 2.4µm
<011>	20 82	2-3 planes 5-6 planes	625nm 2.75µm

Table 4.7: Surface grain slip band details

the foils through a maximum of 3-4° from the 0° tilt angle. Cellular type deformation structures were not observed in any of the cross-sectional foils.

Of all the surface grains observed, slip bands generally ran at an angle of between 30° and 70° to the surface. Occasionally they made angles larger or smaller than those above for example, 24° or 72°, and there were a couple of extreme angles, for example, 2° and 82°.

Fig. 4.54 shows a surface grain from one of the 100%PS foils. Numerous slip bands were evident and the dislocation density was high. A similar observation was made on an 80%PS foil and is illustrated by Fig. 4.55. Both of these examples demonstrate the variations in slip band thickness and material deformation on two active slip systems. Deformation on three active systems was regularly observed in back-thinned foils, however, this was not the case in any of the cross-sectional foils investigated, even in surface grains; the reason for this was not clear.

Moving away from the fatigue surfaces it was noted that the numbers of slip bands and dislocations reduced, but it must be stressed that this can only be a generalisation, since grains at similar depths exhibited very different levels of deformation.

Observations made on the 100%PS specimens were similar to the 80%PS foils, i.e. the lack of any apparent correlation between deformation and grain orientation and deformation and depth. Since <011> type grains were extremely common, both surface and sub-surface, obtaining a <111> reflection for clear dislocation imaging was utilised extensively.

At a depth of 10µm, Fig. 4.56(a) shows a high
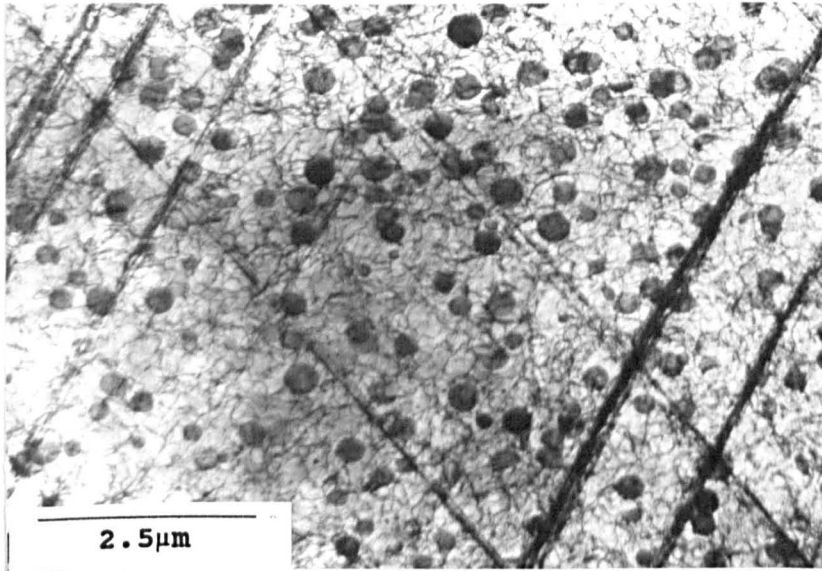
(a)
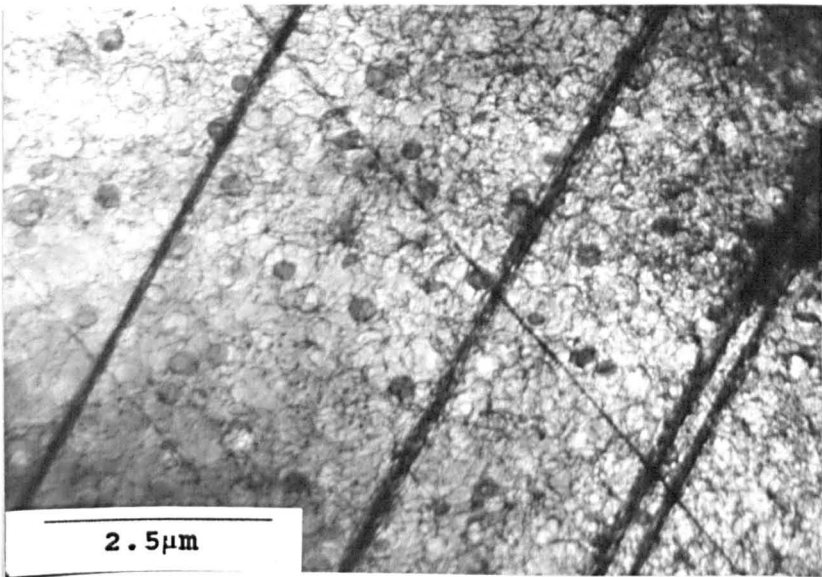
(b)

Fig. 4.54. Bright field transmission electron micrographs of a cross-sectional foil from specimen H2 (fracture at 100%PS) showing a surface grain at a depth of approximately 5μm. Slip has occurred on two active systems and the bands in the above micrographs are lying at angles of 35° and 33° to the fatigue surface. A high dislocation density was evident and the precipitates appear dark (a) because of their encasement by dislocations; <011> orientations.
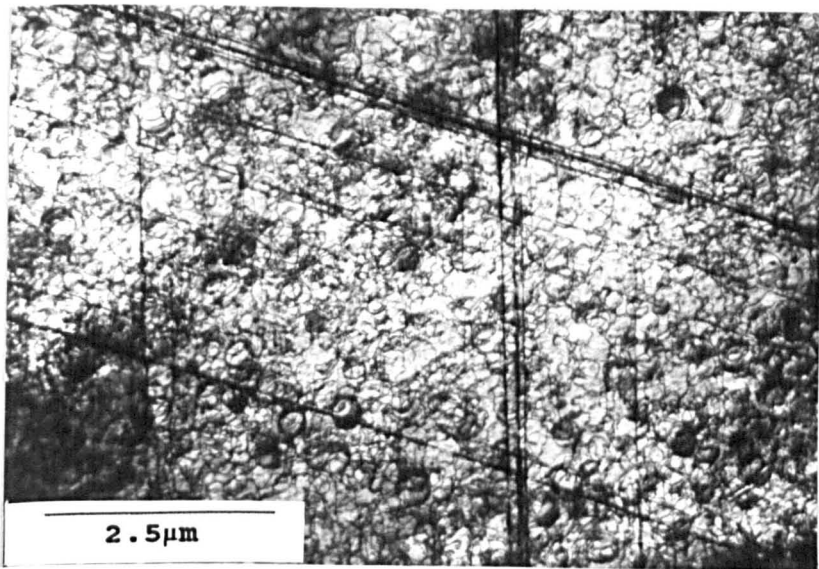
Fig. 4.55. Bright field transmission electron micrograph of
a cross-sectional foil from specimen H3 (fracture at 80%PS)
showing a surface grain at a depth of approximately 10μm.
Slip has clearly occurred on two active systems and the
bands (viewed edge on) are lying at angles of 20° and 82° to
the fatigue surface. The high dislocation densities made it
difficult to image dislocation/precipitate interactions;
<011> orientation.

<111> (label at left of image a, rotated)

2.5μm

(a)

<111> (label at left of image b, rotated)

900nm
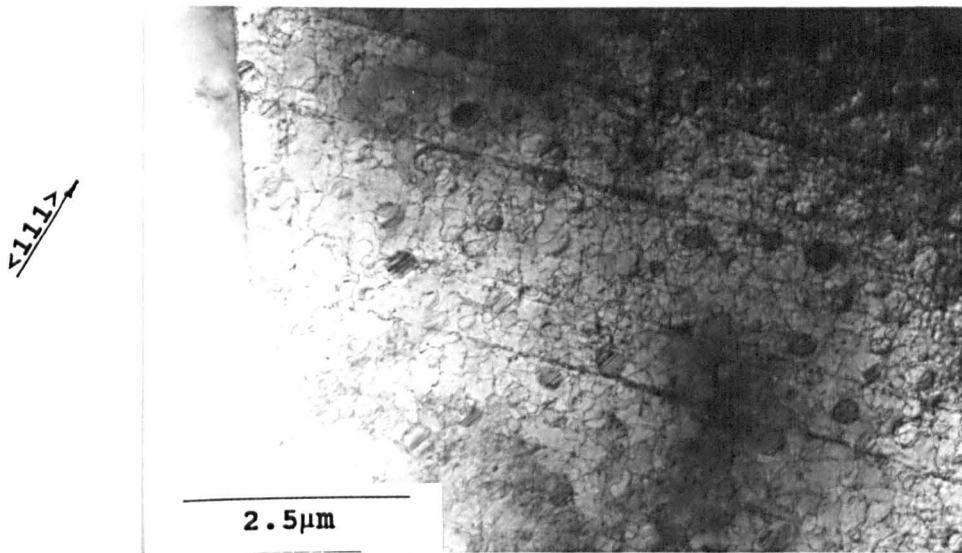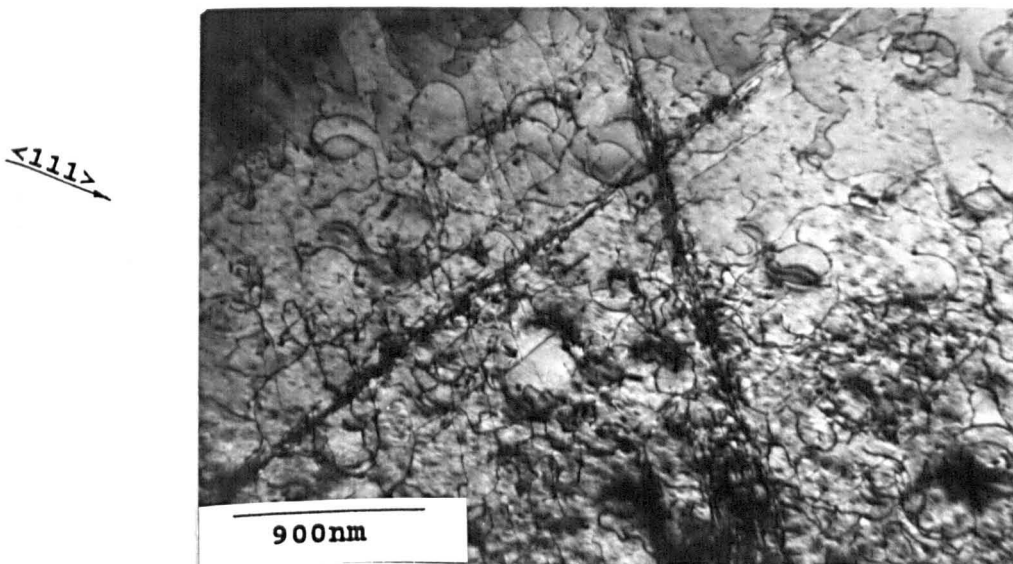
(b)

Fig. 4.56. Bright field transmission electron micrographs of cross-sectional foils, (a) from specimen H2 (fracture at 100%PS) showing the high dislocation density in an annealing twin in a surface grain at a depth of approximately 10μm, the bands lie at 35° to the fatigue surface; (b) from specimen H3 (fracture at 80%PS) illustrating slip on two active systems at a depth of 17μm in a sub-surface grain with the bands lying at angles of 28° and 87° to the fatigue surface, dislocation loops are clearly visible; <011> orientations.

dislocation density and numerous slip bands within an annealing twin from a 100%PS foil; a similar amount of deformation was noted 17μm away from the fatigue surface in an 80%PS foil, as illustrated by Fig. 4.56(b). In this example the material had deformed on two active slip systems and numerous dislocation loops around the large γ' are clearly visible.

At a depth of approximately 40-42μm, large variations in dislocation activity between grains were found. Whereas Fig. 4.57(a) demonstrates a rather high dislocation density and definite evidence of slip on two active systems, Fig. 4.57(b) shows only a few dislocations along with two or three parallel slip bands. The higher dislocation density was found in the sample tested at 80%PS compared to Fig. 4.57(b), the lower dislocation density, which was tested at 100%PS.

A similar observation was made at a depth of approximately 60μm in a 100%PS foil. Fig. 4.58(a) illustrates a grain containing two very obvious slip bands running in different directions, whereas Fig. 4.58(b) shows nothing more than occasional dislocations partially looped around the larger γ'. It was noted however, that no deformation was observed after a depth of 60μm on the 80%PS foils and 62μm and 70μm on the 100%PS foils. At 80%PS, a depth of 60μm would correspond to an applied fatigue stress of 717MPa (from Fig. 4.59); similarly at 100%PS, the depths of 62μm and 70μm would correspond to applied stress values of 896 and 894MPa respectively.
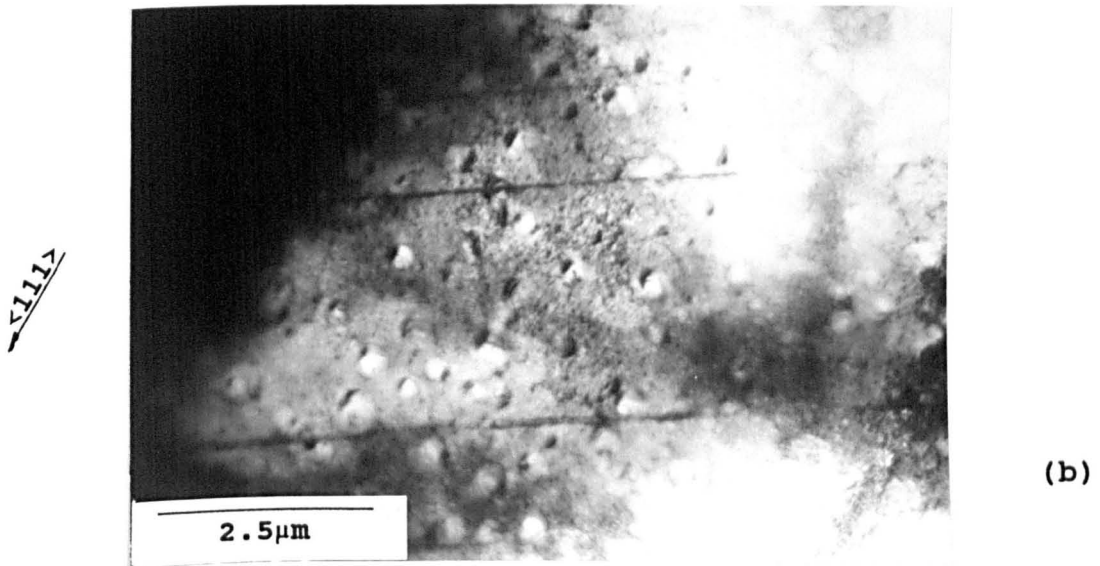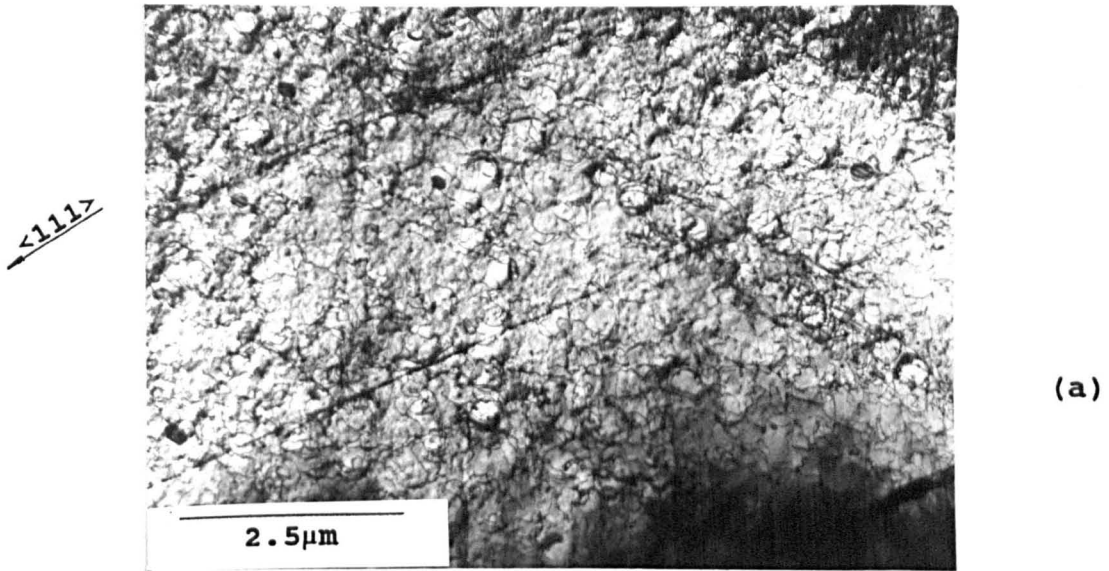
Fig. 4.57. Bright field transmission electron micrographs of cross-sectional foils, at approximate depths of (a) 42μm, and (b) 40μm from the fatigue surfaces of (a) specimen H19 (fracture at 80%PS) and (b) specimen H12 (fracture at 100%PS); the micrographs illustrate examples of the differences in deformation observed at similar depths; (a) shows a high dislocation density in an annealing twin with two active slip systems, the bands lie at 35° and 22° to the fatigue surface; alternatively, (b) shows little deformation with a few bands lying parallel to the fatigue surface; <011> orientations.
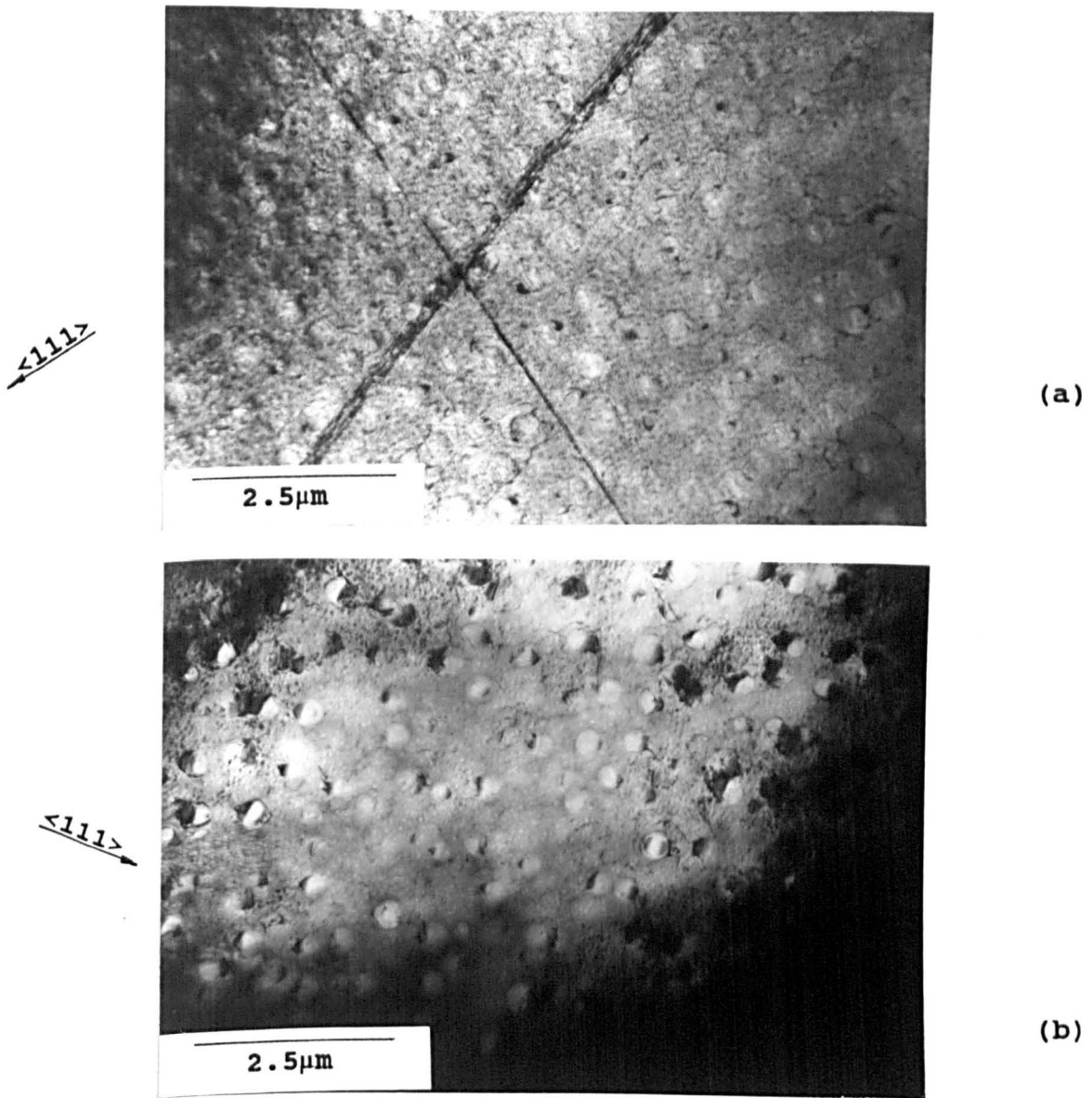
Fig. 4.58. Bright field transmission electron micrographs of cross-sectional foils from specimen H12 (fracture at 100%PS) at approximate depths of (a) 60μm and (b) 62μm from the fatigue surface; the micrographs illustrate examples of the differences in deformation observed at similar depths; (a) shows two very obvious slip bands, running at 68° and 42° to the fatigue surface; in contrast, (b) shows no observable deformation; <011> orientations.
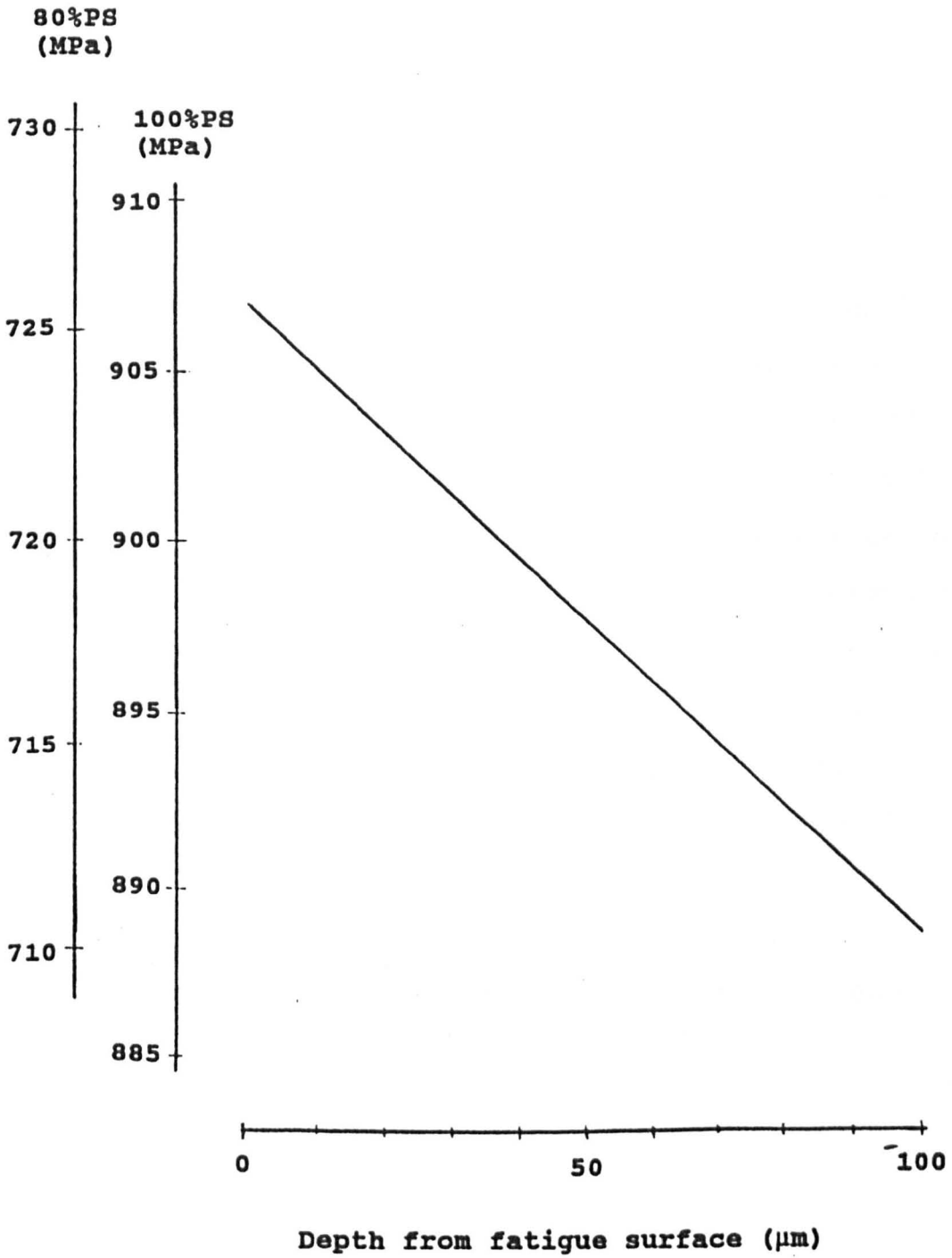
Fig. 4.59. Fatigue stress with depth from gauge surface.

At the absolute fatigue surface, Fig. 4.60(a) shows a particle within the alloy and although there was a slip band very close to it, there was no evidence of any crack initiation either within the particle, at the particle/matrix interface or within the matrix itself. Similarly, Fig. 4.60(b) shows a triple point at a depth of 20µm with a noticeable dislocation activity present. Again, no evidence was seen of any crack initiation.

Fig. 4.61 illustrates observations at two different locations within a particular annealing twin in a 100%PS foil; the twin was angled at 30° to the fatigue surface and Fig. 4.61(a) is situated 4µm from the end of the twin nearest the fatigue surface, 25µm from the surface. A wavy, tangled dislocation substructure was evident, along with planar dislocation lines running parallel to the twin direction. 9µm further along the twin, i.e. 33µm from the fatigue surface, Fig. 4.61(b) illustrates uniformly distributed wavy dislocations present but planar deformation was not visible.

A similar observation was made in a twin running at 45° to the fatigue surface in an 80%PS foil and is shown by Fig. 4.62. Dense, broad slip bands and a high dislocation density were seen at the end of the twin nearest the fatigue surface (Fig. 4.62(a)) but 14µm further along the twin i.e. 10µm further from the surface, only individual planar dislocation lines were visible together with a greatly reduced dislocation density (Fig. 4.62(b)).

Slip continuation in adjoining grains and twins was

(a)

1.5μm

(b)

300nm
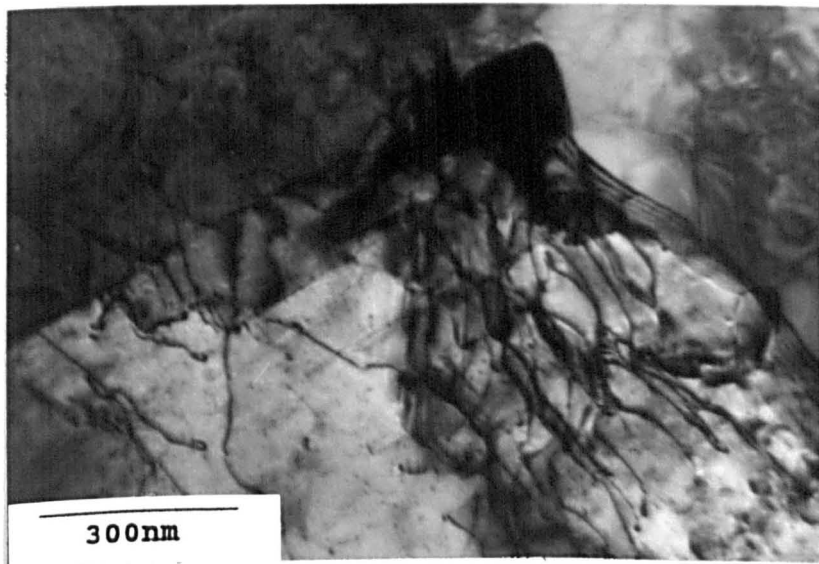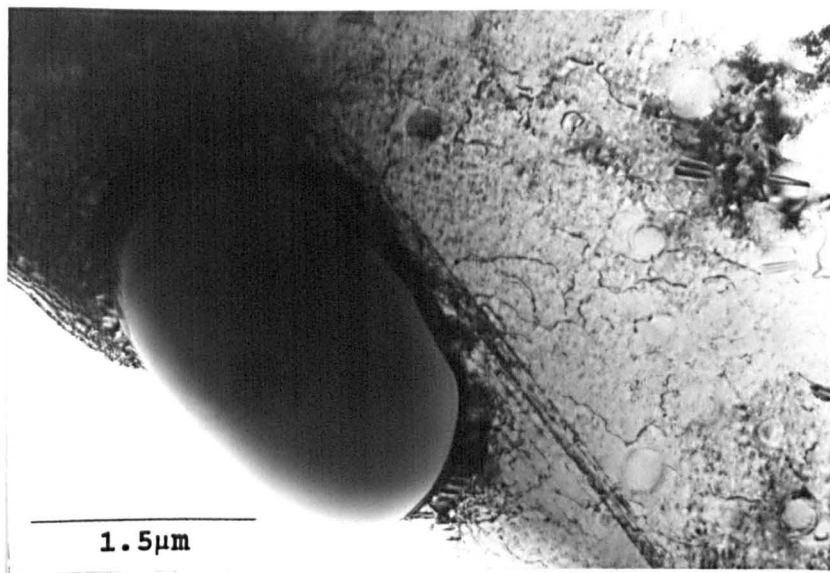
Fig. 4.60. Bright field transmission electron micrographs of cross-sectional foils from specimen H24 (fracture at 100%PS) showing possible crack initiation sites, (a) shows a surface particle or inclusion and (b) shows a grain boundary triple point 20μm from the fatigue surface; neither of the micrographs illustrate any evidence of initiating cracks; (a): <112> orientation.
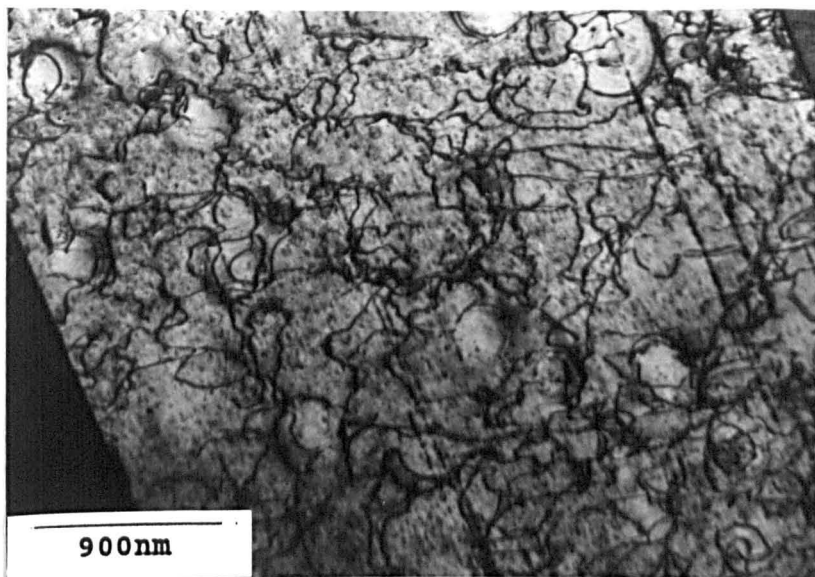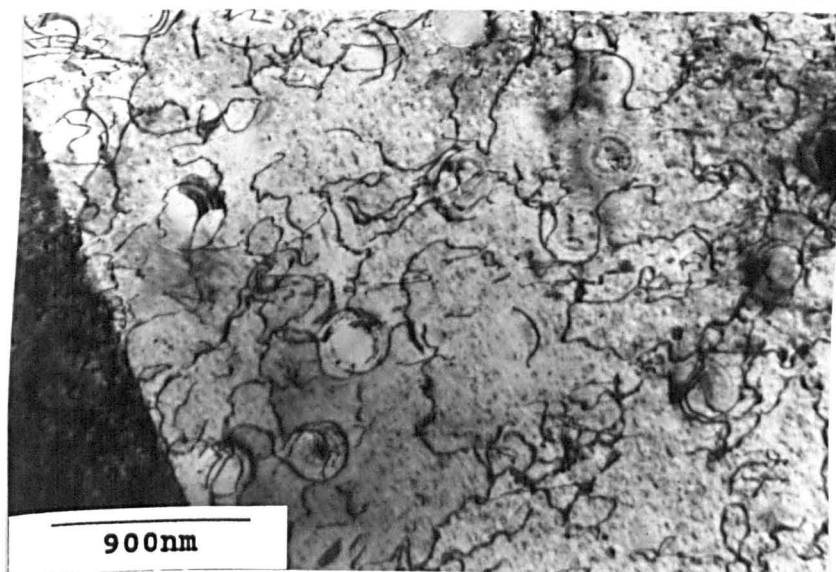
Fig. 4.61. Bright field transmission electron micrographs of a cross-sectional foil from specimen H24 (fracture at 100%PS) showing an annealing twin, lying at an angle of 30° to the fatigue surface, in a sub-surface grain; (a) shows a high density of wavy tangled dislocations and obvious planar dislocations running parallel to the direction of the twin, at a depth of 25μm; (b) shows that at a depth of 33μm, the density of wavy dislocations is reduced and the planar dislocations are not visible; <011> orientations.
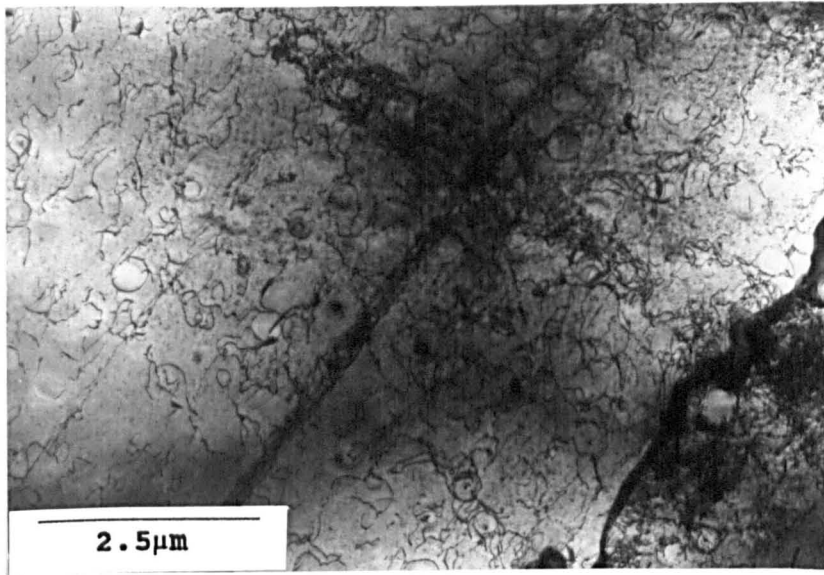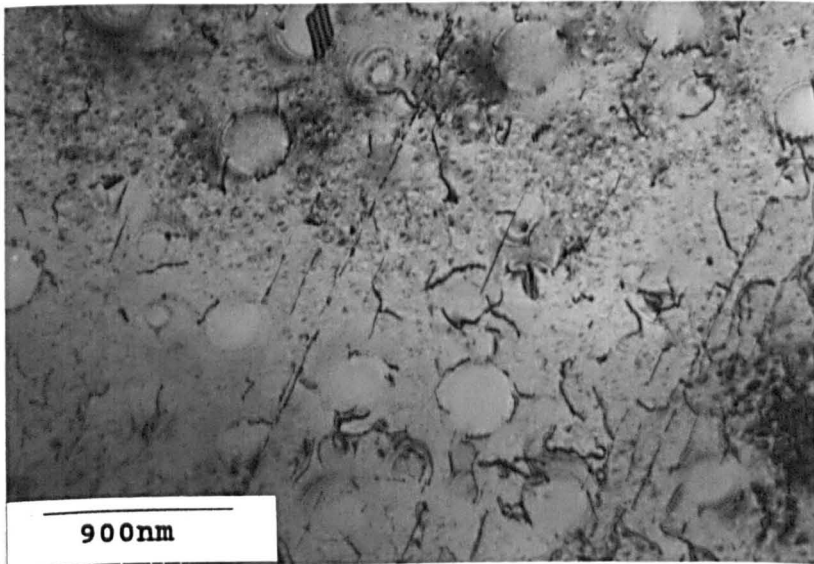
Fig. 4.62. Bright field transmission electron micrographs of a cross-sectional foil from specimen H19 (fracture at 80%PS) showing an annealing twin, lying at an angle of 45° to the fatigue surface, in a sub-surface grain; (a) shows a high density of wavy dislocations and obvious slip bands running parallel and normal to the direction of the twin, at a depth of 25µm; (b) shows that at a depth of 35µm, the density of wavy dislocations is low enough to image them individually and only planar dislocation lines are visible; <011> orientations.

commonly observed at shallow depths from the fatigue surfaces in fractured specimens, well away from the primary crack. Figs. 4.63 and 4.64 show examples of twin boundaries at depths of 12μm and 20μm respectively, whereas Fig. 4.65 illustrates the continuation across grain boundaries, 10μm and 15μm from the surface. In contrast, the arrest of a slip band at a twin boundary was occasionally noted, generally at a greater depth. Fig. 4.66 shows an example of a slip band intersecting with a twin boundary obtained from a distance of 30μm from the fatigue surface of an 80%PS foil. Although there is a number of dislocations present, there was no evidence of slip continuation.

<111>

900nm

(a)

<111>

900nm
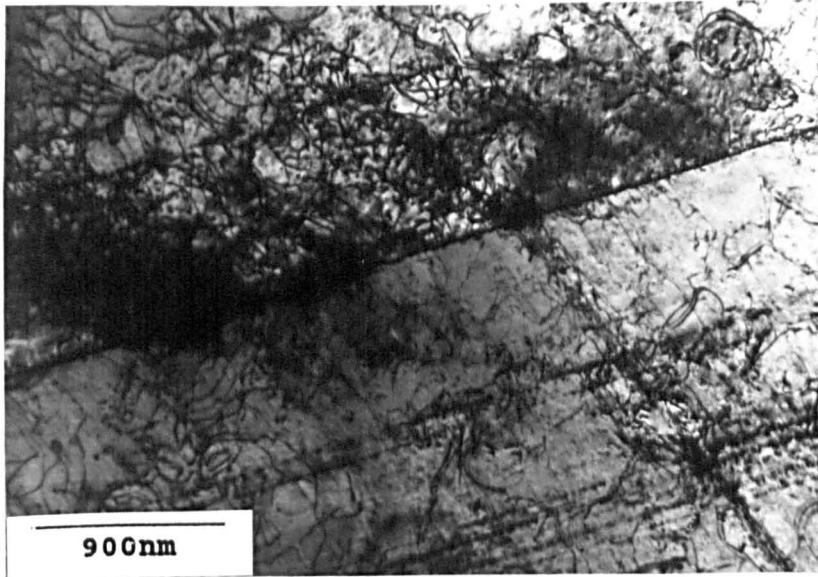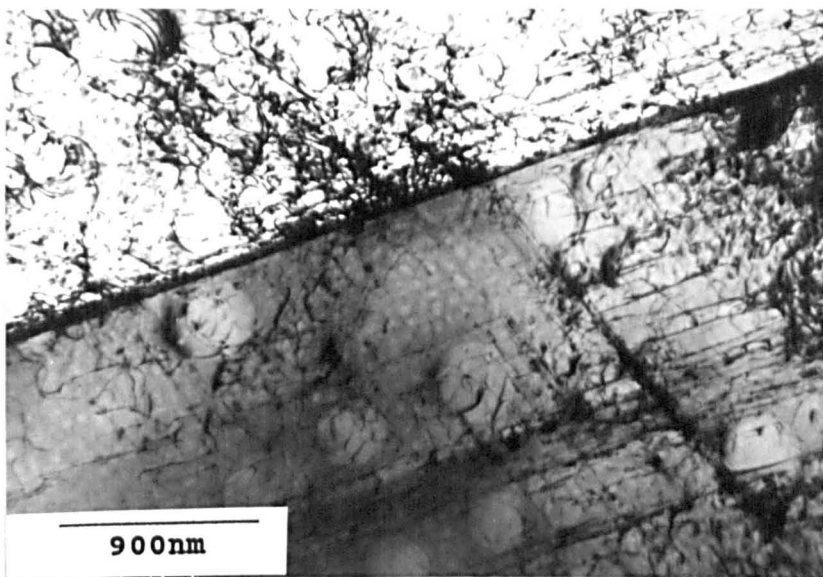
(b)

Fig. 4.63. Bright field transmission electron micrographs of a cross-sectional foil from specimen H19 (fracture at 80%PS) showing the continuation of slip over an annealing twin boundary, at a depth of 12μm; <011> orientations.
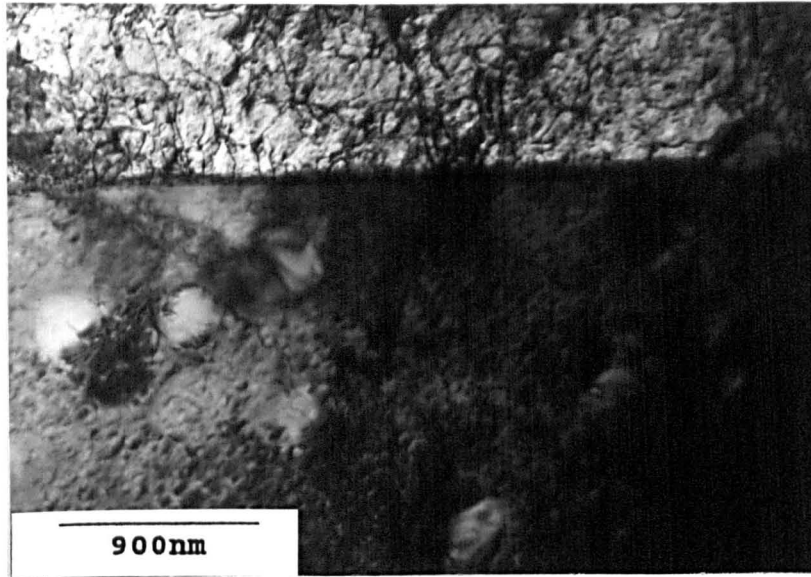
(a)
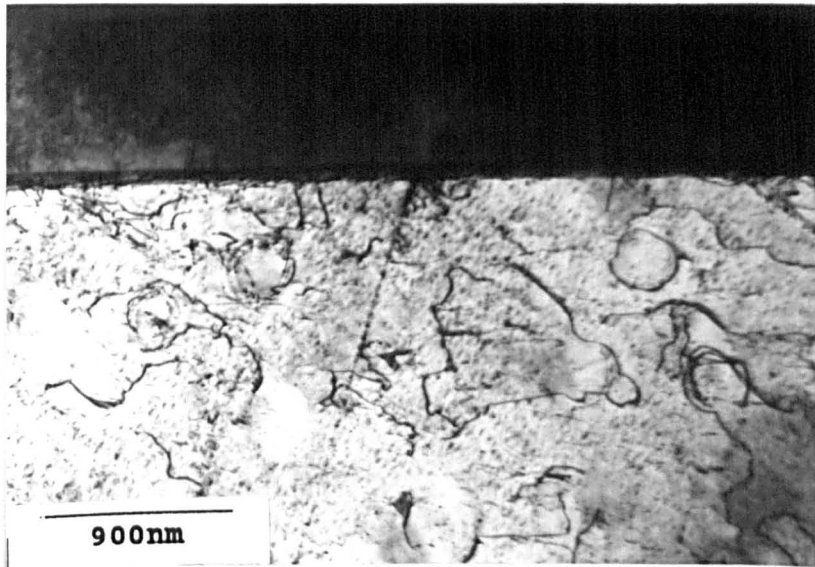
(b)

Fig. 4.64. Bright field transmission electron micrographs of a cross-sectional foil from specimen H2 (fracture at 100%PS) showing the continuation of slip over an annealing twin boundary, at a depth of 20μm.
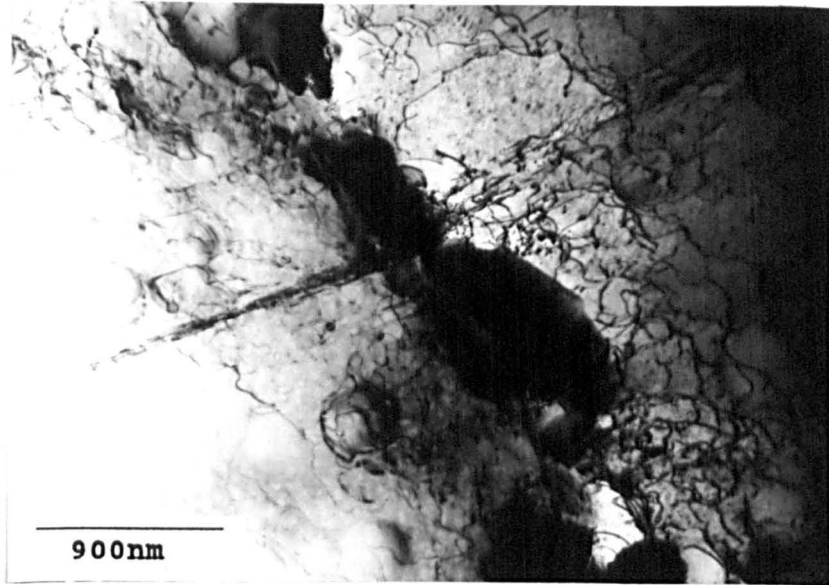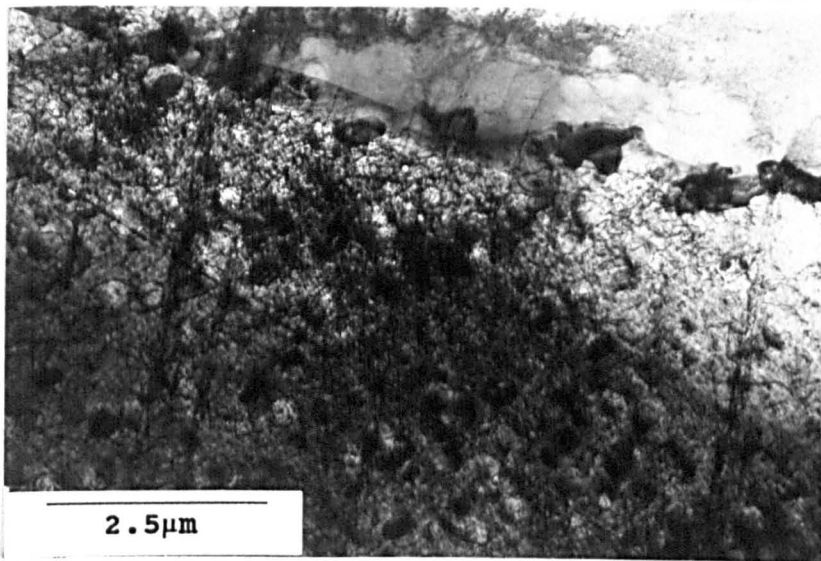
Fig. 4.65. Bright field transmission electron micrographs of cross-sectional foils from (a) specimen H8 (fracture at 80%PS) and (b) specimen H2 (fracture at 100%PS), showing the continuation of slip over grain boundaries, at depths of (a) 10μm and (b) 15μm.

900nm
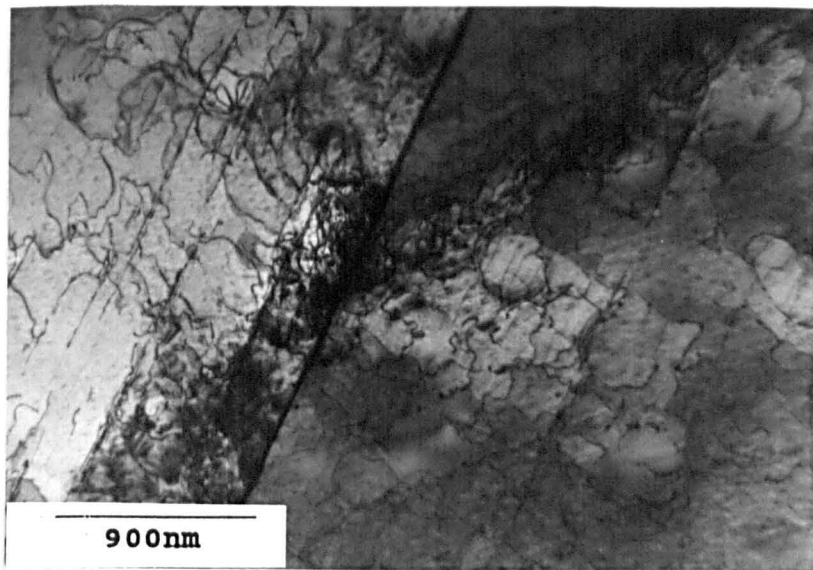
Fig. 4.66. Bright field transmission electron micrograph of a cross-sectional foil from specimen H3 (fracture at 80%PS) showing the arrest of slip over a twin boundary, at a depth of 30μm.

5 Discussion

5.1 Grain Structures

The turbine disc investigated in the current work exhibited a necklace microstructure at certain locations, in specific orientations (see Fig. 4.3(a, b)). It is not clear why the necklace microstructure was so localised, but was probably associated with differences in thermomechanical history across the disc. Miner et al. [10] reported necklace microstructures in both hot isostatically pressed and forged (H+F) Astroloy and H+F Rene' 95. Both of these alloys had higher strengths and contained higher γ' volume fractions than Waspaloy [10]. The higher strengths may not have been solely due to the different grain structures, but also the alloy content. Miner et al. [10] did not, however, report any improvement in fatigue resistances from the H+F Astroloy and H+F Rene' 95, when compared to several other high performance disc alloys which did not contain necklace microstructures. It was therefore, not immediately obvious what advantage in fatigue lifetime could be offered by a necklace microstructure.

5.2 Mechanical Properties

The 0.2% proof stress of the Waspaloy used in the present work was measured as 907-953MPa (specimens H10 and H54 respectively as shown in Table 4.2); the grain sizes at these locations were measured as 166.4 and 159.6µm (specimens H4 and H60 respectively as detailed in Table 4.1). The range in proof stress, was probably due to local

grain size differences, which varied substantially over the disc, as shown by Figs. 4.1-4.3. The values are higher than the 860MPa used by Zhang [46] and Brown et al. [59], for Waspaloy with finer grain sizes, 68μm [46] and 50μm [59] respectively. However, the Waspaloy that Stephens [7] tested also had a 50μm grain size but a proof stress of 930MPa. Furthermore, work carried out on Waspaloy by Antolovich [93] showed a proof stress range of 649-1003MPa, and demonstrated that the property depended not only on grain size but also precipitate size. Clearly, it is not adequate to simply test specimens cut from a turbine disc without knowing the location, orientation and tensile properties of those particular specimens.

5.3 Fatigue Behaviour

5.3.1 Deformation Structures

During the present investigation, three types of deformation were observed; i) planar slip, leading to the formation of persistent slip bands (PSBs), necessary to accommodate the imposed plastic strain during cyclic hardening and ultimately associated with softening due to precipitate shearing; ii) dislocation looping, particularly between PSBs, contributing to the overall cyclic hardening of the alloy; and iii) cellular deformation structures, associated with mild surface hardening due to the pinning of wavy dislocations by the large precipitates.

5.3.1.1 Planar Deformation

Early in fatigue life, i.e. 5,000 cycles at 100%PS and 75,000 cycles at 80%PS, PSB formation and particle shearing were in evidence as shown by Figs. 4.28 and 4.29 respectively. With increasing number of cycles planar deformation became widespread, as PSBs increased in thickness and number and propagated across grain boundaries. Dislocation densities generally increased, making precipitate shearing observations more difficult at higher numbers of cycles. Late in the fatigue life and at fracture, overall PSB densities were extremely high, the bands varied in thickness, contained extremely high dislocation densities and had propagated across the majority of grain boundaries into adjoining grains. However, it was possible to find localised areas of low dislocation density and the beginnings of fresh PSB formation even at fracture.

Calabrese and Laird [58] proposed that deformation occurred earliest in the few grains oriented for maximum resolved shear stress. As cycling continued, the initially deformed grains work hardened, which meant that more of the imposed plastic strain was then accommodated by softer grains, oriented further from the direction of maximum shear stress. This strain transfer continued until all of the grains, even those with slip planes oriented furthest from the maximum resolved shear stress, yielded [58]. Fig. 4.23(a) shows occasional grains early in the fatigue life (5,000 cycles at 100%PS), containing the beginnings of slip bands, which was taken as evidence for this mechanism. The

explanation would also account for the occasionally observed examples of low dislocation density (Fig. 4.48) and slip band formation (Fig. 4.46(b)) late in fatigue life. Clearly, therefore, not all of the structure had yielded at fracture.

Numerous reports have been made of tangling dislocations, PSB formation and precipitate shearing from the first fatigue cycle [16, 20, 21, 33, 49]. However, those tests were undertaken at extremely high strain levels, e.g. 0.83% [16] and 2.4% [33] giving fatigue lifetimes of 550 and 152 cycles respectively. When compared to the lifetimes in the present study, i.e. approximately 300,000 cycles at 100%PS and 3,500,000 cycles at 80%PS, then clearly there were substantial differences between the test parameters. Since extensometers were not used in the present work, strain levels could not be measured, but it is evident that they were substantially lower than those quoted above, hence the cycles were not as damaging. It is considered that deformation observed in the present work was comparable to that in the literature, at a proportional fraction of fatigue life.

Kuhlmann-Wilsdorf and Laird [111] suggested that during PSB formation the mechanisms of cross-slip, defect dragging and forest cutting were operative. However, due to the antiphase boundary (APB) strengthening and low stacking fault energies (SFEs) inherent in superalloys, cross-slip was considered extremely difficult [5, 19, 51]; it is therefore suggested that PSB formation in a superalloy is somewhat different to that in pure copper. The complexity of

a superalloy in itself, may be sufficient to warrant a different description of PSB formation to that in pure copper. Indeed, Lee and Laird [123] proposed that, although PSBs were reported to form from the collapse of loop patches in pure monocrystalline copper, PSB formation was much more complex in their relatively simple Al-4%Cu alloy.

Kuhlmann-Wilsdorf and Laird [112] also proposed that when a stress was applied to a PSB, the edge dislocations on one dipolar wall were transferred to the other, across the channel by similarly aligned screw dislocations. The proposal was based on investigations into pure monocrystalline copper. In the current work, PSBs consisted of numerous, closely spaced active slip planes, in which planar deformation was dominant. Early in fatigue life, individual active planes were visible, as shown by Fig. 4.26; parallel slip planes were also operative close by (see Figs. 4.27 and 4.29). The density of active planes within the bands increased with numbers of cycles, eventually to the extent that individual planes could not be imaged. No evidence of glissile dislocations were found during the early formation of bands, rather the bands were observed as a result of dislocation debris and precipitate shearing, as shown by Figs. 4.28 and 4.29 respectively. Ladder type structures were not evident, hence, it appears that PSB formation in a superalloy is different to that in pure copper [147, 148]. However, the reason why individual operative slip planes cluster, later resulting in a PSB, as opposed to occurring in a uniformly dispersed manner, is not

clear. It is probable that this is determined by a locally
easy path, for example, from a series of smaller
precipitates. This view is supported by the observations
that PSB width was always less than the size of the large
precipitates.

5.3.1.2 Cellular Deformation Structures

After 5,000 cycles at 100%PS and 75,000 cycles at
80%PS, wavy dislocations were observed in a few grains,
tangling into cell walls as shown by Figs. 4.33-4.35. With
increasing numbers of cycles, the cellular structures took
on a more pronounced appearance; after 20,000 cycles at
100%PS and 300,000 cycles at 80%PS, typical observations are
shown in Figs. 4.39 and 4.40. Later in the fatigue lives,
planar deformation became dominant and obscured the
appearance of the cells, Fig. 4.47 illustrates a typical
example of this. At fracture, no cells were observed in any
of the grains investigated. However, their presence could
not be absolutely ruled out because of the obscuring effect
of the very high planar dislocation density.

In addition to the cellular structures described above,
more densely packed dislocation networks were observed
around some of the large γ′, shown by Fig. 4.37(b). Such
dislocations appeared to be discrete and generally did not
extend between the large precipitates. However, an absolute
differentiation between the cellular and interfacial
networks was not possible. Only occasional examples of cell
structures in nickel base superalloys have been reported

[10, 19, 20, 25, 26, 98, 99]. One such example was observed during the 650°C fatigue of Astroloy [10], by Miner et al. [10] who reported that whereas dislocation pairs may have sheared the small spherical (20-50nm diameter) γ' present, there was insufficient stress for them to shear the large (100-300nm) cuboidal γ'. The dislocations were "jammed" between the faces of the large γ' producing a cell-like appearance [10]. This is distinct, therefore, from the normal mechanism of cell formation where recovery mechanisms allow dislocation rearrangement into low energy wall structures. Similar dislocation structures were observed during the high temperature fatigue of several cast nickel base superalloys. Approximate hexagonal networks of interfacial dislocations near edge in character were located at the large γ'/γ interfaces in Rene' 77 [25] and Rene' 80 [26, 98, 99] at various elevated temperatures.

The above alloys contained higher γ' volume fractions than Waspaloy (44% in Astroloy compared to 20% in Waspaloy [10]), with the precipitates in the form of large cuboids surrounded by small spheres [10, 25, 26, 28, 98]. This may have increased the tendency for more homogeneous deformation, similar to the observations made by Miner et al. [10] for a number of superalloys tested under identical conditions. In addition, the fatigue tests were carried out at high temperature, further increasing the probability of homogeneous deformation [5, 17, 19, 35, 42]. The examples of dislocation networks reported for the Astroloy [10], Rene' 77 [25] and Rene' 80 [26, 98, 99] showed some similarities

to the structures observed in the current work (Figs. 4.39 and 4.40) but also important differences. The dislocation networks reported in Rene' 80 at 982°C [26] were very similar in appearance to the interfacial networks shown in Fig. 4.37(b). However, the high temperature employed in the cycling of the Rene' 80 [26] allowed dislocation rearrangement by climb to lower energy structures, i.e., sub boundaries of hexagonal dislocation networks around the γ'. In the Waspaloy of the current work, dislocation rearrangement was very difficult due to the low temperature. Nevertheless, allowing for the differences in temperature, the mechanism in the current work is considered to be similar to that in the Rene' 80 [26].

In general, cellular deformation structures have not been reported during the room and elevated temperature fatigue of low γ' volume fraction superalloys. The exception to this was work carried out on Nimonic 80 by Lerch and Gerold [19, 20], who noted a difference in deformation structures between the surface and interior grains of their LCF specimens. The interior grains, observed in foils taken perpendicular to the stress axis, exhibited very planar slip; these results were in direct agreement with other workers for similar low γ' volume fraction superalloys [15, 16, 22-24, 29, 33, 43]. However, the surface grains, observed in back-thinned foils aligned parallel to the stress axis, exhibited cells bounded by hexagonal networks of dislocations [20]. In addition, a band structure was present, running parallel to {111} planes, on either side of

which existed a network of dislocations. Lerch and Gerold [20] reported that cellular deformation structures were never found in the interior grains of their specimens.

The slip band and its associated dislocation networks observed by Lerch and Gerold [20] was very similar to that of Fig. 4.42(a), also, the cellular deformation was not too dissimilar to the examples shown in Figs. 4.39(a) and 4.47(b). Furthermore, the diffraction pattern of Fig. 4.41 showing spot splitting, was very similar to those reported by Lerch and Gerold [20]. However, one noticeable difference was the obvious way that the dislocations encircled and were pinned by the large γ' precipitates of the Waspaloy in the present work (Fig. 4.39), whereas this was not apparent in the Nimonic 80 [19]. However, the Nimonic 80 [19, 20] only contained very fine spherical γ' (13nm in diameter), hence, such dislocation/precipitate interactions would be more difficult to observe.

Hence, it appears that comparable deformation structures have been observed in the surface grains of similar alloys. This implies that the lack of constraint at the free surface (i.e., a plane stress condition), allowed a dislocation structure normally associated with higher SFE materials. However, Lerch and Gerold [19, 20] failed to report when, during their tests, the cells were observed. References [19] and [20] suggest that the observations were made from specimens at fracture, since cycle numbers were not offered in figure captions or in the text. If that was the case, then an inconsistency exists between the works of

Lerch and Gerold [19, 20] and the present, where only planar deformation was observed at fracture, the cells having been only clearly observed earlier in fatigue life.

During the present work, cells were observed very clearly in early and mid fatigue life back-thinned foils; cells were not apparent at fracture in either back-thinned or cross-sectional foils. Since cross-sectional foils were only produced from fractured specimens, this work has not determined whether they are a two-dimensional feature or otherwise.

5.3.2 Shearing/Looping Observations

Confusion exists concerning the precipitate shearing and dislocation looping tendencies of superalloys [15-17, 35, 52, 54, 62-65]. Hornbogen and Verpoort [62] and Decker [52] reported that for superalloys in general, precipitates below a critical size would be sheared by dislocations, whereas the deformation mechanism for larger precipitates would be Orowan looping. Stoltz and Pineau [16] and Lerch et al. [17] agreed with the above from their investigations into numerous Waspaloy alloys, conditioned to contain different sizes of γ' precipitate. Stoltz and Pineau [16] established that 25nm was the critical particle size for the shearing/looping transition in Waspaloy alloys with a single γ' distribution. Lerch et al. [17] supported this result from their own independent investigation.

In the present study, both small (average 47nm) and large (average 231nm) γ' precipitates were looped,

consistent with the above. In the present work, direct evidence was found for large precipitate shearing. Shearing of the fine γ' was difficult to show conclusively because of the size of the slip band compared to the small γ' but available evidence indicated that both large and small precipitates were sheared within PSBs (see Fig. 4.29). Clearly, precipitates considerably larger than the 25nm transitional size were sheared.

Graf and Hornbogen [63] indicated that precipitate size was not the only factor influencing the shearing/looping transition, particle volume fraction and APB energy also affected the tendency. If the above factors were responsible for the inconsistent behaviour, there ought to be variations in the quantities of alloying elements Al and Ti between the works of [16, 17] and the present. However, Table 5.1 shows that only small, fractional differences are apparent between

Investigation	Alloying Element (wt %)	
	Al	Ti
Stoltz and Pineau [16]	1.37	3.07
Lerch et al. [17]	1.31	2.98
Present study*	1.40	3.00
Merrick [15]	1.37	3.01
Clavel et al. [35]	1.44	2.99

*As supplied by Rolls Royce, Derby.

Table 5.1. Alloying element quantities of Al and Ti.

these three sets of values.

In agreement with the present work, shearing of 150nm [35] and 200-250nm [15] precipitates were reported in Waspaloy alloys containing bimodal distributions of γ'. The amounts of alloying elements Al and Ti were very similar to those above as shown in Table 5.1, therefore variations in γ' volume fractions and APB energies are of secondary importance to the bimodal distribution in determining the interaction mechanism.

Merrick [15] proposed that dislocations initially bowed around the large particles leaving Orowan loops but subsequently sheared the γ'. This is a more feasible description of the behaviour of the Waspaloy currently investigated, than the shearing/looping transition detailed by Stoltz and Pineau [16], in conjunction with γ' volume fraction and APB energy implications from Graf and Hornbogen [63]. Indeed, Brechet and Louchet [64] reinforced the proposal from Merrick [15], demonstrating in an Al-Li alloy, that initially looped precipitates were sheared by the loops, which had become unstable when the stress had increased above a critical value.

Clearly, the results discussed in this sub-section have illustrated that substantial differences in behaviour are possible from an alloy having nominally the same composition, in this case, Waspaloy. To study fatigue deformation purely as a function of precipitate size is academic. The behaviour may well not be consistent with that of the same alloy taken from an actual turbine disc, as in

the present study, or the same alloy which has been conditioned using the conventional heat treatment [15, 35].

5.3.3 Cyclic Response

The Waspaloy used in the present study demonstrated slip band formation and precipitate shearing early in the fatigue life, as shown by Figs. 4.26-4.32. This suggests that the alloy hardened to a peak stress then softened [15-17, 21, 33, 51], as opposed to hardening to a saturation stress (where precipitate shearing would have been absent) as with certain types of Waspaloy [16, 17]. Indeed, it has been demonstrated that Waspaloy alloys containing bimodal γ' distributions have exhibited hardening followed by softening [15, 35].

In addition, since crack initiation in the present Waspaloy was observed early in life, typically 1/12 lifetime, the alloy had probably been heat treated to deform in a planar manner [17, 34, 61, 93]. Since planar conditioned alloys in general exhibit hardening to a peak stress followed by softening [16, 17, 50, 51], then, although cyclic response curves were not obtained during the present investigation, it is probable that the current Waspaloy followed this same behaviour.

The observations of precipitate shearing so early in fatigue life support the suggestions from Merrick [15] and Antolovich and Lerch [51], that softening occurs from the onset of cycling but is masked by the rapid hardening behaviour, from dislocation looping, cell formation and the

tangling of and restriction to mobile dislocations at the intersections of PSBs.

During early fatigue life in the present investigation, dislocation densities were relatively low and the cyclic hardening of the Waspaloy was identified by the beginning of slip band formation, dislocation tangling, cell formation and Orowan looping. The formation of slip bands (shown by Figs. 4.26-4.32) was necessary to accommodate the imposed plastic strain [16, 20, 23, 51]; dislocation tangles at slip band intersections would contribute to hardening by restricting the motion of mobile dislocations [21, 51]. In a similar way, the large γ' pinned wavy dislocations in the walls of the cellular deformation structures, which would further restrict mobile dislocation motion (see Figs. 4.34, 4.39 and 4.40). In addition, Orowan looping of precipitates (e.g. Figs. 4.32 and 4.38(a)) would force slip on to other planes, giving local hardening, contributing to the overall hardening of the alloy [15-17].

With increasing number of cycles, dislocation densities increased substantially, making the description of the hardening mechanism late in fatigue life very difficult. However, it was possible to locate areas of low dislocation density; the formation of fresh slip bands late in life is shown in Fig. 4.45(a), and dislocation pinning by small precipitates is evident from Fig. 4.45(b).

Precipitate disordering [16, 52], dissolution [15, 22] and fragmentation [22] have been proposed as responsible for cyclic softening at room temperature. Clear evidence of

precipitate shearing was obtained, Figs. 4.29 and 4.37(b) illustrate precipitates which have been sheared in early and mid fatigue life respectively. The example shown in Fig. 4.29 has been sheared by two slip bands, each displacement was estimated as 60nm. Taking the Burgers vector, b = a/2<011> and an approximate lattice parameter of 0.36, assuming dislocations of one type moving in one direction, the resultant number of dislocations responsible for this 60nm deflection was (2)(60)/0.36 = 333. Comparing this with approximately 10 dislocations tangling into the beginnings of the cell wall, shown in Fig. 4.33(a), this illustrates the substantial difference in strain accommodation within the PSBs to that between them. Also, assuming the grain illustrated in Fig. 4.29 was of average diameter, i.e., approximately 160μm, the strain imposed on the grain by the individual PSB is: 0.06/160 = 0.038%.

Similarly, the displacement of the sheared precipitate shown in Fig. 4.37(b) was estimated as 34nm, hence, (2)(34)/0.36 = 189 dislocations were responsible. Dislocation densities within the cell walls at comparable lifetimes shown in Figs. 4.39 and 4.40 were still relatively low, therefore the deformation was primarily planar.

Later in the fatigue life, high dislocation densities within bands did not permit the imaging of precipitates, in agreement with Lerch and Gerold [20].

5.3.4 Deformation vs Applied Stress Level

Greater amounts of deformation, in terms of the area

covered by and the severity of appearance of surface slip bands, and the numbers of secondary cracks observed, were noted at higher stress levels. Table 4.4 gives details of crack numbers and Figs. 4.10 and 4.11 show optical examples of the differences in surface deformation which existed. Greater cyclic hardening has been related to increasing strain amplitude [10, 17, 19-21, 23]. Lerch and Gerold [21] proposed that there was less cyclic hardening at low strain ranges because dislocations moved back and forth from one grain boundary to the other, on one slip system only. In agreement, single slip was observed by workers who had subjected alloys to low strain ranges [10, 21-24]. Lerch and Gerold [21] continued to explain that at higher strain ranges, since multiple slip occurred, dislocations could only move from one slip intersection to the next before piling up; dislocation motion was therefore more restricted and the result was greater hardening. Since numbers of slip bands increased to accommodate greater amounts of cyclic strain [16, 20, 23, 51], then the above is in direct agreement with the current work.

TEM observations in the present work however, indicated little, if any, difference in dislocation behaviour, structure or densities for equivalent fatigue lifetimes between the 100%PS and 80%PS levels. Since the Waspaloy used for this work was in an annealed condition prior to usage, and therefore cyclically hardened [94] (see Fig. 5.1) then, although testing was undertaken at 100%PS, i.e. the monotonic yield stress of the alloy, within a few cycles it
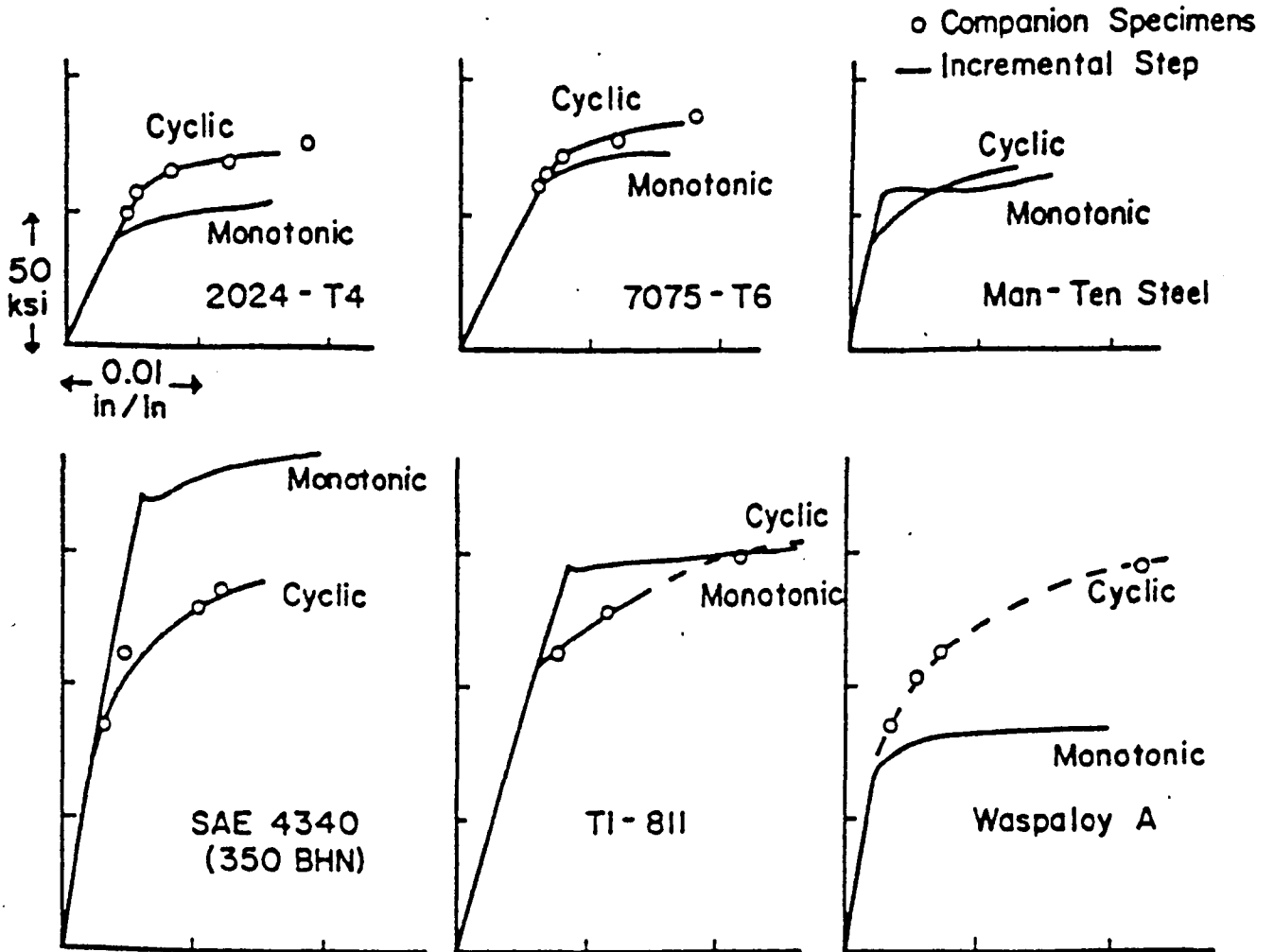
Fig. 5.1. Monotonic and cyclic stress-strain curves for representative materials [94].

had cyclically hardened sufficiently that the level of
100%PS was subsequently lower than the new "cyclic yield
stress". Hence the 100%PS specimens deformed in a similar
manner to the 80%PS specimens, therefore exhibited similar
dislocation behaviour.

A wide variation in deformation levels were observed
during TEM studies, both within an individual sample and
between samples at different stress levels. Indeed, at
similar depths, in one instance, more deformation was
observed from an 80%PS foil than a 100%PS foil (shown by Fig
4.57). This variation is consistent with reports on a number
of nickel base superalloys by Miner et al. [10]. Such
differences were clearly attributable to variations in
resolved shear stress and grain size. Therefore, it would be
extremely difficult to model the behaviour or extent of
deformation with depth using the results from this
investigation. A more extensive research programme would
perhaps allow more accurate correlations to be made
concerning deformation with depth and deformation with grain
orientation. However, it is considered that the maximum
dislocation density observed did increase with applied
stress and that crack initiation would most probably be
associated with the most highly deformed grains.

5.3.5 Crack Initiation

Crack initiation occurred predominantly from inclusions
situated on the gauge surfaces of fatigue specimens; only
occasional observations were made of slip band cracks as

illustrated in Fig. 4.23(e) and possible grain and twin boundary crack initiation is shown by Figs. 4.19 and 4.21 respectively. This result is in contrast to other Waspaloy alloys [7, 15, 17, 43, 46, 47], in which slip band cracking was reported as the dominant mechanism of fatigue failure [7, 15, 17, 43, 46, 47], with twin boundaries and carbides reported as additional initiation sites [15, 43]. In superalloys with similar microstructures to Waspaloy, slip bands [20] and twin boundaries [29, 33] were the most favourable crack initiation sites for room temperature fatigue.

Numerous of the above tests were carried out under fully reversed push pull fatigue [7, 15, 17, 20, 29, 33], in which the compression halves of each cycle may have retarded cracking from inclusions. However, the remainder of the above tests [43, 46, 47] were carried out with specimens taken from actual turbine discs, under conditions similar to those of the present, i.e., R = 0.1 and applied stress levels in the range 75-92% proof stress. It is therefore unclear why the differences in initiation mechanism exist.

In agreement with the present work, Gell et al. [49] stated that inclusions were one of the most common initiation sites for fatigue cracks in nickel base superalloys; Suresh and Richie [68] agreed that, whereas slip bands and their associated extrusions were responsible for cracking in pure metals and alloys, inclusions and intermetallics were to blame for cracking in commercial materials.

Clear differences exist in the appearance of the initiation sites on the two fracture surfaces examined. The initiation site shown in Fig. 4.25(a) appears very smooth, suggesting that a slip band crack has formed. In contrast, the rough appearance of the site shown in Fig. 4.24(a) suggests that the crack faces have contacted. This is consistent with work by Reed and King [79] who reported that crack closure effects at R = 0.1 resulted in fretting damage and surface debris. Features similar in appearance to etch pits are clearly visible on Fig. 4.24(a), indicating that crack face contact may have removed γ' precipitates from the alloy matrix.

Cracked inclusions were present on gauge surfaces of specimens prior to fatigue testing, Fig. 4.22(a) shows an example of a cluster of pre-cracked inclusions. However, the crack shown in Fig. 4.22(c) has propagated from the inclusion into the matrix, but it has not caused failure of that specimen. This suggests that the Waspaloy investigated exhibits a degree of tolerance towards cracked particles, even though they were situated on the fatigue surface and hence subjected to the maximum tensile stress, and were the most common crack initiation site.

Merrick [15] reported that MC carbides in his Waspaloy were sources of crack initiation, but the cracks rarely propagated more than a few particle diameters. Merrick [15] suggested that the carbide cracks formed later in the tests and played a key role in crack coalescence during propagation. However, the above suggestion is in contrast to

the present work where pre-cracked particles were observed.

The inclusions observed were generally angular in shape, as shown by the examples of Fig. 4.22. Gell and Leverant [103] reported pre-cracked carbides in their Mar-M200, the cracks always being parallel to the long dimension of the intermetallics and closely following any contour(s) of an irregular shaped particle. However, the intermetallics contained in the Mar-M200 are sufficiently different in appearance to those in the present investigation.

From replica studies, crack initiation predominantly occurred from inclusions, however, no evidence of cracks associated with particles was observed during TEM investigations. This may be due to the constraints imposed on the project, i.e. having only limited time to search and eventually find initiating inclusions or those containing cracks. This is feasible since, not all of the inclusions observed on replicas were associated with crack initiation.

Table 4.4 shows that at low stresses there were very few secondary cracks observed on specimens, whereas at higher levels, the numbers had increased dramatically. This is in direct agreement with studies made by Gell et al. [49], who also reported that crack coalescence was greater at higher fatigue strains. Coalescence of the fatal crack was demonstrated in specimen H25 and is shown in Fig. 4.13; it is feasible that the greater numbers of fatigue cracks observed at the higher stress levels in the current study, would make crack link-up easier than at lower stresses,

where only 4-5 cracks were observed over the entire gauge surface of a specimen.

It is not clear why most of the cracks initiated near to a load point of the span in the bending configuration; in four point or pure bending, according to simple bending theory [146], the maximum stress is constant on the tensile surface between the two points of the span. In similar work carried out by Zhang [46], two different span/width ratios were used, i.e. 2.5 and 1.0; she reported that for the longer span, cracks always initiated close to a load point, whereas initiation occurred more centrally in the case of the shorter span. It was thought that the latter case could be considered more equivalent to a three point bend configuration [46]; additionally, in work carried out by Baxter [48], a span/width ratio of 3.5 was used and here also, cracking occurred close to a load point. Nisitani and Mori [149] demonstrated that the stress intensity factors for small cracks in four point bending increased by up to 7% when the span/width ratio was reduced from 2.5 to 1.0. Following this, tests undertaken by Zhang [46] in the shorter span configuration, ought to have given shorter fatigue lifetimes than those in the longer span configuration, she did not however, report any significant difference in lifetimes between the two test configurations. However, only four specimens were tested in each case and a more extensive research programme may have uncovered significant differences.

According to the principle of de St. Venant [150], the

stress across the span in four point bending is constant, and while this is almost correct it is not strictly so. The fringe pattern obtained from photoelasticity studies [150] shown in Fig. 5.2 illustrates the almost constant stress distribution on the tensile surface of the plastic specimen, but whereas the fringes deviate from being parallel to the surface at locations corresponding to the load points on the compressive surface, they actually indicate a decrease in stress as opposed to a stress concentration. It would therefore appear that uneven roller contact was responsible for the cracking in these locations.

Cracks initiated from gauge surface edges, even though they were radiused during electropolishing. It is not clear whether the initiation was due to radii being too small, or due to inclusions situated on the gauge surface edges. Yates [45] reported that a great advantage of round section fatigue specimens was that there were no edges from which preferential crack initiation may occur, hence the edges of bend specimens may still pose a problem.

5.3.6 Fracture Surface Analysis

Fatigue crack propagation initially occurred by a stage-I mode, leaving a fracture surface exhibiting crystallographic facets. Since both the γ matrix and the γ' slip on $\{111\}<011>$ at low temperatures [5, 56] and near threshold growth occurs on slip planes in the crack tip plastic zone [5], then it can be considered that the crystallographic facets have a $\{111\}$ orientation. Indeed,
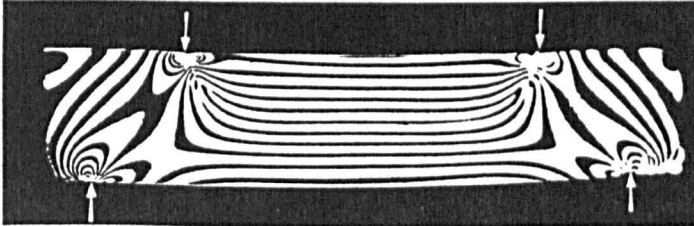
Fig. 5.2. Fringe pattern in beam under flexure, showing
rapid disappearance of effects due to local stresses
produced by end loads [150].

both Laue back reflection x-ray techniques and etching experiments have confirmed this [83, 151, 152].

A transition from faceted to striated growth was observed at a crack depth of 1.0mm (approximately 6 grains) at 100%PS and 2.1mm (approximately 12 grains) at 80%PS, as the crack growth changed to a stage-II mechanism [5]. To calculate the stress intensity factors at the stage-I/stage-II transitions, the following LEFM expression [146] was used:

$$\Delta K_1 = Y \Delta \sigma (\pi b)^{1/2} \qquad (5.1)$$

where ΔK_1 = stress intensity factor range

Y = geometrical loading factor

$\Delta \sigma$ = applied stress range

b = crack depth

The surface crack lengths at the transitions were measured as approximately 2.48 and 5.18mm for the 100%PS and 80%PS cases respectively. Therefore, if the surface crack length is denoted by "2a" as shown in Fig. 5.3, then the aspect ratios for the stage-I/stage-II crack transitions, b/a are approximately 0.8 at both stress levels, which is in direct agreement with the results of Zhang [46].

Since stress intensity factors are dependent on specimen geometry and the applied loading mode, the factor Y was calculated according to Newman and Raju [153]. For semi-elliptical cracks with the above dimensions under
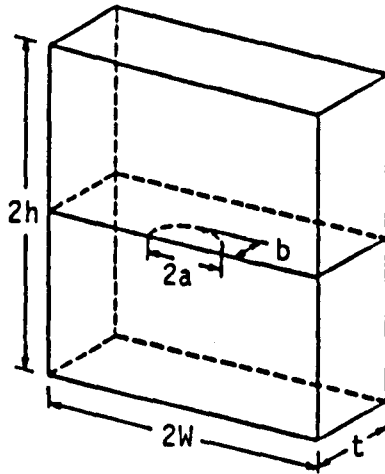
Fig. 5.3. Semi-elliptical surface crack geometry under pure bending [153].

bending, the stress intensity factor expressions were determined as:

$$\Delta K_1 = 0.652\Delta\sigma(\pi b)^{1/2} \qquad (5.2)$$

for the 100%PS specimen and

$$\Delta K_1 = 0.568\Delta\sigma(\pi b)^{1/2} \qquad (5.3)$$

for the 80%PS specimen. Substituting values of stress range and crack depth into equations (5.2) and (5.3) yielded ΔK_1 values of 29.8 and 30.1MPa.m$^{1/2}$ at 100%PS and 80%PS respectively. These transitional ΔK_1 values appear higher than those from other work on Waspaloy; a value of 14MPa.m$^{1/2}$ was reported by Clavel et al. [35] and Clavel and Pineau [36], and 19MPa.m$^{1/2}$ was determined by Stephens [7] from linear regression of his in-situ SEM work. However, the above results were obtained from Waspaloy alloys having smaller grain sizes than that of the current work, approximately 50μm as opposed to the current 160μm. The coarse (125μm) grained Waspaloy specimens used by Antolovich and Jayaraman [61] yielded transitional ΔK_1 values in the range 44-71MPa.m$^{1/2}$. In addition, King [5] noted that for coarse grained superalloys in general, it was possible for the structure sensitive, faceted growth to extend up to ΔK_1 values of 40MPa.m$^{1/2}$. Hence the ΔK_1 values determined from the current work compare well with those from coarser grained alloys. Moreover, an absolute measure of the transition was difficult. Very fine striations were

occasionally observed on grains which were essentially faceted and it was only after further crack propagation that striations were found to dominate the crack surface.

The cause of the stage-I/stage-II transition was associated with microstructural features such as grain boundaries [154] and/or due to a decrease in the τ/σ ratio at the crack tip resulting from movement away from the free surface [155], where τ and σ are the shear and tensile stresses respectively.

The current work has shown stage-I/stage-II transition crack depths of 1.0 and 2.1mm (at 100%PS and 80%PS respectively); in order to determine the plastic zone size ahead of the crack tip at the transition, the following LEFM expression [146] was applied:

$$r_s = (1/2\pi)(\Delta K_1/\sigma_y)^2 \qquad (5.4)$$

where r_s = plastic zone size

ΔK_1 = stress intensity factor range

σ_y = yield stress

Substituting known values into equation (5.4) yielded plastic zone sizes of 84.0 and 85.5µm at 100%PS and 80%PS respectively. However, Brown [156] explained that for LEFM to be valid, only small scale yielding was permitted at the crack tip; equation (5.4) taken with the generally accepted small scale requirement $r_s < b/50$, provides the restriction that the applied stress should not exceed one third of the

yield stress [156]. Hence equation (5.4) was considered unsuitable for application to the high stress situations of the current work. Alternatively, the following elasto-plastic fracture mechanics (EPFM) expression, from modelling work by Brown et al. [157] was applied:

$$r_p = b\{\sec(\pi\Delta\sigma/2\Delta\sigma_o)-1\} \qquad (5.5)$$

where r_p = plastic zone size at crack tip

b = crack depth

$\Delta\sigma$ = applied stress range

$\Delta\sigma_o$ = cohesive stress within plastic zone

Substituting known values into equation (5.5) and equating the cohesive stress with twice the tensile strength [156], the plastic zone sizes were determined as 135µm (100%PS) and 175µm (80%PS), i.e. of the order of the grain size in both cases.

In TEM studies, continuation of slip in adjoining grains was not observed before fracture, in contrast to the optical results shown in Fig. 4.23. Slip had clearly propagated over grain boundaries by 50,000 cycles at 100%PS (Fig. 4.23(c)). It is unclear why this was not observed in earlier fatigue life foils in TEM. It is suggested that the problem was one of sampling and the TEM results concerning slip continuation, are not representative of the material behaviour in general.

At the 100%PS level, the crack depth at the

faceted/striated transition was measured as 1.0mm, or 6 grain diameters; from replica studies, cracks had propagated over 5-6 grains (i.e., the short/long crack transition) after 150,000 cycles. Therefore, the plastic zone size was comparable to the grain size by 150,000 cycles. Since slip had clearly propagated over grain boundaries by 50,000 cycles (Fig. 4.23(c)), this suggests that active slip bands were required before a crack could propagate, as opposed to the plastic zone at the crack tip initiating slip band formation.

5.4 The Modelling of Fatigue Damage Accumulation

It would prove extremely difficult to apply a model predicting fatigue crack initiation, based on dislocation activity, to the current work, due to the wide variation in dislocation densities between neighbouring grains. In addition, determining the parameters APB energy, dislocation flexibility, interface energy and line tension was reported as being difficult if not impossible [58, 130]. However, primary crack propagation is probably predicted from a combination of i) grains containing the highest dislocation densities, i.e. those oriented for maximum resolved shear stress, ii) grains containing PSBs orientated for the maximum resolved tensile stress, i.e. the maximum crack opening force and iii) similarly oriented neighbouring grains, with slip transferral over their grain boundaries.

6 Conclusions

(1) Considerable differences in grain structure were found across the turbine disc; it is proposed that the different grain sizes account for the variation in proof stress measurements.

(2) Fatigue damage occurred as a result of cell formation and Orowan looping, but predominantly by persistent slip band (PSB) formation and associated precipitate shearing.

(3) The number of PSBs increased throughout the fatigue life, as did the number of grains exhibiting deformation. Early in fatigue lives, only occasional grains had deformed by a single slip system, whereas late in life, multiple slip was evident in many grains; there was however, a large variation in deformation levels. It is proposed that deformation occurred earliest in those grains oriented for maximum resolved shear stress, as these grains work hardened, the strain was transferred to less favourably oriented grains. This strain transfer continued until eventually all grains had deformed, even those with orientations furthest from the direction of maximum resolved shear stress.

(4) PSBs consisted of numerous operative, closely spaced slip planes, which increased in density with number of cycles, until individual slip planes could not be imaged.

Ladder structures and glissile dislocations were not observed, rather the slip bands were visible as a result of dislocation debris and precipitate shearing.

(5) An homogeneous deformation structure, with walls of wavy dislocations pinned by large precipitates, dividing the grains into sub-grains or cells, was observed in a small number of grains. Cellular structures were only clearly observed during early and mid fatigue lives; after greater numbers of cycles, planar deformation became widespread and obscured the cells. The density of dislocations in cell walls and the misorientation between adjacent cells increased during early fatigue life. A misorientation of approximately 1.5° between neighbouring cells was evident during mid fatigue life, which was established from spot splitting in diffraction patterns. The plane stress lack of constraint at the free surface is considered responsible for allowing this dislocation structure, normally associated with higher stacking fault energy materials.

(6) Orowan looping occurred for both large and small precipitates. Shearing also occurred for both large and small precipitates. It is proposed that initially looped precipitates were subsequently sheared and that cyclic softening occurred immediately in the fatigue process, but was masked by the rapid hardening from dislocation tangles, cell formation and dislocation looping. Later life dislocation densities were extremely high in slip bands,

which did not permit the imaging of any precipitate fragments within the bands; however, sheared precipitates were observed early in the fatigue life, when dislocation densities were lower.

(7) The extent of deformation, in terms of surface slip bands and number of secondary cracks, increased with increasing stress level; crack coalescence was observed at higher stress levels. However, TEM investigations revealed no substantial differences in dislocation activity between the two selected stress levels: 100%PS and 80%PS. It is proposed that the cyclic hardening nature of the alloy accounted for this.

(8) It is proposed that the alloy cyclically hardened then softened, from evidence of slip band formation, dislocation tangles, Orowan looping and precipitate shearing. This is in agreement with other Waspaloy alloys which contained a bimodal γ' distribution.

(9) Crack initiation was observed by 1/12 of fatigue lifetime; predominant initiation sites were surface inclusions. A number of inclusions contained cracks prior to fatigue testing. Most fatal cracks were initiated close to one end of the four point bend span; this suggests that there are small variations in stress distribution in the localities of the load points.

(10) Fatigue crack propagation initially occurred by a stage-I mechanism, leaving facets on the fracture surface. A transition to a stage-II mechanism occurred at approximate ΔK_1 values of 30MPa.m$^{1/2}$, when the plastic zone size was comparable to the material grain size. The transitional ΔK_1 values are consistent with those for other coarse grained nickel base superalloys.

(11) Fatigue crack initiation was observed as early as 1/12 of the fatigue life; however, the short/long crack transition did not occur until approximately 1/2 of life. This transition quantitatively agreed with observations that slip transferral occurred between grains after 1/6 of life. This implies that short crack growth requires prior PSB deformation.

(12) The application of any model predicting fatigue crack initiation from dislocation activity, is far from straightforward. This is due to the large variations in dislocation density and slip band density between grains and the difficulty in the determination of model parameters. However, fatal crack propagation is probably predicted from a combination of the grains containing the highest dislocation densities, with slip bands and/or particle cracks oriented for the maximum resolved tensile stress and with neighbouring grains similarly oriented, with slip transferral between them.

7 Future Work

To obtain cross-sectional foils from specimens cycled to various fractions of fatigue lifetime would allow a greater understanding of fatigue damage accumulation. The development of the cellular structures could be further investigated, depending on whether they appear similar in cross-sectional specimens to back-thinned samples, i.e., as to whether they are a two or three dimensional feature.

Similar investigations at different locations of the disc would provide more insight into the influence of the grain size/structure; also, for a given location on the disc, investigating specimens in different orientations would highlight any variations in behaviour which may be evident. In addition, examining the rim of the disc would be useful since, this region is also prone to cracking, due to the fixing of blades.

Investigating the push pull cycling of Waspaloy turbine disc bore section material, would allow a direct comparison of surface/interior deformation behaviour. In addition, any differences in cracking mechanisms between the surfaces of the tension and bending specimens could be examined.

8 References

1   J. Stringer, Mater. Sci. Tech. **3**, 482 (1987).

2   D. Driver, Met. Mater. **1**, 345 (1985).

3   D. Driver, D. W. Hall and G. W. Meetham, in Development of gas turbine materials, (edited by G. W. Meetham), Applied Science Publishers Ltd., Essex, p.1 (1981).

4   A. S. Radcliff, Mater. Sci. Tech. **3**, 554 (1987).

5   J. E. King, Mater. Sci. Tech. **3**, 750 (1987).

6   K. J. Miller, Fat. Fract. Engng Mater. Struct. **10**, 93 (1987)

7   R. R. Stephens, Ph. D. Dissertation, University of Utah (1991).

8   N. A. Wilkinson, Met. Tech. **4**, 346 (1977).

9   F. Turner, in Development of gas turbine materials, (edited by G. W. Meetham), Applied Science Publishers Ltd., Essex, p.177 (1981).

10   R. V. Miner, J. Gayda and R. D. Maier, Metall. Trans. **13A**, 1755 (1982).

11   G. P. Sabol and R. Stickler, Phys. Stat. Sol. **35**, 11 (1969).

12   A. K. Jena and M. C. Chaturvedi, J. Mater. Sci. **19**, 3121 (1984).

13   E. W. Ross and C. T. Sims, in Superalloys II: High temperature materials for aerospace and industrial power (edited by C. T. Sims, N. S. Stoloff and W. C. Hagel), Wiley, New York, p.97 (1987).

14   B. A. Lerch, NASA Contract Report CR-165497 (1982).

15   H. F. Merrick, Metall. Trans. **5**, 891 (1974).

16   R. E. Stoltz and A. G. Pineau, Mater. Sci. Engng **34**, 275 (1978).

17   B. A. Lerch, N. Jayarman and S. D. Antolovich, Mater. Sci. Engng **66**, 151 (1984).

18   J. Bressers and B. Verhegghe, Res Mech. Lett. **1**, 55 (1981).

19   B. A. Lerch and V. Gerold, in Deformation of multiphase and particle containing materials (edited by J. B.

Bilde-Sorensen et al.), Riso National Laboratory, p.375 (1983).

20   B. Lerch and V. Gerold, Acta metall. **33**, 1709 (1985).

21   B. A. Lerch and V. Gerold, Metall. Trans. **18A**, 2135 (1987).

22   M. Sundararaman, W. Chen, V. Singh and R. P. Wahi, Acta metall. **38**, 1813 (1990).

23   V. Singh, M. Sundararaman, W. Chen and R. P. Wahi, Metall. Trans. **22A**, 499 (1991).

24   M. Sundararaman, W. Chen and R. P. Wahi, Scripta Metall. **23**, 1795 (1989).

25   S. D. Antolovich, E. Rosa and A. Pineau, Mater. Sci. Engng **47**, 47 (1981).

26   S. D. Antolovich, S. Liu and R. Baur, Metall. Trans. **12A**, 473 (1981).

27   C. J. Mc Mahon and L. F. Coffin Jr., Metall. Trans. **1**, 3443 (1970).

28   G. Jianting and D. Ranucci, Int. J. Fatigue **5**, 95 (1983).

29   D. Fournier and A. Pineau, Metall. Trans. **8A**, 1095 (1977).

30   G. Jianting, D. Ranucci, E. Pico and P. M. Strocchi, Proc. Symp. on High temperature alloys for gas turbines, Liege, October 4-6, 1982, Reidel, Dordrecht, p.805 (1982).

31   S. D. Antolovich, P. Domas and J. L. Strudel, Metall. Trans. **10A**, 1859 (1979).

32   L. F. Coffin Jr. Metall. Trans. **2**, 3105 (1971).

33   C. H. Wells and C. P. Sullivan, Trans ASM **57**, 841 (1964).

34   N. Jayaraman and M. M. Ditmars, Int. J. Fatigue **11**, 309 (1989).

35   M. Clavel, C. Levaillant and A. Pineau, in Creep-Fatigue-Environment-Interactions (edited by R. M. Pelloux and N. S. Stolloff), Metallurgical Society of AIME, Warrendale, Pa, p.24 (1980).

36   M. Clavel and A. Pineau, Mater. Sci. Engng **55**, 157 (1982).

37 C. H. Wells and C. P. Sullivan, Trans ASM **58**, 391 (1965).

38 C. H. Wells and C. P. Sullivan, Trans ASM **60**, 217 (1965).

39 F. E. Organ and M. Gell, Metall. Trans. **2**, 943 (1971).

40 M. Clavel and A. Pineau, Mater. Sci. Engng **55**, 173 (1982).

41 D. Diederich, B. Lerch and S. D. Antolovich, (Proc. Conf.) 8th Inter-American Conference on Materials, p.7.1 (1984).

42 C. H. Wells and C. P. Sullivan, Trans ASM **61**, 149 (1968).

43 J. C. Healy, L. Grabowski and C. J. Beevers, Int. J. Fatigue **13**, 133 (1991).

44 L. Grabowski and J. R. Yates, Int. J. Fatigue **14**, 227 (1992).

45 J. R. Yates, Final report for Rolls Royce Brochure B1J1-81D SMP 1058/3 (1990).

46 W. Zhang, Ph. D. Thesis, University of Sheffield (1991).

47 J. R. Yates, W. Zhang and K. J. Miller, (Proc. Conf.) Short Fatigue Cracks, E.S.I.S., Sheffield (1990).

48 G. J. Baxter, Ph. D. Thesis, University of Sheffield (1994).

49 M. Gell, G. R. Leverant and C. H. Wells, in Achievement of High Fatigue Resistance in Metals and Alloys, ASTM STP 467, p.113 (1970).

50 S. Y. Zamrik and D. C. Davies, in Life assessment and repair: Technology for combustion turbine hot section components (edited by R. Viswanathan and J. M. Allen), Phoenix, Arizona, p.77 (1990).

51 S. D. Antolovich and B. A. Lerch, in Superalloys, Supercomposites and Superceramics (edited by J. K. Tien and T. Caulfield), Academic Press Inc., p.363 (1989).

52 R. F. Decker, (Symp.) Steel Strengthening Mechanisms, Zurich, 1969, Climax Molybdenum Co., Greenwich, Conn. p.147 (1970).

53 B. H. Kear and D. P. Pope, in Superalloys, Supercomposites and Superceramics (edited by J. K. Tien and T. Caulfield), Academic Press Inc., p.545

(1989).

54   W. Huther and B. Reppich, Z. Metallkde **69**, 628 (1978).

55   P. A. S. Reed and J. E. King, in Short Fatigue Cracks, E.S.I.S. 13 (edited by K. J. Miller), M. E. P., London, p.153 (1992).

56   B. H. Kear and J. M. Oblak, J. de Physique **12**, 35 (1974).

57   R. F. Decker, in High temperature materials in gas turbines (edited by P. R. Sahm and M. O. Speidel), Elsevier Scientific, p.49 (1974).

58   C. Calabrese and C. Laird, Mater. Sci. Engng **13**, 141 (1974).

59   C. W. Brown, J. E. King and M. A. Hicks, Met. Sci. **18**, 374 (1984).

60   H. F. Merrick, D. H. Maxwell and R. C. Gibson, in Fatigue at elevated temperatures, ASTM STP 520, p.285 (1973).

61   S. D. Antolovich and N. Jayaraman, in Fatigue, Environment and Temperature Effects (edited by J. J. Burke and V. Weiss), Plenum Press, NY, p.119 (1983).

62   E. Hornbogen and C. Verpoort, in Superalloys 1980 (edited by J. T. Kien et al.), A.S.M., Champion, Pa, p.585 (1980).

63   M. Graf and E. Hornbogen, Scripta Metall. **12**, 147 (1978).

64   Y. Brechet and F. Louchet, Acta Metall. **37**, 2469 (1989).

65   E. Nembach, K. Suzuki, M. Ichihara and S. Takeuchias, Phil. Mag. **56A**, 439 (1987).

66   C. E. Feltner and P. Beardmore, in Achievement of High Fatigue Resistance in Metals and Alloys, ASTM STP 467, p.77 (1970).

67   J. C. Healy, L. Grabowski and C. J. Beevers, Fat. Fract. Engng Mater. Struct. **15**, 309 (1992).

68   S. Suresh and R. O. Richie, Int. Metal Rev. **29**, 445 (1984).

69   K. J. Miller, (Symp.) Fundamentals of Deformation and Fracture (edited by B. A. Bilby et al.), Cambridge University Press, p.477 (1985).

70   K. J. Miller, Fat. Engng Mater. Struct. **5**, 223 (1982).

71   P. Lukas, L. Lunz, B. Weiss and R. Stickler, Fat. Fract. Engng Mater. Struct. **9**, 195 (1986).

72   K. Yamada, M. G. Kim and T, Kunio, in The behaviour of short fatigue cracks (edited by K. J. Miller and E. R. de los Rios), M.E.P., I.Mech.E., London, p.261 (1986).

73   K. J. Miller, Twenty-seventh John-Player Lecture: Metal Fatigue-past, current and future, M.E.P., I.Mech.E., London, (1991).

74   S. Z. Wang, K. J. Miller, M. W. Brown and E. R. de los Rios, Fat. Fract. Engng Mater. Struct. **14**, 351 (1991).

75   D. L. Anton and M. E. Fine, Mater. Sci. Engng **58**, 135 (1983).

76   S. Pearson, Engng Fract. Mech. **7**, 235 (1975).

77   W. L. Morris, Metall. Trans. **10A**, 5 (1979).

78   K. Tanaka, Y. Nakai and M. Yamashita, Int. J. Fract. **17**, 519 (1981).

79   P. A. S. Reed and J. E. King, Scripta Metall. **26**, 1829 (1992).

80   P. A. S. Reed, P. Woolin and J. E. King, in Fatigue '90: 4th International Conference on Fatigue and Fatigue Thresholds, Honolulu, Hawaii, M.C.E.P., Vol.II, p.1085 (1990).

81   L. A. James and W. J. Mills, Engng Fract. Mech. **22**, 797 (1985).

82   J. E. King, Met. Sci. **16**, 345 (1982).

83   J. E. King, Fat. Engng. Mater. Struct. **4**, 311 (1981).

84   H. W. Liu and Y. Oshida, NASA Contract Report CR-3003-3 (1988).

85   B. A. Lerch, Ph. D. Dissertation, University of Stuttgart, West Germany (1983).

86   J. Bressers and M. Roth, in Advances in life prediction methods (edited by D. A. Woodford and J. R. Whitehead), ASME, NY, p.85 (1983).

87   R. A. Venables and J. E. King, in Fatigue '84 (edited by C. J. Beevers), Warley, W. Midlands, E.M.A.S., Vol. 3, p.1371 (1984).

88 R. W. Hayes and W. C. Hayes, Acta metall. **30**, 1295 (1982).

89 R. A. Mulford and U. F. Kocks, Acta Metall. **27**, 1125 (1979).

90 T. A. Bloom, U. F. Kocks and P. Nash, Acta Metall. **33**, 265 (1985).

91 A. K. Koul and F. B. Pickering, Scripta Metall. **16**, 119 (1982).

92 J. L. Kaae and R. E. Villagrama, in Alloy 800 (edited by W. Betteridge et al.), North-Holland, Amsterdam, p.181 (1978).

93 S. D. Antolovich, (Proc.) Japan-U.S. Seminar on Superalloys, Susono, Japan, p.369 (1985).

94 R. W. Landgraf, in Achievement of High Fatigue Resistance in Metals and Alloys, ASTM STP 467, p.3 (1970).

95 G. Jianting, D. Ranucci and E. Picco, Mater. Sci. Engng **58**, 127 (1983).

96 G. Jianting and D. Ranucci, Int. J. Fatigue **6**, 95 (1984).

97 L. F. Coffin Jr., Metall. Trans. **5**, 1053 (1974).

98 S. D. Antolovich, P. Domas and J. L. Strudel, Metall. Trans. **10A**, 1859 (1979).

99 S. D. Antolovich and N. Jayaraman, High Temp. Tech. **2**, 3 (1984).

100 G. R. Leverant and M. Gell, Trans. AIME **245**, 1167 (1969).

101 W. W. Milligan, N. Jayaraman and R. C. Bill, Mater. Sci. Engng **82**, 127 (1986).

102 T. P. Gabb, G. Welsch and R. V. Miner, Scripta Metall. **21**, 987 (1987).

103 M. Gell and G. R. Leverant, Trans. AIME **242**, 1869 (1968).

104 M. Gell and G. R. Leverant, Acta Metall. **16**, 553 (1968).

105 J. W. Provan, (Proc. Conf.) 10th Canadian Fracture Conference, Waterloo, Canada, p.131 (1983).

106 J. W. Provan and Z. H. Zhai, [Proc. Conf.] 11th

Canadian Fracture Conference, Waterloo, Canada, p.201 (1984).

107 D. Kuhlmann-Wilsdorf, Mater. Sci. Engng **39**, 127 (1979).

108 D. Kuhlmann-Wilsdorf, Mater. Sci. Engng **39**, 231 (1979).

109 H. Mughrabi, Mater. Sci. Engng **33**, 207 (1978).

110 B. Ramaswani, Bull. Mater. Sci. **12**, 195 (1989).

111 D. Kuhlmann-Wilsdorf and C. Laird, Mater. Sci. Engng **46**, 209 (1980).

112 D. Kuhlmann-Wilsdorf and C. Laird, Mater. Sci. Engng **27**, 137 (1977).

113 D. Kuhlmann-Wilsdorf and C. Laird, Mater. Sci. Engng **37**, 111 (1979).

114 U. Essmann, U. Goesele and H. Mughrabi, Phil. Mag. A **44**, 405 (1981).

115 C. Laird, P. Charsley and H. Mughrabi, Mater. Sci. Engng **81**, 433 (1986).

116 W. H. Kim and C. Laird, Acta metall. **26**, 777 (1978).

117 W. H. Kim and C. Laird, Acta metall. **26**, 789 (1978).

118 C. E. Feltner and C. Laird, Acta Metall. **15**, 1621 (1967).

119 C. E. Feltner and C. Laird, Acta Metall. **15**, 1633 (1967).

120 A. Abel, M. Willhelm and V. Gerold, Mater. Sci. Engng **37**, 187 (1979).

121 L. P. Karjalainen, Mater. Sci. Engng **38**, 145 (1979).

122 C. H. Wells, Acta Metall. **17**, 443 (1969).

123 J. K. Lee and C. Laird, Mater. Sci. Engng **54**, 53 (1982).

124 S. P. Bhat and C. Laird, Acta Metall. **27**, 1873 (1979).

125 K. C. Russel and M. F. Ashby, Acta Metall. **18**, 891 (1970)

126 C. Calabrese and C. Laird, Mater. Sci. Engng **13**, 159 (1974).

127 N. J. Petch, J. Iron & Steel Inst. **174**, 25 (1953).

128 H. Gleiter and E. Hornbogen, Mater. Sci. Engng **2**, 287 (1968).

129 P. Guyot, Phil. Mag. **24**, 987 (1971).

130 A. J. Ardel and J. C. Huang, Phil. Mag. Lett. **58**, 187 (1988).

131 W. J. Baxter, in The behaviour of short fatigue cracks (edited by K. J. Miller and E. R. de los Rios), M.E.P., I.Mech.E., London, p.193 (1986).

132 W. J. Baxter and P. C. Wang, Metall. Trans. **19A**, 2457 (1988).

133 V. M. Radhakrishnan and Y. Mutoh, in The behaviour of short fatigue cracks (edited by K. J. Miller and E. R. de los Rios), M.E.P., I.Mech.E., London, p.87 (1986).

134 J. Polak, Mater. Sci. Engng **92**, 71 (1981).

135 M. R. Lin, M. E. Fine and T. Mura, Acta Metall. **34**, 619 (1986).

136 C. V. Cooper and M. E. Fine, Scripta Metall. **18**, 593 (1984).

137 P. D. Hobson, M. W. Brown and E. R. de los Rios, in The behaviour of short fatigue cracks (edited by K. J. Miller and E. R. de los Rios), M.E.P., I.Mech.E., London, p.441 (1986).

138 P. D. Hobson, Fat. Engng Mater. Struct. **5**, 323 (1982).

139 M. W. Brown, in The behaviour of short fatigue cracks (edited by K. J. Miller and E. R. de los Rios), M.E.P., I.Mech.E., London, p.423 (1986).

140 J. Lankford, Fat. Engng Mater. Struct. **5**, 233 (1982).

141 J. R. Yates and L. Grabowski, in Fatigue '90: 4th International Conference on Fatigue and Fatigue Thresholds, Honolulu, Hawaii, M.C.E.P., Vol.13, p.2369 (1990).

142 A. Navarro and E. R. de los Rios, Fat. Fract. Engng Mater. Struct. **10**, 169 (1987).

143 A. Navarro and E. R. de los Rios, Phil. Mag. **57A**, 37 (1988).

144 A. Navarro and E. R. de los Rios, Phil. Mag. **57**, 15 (1988).

145 Zuyu Sun, E. R. de los Rios and K. J. Miller, Fat.

Fract. Engng Mater. Struct. **14**, 277 (1991).

146 P. P. Benham and R. J. Crawford, Mechanics of Engineering Materials, Wiley, New York (1987).

147 R. Wang and H. Mughrabi, Mater. Sci. Engng **63**, 147 (1984).

148 R. Wang and H. Mughrabi, Mater. Sci. Engng **65**, 235 (1984).

149 H. Nisitani and K. Mori, in Tech. Reports of the Kyushu Univ., Vol.58, No.5, p.751 (1985).

150 S. Flugge (editor), Encyclopedia of Physics, Vol. VI, Elasticity and Plasticity, Springer-Verlag, p.203 (1958).

151 D. J. Duquette and M. Gell, Metall. Trans. **2**, 1325 (1971).

152 N. J. Vincent and L. Remy, in Fatigue Thresholds (edited by J. Backlund et al.), Warley, W. Midlands, E.M.A.S., Vol.1, p.441 (1983).

153 J. C. Newman, Jr and I. S. Raju, Engng Fract. Mech. **15**, 185 (1981).

154 M. W. Brown and K. J. Miller, Fat. Engng Mater. Struct. **1**, 231 (1979).

155 W. J. Plumbridge and D. A. Ryder, Metall. Rev. **14**, 119 (1969).

156 M. W. Brown, (Proc.) I. Mech. E., Vol. 202, C1, p.19 (1988).

157 M. W. Brown, E. R. de los Rios and K. J. Miller, (Symp.) Fundamental Questions and Critical Experiments on Fatigue, Dallas, A.S.T.M. (1984).